ANISOTROPIC CHARACTERIZATION AND PERFORMANCE PREDICTION OF CHEMICALLY AND HYDRAULICALLY BOUNDED PAVEMENT FOUNDATIONS

A Dissertation

by

REZA SALEHI ASHTIANI

Submitted to the Office of Graduate Studies of
Texas A&M University
in partial fulfillment of the requirements for the degree of

DOCTOR OF PHILOSOPHY

August 2009

Major Subject: Civil Engineering

ANISOTROPIC CHARACTERIZATION AND PERFORMANCE PREDICTION OF CHEMICALLY AND HYDRAULICALLY BOUNDED PAVEMENT FOUNDATIONS

A Dissertation

by

REZA SALEHI ASHTIANI

Submitted to the Office of Graduate Studies of
Texas A&M University
in partial fulfillment of the requirements for the degree of

DOCTOR OF PHILOSOPHY

Approved by:

Chair of Committee,	Dallas N. Little
Committee Members,	Robert Lytton
	Eyad Masad
	Bruce Herbert
Head of Department,	David Rosowsky

August 2009

Major Subject: Civil Engineering

ABSTRACT

Anisotropic Characterization and Performance Prediction of Chemically and Hydraulically Bounded Pavement Foundations. (August 2009)

Reza Salehi Ashtiani, B.S., Azad University, Tehran, Iran

M.S. Tarbiat Modares University, Tehran, Iran

Chair of Advisory Committee: Dr. Dallas Little

The aggregate base layer is a vital part of the flexible pavement system. Unlike rigid pavements, the base layer provides a substantial contribution to the load bearing capacity in flexible pavements, and this contribution is complex: stress dependent, moisture dependent, particle size dependent, and is anisotropic in nature. Furthermore, the response of the aggregate layer in the pavement structure is defined not only by resilient properties of the base layer but also by permanent deformation properties of the aggregate layer. Before the benefits of revolutionary changes in the typical pavement structures, such as deep unbound aggregate base (UAB) layers under thin hot mix asphalt surfaces and inverted pavement systems can be justified, an accurate assessment of the UAB is required.

Several researchers identified that in order to properly assess the contribution of the UAB in the pavement structure, it is necessary to consider not only the vertical modulus but also the horizontal modulus as this substantially impacts the distribution of stresses within the pavement structure. Anisotropy, which is defined as the directional dependency of the material properties in unbound granular bases, is inherent even before the aggregate layer is subjected to traffic loads due to random arrangement of particles upon compaction. Distribution of particle contacts is dominated by the geometry of the aggregates as well as the compaction effort at the time of construction.

Critical pavement responses and therefore performance of flexible pavements are significantly influenced by the level of anisotropy of aggregate layers. There are several ways to characterize the level of anisotropy in unbound aggregate systems. Previous research at

Texas A&M University suggests functions of fitting parameters in material models (k-values) as characterizers of the level of anisotropy. In the realm of geotechnical engineering, the ratio of the horizontal modulus to vertical modulus is commonly referred to as the level of anisotropy. When the vertical and horizontal moduli are equal, the system is isotropic, but when they differ, the system is anisotropic.

This research showed that the level of anisotropy can vary considerably depending on aggregate mix properties such as gradation, saturation level, and the geometry of the aggregate particles. Cross anisotropic material properties for several unbound and stabilized aggregate systems were determined. A comprehensive aggregate database was developed to identify the contribution level of aggregate features to the directional dependency of material properties. Finally a new mechanistic performance protocol based on plasticity theory was developed to ensure the stability of the pavement foundations under traffic loads.

DEDICATION

To my parents for their love and patience

ACKNOWLEDGEMENTS

I would like to express my deepest gratitude to my committee chairman, Professor Dallas N. Little for his constant support and valuable insights on both an academic as well as personal level. My sincere appreciation and thanks goes to Professor Robert L. Lytton and Professor Eyad Masad for their guidance and support throughout the course of this research. I would also like to thank Professor Bruce Herbert for serving in my committee and providing me with comments on my dissertation.

I would also want to extend my gratitude to the International Center for Aggregate Research (ICAR), which provided the funding of this study through several projects.

My sincere appreciation goes to my friends and colleagues: Kamilla Vasconcelos, Gleb Mejeoumov, Edith Arambula, Corey Zollinger, David Haubrich, Sang-Ick Lee, Geyong-Taek Hong, Allex Alvarez, Silvia Caro, Christopher Jones, and the department faculty and staff for making my time at Texas A&M University a great experience.

Last but definitely not the least; I would like to express my deepest gratitude to my mother, father, and my aunt for their love, patience, encouragement, and support throughout the course of my study.

NOMENCLATURE

ANN	Artificial Neural Networks
ASTM	American Society for Testing and Materials
CCP	Constant Confining Pressure
CTC	Conventional Triaxial Compression
CTE	Conventional Triaxial Extension
FDA	Fisher's Discriminant Analysis
HC	Hydrostatic Compression
ICAR	International Center for Aggregate Research
LDA	Linear Discriminant Analysis
KNN	k-Nearest Neighbor
MEPDG	Mechanistic Empirical Pavement Design Guide
NCHRP	National Cooperative Highway Research Program
RTC	Reduced Triaxial Compression
RTE	Reduced Triaxial Extension
SS	Simple Shear
TC	Triaxial Compression
TE	Triaxial Extension
UAB	Unbound Aggregate Base
UCCS	Unconfined Compressive Strength
VCP	Variable Confining Pressure
VDCP	Variable Dynamic Confining Pressure

TABLE OF CONTENTS

Page

CHAPTER Page

CHAPTER Page

CHAPTER Page

CHAPTER Page

CHAPTER Page

Page

LIST OF FIGURES

Page

Page

Page

Page

Page

Page

Page

Page

Page

LIST OF TABLES

Page

CHAPTER I

INTRODUCTION

STATEMENT OF THE PROBLEM

Pavement design has shifted from an empirically based approach toward a mechanistic-empirical approach. The obvious example of this is the National Cooperative Highway Research Project (NCHRP) 1-37a, development of Mechanistic-Empirical Pavement Design Guide (MEPDG). This is most often referred to as the 2002 American Association of State Highway and Transportation Officials (AASHTO) Pavement Design Guide or simply the MEPDG.

Isotropic elastic solutions were used in the recent version of the MEPDG to calculate pavement responses under traffic load. Critical pavement responses were in turn used as input to pavement life prediction models in order to estimate the number of equivalent single axle loads (ESALs) that the pavement can sustain until failure.

Previous research identified that an isotropic model of the unbound granular layer will result in unrealistic stress/strain distribution in the pavement systems. Several researchers reported significant differences between stresses and strains measured in the field and those calculated using isotropic layered elastic solutions. The ability to develop a better match between field measurements and calculations was improved substantially by considering stress dependency and nonlinearity. Additional and equally significant improvement occurred when directional dependencies of the material properties were considered in the model.

This dissertation follows the style of the *Journal of Materials in Civil Engineering.*

Previous research identified that in order to properly assess the contribution of the unbound aggregate base (UAB) in the pavement structure, it is necessary to consider not only the vertical modulus but also the horizontal modulus as this substantially impacts the distribution of stresses within the pavement structure. The ratio of the horizontal modulus to vertical modulus is referred to as the level of anisotropy in this study. When the vertical and horizontal moduli are equal, the system is isotropic, but when they differ, the system is anisotropic.

One of the objectives of this study is to find out the aggregate features that influence the level of anisotropy as well as their level of contribution to the directional dependency of the material properties in particulate systems. Therefore this study considers aggregate systems with different lithologies, size distributions, and saturation levels to develop a comprehensive aggregate database. This aggregate database will in turn be used for developing the anisotropy prediction models, sensitivity analyses, and parametric studies as well as validation of the material model using statistical pattern classification techniques. Anisotropic material properties calculated using the stress path tests will be used to develop a design control protocol based on plasticity theory. The proposed protocol will provide a mechanistic means for the pavement design industry to assess the performance of pavement foundations in flexible pavements.

RESEARCH OBJECTIVES AND SCOPE OF THE STUDY

This study is primarily focused on the anisotropic modeling of pavement foundations. This research was conducted within the scope of laboratory characterization of unbound and stabilized aggregate layers as well as theoretical study of the performance of pavement foundations. The main focus of this study was to develop a methodology to characterize the directional dependency of the material properties in the lab and relate those properties to field performance. The following subtasks were pursued in this dissertation.

Task 1: Review of the Literature

A comprehensive literature review was conducted on the following topics:

- Constitutive behavior of aggregate systems and material models
- Loading protocols and stress path testing of geomaterials in the lab and their relations to the stress states and stress regimens induced by traffic load in the field
- Unbound base layer performance prediction protocols
- Failure functions and their applications in stability control of pavement

Task 2: Materials and Gradation Selection

Several aggregate types were selected with different gradations and molded at different moisture states to study their impact on cross anisotropic behavior of aggregate systems under triaxial loading. The synergistic impact of fines, level of saturation, particle size, and particle geometry on the directional stiffness of both unbound systems as well as lightly stabilized systems were studied. Four gradations of Texas limestone with varying fine contents were considered when evaluating the impact of low levels of stabilization on directional properties of the mixes. Aggregate samples were molded at different moisture states to study the effect of moisture content on laboratory performance of aggregate systems.

Task 3: Laboratory Testing of the Materials

Stress-induced directional dependency of material properties was determined using multiple variable dynamic confining pressure (MVDCP) stress path tests for several aggregate systems. Anisotropic material properties for three gradations and at three saturation levels were determined for each aggregate system. Aggregate geometry was characterized in terms of particle form, angularity, and texture using the Aggregate Imaging System (AIMS). The scale parameter and shape parameter of the cumulative Weibull distribution function were used to describe aggregate size and particle geometry. The fine portion of the gradation was characterized by the Rigden voids test and Methylene blue test to account for fine particle shape properties and deleterious effect of

plastic fines, respectively. Cross-anisotropic modular ratios were defined as indicators of the level of anisotropy. The modular ratios were in turn used in the aggregate database to develop the level of anisotropy prediction models described in tasks 6 and 7. In the experiments regarding stabilized aggregate systems, in addition to the anisotropic stress path tests, repeated load permanent deformation tests and unconfined compressive strength tests were performed on the stabilized and unstabilized aggregate systems to assess the laboratory performance of aggregate systems. The samples were conditioned in the moisture room for 48 hours prior to testing to allow for the initial stages of the pozzolanic reactions to take place.

Task 4: Determination of Resilient, Deformation, and Strength Properties of Unbound Aggregate Systems

Small strain (VDCP) stress path tests were used to determine the resilient properties of aggregate systems in the lab. This protocol provides a means to determine cross-anisotropic material properties: E_x and E_y (elastic modulus in the horizontal and vertical directions, respectively), ν_{xy} and ν_{xx} (Poisson's ratio in the horizontal direction due to vertical loading and Poisson's ratio in the horizontal direction due to horizontal loading, respectively) and G_{xy}, shear modulus. Applied stresses and measured strains were in turn used as input to an iterative error minimization technique called the system identification method to simultaneously solve four of the five anisotropic material properties (E_x, E_y, ν_{xx}, and ν_{xy}). The fifth material property, G_{xy}, was directly determined using elastic work potential relationships derived specifically for the shear stress regimen. The five cross anisotropic material properties as well as prescribed stresses in the lab were later fitted to the material model to calculate the nine k-parameters for each aggregate system. The calculated k-values will be used as input to characterize nonlinearity, stress dependency, and anisotropic behavior of unbound aggregate systems in the lab. Repeated load permanent deformation tests and unconfined compressive strength tests were also performed on the aggregate systems selected for the stabilization task to assess the laboratory performance of the aggregate systems.

Task 5: Evaluation of the Anisotropic Behavior of Lightly Cement Stabilized Aggregate Systems

The objective of this task was to evaluate the impact of increasing fines content on the performance of unbound (unstabilized) and lightly stabilized aggregate systems. Several gradations of Texas Limestone with varying fine contents and Portland cement contents were molded at different moisture states in this task. The synergistic impact of fines, moisture states, and stabilizer contents were assessed through measurements of anisotropic stiffness properties, permanent deformation after 10,000 load cycles, and unconfined compressive strengths of aggregate systems. In addition, anisotropic solutions were used in a finite element scheme to calculate nonlinear and anisotropic responses of aggregate systems subjected to traffic load. The performance of aggregate systems was determined through the shear strength ratio concept.

Task 6: Determination of the Level of Anisotropy Based on the Features of the Aggregate Database

The objective of this task was to develop a methodology to predict the level of anisotropy (characterized by modular ratios) based on comprehensive analysis of aggregate features such as gradation, particle geometry, moisture state, density, and anisotropic response parameters.

The first generation of the anisotropy level prediction model was re-evaluated by including more data and measuring new features of the aggregate systems and including these to bolster the model. New fitting functions to characterize aggregate geometry and particle size distributions were used to develop the new model. The re-evaluated model parameters were used as new aggregate features in the database, and the significance of each aggregate feature in the prediction model was evaluated. A sensitivity analysis in turn performed on the model to assess the level of contribution of the selected aggregate is featured in the prediction model.

Task 7: Development and Sensitivity Analysis of the Artificial Neural Network (ANN) Based Anisotropy Model

The objective of this task was to develop a toolkit based on nontraditional mathematical techniques such as neural networks for predicting the inputs of finite element software as a function of lithology, aggregate geometry, moisture state, gradation parameters. and physio-chemical properties of the fine portion of the mix. A sensitivity analysis was performed on the model to extract physically meaningful relations between the aggregate features and modular ratios.

Task 8: Application of Pattern Recognition Techniques in Validating the Material Model

The objective of this task was to unravel underlying relations between aggregate features and to identify the significance of each aggregate feature to describe the variations in the aggregate database.

Unsupervised clustering techniques were performed on the features of the aggregate system to identify natural groupings present in the aggregate database.

Dimensionality reduction techniques were also employed to find class discriminatory information between the observations. This information can be useful later as a means to eliminate the number of features needed to be measured in the lab for a more cost-effective testing protocol.

A secondary objective of this task was to evaluate important physical information such as aggregate mineralogy, moisture state, particle size distributions as pre-defined classes (as in the supervised clustering analysis), and to observe which classification criteria is superior in terms of classification performance. In other words, we identified which classification criteria resulted in better grouping of the observations in the aggregate matrix. The other objective of this task was to extract any physically meaningful relationship between the features of the aggregate database. An example for

this objective was the investigation of the relationship between the softening behavior and moisture state in unbound aggregate systems.

In another attempt in this study, Fisher's Linear Discriminant Analysis (LDA) accompanied by K Nearest Neighbor (KNN) algorithm was used to find class discriminatory information based on the features selected in the previous subtask. To accomplish this, the Eigenvectors of the Fishers' LDA were calculated, and the data was projected onto the two principal components with highest Eigenvalues. The KNN algorithm was used to calculate class rates according to the true class labels.

Task 9: Development of a Performance Prediction and Stability Control Protocol for Aggregate Layers

The objective of this task was to develop a protocol for the stability control of the aggregate layers based on fundamental properties of geomaterials. Plasticity theory and failure functions were employed considering different failure criteria to identify the stress states at which the pavement is prone to develop plastic deformation. Based on yield functions, an upper bound limit was defined for the stress states induced by traffic loads.

The proposed performance control protocol can serve as a design check for the pavement engineer in the mechanistic design of flexible pavements. The importance of stability control of pavement foundations becomes more pronounced when nontraditional and innovative design techniques such as inverted pavements or thin asphalt pavements are considered as alternative design methodology. The protocol developed in this task will also provide information on the critical locations in the aggregate layer for which the stability of the pavements needs to be checked under traffic load.

Task 10: Theoretical Study of the Cross-Anisotropic Failure Functions and Their Relationship to Field Performance

The objective of this task was to evaluate the applications of different cross-anisotropic failure criteria to better understand the response behavior of aggregate layers subjected to moving wheel load. Two failure criterion based on two different approaches were used to

describe the orthogonal load bearing capacity of frictional geomaterials. In the first approach proposed by Lade, failure in the cross-anisotropic frictional materials is a function of stress invariants acting upon geomaterials whereas in the second approach proposed by Mroz, the failure function is related to directional stiffness and the inclination of the loading plane. Since both functions tend to model the onset of failure in geomaterials, the two relationships can be combined. A parametric study was performed on the model to better understand the relationship between directional stiffness properties and rotation of the principal plane under the moving wheel load. An example of this parametric study would be looking at the confinement column induced by the moving wheel load in the base layer and its impact on the on the stability of the pavement foundations.

OUTLINE OF THE DISSERTATION

The contents of this dissertation can be logically divided into five sections. The first section deals with the anisotropic characterization of granular layers subjected to traffic loads. Discussions regarding the methodologies previously used to determine anisotropic material properties in particulate systems as well as material models were presented in this section. The second section presents detailed discussion about the stress path testing of geomaterials. Current protocols typically used to characterize aggregate layers were discussed, and the parameters of the stress path were compared against stress states. Stress ratios resulted from finite element simulation of pavement sections. Anisotropic behavior of stabilized aggregate systems is discussed in the third section of this dissertation. Analysis of the synergistic impact of fines content, stabilizer content, and saturation level on the performance of chemically stabilized systems is documented in this study. The fourth section deals with the analysis of the comprehensive aggregate database developed in this study. A regression-based model and an ANN-based model were developed to predict the level of anisotropy in aggregate systems based on features of aggregate database. Sensitivity analysis performed on both models revealed the contribution of aggregate features to the directional dependency of material properties in

unbound layers. Pattern recognition techniques were also employed to identify the dynamic of the system. Finally, discussions regarding performance prediction and stability control of aggregate systems were presented in the fifth section of this dissertation. A theoretical study regarding the impact of the rotation of principal plane under moving loads and its impact on the stability of the aggregate systems was also documented in this study.

CHAPTER II

ANISOTROPIC BEHAVIOR OF AGGREGATE LAYERS

INTRODUCTION

Mechanical behavior of particulate materials is significantly influenced by the directional dependency of material properties. This behavior can be accommodated using anisotropic characterization of geomaterials used in pavement systems.

Anisotropy of strength and deformation is typically ignored due to complexity of the problem. Isotropic characterization of layered systems typically results in high tensile stresses in the intermediate layers when the stiffnesses of subsequent layers are significantly different. For instance, analysis of a typical three-layer flexible pavement system using isotropic solutions will result in very high horizontal stresses when the modular ratio (the ratio of the stiffness of base layer to subgrade) is high. Considering the fact the mechanism of load distribution in particulate systems is through contact forces and aggregate interlock and knowing that geomaterials have very limited tension taking capacity, unbound systems cannot sustain such calculated large tensile stresses. Anisotropic characterization of geomaterials, however, substantially reduces or even eliminates these unrealistic tensile stresses.

On the other hand, Tutumluer showed that stresses and strains measured in the field had a much closer match to calculated responses when the aggregate layers were characterized as anisotropic materials (Tutumluer et al. 2003). Anisotropic stress path testing of geomaterials in the lab also resulted in much higher plastic deformations and significantly better correlations with field rutting data (Tutumluer and Kim 2003).

This chapter provides detailed discussion on the fundamentals of anisotropic characterization of materials. The methodology for determination of cross-anisotropic material properties will also be presented in detail.

ANISOTROPIC ELASTICITY

The anisotropic behavior of aggregate systems can be investigated within the framework of elasticity. The general form of constitutive behavior is the generalized Hooke's law. In generalized Hooke's law, any strain component can be found as a function of all the stress components that act on the body of a material. Equation 2-1 presents the generalized Hooke's law in indicial notations.

$$\varepsilon_{ij} = S_{ijkl}\sigma_{kl} \tag{2-1}$$

where: ε represent the strain; σ is the stress; and S is known as the stiffness or compliance matrix that relates the applied stresses and measured strains. In the general form, the compliance matrix has (3^4=81) components. Symmetry of the response of the geomaterials results in reduction of the number of components in the compliance matrix from 81 to 36. Equation 2-2 presents the matrix representation of the constitutive equation with 36 components.

$$\begin{bmatrix} S_{12} & S_{12} & S_{13} & S_{14} & S_{15} & S_{16} \\ S_{21} & S_{22} & S_{23} & S_{24} & S_{25} & S_{26} \\ S_{31} & S_{32} & S_{33} & S_{34} & S_{35} & S_{36} \\ S_{41} & S_{42} & S_{43} & S_{44} & S_{45} & S_{46} \\ S_{51} & S_{52} & S_{53} & S_{54} & S_{55} & S_{56} \\ S_{61} & S_{62} & S_{63} & S_{64} & S_{65} & S_{66} \end{bmatrix} \begin{bmatrix} \sigma_x \\ \sigma_y \\ \sigma_x \\ \tau_{yz} \\ \tau_{zx} \\ \tau_{xy} \end{bmatrix} = \begin{bmatrix} \varepsilon_{xx} \\ \varepsilon_{yy} \\ \varepsilon_{zz} \\ \gamma_{yz} \\ \gamma_{zx} \\ \gamma_{xy} \end{bmatrix} \tag{2-2}$$

where ε and γ represent the strain components, and σ and τ are the stress components in the constitutive equation. Love showed for an elastic material the compliance matrix (S matrix) should be symmetrical because of thermodynamic requirements and strain energy considerations (Love 1944). Therefore:

$$S_{ij}=S_{ji} \tag{2-3}$$

The thermodynamic considerations and positive strain energy requirements reduce the number of independent elastic constants in the compliance matrix from 36 to 21. Therefore, for a general anisotropic material, we need to define 21 components in the

compliance matrix to fully characterize the anisotropic behavior of the geomaterials. However, aggregate systems generally show symmetry in terms of response behavior under the load. This symmetry results in cross-coupling between the normal and shear component of the stress and strains (Lekhnitskii 1963). Therefore, due to the symmetry in the response under the load, number of required components needed to fully characterize geomaterials can be reduced. Hoek showed that the presence of the axis of symmetry in the material de-couples some of the stress-strains relations and reduces the number of independent material constants required to characterize anisotropic behavior of a material (Hoek and Brown 1997). For orthotropic materials in which the materials axis of symmetry coincides with loading directions, the number of independent components can be reduced to 9. Number of independent material parameters needed to characterize the response behavior of the materials is presented in Table 2-1.

Table 2-1 Number of Distinct Components to Characterize Materials (Ishai 1994)

Material behavior	Number of distinct material constants
General anisotropic material	81
Anisotropic material considering symmetry of stress strain tensor ($\sigma_{ij}=\sigma_{ji}$, $\varepsilon_{ij}=\varepsilon_{ji}$)	36
Anisotropic material considering elastic energy considerations	21
General orthotropic material	9
Orthotropic material with transverse isotropy (cross-anisotropic material)	5
Isotropic material	2

As discussed earlier, aggregate particles tend to orient themselves to the horizontal direction upon compaction. This preferred orientation of the aggregate particles results in directional dependency of the material properties in aggregate layers.

One simplifying assumption in modeling the aggregate layers would be to consider the aggregate system is cross anisotropic. In other words the material is considered to be isotropic in the horizontal plane and anisotropic in vertical plane, for this reason it is also known as transversely isotropic material. In transversely isotropic materials, mechanical properties in horizontal plane are the same, and they change with depth in the aggregate layer. Ishai defined the cross anisotropic geomaterials as "an orthotropic material is called transversely isotropic (or cross- anisotropic) when one of the principal planes is the plane of isotropy, that is, at every point there is a plane on which the mechanical properties are the same in all directions (Ishai 1994)." Figure 2-1 shows the analogy of the stack of cards for describing the cross-anisotropic materials.

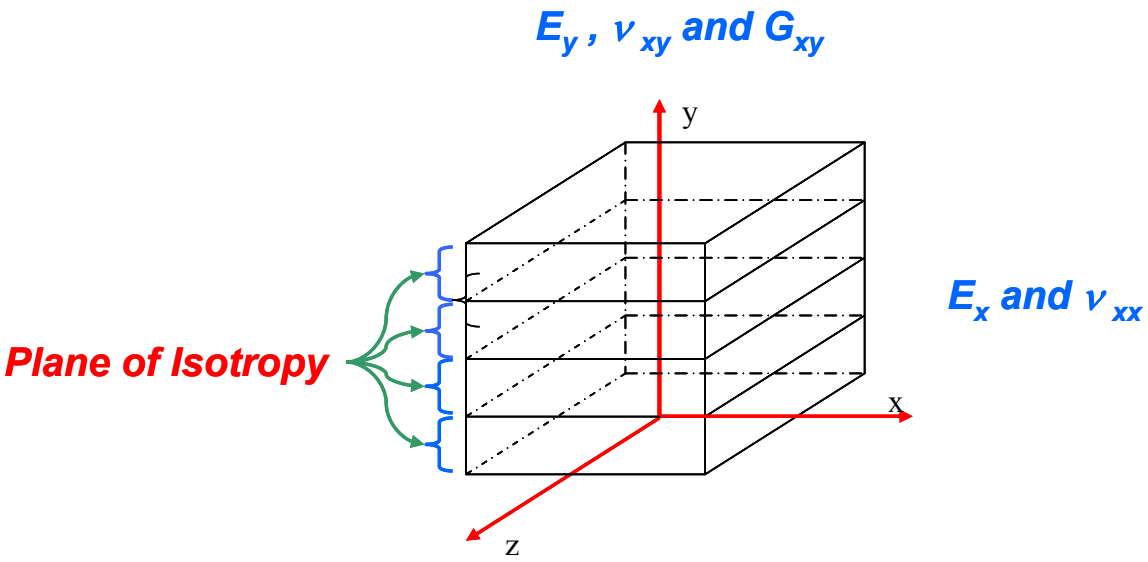

Figure 2-1 Schematic representation of cross-anisotropic materials

TRANSVERSELY ISOTROPIC OR CROSS-ANISOTROPIC MATERIALS

For the case of transversely isotropic (cross-anisotropic) material, considering axis 1 to represent the axis of symmetry, the stress strain relations presented in equation 2-2 can be written as:

$$\sigma_{11} = S_{11}\,\varepsilon_{11} + S_{12}\,\varepsilon_{22} + S_{12}\,\varepsilon_{33} \tag{2-4}$$

$$\sigma_{22} = S_{12}\,\varepsilon_{11} + S_{22}\,\varepsilon_{22} + S_{22}\,\varepsilon_{33} \tag{2-5}$$

$$\sigma_{22} = S_{12}\,\varepsilon_{11} + S_{22}\,\varepsilon_{22} + S_{22}\,\varepsilon_{33} \tag{2-6}$$

$$\sigma_{12} = 2\,S_{66}\,\varepsilon_{12} \tag{2-7}$$

$$\sigma_{31} = 2\,S_{66}\,\varepsilon_{31} \tag{2-8}$$

$$\sigma_{23} = (S_{22} - S_{23})\,\varepsilon_{12} \tag{2-9}$$

The five independent material constants, S_{11}, S_{12}, S_{22}, S_{23}, and S_{66} are needed to characterize the cross-anisotropic materials. Although these five constants fully describe the behavior of the transversely isotropic media, they are not convenient terms in the realm of engineering. These material constants acquire more physical meaning when they are expressed using engineering constants such as moduli and Poisson's ratios. These engineering constants can be experimentally found in the lab using triaxial cell or hollow cylinder for geomaterials.

The constitutive relation presented in equation 2-2 can be expressed in terms of engineering constants while considering the symmetry of the material as follows:

$$\begin{bmatrix} \frac{1}{E_x} & \frac{-\upsilon_{yx}}{E_y} & \frac{-\upsilon_{yx}}{E_y} & 0 & 0 & 0 \\ \frac{-\upsilon_{xy}}{E_x} & \frac{1}{E_y} & \frac{-\upsilon_{zy}}{E_y} & 0 & 0 & 0 \\ \frac{-\upsilon_{xy}}{E_x} & \frac{-\upsilon_{yz}}{E_y} & \frac{1}{E_y} & 0 & 0 & 0 \\ 0 & 0 & 0 & \frac{1}{G_{yz}} & 0 & 0 \\ 0 & 0 & 0 & 0 & \frac{1}{G_{xz}} & 0 \\ 0 & 0 & 0 & 0 & 0 & \frac{1}{G_{xy}} \end{bmatrix} \begin{bmatrix} \sigma_x \\ \sigma_y \\ \sigma_x \\ \tau_{yz} \\ \tau_{zx} \\ \tau_{xy} \end{bmatrix} = \begin{bmatrix} \varepsilon_{xx} \\ \varepsilon_{yy} \\ \varepsilon_{zz} \\ \gamma_{yz} \\ \gamma_{zx} \\ \gamma_{xy} \end{bmatrix} \qquad (2\text{-}10)$$

E_x= Elastic modulus in horizontal direction

E_y= Elastic modulus in vertical direction

ν_{yx}= Poisson's ratio in horizontal direction due to imposed vertical stress

ν_{xy}= Poisson's ratio in vertical direction due to imposed horizontal stress

ν_{xy}= Poisson's ratio in horizontal direction due to imposed horizontal stress

G_{xz}= Shear modulus in x-z plane

G_{yz}= Shear modulus in y-z plane

G_{xy}= Shear modulus in x-y plane

It is important to note that using ($\nu_{xy} \neq \nu_{yx}$) from equation 2-10 and the symmetry of the compliance matrix we have:

$$\frac{\upsilon_{xy}}{E_x} = \frac{\upsilon_{yx}}{E_y} \qquad (2\text{-}11)$$

The above form was originally developed by Betti and is known as Betti's reciprocal law. Betti proved that transverse deformation due to stresses applied in the longitudinal direction is equal to the longitudinal deformation due to an equal stress applied in the transverse direction. The general form for Betti's reciprocal law is presented in equation 2-12 (Ishai 1994).

$$\frac{\upsilon_{ij}}{E_i} = \frac{\upsilon_{ji}}{E_j} \qquad (i,j=1,2,3) \tag{2-12}$$

For the case of transversely isotropic (cross-anisotropic) materials, a plane of isotropy exists such that material properties in the x and z directions are equal. Since the horizontal plane is the plane of isotropy, shear modulus in horizontal direction (G_{xx}) is related to elastic modulus and Poisson's ratio in horizontal plane following equation 2-13:

$$G_{xx} = \frac{E_x}{2\,(1+\nu_{xx})} \tag{2-13}$$

Considering equations 2-11 and 2-13, the number of independent elastic constants can be reduced to five. The general form of the constitutive equation for the cross-anisotropic material is presented in equation 2-14.

$$\begin{bmatrix} \frac{1}{E_x} & \frac{-\upsilon_{xx}}{E_x} & \frac{-\upsilon_{yx}}{E_y} & 0 & 0 & 0 \\ \frac{-\upsilon_{xx}}{E_x} & \frac{1}{E_x} & \frac{-\upsilon_{yx}}{E_y} & 0 & 0 & 0 \\ \frac{-\upsilon_{yx}}{E_y} & \frac{-\upsilon_{yx}}{E_y} & \frac{1}{E_y} & 0 & 0 & 0 \\ 0 & 0 & 0 & \frac{1}{G_{xy}} & 0 & 0 \\ 0 & 0 & 0 & 0 & \frac{1}{G_{xy}} & 0 \\ 0 & 0 & 0 & 0 & 0 & \frac{2(1+\upsilon_{xx})}{E_x} \end{bmatrix} \begin{bmatrix} \sigma_x \\ \sigma_y \\ \sigma_x \\ \tau_{yz} \\ \tau_{zx} \\ \tau_{xy} \end{bmatrix} = \begin{bmatrix} \varepsilon_{xx} \\ \varepsilon_{yy} \\ \varepsilon_{zz} \\ \gamma_{yz} \\ \gamma_{zx} \\ \gamma_{xy} \end{bmatrix} \tag{2-14}$$

Equation 2-14 indicates that five anisotropic elastic material properties: E_x, E_y, ν_{xy}, ν_{xx}, and G_{xy} are needed to fully characterize the cross-anisotropic nature of geomaterials. Discussions pertaining to stress path testing of geomaterials for determination of anisotropic material properties will be provided in Chapter III.

BOUNDS ON MATERIAL CONSTANTS

Pickering derived several bounds for cross-anisotropic material constants. He showed that in order to satisfy the thermodynamic requirement of positive strain energy, the Poisson's ratio in horizontal direction must be: $-1 < \nu_{xx} < 1$ (Pickering 1970).

Raymond showed that equation 2-15 must hold to satisfy the thermodynamic requirements in transversely isotropic material (Raymond 1970).

$$\frac{E_x}{E_y}\left[1-\upsilon_{xx}\right]-2\upsilon_{xy}^2 \geq 0 \tag{2-15}$$

Later Lings derived the bounding expression for shear modulus in x-y plane as presented in equation 2-16 (Lings et al. 2000):

$$G_{xy} \leq \frac{E_y}{2\upsilon_{xy}(1+\upsilon_{xx})+2\sqrt{\left(\frac{E_y}{E_x}\right)\left(1-\upsilon_{xx}^2\right)\left[1-\upsilon_{xy}^2\left(\frac{E_x}{E_y}\right)\right]}} \tag{2-16}$$

EXPERIMENTAL DETERMINATION OF ANISOTROPIC MATERIAL PROPERTIES

As discussed in the previous section, five anisotropic elastic properties are needed to characterize the cross-anisotropic behavior of the aggregate layers in pavement foundations. In order to solve for these five material properties, a small strain stress path was used to find these five distinct elastic constants.

In order to assess the directional dependency of the response of aggregate systems in the lab, aggregate samples were tested following a small strain-loading protocol to ensure the material stays in the elastic region and does not undergo plastic collapse. This test protocol assumes the orthogonal elastic moduli as well as shear modulus are nonlinear functions of stress invariants. Another assumption is that the variations of these tangential moduli are negligible within small changes in the prescribed state of the stresses so the behavior of the material stays elastic. This loading protocol uses three stress regimes: compression, shear, and extension as shown in figure 2-2.

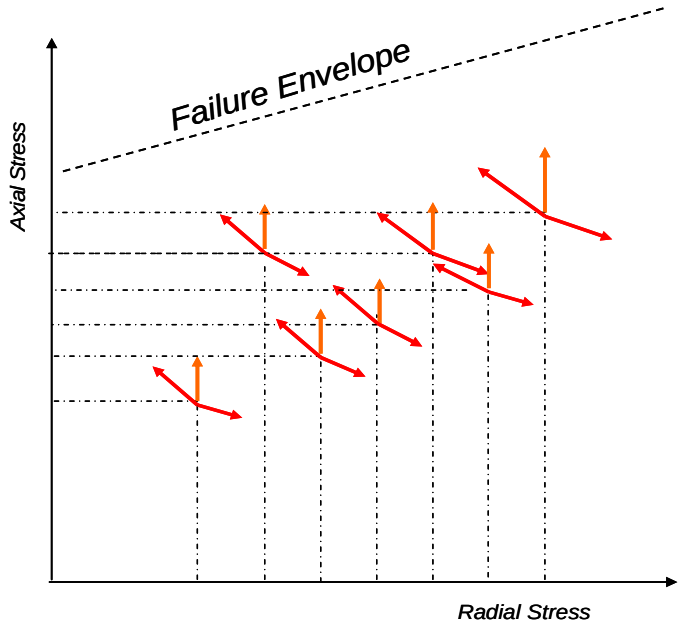

Figure 2-2 Schematic representations of small strain stress path tests in σ_1-σ_3 plane

Table 2-2 represents the stress sequence and the magnitude of the stress states applied on the aggregate samples in the lab.

Table 2-2 Prescribed Stress States and Stress Magnitudes in the Lab

	Static Stress (Kpa)		Dynamic stress (Kpa)					
			Compression		Shear		Extension	
Stress state	σ_y	σ_x	$\Delta\sigma_y^c$	$\Delta\sigma_X^c$	$\Delta\sigma_y^s$	$\Delta\sigma_X^s$	$\Delta\sigma_y^e$	$\Delta\sigma_X^e$
1	40	25	5	0	10	-5	-5	5
2	50	25	10	0	10	-5	-10	10
3	70	40	10	0	10	-5	-10	10
4	130	60	20	0	20	-10	-10	10
5	150	70	20	0	20	-10	-10	10
6	170	100	20	0	20	-10	-20	20
7	220	120	30	0	30	-15	-20	20
8	250	140	30	0	30	-15	-20	20
9	250	120	30	0	30	-15	-20	20
10	250	105	30	0	30	-15	-20	20

This protocol provides a means to determine cross-anisotropic material properties: E_x and E_y (elastic modulus in the horizontal and vertical directions, respectively), ν_{xy} and ν_{xx} (Poisson's ratio in the horizontal direction due to vertical loading and Poisson's ratio in the horizontal direction due to horizontal loading, respectively), and G_{xy}, shear modulus. Applied stresses and measured strains are then input to an iterative error minimization technique called the system identification method to simultaneously solve for four of the five anisotropic material properties (E_x, E_y, ν_{xx}, and ν_{xy}). More discussion on the theory and the rationale behind a system identification method will be presented in the following section.

The cross-anisotropic constitutive equation for aggregate samples tested in the lab using a triaxial device can be written as:

$$\begin{bmatrix} \frac{1}{E_x} & -\frac{\nu_{xy}}{E_x} & -\frac{\nu_{xx}}{E_x} \\ -\frac{\nu_{xy}}{E_x} & \frac{1}{E_y} & -\frac{\nu_{xy}}{E_x} \end{bmatrix} \begin{bmatrix} \sigma_x \\ \sigma_y \\ \sigma_x \end{bmatrix} = \begin{bmatrix} \varepsilon_x \\ \varepsilon_y \end{bmatrix} \tag{2-17}$$

In the case of the small strain protocol, the constitutive equation can be written in the incremental form as shown in equation 2-18 (Adu-Osei et al. 2001):

$$\begin{bmatrix} \frac{1}{E_x} & -\frac{\nu_{xy}}{E_x} & -\frac{\nu_{xx}}{E_x} \\ -\frac{\nu_{xy}}{E_x} & \frac{1}{E_y} & -\frac{\nu_{xy}}{E_x} \end{bmatrix} \begin{bmatrix} \Delta\sigma_x \\ \Delta\sigma_y \\ \Delta\sigma_x \end{bmatrix} = \begin{bmatrix} \Delta\varepsilon_x \\ \Delta\varepsilon_y \end{bmatrix} \tag{2-18}$$

Before we discuss the details about the loading protocol, it is necessary to discuss the anisotropic work potential and the assumptions used in establishing the variable dynamic confining pressure stress paths.

ANISOTROPIC WORK POTENTIAL

The anisotropic work potential plays an important role in determination of recoverable and plastic deformation in geomaterials. The total work completed per unit volume on a deformable body subjected to a strain increment can be written as:

$$dW = \sigma_{ij}\ d\varepsilon_{ij} \tag{2-19}$$

where $d\varepsilon_{ij}$ is the strain increment, and dW is the work completed on the continuum per unit volume. Since the total strain can be decomposed into elastic and plastic components, dW can also be presented as elastic work and plastic work as shown in equation 2-21:

$$dW = \sigma_{ij}\ (d\varepsilon_{ij}^{e} + d\varepsilon_{ij}^{e}) \tag{2-20}$$

$$dW = dW^{e} + dW^{p} \tag{2-21}$$

where dW^{e} is the elastic work, and dW^{p} is the plastic work done on the deformable body. Since we chose the stress states to be low enough not to induce any damage on the system and the material stay in the elastic region, we can assume the plastic work is negligible. Therefore the total elastic work can be written as (Desai et al. 1987):

$$\oint dW = \oint [\sigma]\, d\varepsilon \tag{2-22}$$

Due to the energy conservation requirements and the fact that the total work on a deformable body is path independent, total work for an anisotropic material in terms of stress invariants can be written as (Adu-Osei et al. 2001):

$$\oint dW = \oint \frac{I_1 dI_1}{9E_y}\left[1 + 2\frac{E_y}{E_x} - 4\nu_{xy}\frac{E_y}{E_x} - 2\nu_{xx}\frac{E_y}{E_x}\right] + \frac{dJ_2}{2G_{xy}} \tag{2-23}$$

In equation 2-23, I_1 is the first invariant of the stress tensor, and J_2 is the second invariant of the deviatoric stress tensor.

According to the Green's theorem, equation 2-23 can be written as:

$$\oint (Pdx + Qdy) = \iint \left[\frac{dQ}{dx} - \frac{dP}{dy} \right] dA \tag{2-24}$$

where:

$$P = \frac{dW}{dx} \text{ , and} \tag{2-25}$$

$$Q = \frac{dW}{dy} \tag{2-26}$$

Considering the general form of the work potential can also be expressed as:

$$dW = \frac{dW}{dI_1} dI_1 + \frac{dW}{dJ_2} dJ_2 \tag{2-27}$$

Taking the derivatives of the equation 2-23 results:

$$\frac{dW}{dI_1} = \frac{I_1}{9E_y} \left[1 + 2\frac{E_x}{E_y} - 4\upsilon_{xy} \frac{E_x}{E_y} - 2\upsilon_{xx} \frac{E_x}{E_y} \right] \tag{2-28}$$

$$\frac{dW}{dJ_2} = \frac{1}{2G_{xy}} \tag{2-29}$$

Therefore the incremental anisotropic work potential can be written as:

$$dW = \frac{I_1}{9E_y} \left[1 + 2\frac{E_x}{E_y} - 4\upsilon_{xy} \frac{E_x}{E_y} - 2\upsilon_{xx} \frac{E_x}{E_y} \right] + \frac{1}{2G_{xy}} \tag{2-30}$$

We will use the above mentioned formulations to determine the five anisotropic elastic material properties of samples subjected to stress path tests in the lab.

In the following section, a thorough discussion on the rationale behind the dynamic variable confining pressure stress paths tests is provided.

Compression Regime

In this test mode, the confining stress at each stress state is kept constant while the axial stress is increased by $\Delta\sigma y^c$. Thus, the sample is loaded to ($\sigma_y{}^c$, $\sigma_x{}^c$), reloaded to (σy^c + $\Delta\sigma y^c$, $\Delta\sigma x^c$), and unloaded back to ($\sigma y^{\,c}$, $\Delta\sigma x^c$) for each cycle.

$$\begin{bmatrix} \frac{1}{E_x} & -\frac{\nu_{xy}}{E_x} & -\frac{\nu_{xx}}{E_x} \\ -\frac{\nu_{xy}}{E_x} & \frac{1}{E_y} & -\frac{\nu_{xy}}{E_x} \end{bmatrix} \begin{bmatrix} \Delta\sigma_x^c \\ \Delta\sigma_y^c \\ \Delta\sigma_x^c \end{bmatrix} = \begin{bmatrix} \Delta\varepsilon_x^c \\ \Delta\varepsilon_y^c \end{bmatrix} \tag{2-31}$$

where:

$\Delta\varepsilon x^c$ = a change in radial strain due to an infinitesimal change in axial stress $\Delta\sigma y^c$

in triaxial compression,

$\Delta\varepsilon y^c$ = a change in axial strain due to an infinitesimal change in axial stress $\Delta\sigma y^c$

in triaxial compression, and

$\Delta\sigma x^c = 0$.

Shear Regime

In this phase of the test, the axial stress is increased slightly by $\Delta\sigma_y^s$, and the confining stress is decreased by $\Delta\sigma_x^s = ½\ \Delta\sigma_y^s$. Thus, at the stress state (σ_y^s, σ_x^s), the sample is loaded to ($\sigma_y^s + \Delta\sigma_y^s$, $\sigma_x^s - \Delta\sigma_x^s$) and unloaded back to ($\sigma_y^s$, σ_x^s) in each cycle. This way, there is no change in the first stress invariant, I.

$$\begin{bmatrix} \frac{1}{E_x} & -\frac{\nu_{xy}}{E_x} & -\frac{\nu_{xx}}{E_x} \\ -\frac{\nu_{xy}}{E_x} & \frac{1}{E_y} & -\frac{\nu_{xy}}{E_x} \end{bmatrix} \begin{bmatrix} \Delta\sigma_x^s \\ \Delta\sigma_y^s \\ \Delta\sigma_x^s \end{bmatrix} = \begin{bmatrix} \Delta\varepsilon_x^s \\ \Delta\varepsilon_y^s \end{bmatrix} \tag{2-32}$$

Since the change in the first invariant of the stress tensor is zero (Adu-Osei et al. 2001):

$$\Delta I_1 = \Delta\sigma_y^s + 2\Delta\sigma_x^s = \Delta\sigma_y^s + 2\frac{1}{2}\Delta\sigma_y^s = 0$$

(2-33)

Incremental change in the second invariant of the deviatoric stress tensor can be written as:

$$\Delta J_2^s = \frac{1}{3}(\Delta\sigma_y^s - \Delta\sigma_x^s) = \frac{3}{4}\left[\Delta\sigma_y^s\right]^2 \tag{2-34}$$

The change in the strain energy for an elastic body can be presented as:

$$\Delta E^s = \frac{1}{2}\left[\Delta\sigma_x^s\Delta\varepsilon_x^s + \Delta\sigma_y^s\Delta\varepsilon_y^s + \Delta\sigma_x^s\Delta\varepsilon_x^s\right] = \frac{1}{2}\Delta\sigma_x^s\left[\Delta\varepsilon_y^s\Delta\varepsilon_x^s\right] \tag{2-35}$$

Considering equation 2-12 and the fact that the change in the first invariant of the stress tensor is zero in this regimen, we can conclude that the total strain energy is a function of

shear modulus and the second invariant of the deviatoric stress tensor, as shown in equation 2-36:

$$\Delta E^{s} = \frac{\Delta J_2}{2G_{xy}} \tag{2-36}$$

Now by substituting equations 2-34 and 2-35 into equation 2-36 we have:

$$G_{xy} = \frac{3}{4}\frac{\Delta\sigma_y}{(\Delta\varepsilon_y - \Delta\varepsilon_x)} \tag{2-37}$$

Equation 2-37 is used to directly calculate the shear modulus, G_{xy}, specifically in this stress regimen.

Extension Regime

In this phase of the test, there is a slight decrease in the axial stress by $\Delta\sigma y^{\varepsilon}$ and a slight increase in the confining stress by $\Delta\sigma x^{\varepsilon}$. Thus, at the stress state (σy^{ε}, σx^{ε}), the sample is loaded to ($\sigma y^{\varepsilon} - \Delta\sigma y^{\varepsilon}$, $\sigma x^{\varepsilon} + \Delta\sigma x^{\varepsilon}$) and unloaded back to ($\sigma y^{\varepsilon}$, σx^{ε}) in each cycle.

$$\begin{bmatrix} \frac{1}{E_x} & -\frac{\nu_{xy}}{E_x} & -\frac{\nu_{xx}}{E_x} \\ -\frac{\nu_{xy}}{E_x} & \frac{1}{E_y} & -\frac{\nu_{xy}}{E_x} \end{bmatrix} \begin{bmatrix} \Delta\sigma_x^e \\ \Delta\sigma_y^e \\ \Delta\sigma_x^e \end{bmatrix} = \begin{bmatrix} \Delta\varepsilon_x^e \\ \Delta\varepsilon_y^e \end{bmatrix} \tag{2-38}$$

where:

$\Delta\varepsilon x^{\varepsilon}$ = Change in radial strain due to an infinitesimal change in axial stress $\Delta\sigma y^{c}$ and radial stress $\Delta\sigma x^{\varepsilon}$, and

$\Delta\varepsilon y^{c}$ = Change in axial strain due to an infinitesimal change in axial stress $\Delta\sigma y^{c}$ and radial stress $\Delta\sigma x^{\varepsilon}$.

The stresses applied and the strains obtained from the three stress regimes described above are used in a system identification scheme to determine the five cross-anisotropic parameters.

At each static stress state, small dynamic changes in stresses are applied to obtain three triaxial stress regimes such that the net stress changes represent triaxial compression, triaxial shear, and triaxial extension. A loading cycle of dynamic stress consists of 1.5 seconds of loading and 1.5 seconds of unloading. As for sample conditioning, a dynamic loading is applied to a sample for 25 repetitions until a stable resilient strain is achieved. The resilient axial and radial strains are determined for each stress regime and implemented in the system identification scheme to back-calculate the five anisotropic elastic properties at that particular stress state.

SYSTEM IDENTIFICATION METHOD

System identification is a mathematical term for procedures and algorithms that is used to capture the dynamic behavior of the datasets based on actual measurements. This data-driven iterative approach is used to describe systems that are not easily modeled from first principles or specifications, such as chemical processes and engine dynamics (Ljung 1999). The system is called identified when the error between the two consecutive iterations becomes smaller than a predefined threshold.

Modeling the behavior of the materials can be categorized into three groups: white box, gray box, and black box. White box models consist of closed form solutions solely based on principal laws such as Newton's equations. In so many cases and specifically when dealing with experimental data, developing such models will be overly complex and probably not feasible. This is where gray box and black box models come into play. Gray box and black box modeling approaches start from the measurements of the response of the system to external influences (such as mechanical loading or temperature gradient) and tend to mathematically simulate the relation between the influences (input) and the responses (output) of the system. Gray box and black box modeling approaches tend to model the response of the system without getting into the details of what actually is happening inside the system. The algorithm to develop gray box and black box models is called the system identification method.

In gray box models, although the specifics of the interactions between the input and output are unknown, some prior knowledge of the data can be applied to the system. Most common of these constraints are bounds on the output of the system such as positive moduli values and bounds on the Poisson's ratios as discussed earlier in this chapter. Initial values or seed values as starting points in the algorithm are other examples of applying prior knowledge of the data for defining the system in the gray box algorithms. We used linear isotropic elastic solutions as starting points for determining the nonlinear cross-anisotropic material properties in this research. Applying prior knowledge of the data results in reduction of computation time and guarantees convergence of the algorithm.

On the other hand, the black box approach considers no prior knowledge of the data and tends to model the system only based on input and measured responses. Neural network based models use the black box approach in determining the dynamics of a system. More discussion on the rationale behind the neural network based models and its application in determining the cross-anisotropic material properties will be discussed later in this dissertation.

Determination of Anisotropic Material Properties Using Gray Box Algorithms

Gray box type system identification algorithm was employed to determine the cross-anisotropic material properties. Equation 2-39 shows the general form of influence-response relationship in gray box algorithms (Adu-Osei et al. 2001):

$$[F]\{\alpha\} = [r] \tag{2-39}$$

In equation 2-39, [F] is called the sensitivity matrix because it shows the sensitivity of the output of the system to changes of an input parameter. The components of the F matrix are the differentials of the output (ε_i) with respect to the input parameter (X_i) as formulated in equation 2-40.

$$[F] = \frac{\partial \varepsilon_i}{\partial X_i}\frac{X_i}{\varepsilon_i} \tag{2-40}$$

In equation 2-39 vector $\{\alpha\}$ shows the relative changes of the parameter and can be determined using equation 2-41:

$$\{\alpha\} = \frac{\Delta X_i^{n+1}}{X_i^n} \tag{2-41}$$

In equation 2-39 [r] is called the residual matrix and can be determined using equation 2-42.

$$[r] = \frac{\Delta\varepsilon_x^m - \Delta\varepsilon_x}{\Delta\varepsilon_x} \tag{2-42}$$

In equation 2-42 $\Delta\varepsilon_x^m$ is the actual measured response, and $\Delta\varepsilon_x$ is the model calculated response of the system.

By applying the gray box algorithm described above to variable confining pressure (VCP) stress path tests (inputs) and measured strains (output) of the system, we determine anisotropic material properties. The difference between calculated material parameter and measured strains can be minimized through iterative parameter adjustment until the error becomes smaller than a predefined value.

Components of the system identification method for the triaxial test can be written as:

$$F = \begin{bmatrix} \frac{\partial(\Delta\varepsilon_x)}{\partial E_x}\cdot\frac{E_x}{\Delta\hat{\varepsilon}_x} & \frac{\partial(\Delta\varepsilon_x)}{\partial \upsilon_{xy}}\cdot\frac{\upsilon_{xy}}{\Delta\hat{\varepsilon}_x} & \frac{\partial(\Delta\varepsilon_x)}{\partial \upsilon_{xx}}\cdot\frac{\upsilon_{xx}}{\Delta\hat{\varepsilon}_x} & \frac{\partial(\Delta\varepsilon_x)}{\partial E_y}\cdot\frac{E_y}{\Delta\hat{\varepsilon}_x} \\ \frac{\partial(\Delta\varepsilon_y)}{\partial E_x}\cdot\frac{E_x}{\Delta\hat{\varepsilon}_y} & \frac{\partial(\Delta\varepsilon_y)}{\partial \upsilon_{xy}}\cdot\frac{\upsilon_{xy}}{\Delta\hat{\varepsilon}_y} & \frac{\partial(\Delta\varepsilon_y)}{\partial \upsilon_{xx}}\cdot\frac{\upsilon_{xx}}{\Delta\hat{\varepsilon}_y} & \frac{\partial(\Delta\varepsilon_y)}{\partial \upsilon_{xx}}\cdot\frac{\upsilon_{xx}}{\Delta\hat{\varepsilon}_y} \end{bmatrix} \tag{2-43}$$

$$\alpha = \begin{bmatrix} \frac{E_x^{r+1}}{E_x^r} & \frac{\upsilon_{xy}^{r+1}}{\upsilon_{xy}^r} & \frac{\upsilon_{xx}^{r+1}}{\upsilon_{xx}^r} & \frac{E_y^{r+1}}{E_y^r} \end{bmatrix} \tag{2-44}$$

$$r = \begin{bmatrix} \frac{\Delta\varepsilon_x^m - \Delta\hat{\varepsilon}_x}{\Delta\hat{\varepsilon}_x} \\ \frac{\Delta\varepsilon_y^m - \Delta\hat{\varepsilon}_y}{\Delta\hat{\varepsilon}_y} \end{bmatrix} \tag{2-45}$$

In order to generate enough components in the sensitivity matrix [F], the aggregate materials were subjected to three stress regimens namely compression, extension, and shear. The rows were in turn combined, and the cross-anisotropic material parameters were determined using equation 2-46:

$$\underset{(6\times 4)}{\begin{bmatrix} F^{TC} \\ F^{TS} \\ F^{TE} \end{bmatrix}} \underset{(4\times 1)}{\{\alpha\}} = \underset{(6\times 1)}{\begin{bmatrix} r^{TC} \\ r^{TS} \\ r^{TE} \end{bmatrix}} \tag{2-46}$$

where:

F^{TC}= Sensitivity matrix for triaxial compression regimen

F^{TS}= Sensitivity matrix for triaxial shear regimen

F^{TE}= Sensitivity matrix for triaxial extension regimen

r^{TC}= Residual vector for triaxial compression regimen

r^{TS}= Residual vector for triaxial shear regimen

r^{TE}= Residual vector for triaxial extension regimen

Using the above algorithm, four of the five material properties needed to characterize cross-anisotropic materials (E_x, E_y, ν_{xx}, and ν_{xy}) can be determined. The fifth material property, G_{xy}, can be found directly from shear stress path regimen using equation 2-19. Figure 2-3 shows the flowchart for determination of cross-anisotropic material properties using the system identification method.

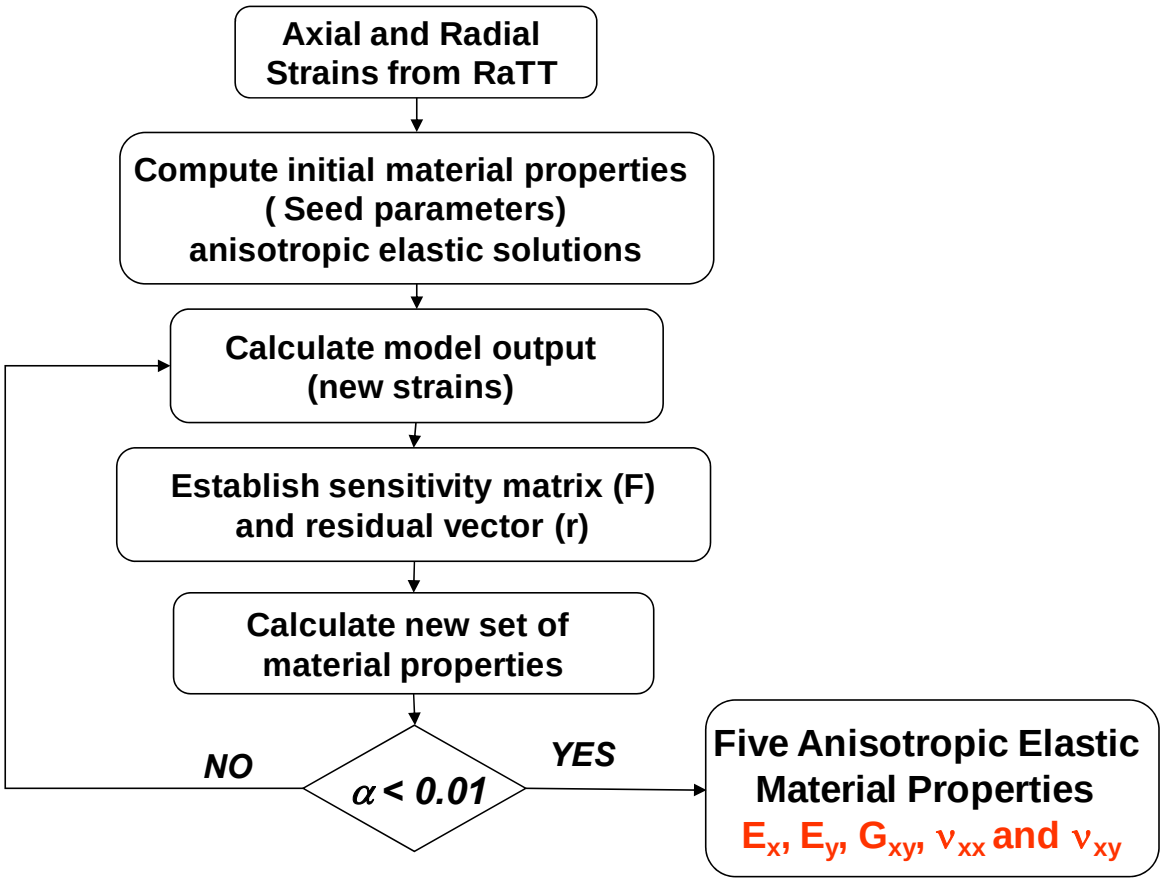

Figure 2-3 Flowchart for determination of cross-anisotropic material properties using system identification method

DETERMINATION OF ANISOTROPIC SHEAR MODULUS USING SHEAR WAVE METHOD

Anisotropic stiffness of geomaterials at small strains can be found by shear wave velocity measurements using piezoelectric bender elements in the lab. Shear modulus of the aggregate sample can be found from equation 2-47:

$$G_o=\rho V_S^2 \tag{2-47}$$

where G_o is the shear modulus at small strain, ρ is the bulk density of the aggregate sample, and V_s is the speed of the shear wave propagating through the sample.

Several researchers used this concept to determine the shear stiffness of aggregate samples by propagation of shear waves with horizontal polarization emitted by bender elements embedded in the triaxial cell. Once the shear wave transmitted throughout the aggregate specimen, shear modulus in orthogonal plane, G_{xy}, can be determined using equation 2-47.

Fioravante showed that accurate wave propagation and measurement of shear wave velocity with both horizontal and vertical polarization can be used to determine anisotropic shear stiffness of geomaterials (Fioravante and Capoferri 2000). He mounted two orthogonal bender elements diametrically across the specimen and measured shear wave velocity in horizontal $V_{S(xx)}$ and vertical planes $V_{S(xy)}$. Therefore he was able to calculate G_{xx} and G_{xy}, shear modulus in horizontal plane and shear modulus in xy plane, respectively. He used equations 2-48 and 2-49 for determination of anisotropic shear moduli in geomaterials.

$$G_{xx}=\rho V_{S(xx)}^2 \tag{2-48}$$

$$G_{xy}=\rho V_{S(xy)}^2 \tag{2-49}$$

In another study, Hardin proposed an equation for calculating the shear modulus as a function of stress states, stress history, and void ratio for sands (Hardin 1978). His formulation is presented in equation 2-50:

$$G_o = S\ f(e)(OCR)^k Pa^{(1-n)} p^n \tag{2-50}$$

where:

S= dimensionless material constant reflecting the soil fabric

f(e)= void ratio function

OCR= over consolidation ratio

P= mean effective stress

Pa= atmospheric pressure

k and n= model parameters

Later Ng used the above formulation to calculate the anisotropic shear moduli using shear wave velocity and state of the stresses in the soil samples (Ng 2001) . Ni showed that the shear modulus at very small strains is a function of stresses in the direction of wave propagation (Ni 1987). Using the concept, Ng used equations 2-51 and 2-52, which are based on Hardin's equation for isotropic soil, to calculate the anisotropic shear modulus in the soil samples (Ng 2001).

$$G_{xy} = S_{xy}\ f(e)(OCR)^k Pa^{(1-nx-ny)} (\sigma_x)^{nx} (\sigma_y)^{ny} \tag{2-51}$$

$$G_{xx} = S_{xx}\ f(e)(OCR)^k Pa^{(1-2ny)} (\sigma_x)^{2nx} \tag{2-52}$$

In equations 2-33 and 2-34, σ_x and σ_y are horizontal effective stress and veridical effective stress, respectively. Model parameters (ν_x) and (ν_y) can be determined experimentally in the lab.

Figure 2-4 schematically shows the laboratory arrangements of bender elements and shear propagation technique for determination of cross-anisotropic shear modulus of geomaterials.

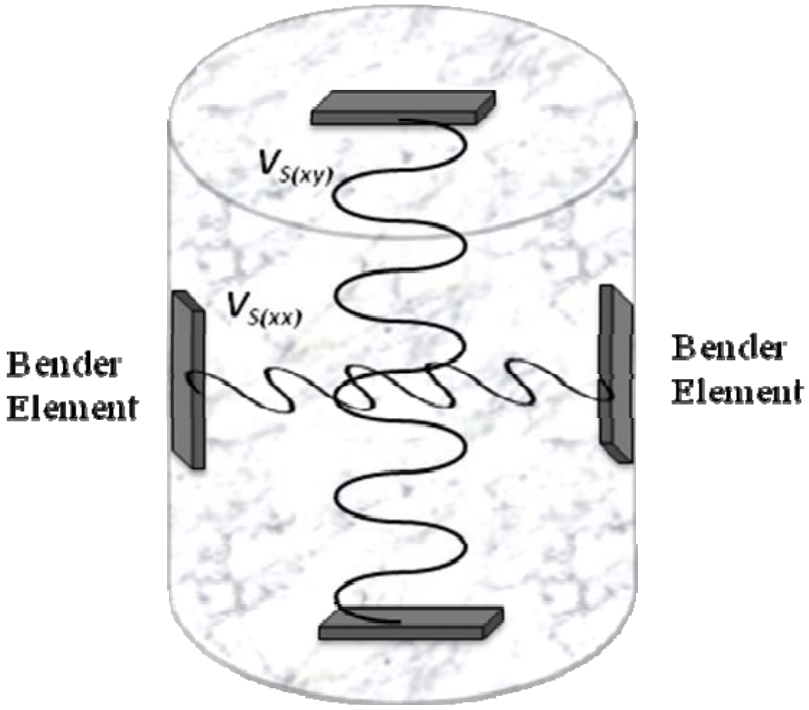

Figure 2-4 Bender elements arrangement for aggregate samples

ANISOTROPY IN GEOMATERIALS

Material properties in different directions vary for most naturally deposited materials as well as compacted aggregate layers. As previously described in this chapter, directional dependency of material properties, also known as anisotropic material behavior, significantly influences the distribution of stresses and strains in the aggregate systems. Therefore it appears necessary to consider aggregate layers as anisotropic materials for the design of pavement foundations.

As discussed earlier in the general form of anisotropy, no symmetry of the material structure is assumed, therefore, it would be extremely difficult to characterize the materials as fully anisotropic. In most engineering materials we can find or assume a single symmetry plane, three planes of symmetry as in orthotropic materials, or a single axis of symmetry. Most geological materials fall into the last category. Materials with one axis of symmetry have similar material properties along that axis. Such materials are defined as transversely isotropic or cross-anisotropic materials. Anisotropy of geomaterials can be studied in two categories:

- Particle induced anisotropy
- Stress induced anisotropy

Size, shape, angularity, and texture of the aggregate particles significantly influence the anisotropic behavior of geomaterials. The primary reason for this behavior is the fact that random assemblies have random distribution of inter-particle contacts. It is well established in the literature that aggregate interlock is the primary mechanism for the distribution of loads in aggregate systems. Aggregate interlock by itself is determined by the inter-particle friction forces, which are a function of particle contact areas. Due to the random nature of the distribution of the orientation of particles and consequently random distribution of particle contacts, particulate systems exhibit directional dependency even though they are subjected to hydrostatic stresses. This type of anisotropy is called particle induced anisotropy.

The type of anisotropy that is induced on the aggregate samples due to the nature of state of stresses and stress regimes is referred to as stress induced anisotropy.

In the following chapters we will discuss the influence of saturation level and stabilizer content as well as features of the aggregate particle such as size and geometry of the rock particles. We will use modular ratios which are the ratio of horizontal to vertical resilient modulus (E_x/E_y), horizontal resilient modulus to shear modulus (E_x/G_{xy}), and the ratio of shear modulus in orthogonal directions (G_{xx}/G_{xy}) as measures of the level of anisotropy in aggregate systems.

The following section provides comprehensive discussion on the types of anisotropy and the methods to quantify each component of anisotropy in aggregate systems.

Inherent Anisotropy

The directional dependency of material properties or anisotropic behavior of geomaterials stems from the particle geometry and particle size distribution as well as stresses applied on the system in geomaterials. Geometry of aggregates can be characterized by shape, angularity, and texture of the aggregate particles. If all aggregate particles were single sized, equi-dimensional, and subjected to hydrostatic stresses, then response would be isotropic, however, particle size distribution, particle geometry, and the nature of stresses in the field dictates anisotropic behavior. The component of the anisotropic behavior that is related to particles is called particle induced anisotropy or inherent anisotropy. Inherent anisotropy is also referred to as initial anisotropy in rock mechanics literature.

Several researchers studied the influence of the particle shape and particle arrangement on the mechanical behavior of geomaterials. Parkin, El-Sohby, and Oda were first to characterize fabric characteristics in random assemblies (Parkin et al. 1968), (El-Sohby 1969), and (Oda 1972). Early work in the area of geotechnical engineering revealed that even rounded natural sands deposited under gravity forces exhibit some degree of cross anisotropy. The major reason for such behavior was found to be non-

homogenous distribution of particle orientations with proffered orientation in the direction of deposition. Figure 2-5 shows distribution of particle orientation for Cambria sands. This rose plot clearly demonstrates the preferred orientation of deposited sand particles tends to align with horizontal plane.

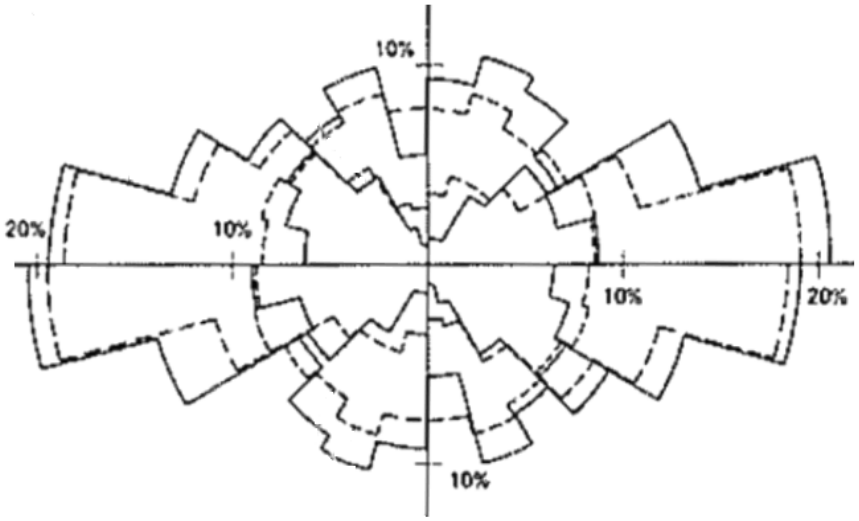

Figure 2-5 Rose diagram for particle long axis orientations of Cambria sands (Lade and Wasif 1988)

Maximum packing or density of aggregate systems is controlled by aggregate geometry, particle size distribution, degree of saturation, and the compaction energy. Upon compaction, aggregate particles subjected to compaction rollers tend to rearrange themselves in a way as to increase particle contacts and reduce air voids to achieve maximum density. Figure 2-6 shows a schematic representation of particle orientation before and after compaction. In the compaction process, an aggregate's longest axis tends to align with the horizontal plane, as illustrated in figure 2-6.

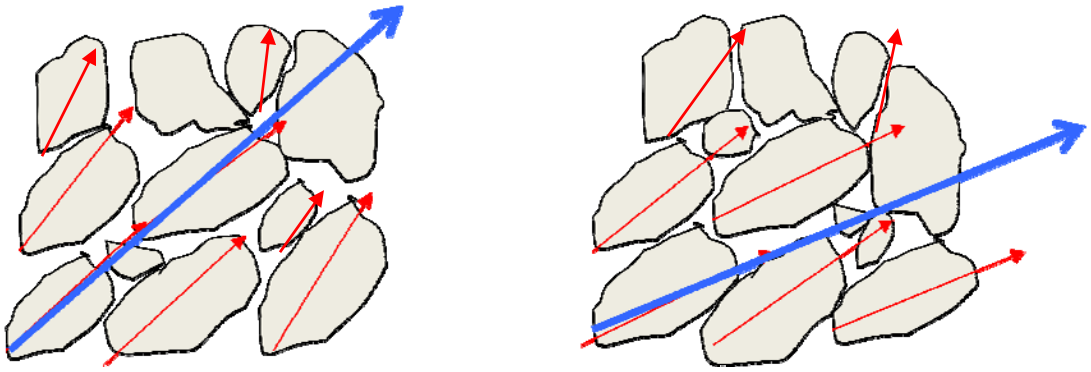

(a) (b)

Figure 2-6 Preferred orientations of aggregate particles (a) before compaction (b) after compaction

Characterization of the Particle Orientation

Directional distribution of aggregate particles can be characterized in different means. Several researchers worked on implementation of a microstructure tensor in addition to the stiffness matrix to capture the influence of particle orientat`ion in the response behavior of geomaterials (Kanatani 1984), (Oda 1972), (Bathurst and Rothenburg 1990), and (Masad et al. 2005) to name a few.

Figure 2-7 shows four of the methods employed by aforementioned researchers to characterize particle orientations in the soil samples. Figure 2-6 (a) shows the characterization of aggregate particles using the direction of the longest axis. Figure 2-6 (b) illustrates the characterization method in which the distribution of particles is characterized by the orientation of the normal to the particle interface.

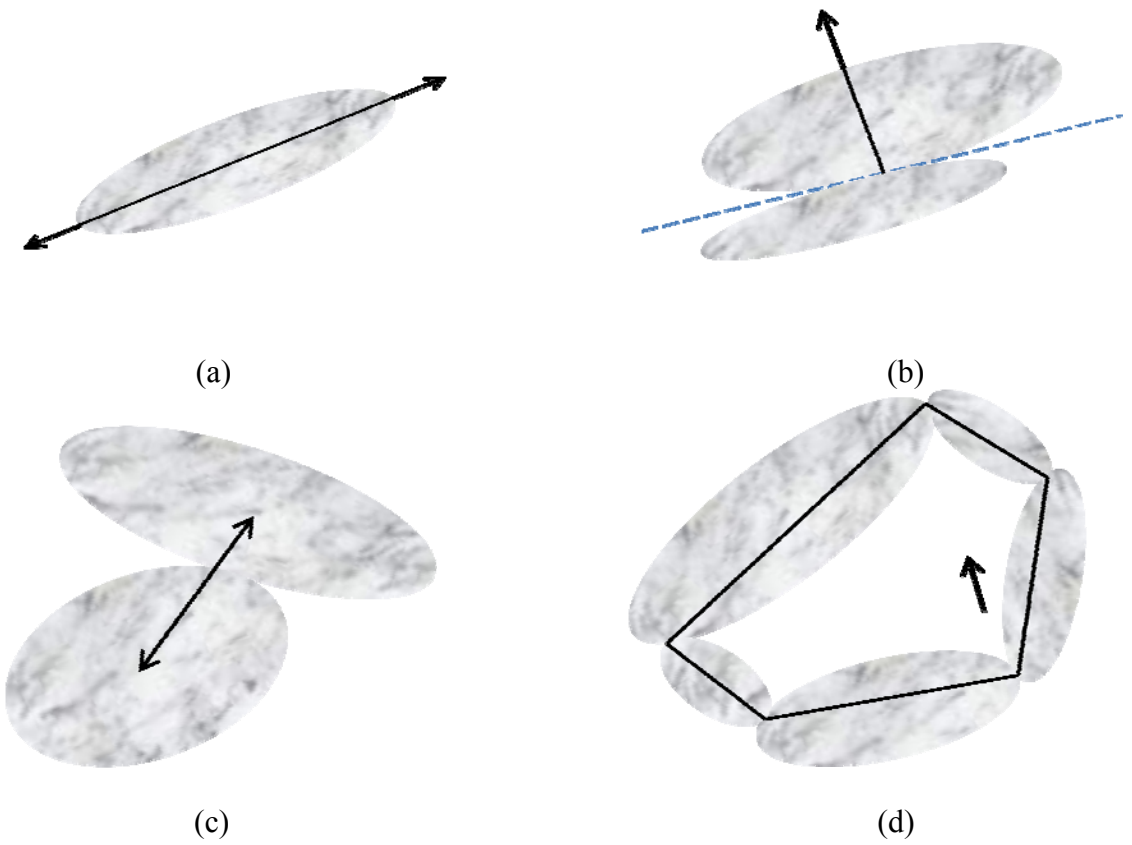

Figure 2-7 Characterization of th- particle orientation (a) direction of the longest axis (b) normal to the particle interface (c) branch vector (d) normal to the polygon representing the air void

Figure 2-7 (c) shows the branch vector in which particle orientation is characterized by the vector connecting the center of the projection of the aggregates in two dimensions. This method is also referred to by the cord method in microstructure characterization of particulate media. Figure 2-7 (d) illustrates the air void method. In this method, distribution of the vector assigned to the polygon representing the air void trapped between the particles is used to characterize the shape properties of aggregates present in the mix. The idea behind this method is that since maximum packing is a function of particle geometry, particle size distribution as well as compaction energy, the air void distribution is also affected by particle shape properties.

Representation of the contact distribution of the particles in the aggregate samples can be achieved through the definition of the orientation distributions. The microstructure added to the constitutive model can be used to assess the impact of inherent anisotropy on the directional dependency of material properties. Mehrabadi used a microstructure tensor, which is a function of contact area, length of the branch vector, direction cosines of contacts normal, and direction cosines of branch vectors (Mehrabadi et al. 1982). Kanatani, Oda, and Tobita later used a probability density function E(I) to represent the microstructure tensor (M_{ij}) as illustrated in equation 2-53 (Oda et al. 1982) and (Kanatani 1984):

$$M_{ij} = E(I) l_i l_j d\Omega \tag{2-53}$$

where l_i is the unit normal of an elementary solid angle $d\Omega$, and Ω captures the whole surface of the representative volume element. Masad argued that the form presented in equation 2-53 can be used to model the orientation distribution of the particles using either of the methods previously discussed in this section (Masad et al. 2005).

On the other hand, the probability density function can be expressed as a function of microstructure tensor as presented in equation 2-54:

$$E(I) = \frac{15}{8\pi}\left[M_{ij} - \frac{\delta_{ij}}{5} \right] l_i l_j \tag{2-54}$$

where δ_{ij} is the kronecker's delta.

Later Kanatani provided equation 2-55 to find the probability density function to quantify particle orientation in the constitutive models.

$$E(I) = \frac{1}{4\pi}\left[1 + M'_{ij}\, l_i l_j \right] \tag{2-55}$$

In equation 2-55 M'_{ij} is the deviatoric component of the microstructure tensor. Later Masad used the microstructure tensor presented in equation 2-38 to show the influence of particle orientation on orthogonal stiffness properties of aggregate samples.

$$M_{ij} = \begin{bmatrix} \frac{2+A}{6+A} & 0 & 0 \\ 0 & \frac{2+A}{6+A} & 0 \\ 0 & 0 & \frac{2-A}{6+A} \end{bmatrix} \tag{2-56}$$

where A is called the anisotropy parameter, which is a function of particle orientation and can be calculated from equation 2-57:

$$A = \frac{\sum_{k=1}^{N} \cos(2\theta)}{N} \tag{2-57}$$

where θ is the orientation of the particles in the mix and can take values ranging from -90 to 90 degrees. For an isotropic material with no fabric orientation, the value of A is zero while for a material with all particles oriented in the same direction the value of A equals to unity.

Figure 2-8 schematically shows a rose diagram of the preferred orientation of aggregate particles in a random assembly. This plot shows the frequency and the angle of inclination of particles for three different aggregate systems. Inclination of the longest axis is used to characterize the orientation of the particles in this plot.

Figure 2-8 (a) shows an ideal system consisting of single size spherical particles. This system shows no inherent anisotropy and under hydrostatic stresses will be fully isotropic. There will be no dependency of material properties for this system.

Figure 2-8 (b) shows a typical aggregate system consisting of mixed size particles. This material exhibits anisotropic behavior even under hydrostatic stresses.

Stiffness properties of such a system are different in different directions due to non-homogeneous distribution of particle contacts.

Figure 2-8 (c) shows preferred orientation and frequency of a particulate system consisting of flat and elongated platelet particles. This plot shows the platelet particles tend to orient themselves parallel to a horizontal plane when subjected to compaction. The distribution of the contact points in this system are highly non-uniform, therefore this system is highly anisotropic, and the material properties vary significantly in different directions. Platelet particles stacked on the top of each other create a high contact area aligned with a horizontal plane; therefore stiffness in a vertical direction will be high. However, when such a system is subjected to shear loads, the assembly rapidly becomes unstable. The aforementioned system is prone to develop significant plastic deformations when subjected to lateral or shearing forces.

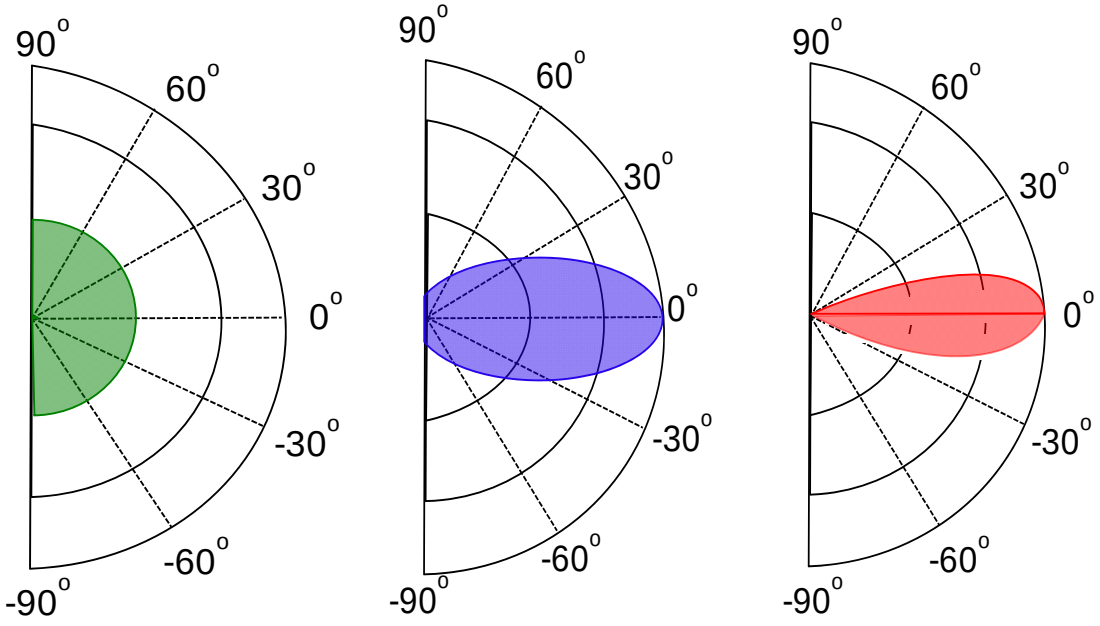

(a) (b) (c)

Figure 2-8 Particle orientation distributions of aggregate systems (a) equi- dimensional single size aggregate system (b) mix size aggregate system (c) mix size flat and elongated aggregate system

Stress Induced Anisotropy

The nature of moving wheel loads adds another component to the directional dependency of stiffness properties in aggregate layers. Schematic representation of the stresses induced by moving wheel load on the pavement is presented in Figure 2-9. In this figure, vertical stress (σ_y) is the largest at the centerline of the wheel load and reduces nonlinearly as the wheel moves away from the reference point. Horizontal stress (σ_x) follows the same manner but with a much lower magnitude. The rate of dissipation of the stresses, slope of the stress plots, is much higher for a vertical stress plot compared to the horizontal stress distribution. Therefore, at some point away from the wheel load, the total stress felt by a soil particle changes from compression to tension. Although the magnitude of the tensile stresses at this region is very small, the change in the stress regimen (stress history) will induce additional dependency of material properties in pavement foundations.

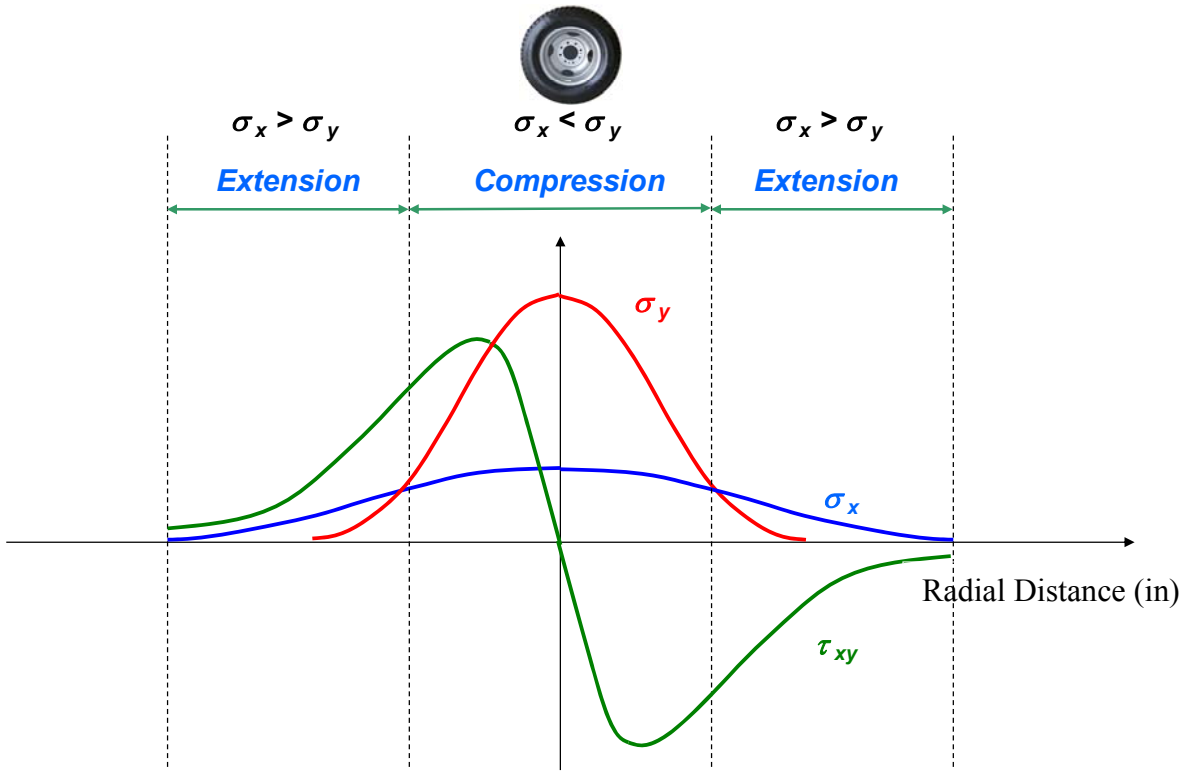

Figure 2-9 Schematic representations of stresses induced by wheel load in pavements

Moving wheel load induces nonlinear shear stresses on the pavement. The nature of these stresses results in accumulation of plastic strain in the aggregate layers. The shear stresses induced on the pavement results in the rotation of the principal plane. Principal plane is the plane on which the shear stress is zero. The orientation of this plane can be found by finding the rotation angle that result in zero components of shear stresses. As illustrated in Figure 2-10, we intend to find the rotation angle θ so we only have σ_x and σ_y. Equation 58 can be used to calculate the orientation of the principal plane using Mohr circle.

$$\theta_{\sigma_1,\sigma_1} = \frac{1}{2}\tan^{-1}\left(\frac{2\tau_{xy}}{\sigma_x - \sigma_y}\right) \tag{2-58}$$

where θ is the orientation of the principal plane, σ_x is horizontal stress, σ_x is vertical stress, and τ_{xy} denotes shear stress.

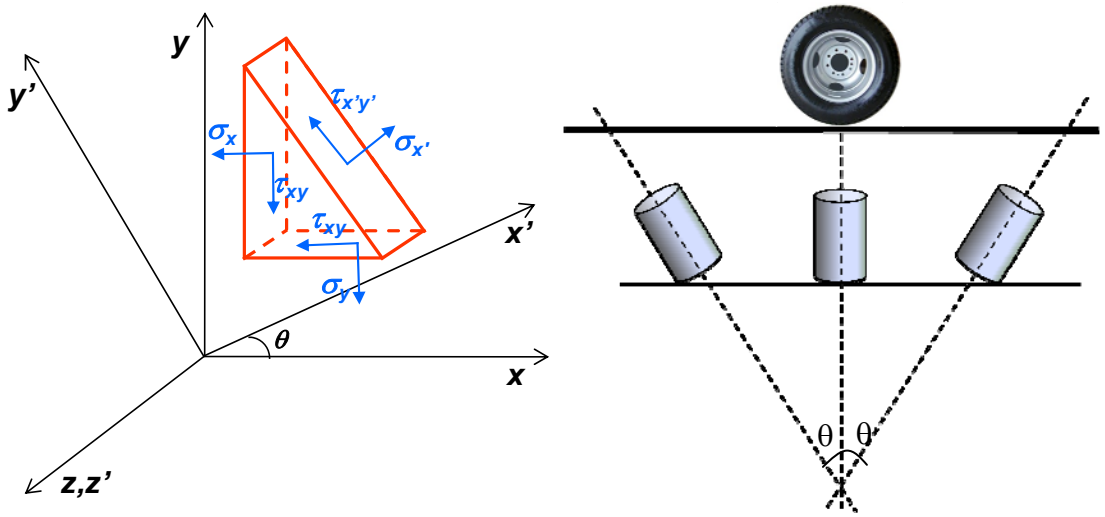

Figure 2-10 Rotation of the orientation of the principal plane under the moving wheel load

Figure 2-11 shows the rotation of the principal plane for an assumed pavement profile under traffic load. Cross-anisotropic solutions were used to calculate pavement responses under wheel load. It was assumed that the horizontal stiffness of the aggregate layer was 30 percent of the vertical stiffness. Equation 2-40 was used to calculate the orientation of the principal plane.

As illustrated in Figure 2-11, the orientation of the principal plane changes as the wheel load passes the reference point. As demonstrated in plot, the inclination of the principal plane is zero at the centerline. In other words, the stresses under the centerline of the wheel load are principal stresses, and the shear stress is zero. This is also in conformity with shear stress plot in Figure 2-9. As the wheel passes over the pavement, the inclination of the principal plane increases up to a certain point but it reduces as the shear stresses dissipate in the aggregate layer. At certain radial distances away from the wheel load, the inclination of the principal plane is negligible while at radial distances close to the tire edge, the inclination of the principal plane is significant. Therefore, it is necessary to consider the effect of moving wheel load and stress induced anisotropy for mechanistic analysis and design of aggregate layers.

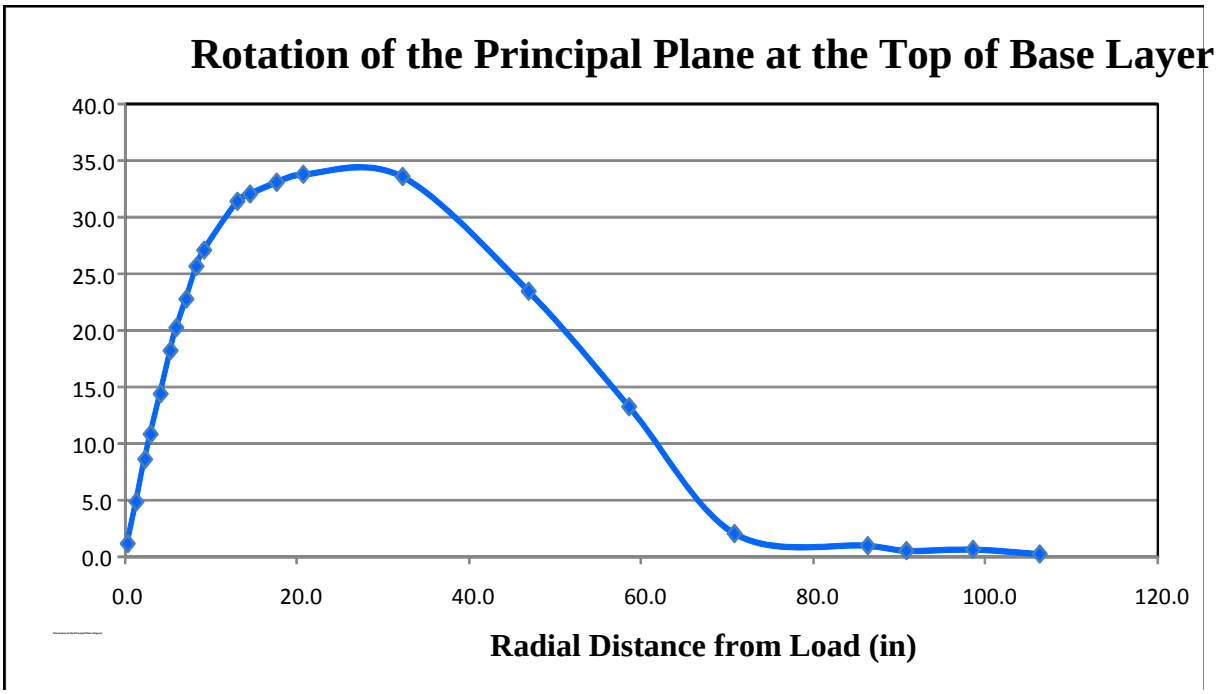

Figure 2-11 Rotation of the principal plane at the top of the base layer

Impact of Stress Ratio, Particle Size, and Geometry of Particles on the Anisotropy of Geomaterials

Tatsuoka performed isotropic and anisotropic stress path tests on three sand and three gravel samples. He used the ratio of horizontal to vertical resilient modulus (E_v/E_h) as an indicator of the level of anisotropy in aggregate samples. Figure 2-12 shows the variation of modular ratios as a function of stress states (Jiang et al. 1997) . The stress path results for aggregate samples are presented in figure 2-12. In this figure, the green line shows an ideal case for an isotropic material with no stress dependency where the stiffness properties are equal throughout the range of the stress ratios. However, as illustrated in this plot, the mechanical behavior of the aggregate samples is far from isotropic. This plot shows all aggregate samples regardless of particle size (sand or gravel) and shows some degree of anisotropy under anisotropic stress path tests.

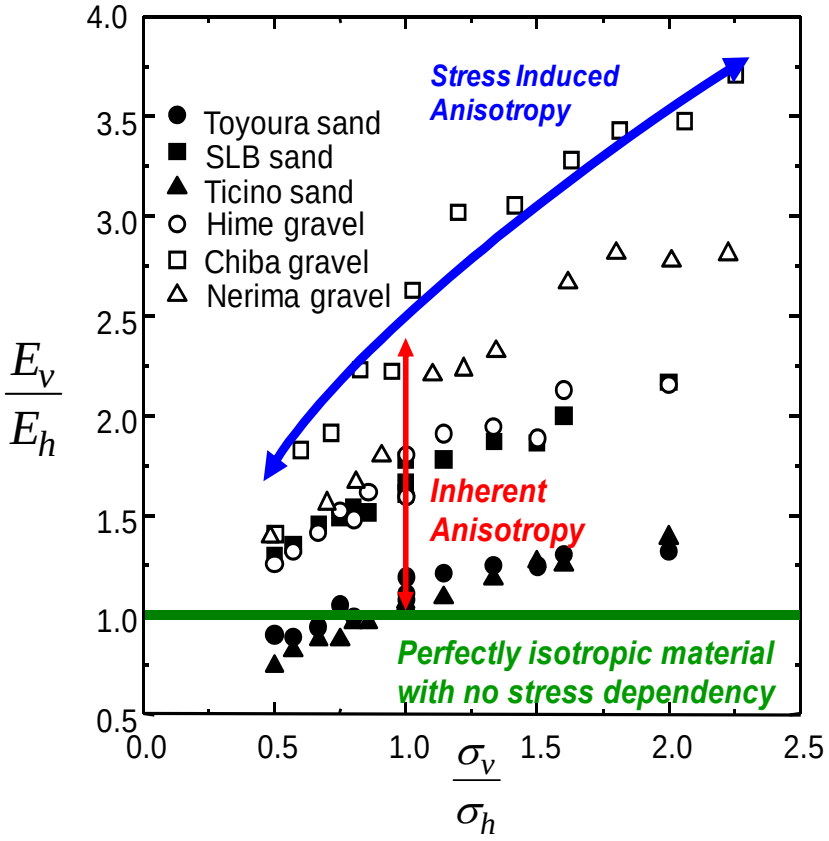

Figure 2-12 Particle induced and stress induced anisotropy in aggregate samples

(Jiang et al. 1997)

Figure 2-12 shows aggregate samples subjected to isotropic stress states have different orthogonal stiffness properties. This difference is due to the intrinsic nature of the particles, which are aggregate geometry and size distribution of the particles in the assembly. As illustrated in this plot at a stress ratio of one (isotropic stress state) coarse-grained materials were found to have more directional dependency of stiffness properties compared to fine-grained aggregate systems.

Figure 2-12 clearly shows the effect of stress ratio on the directional dependency of the material properties. As illustrated in this figure, the anisotropic modular ratios increase in a nonlinear fashion as the prescribed stress ratio increases. The rate of this increase, the slope of the curve, is determined by the size and geometry of the particles present in the assembly.

The level of anisotropy in fine-grained materials (Tayoura sand, Ticino sand, and SLB sand) showed less stress sensitivity while coarse-grained materials (Hime gravel, Chiba gravel. and Nerima gravel) were more sensitive to stress ratios and the anisotropic stress path tests. It can be concluded from this plot that the directional dependency of material properties are more pronounced for coarse-grained materials, and the orthogonal stiffness of the aggregate samples are more affected by stress induced anisotropy as compared to fine-grained samples. This was confirmed by the anisotropic stress path test results on coarse-grained and fine-grained aggregate systems, which will be discussed later in this dissertation.

Based on the anisotropic stress path results presented in figure 2-12, Tatsuoka quantified and decomposed the level of anisotropy of geomaterials into an inherent term and a stress induced term. He used modular ratios at isotropic stress states to characterize the initial anisotropy (or inherent anisotropy) and prescribed a stress ratio to characterize the stress induced anisotropy. He proposed equation 59 to calculate the level of anisotropy of geomaterials (Jiang et al. 1997).

$$\frac{E_y}{E_x} = \left(\frac{E_y}{E_x}\right)_o \left(\frac{\sigma_y}{\sigma_x}\right)^m \tag{2-59}$$

where $(E_y/E_x)_o$ is the modular ratio at isotropic stress state, and m is the fitting parameter found from the regression analysis.

STIFFNESS NONLINEARITY IN GEOMATERIALS

Stiffness nonlinearity is a common and important feature of compacted granular materials. This property has usually been represented by a nonlinear stress dependent relationship between resilient modulus and stresses induced on the aggregate system.

Figure 2-13 and figure 2-14 present distributions of the resilient modulus in horizontal and vertical directions in the base layer. A highly anisotropic system with modular ratio of 0.1 was considered in this simulation. Figure 2-13 shows the nonlinear distribution of the stiffness in a vertical direction. The stiffness of the aggregate layer is

maximum at the centerline of the wheel load, and its value reduces with radial distance and with depth.

The same trend is valid for horizontal stiffness as evidenced in figure 2-14. The magnitude of horizontal modulus is significantly lower than the vertical modulus. Figures 2-13 and 2-14 also show the stress dependency of the response of geomaterials.

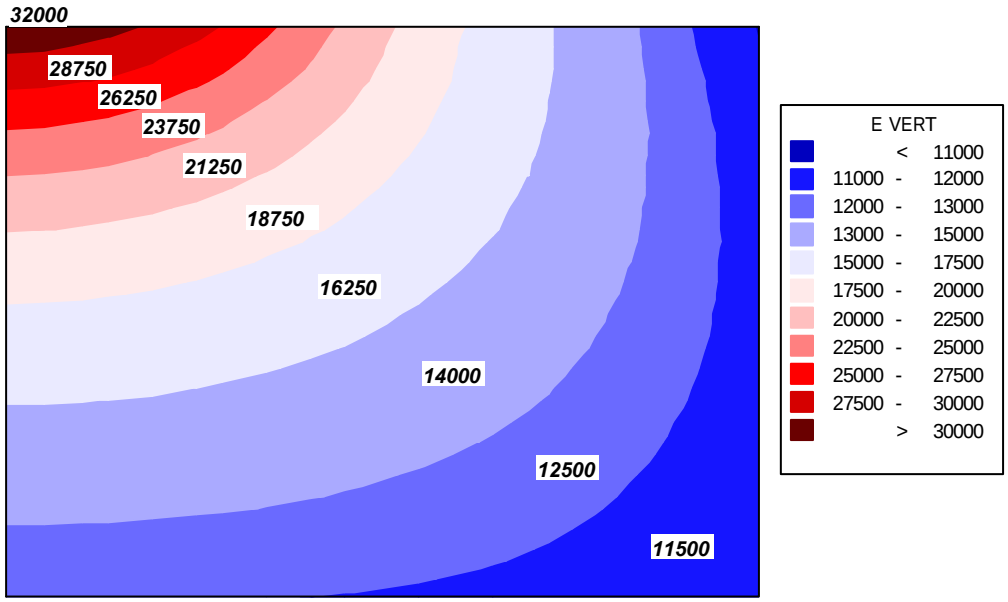

Figure 2-13 Distribution of vertical modulus in the base layer

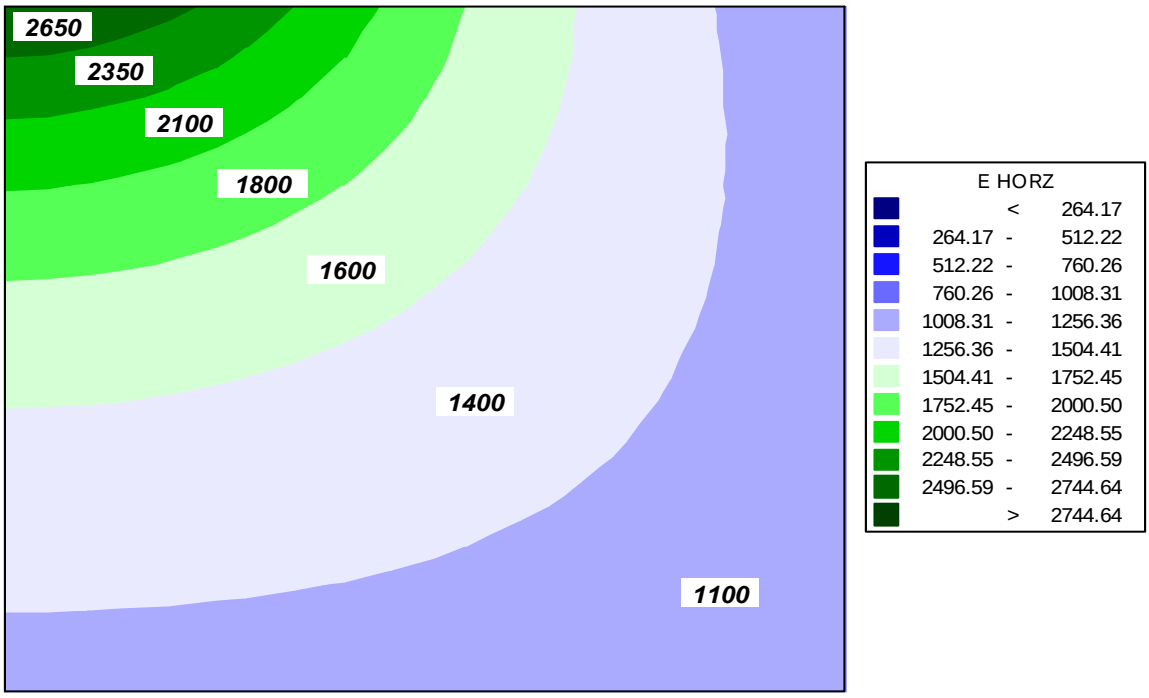

Figure 2-14 Distribution of horizontal modulus in the base layer

Measures of Nonlinearity

Several researchers proposed protocols as to quantify the nonlinearity of geomaterials. This section presents two of the most popular methods for characterization of the nonlinearity of geomaterials.

Figure 2-15 schematically illustrates the typical stress-strain curve for two aggregate samples. The stiff system, which shows less nonlinearity, is represented by a red curve, and the softer aggregate system with a larger nonlinear range is presented in blue. In this figure, q is the deviator stress that is the difference between axial and radial stresses, and ε_f is the strain at the onset of failure. E_o is the initial modulus that is the tangent modulus calculated in the initial stress path. In Figure 2-15, q_f denotes the deviatoric stress at failure.

The ratio of a measure of stiffness to a measure of strength appears in many geotechnical models. An example of this model is solutions for cavity expansion developed by Vesic.

He presented an argument on the validity of the stiffness-strength ratio as the criterion that determines the ductility or brittleness of materials. He later defined the ratio of shear modulus (G_{xy}) to undrained strength (S_u) in the triaxial test as the rigidity index for geomaterials (Vesic 1970).

It is important to note that both stiffness and strain at failure and the coupling effect between the responses needed to be considered for characterization of the nonlinearity of response in unbound aggregate systems.

(Atkinson 2000) proposed two measures, namely rigidity (R) and degree of nonlinearity (m), to quantify the nonlinearity of the stress-strain curve for cohesive soils. He used the stiffness-strength ratio concept and defined rigidity as the ratio of elastic modulus to the strength at failure in the shear test as presented in equation 2-60.

$$r = \frac{E_o}{q_f} = \frac{1}{\varepsilon_o} \tag{2-60}$$

In order to characterize the nonlinearity of the geomaterials, two measures were defined. Atkinson proposed the ratio of strains as a measure of the nonlinearity of geomaterials as presented in equation 2-60:

$$m_1 = \frac{\varepsilon_f}{\varepsilon_r} \tag{2-61}$$

where ε_f is the strain at failure as graphically illustrated in Figure 2-15.

An alternative measure to quantify nonlinearity of geomaterials based on deviatoric stresses is presented in equation 2-61.

$$m_2 = \frac{q_f}{q_r} \tag{2-62}$$

q_f= Deviatoric stresses at failure,

q_r= Maximum deviatoric stress in the linear portion of the stress-strain curve

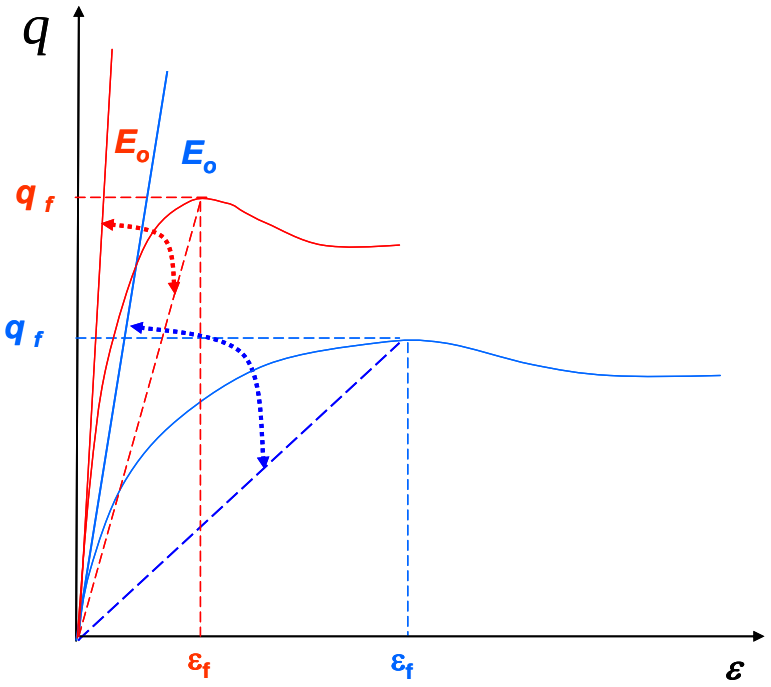

Figure 2-15 Typical stress-strain behavior for stiff and soft aggregate system

CHAPTER III

STRESS PATH TESTING OF GEOMATERIALS

BACKGROUND

The mechanical behavior of geomaterials is greatly influenced by the stress states and stress history. This chapter provides various stress path tests and quantification methods used by geotechnical scientists to mechanistically simulate the response behavior of aggregate systems.

Desai explained the concept of stress path using a drilled pile problem in an elastic half space homogeneous soil medium (Desai et al. 1987). As shown in figure 3-1, the pile is loaded in both vertical and horizontal directions. Under the illustrated loading conditions, different elements of the soil continuum experience different loading paths or undergo different stress paths. A stress path in general shows the deviation from the initial stress states due to an external load to reach terminal stress conditions. Initial stresses felt by an arbitrary point in the soil continuum is primarily due to the weight of the overburden and the residual stresses. The residual stresses are the type of stress that is imposed by compaction or due to time-dependent consolidation of the soil strata. Residual stresses inflicted by drum rollers and compactors are typically highest at the surface, where the compaction energy is applied, and reduces with depth of the aggregate layer. Initial stresses induced by weight of the soil is a function of soil density, saturation level, and the depth of the soil, therefore in unsaturated state and equal conditions, soil sample A has the highest initial vertical stress while soil samples C and D have the smallest initial vertical stresses. In deep foundations, the effect of soil overburden is more significant than the residual stresses.

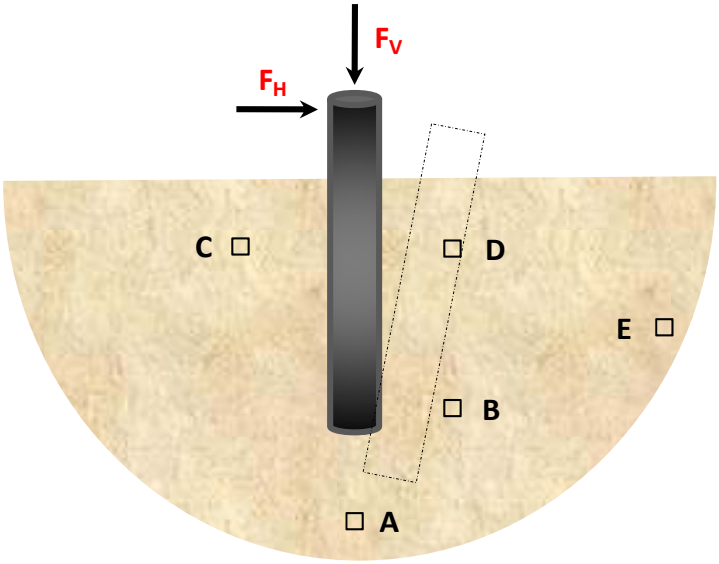

Figure 3-1 Schematic representation of a vertically and laterally loaded pile

(Desai et al. 1987)

Figure 3-2 shows the initial stress states and the stress path for different soil particles previously described in this chapter. Deviatoric place is typically used by geotechnical engineering to represent the stress path plots, therefore (q-p) stress space is used to show stress path in this example. In figure 3-2, q is the deviatoric stress, and p is the average of the principal stresses experienced by the soil particle.

Under loading, soil sample A may load in shear while the mean principal may stay constant. Therefore the stress path for soil sample A will be a straight vertical line connecting the initial stress state A to terminal stress state A'. For soil sample B, upon loading soil sample B initially loads and then essentially unloads in mean principal stress, with a small increase (or decrease) in deviatoric stress. Soil sample C can basically experience tension when subjected to vertical and horizontal loading conditions as the pile moves away from this point and relieves the pressure. Soil sample D indicates the general condition of a soil sample for which the mean stress and deviatoric stress increases under loading. Point E considered to be out of the impact zone, therefore the loading conditions had no effect on the initial stress states.

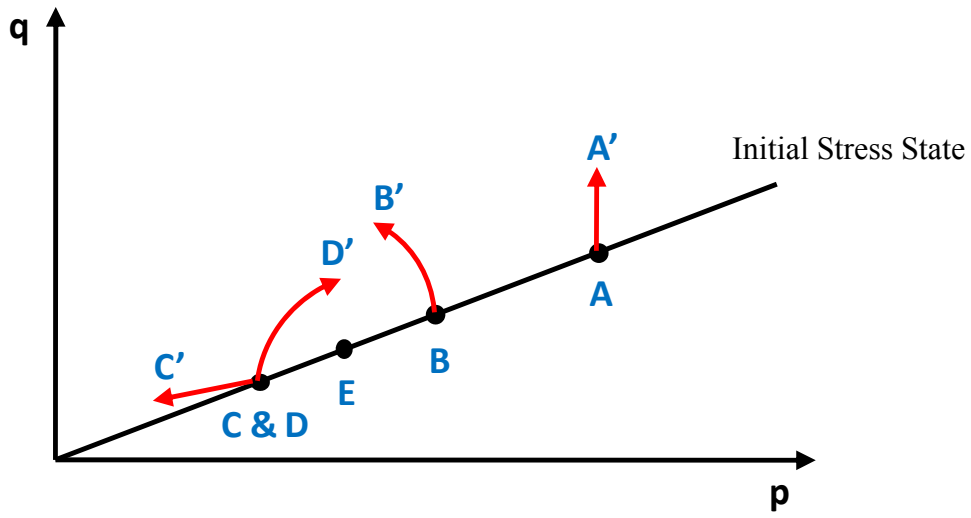

Figure 3-2 Stress path plots for different soil samples (Desai et al. 1987)

This example shows a simple structure under static loading conditions that creates a different stress path. Therefore it is imperative to subject the aggregate systems to a different loading path in the lab to mechanistically characterize the behavior of the geomaterials. The following section provides commonly used stress path test methods for constitutive modeling of geomaterials.

STRESS PATH TYPES

Figure 3-3 schematically represents the common stress path types used in modeling the geomaterials. In this figure σ_1, σ_2, and σ_3 are the principal stresses acting on geomaterials. As shown in this figure, all prescribed stress paths using a triaxial apparatus will fall on the plane in which ($\sigma_2 = \sigma_3$). This plane is called the triaxial plane. Octahedral plane normally makes equal angles with the principal stresses. The normal to the octahedral plane is also called the space diagonal.

In the subsequent section we present the different types of stress path tests and their significance in constitutive modeling of the aggregate systems. The discussion will be presented in the triaxial plane.

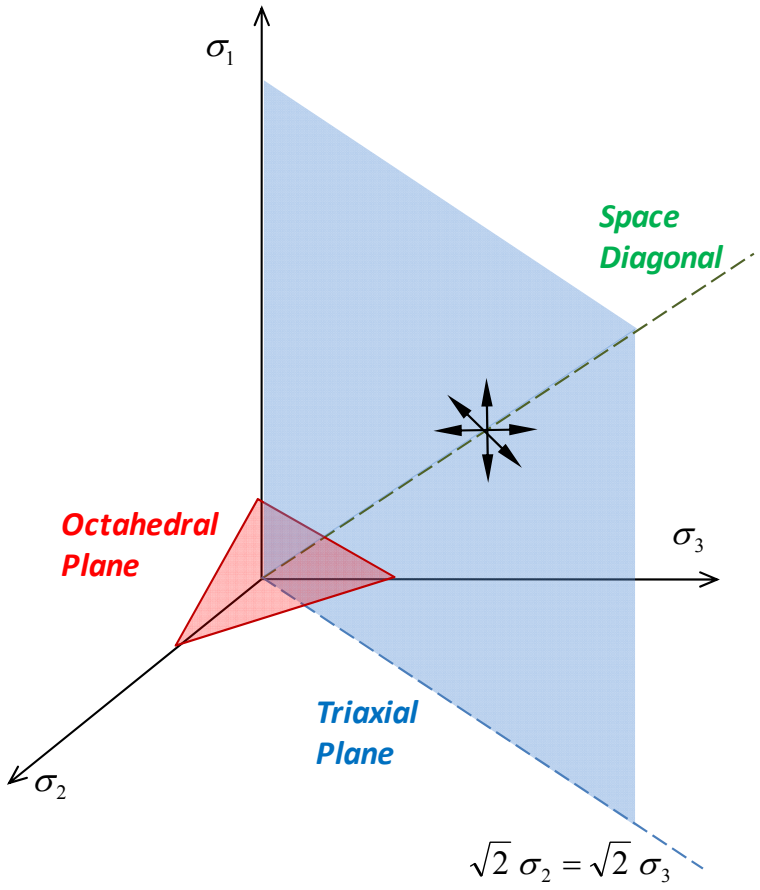

Figure 3-3 Representation of stress path in triaxial stress space

Hydrostatic Compression Stress Path (HC)

As illustrated in figure 3-4 in hydrostatic compression (HC) stress path tests, a specimen is subjected to initial hydrostatic stress states, and then the aggregate sample undergoes increments of hydrostatic mean stress ($p=I_1/3$) along the same line. Therefore loading in this type of stress path occurs along the space diagonal.

The hydrostatic stress path provides information on the volumetric or bulk behavior of the soil medium and an essential factor in constitutive modeling the geologic materials (Desai et al. 1987). The measured strains and prescribed stresses using this type of stress path provide information for determining the bulk modulus of the aggregate system. Hardening behavior of geomaterials is also another factor to be determined using

hydrostatic stress path tests. Some constitutive models use material parameters at initial states such as initial density, initial void ratio, or initial pore pressure measured at hydrostatic stress states as input to characterize the initial state of the systems in boundary value problems.

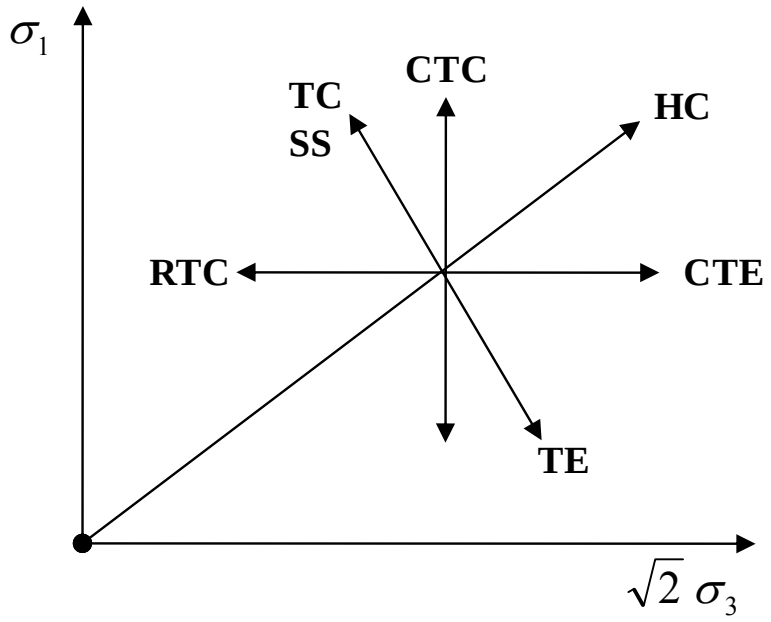

Figure 3-4 Projections of different stress path types on the triaxial plane (Desai et al. 1987)

Conventional Triaxial Compression Stress Path (CTC)

In this type of stress path test, the aggregate specimen is first subjected to a hydrostatic stress state, and then the confining pressure (σ_3) is kept constant while the vertical stress is increased. In this case (σ_1) is the major principal stress, and (σ_3) is the minor principal stress. This stress path is designated as CTC stress path in figure 3-4.

Shear stress and normal stress on the octahedral plane can be found using equations 3-1 and 3-2, respectively.

$$\tau_{oct} = \frac{1}{3}\sqrt{(\sigma_1 - \sigma_2)^2 + (\sigma_2 - \sigma_3)^2 + (\sigma_1 - \sigma_3)^2} \quad (3\text{-}1)$$

$$\sigma_{oct} = \frac{\sigma_1 + \sigma_2 + \sigma_3}{3} \quad (3\text{-}2)$$

In the case of a triaxial device where $\sigma_2 = \sigma_3$, equations 3-1 and 3-2 can also be written as:

$$\tau_{oct} = \frac{\sqrt{2}}{3}(\sigma_1 - \sigma_3) \quad (3\text{-}4)$$

$$\sigma_{oct} = \frac{\sigma_1 + 2\sigma_3}{3} \quad (3\text{-}5)$$

In conventional triaxial compression stress path tests, the change in the octahedral shear stress and the octahedral normal stress is presented in expression 3-6 and 3-7, respectively.

$$\Delta\tau_{oct} = \frac{\sqrt{2}}{3}\Delta\sigma_1 \quad (3\text{-}6)$$

$$\Delta\sigma_{oct} = \frac{\Delta\sigma_1}{3} \quad (3\text{-}7)$$

In equations 3-6 and 3-7, $\Delta\tau_{oct}$ and $\Delta\sigma_{oct}$ are the changes in the octahedral shear stress and octahedral normal stress due to application of conventional triaxial compression stress path.

Reduced Triaxial Extension Stress Path (RTE)

In this type of stress path testing of aggregate systems, the specimen is subjected to an initial hydrostatic stress state, and then the confining pressure (σ_3) is kept constant while

the vertical stress (σ_1) is increased. In this case, (σ_3) becomes the major principal stress, and (σ_1) is the minor principal stress.

Changes in the octahedral shear stress and octahedral normal stress follow the same equations as (CTC) stress path types but with negative signs (equations 3-6 and 3-7, respectively). In (CTC) stress path tests, the change in the stresses in the octahedral plane is positive, therefore, the path is considered a loading path while the change in octahedral stresses in (RTE) stress path tests is negative and is considered an unloading path.

Conventional Triaxial Extension Stress Path (CTE)

In this type of stress path the material is subjected to an initial hydrostatic stress state and, then the vertical stress is kept constant while the confining pressure is increased. This stress path is designated as (CTE) in figure 3-4.

In this type of stress path, (σ_1) becomes the minor principal stress, and (σ_3) becomes the major principal stress. The change in the octahedral shear stress and octahedral normal tress in this type of stress path is presented in equations 3-8 and 3-9, respectively.

$$\Delta\tau_{oct} = \frac{\sqrt{2}}{3}\Delta\sigma_3 \tag{3-8}$$

$$\Delta\sigma_{oct} = \frac{2\Delta\sigma_3}{3} \tag{3-9}$$

Reduced Triaxial Compression Stress Path (RTC)

In this type of triaxial stress path test, the sample undergoes an initial hydrostatic stress state, and then the confining pressure (σ_3) is reduced while the vertical stress (σ_1) is held constant.

In the (RTC) stress path test, the sample undergoes significant shear stresses while the octahedral normal stress is reduced according to equations 3-10 and 3-11.

$$\Delta\tau_{oct} = \frac{\sqrt{2}}{3}\Delta\sigma_3 \tag{3-10}$$

$$\Delta\sigma_{oct} = -\frac{2\Delta\sigma_3}{3} \tag{3-11}$$

Triaxial Compression (TC) and Triaxial Extension (TE) Stress Path Tests

In triaxial compression (TC) and triaxial extension (TE) stress path tests, the stresses are applied such that we remain on the octahedral plane (Desai, 1984). Therefore in these types of stress path tests, the change in the first invariant of the stress tensor, or in other words the mean pressure, stays constant. These stress paths were schematically illustrated in figure 3-4 and designated as (TC) and (TE) for triaxial compression and triaxial extension stress path tests. We will later show that we used this type of stress path in our loading protocol to determine the shear modulus of the aggregate systems.

In the triaxial compression stress path (TC) the specimen was first subjected to hydrostatic stress states, and then (σ_1) was increased and (σ_3) was reduced such that the (σ_{oct}) stays constant. In other words in the vertical stress (σ_1) is increased by ($\Delta\sigma_1$), and then the confining pressure (σ_3) should be reduced by ($\Delta\sigma_1/2$).

In triaxial extension stress path tests (TE), the specimen is subjected to an initial hydrostatic stress state and then the confining pressure (σ_3) increased while the vertical

stress ($\Delta\sigma_1$) decreased in a manner that the first invariant of the stress tensor remains unchanged. The change in the octahedral shear stress is presented in equation 3-12.

$$\Delta\tau_{oct} = \frac{1}{\sqrt{2}}\Delta\sigma_3 \tag{3-12}$$

As previously mentioned in this chapter, the hydrostatic compression stress path tests provide information on the hardening and volumetric behavior of the aggregate system. Triaxial compression (TC) and triaxial extension stress path tests isolate the behavior of the material under shear stress. This feature of (TC) and (TE) stress path tests in conjunction with anisotropic work potential was later used for determination of the anisotropic shear modulus in aggregate systems.

Simple Shear Stress Path Tests (SS)

Similar to triaxial extension (TE) and triaxial compression (TC) stress path, simple shear (SS) stress path is also conducted on the octahedral plane, and the first invariant of the stress tensor remains unchanged. Therefore the (SS) stress path essentially follows the same path as (TC) or (TE) but in opposite directions. In simple shear stress path tests (SS) the change in the vertical stress and horizontal stresses are equal but with different signs. In other words in simple shear stress path tests the vertical stress is increased by ($\Delta\sigma_1$) while the confining pressure ($\Delta\sigma_3$) is decreased by the same magnitude therefore ($\Delta\sigma_1 = -\Delta\sigma_3$).

For this type of stress path test, the increase in octahedral shear stress is presented in equation 3-13 and, as previously mentioned in this section, the change in octahedral normal stress is zero.

$$\Delta\tau_{oct} = \frac{\sqrt{2}}{\sqrt{3}}\Delta\sigma_1 \tag{3-13}$$

LABORATORY STRESS PATH TESTING OF GRANULAR MATERIALS

Proper simulation of the stress states and stress history induced by traffic loads are of major concern in mechanistic analysis and design of pavement sections. In this section discussions on the rationale behind the stress path testing in the lab, quantification methods, and the nature of stresses induced by moving wheel loads will be presented.

A stress path is typically charted on a p-q plot, where p is the average of the principal stresses $(\sigma_1+2\sigma_3)/2$, and q is twice as the radius of the Mohr circle $(\sigma_1-\sigma_3)$. Figure 3-5 shows the representation of stress paths in both Mohr-Coulomb and q-p stress space. The stress path plotted in figure 3-5 demonstrates a condition starting from a hydrostatic stress state at which ($\sigma_1=\sigma_3$ therefore q=0) to higher and higher shearing stresses. The length of the stress path is L, which characterizes the magnitude of the stresses applied on the specimen, and the slope is m, which is an indicator of the stress regimen or the gradient assent to the failure envelope.

Length of Stress Path $$L = \sqrt{p^2 + q^2}$$

Slope of Stress Path $$m = \frac{q}{p}$$

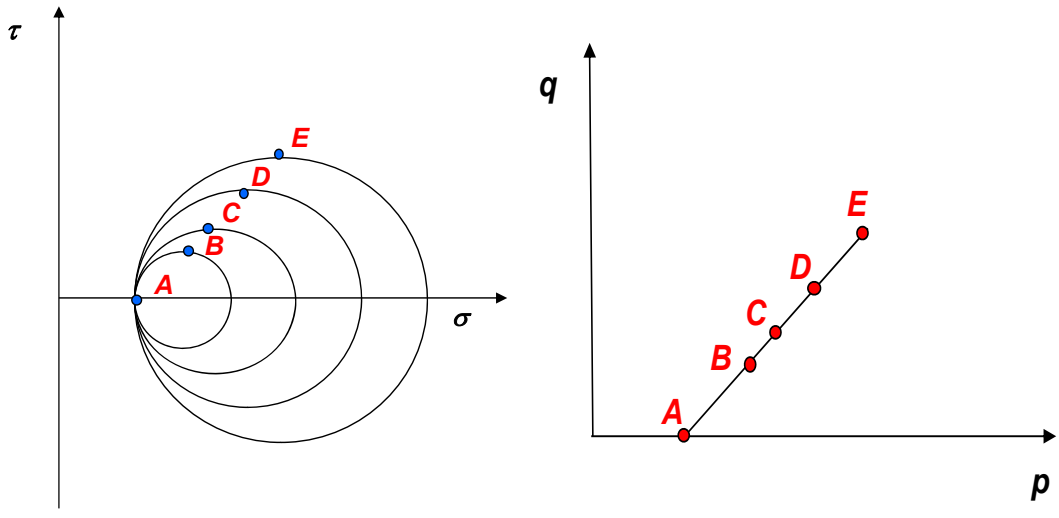

(a) (b)

Figure 3-5 Schematic representation of stress path (a) Mohr-circle (b) q-p plot

The rationale behind stress path testing of the geomaterials is presented in figure 3-6. There are two types of stresses in the pavement foundations: static stress and dynamic stresses. Static stresses are caused by the weight of the overburden while the residual stresses are induced during compaction. The residual stresses are compressive in nature and contribute to particle interlock in aggregate layers. Traffic loads are dynamic by nature and are highest at the centerline of the wheel load, and the load magnitude reduces in nonlinear fashion with depth and radial distance. More discussion on the stress states and stress regimens induced by moving axle loads will be presented later in this chapter.

Figure 3-6 (a) presents the slope of the stress path as an indication of the stress regimen. Stress path slope m=0 represents a hydrostatic stress condition at which ($\sigma_1=\sigma_3$) therefore q=0. Stress path slopes greater than zero represent compressive stress regimens while negative m values represent extension conditions. Stress paths with higher slopes correspond to more critical conditions whereas ascend to the failure surface happens faster.

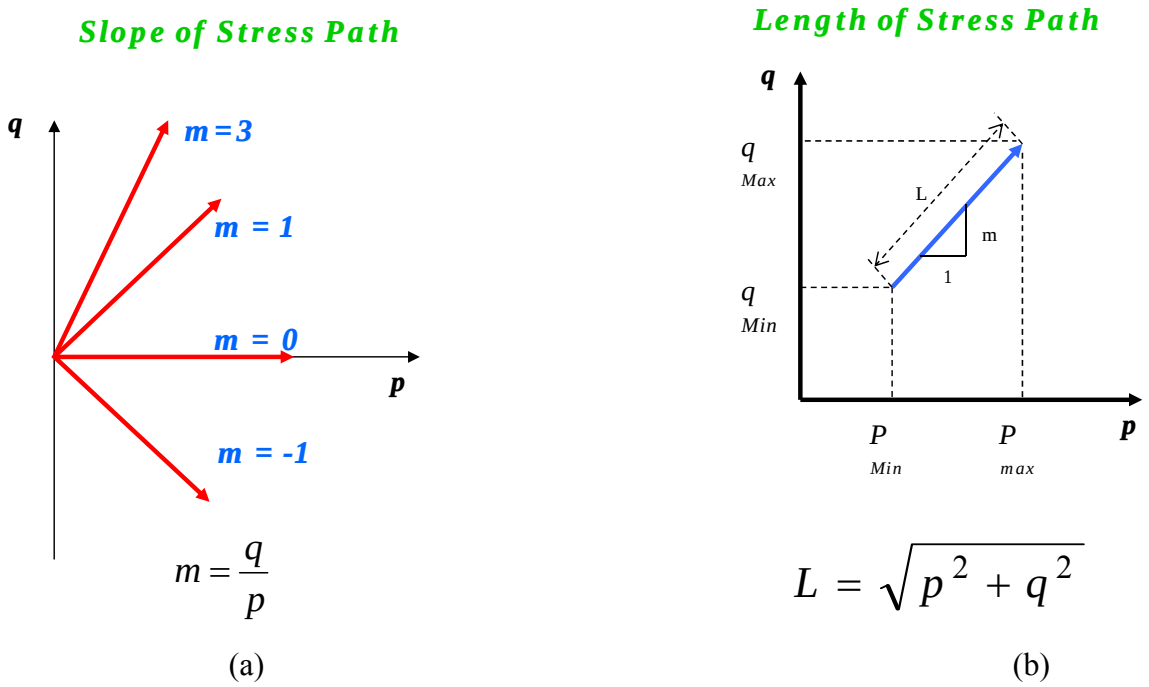

Figure 3-6 Characterization of stress path applied/induced on geomaterials (a) stress path slope (b) stress path length

Figure 3-6 (a) presents stress path length as a measure of stress magnitudes applied/induced on aggregate systems. Static stress states consisting of overburden pressure and residual stresses are depicted as q_{min} and p_{min} in figure 3-6 (b).

Stress paths with a larger L value correspond to situations where higher stress amplitudes were acting on the sample and, therefore, this condition represents more critical conditions. Aggregate systems subjected to larger stress path lengths are more prone to develop plastic deformation.

Kim conducted a series of stress path tests to demonstrate the importance of stress path slope and stress path length on the accumulation of plastic strains in aggregate bases (Tutumluer and Kim 2003). They performed variable confining pressure stress path tests on two aggregate sources and at four stress ratios. The repeated load permanent deformation test results are presented in figures 3-7 through 3-8.

Figure 3-7 shows the combined effect of stress ratio and deviatoric stresses on the accumulation of plastic strains of aggregate specimen in the lab.

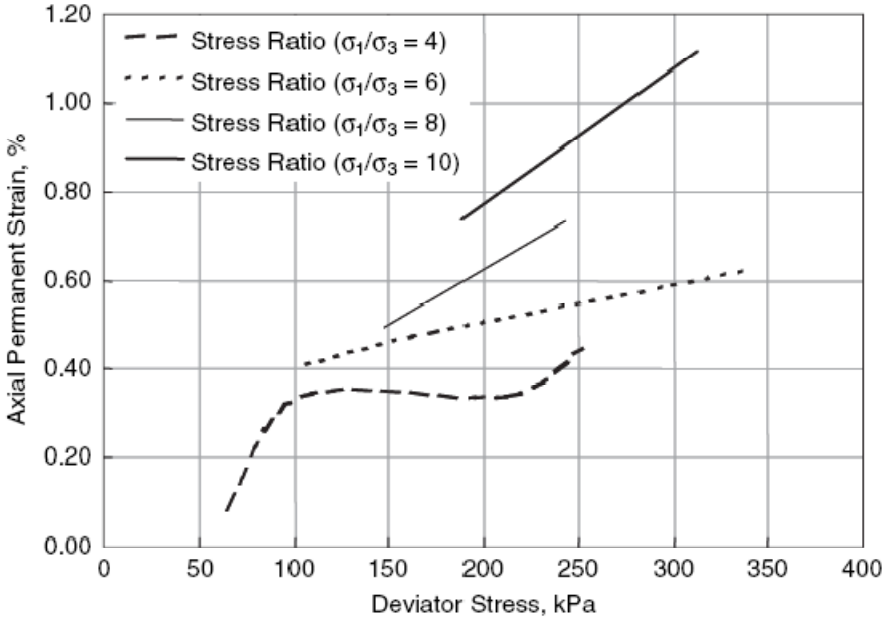

Figure 3-7 Impact of stress ratio on the accumulation of plastic strains (Tutumluer and Kim 2003)

As depicted in this plot, the rate of accumulation of nonrecoverable strains in the aggregate systems significantly increases as the stress ratio and shear stresses applied on the samples increase.

Figure 3-8 shows the impact of stress path length on the accumulation of nonrecoverable strains after 10,000 load cycles. This figure shows the accumulation of plastic strains at three stress path lengths: 9.5 psi, 15.8 psi, and 22.1 psi as a function of number of load cycles. As illustrated in this plot, aggregate samples subjected to larger stress path length developed higher plastic strains upon applying 10,000 load cycles. This is also of importance to note that the rate of the accumulation of the plastic strains also increases as the magnitude of the stresses applied on the samples increases at constant confining pressure. In other words the intuitive and obvious are true: aggregate layers subjected to higher stress path length or higher load axles are more prone to develop rutting during their life.

Figure 3-9 shows the effect of stress path slope on the accumulation of plastic strains in aggregate samples. The repeated load permanent deformation tests were conducted on four aggregate samples with varying stress path slopes. Extension stress path regimen was simulated with stress path slope m=-1, hydrostatic stress state with m=0, and compressive stress regimens with stress path slopes m=1.5 and m=3.

In the extension mode (m=-1) plastic strains were initially negative corresponding to dilation behavior in the aggregate systems. Later after several hundreds of load cycles and around 1000 load pulses, the strains became positive. This behavior resembles the volumetric behavior of dense sands which is well documented in the realm of geotechnical engineering.

As for compression stress regimen (m=1.5 and m=3), aggregate samples subjected to higher stress ratio (m=3) showed higher plastic strains at the end of the repeated load stress path test. This trend is generally valid in all samples as the increase in stress path slope results in higher plastic strains upon applying 10,000 load cycles in the lab.

It is also interesting to note that even under hydrostatic stress states; the axial permanent deformation does not reach an asymptotic behavior, and the plastic strain rate increases even after 10,000 cycles.

The authors concluded that the permanent deformation accumulation at the centerline of the wheel load (where the stresses are compressive and stress path length is the highest) and higher stress path ratio creates the most critical condition.

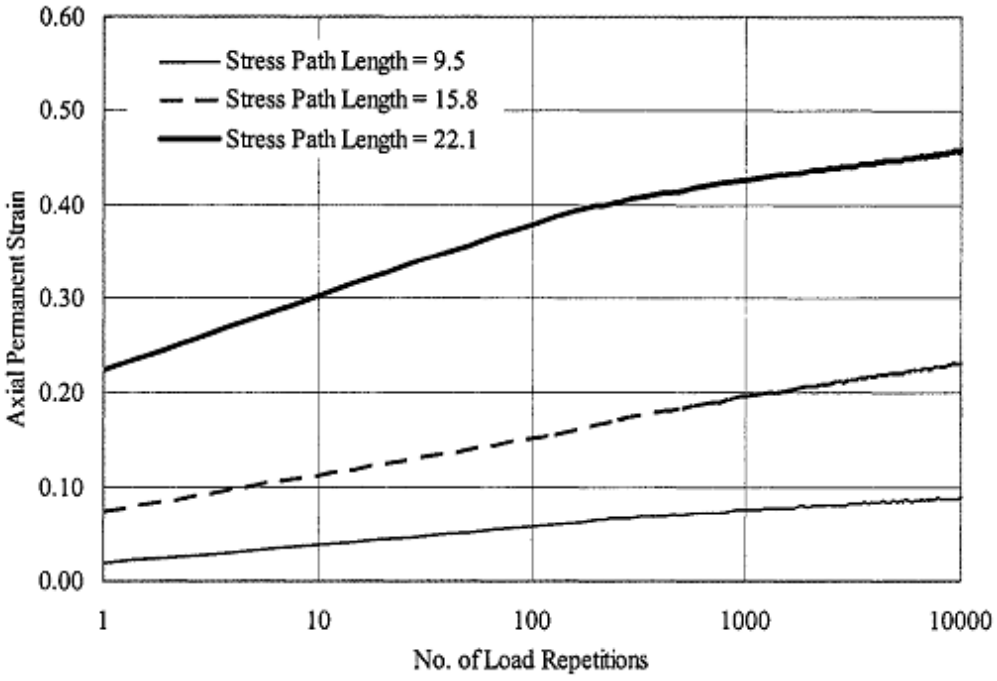

Figure 3-8 Impact of stress path length on the accumulation of plastic strains at 3 psi confining pressure (Tutumluer and Kim 2003)

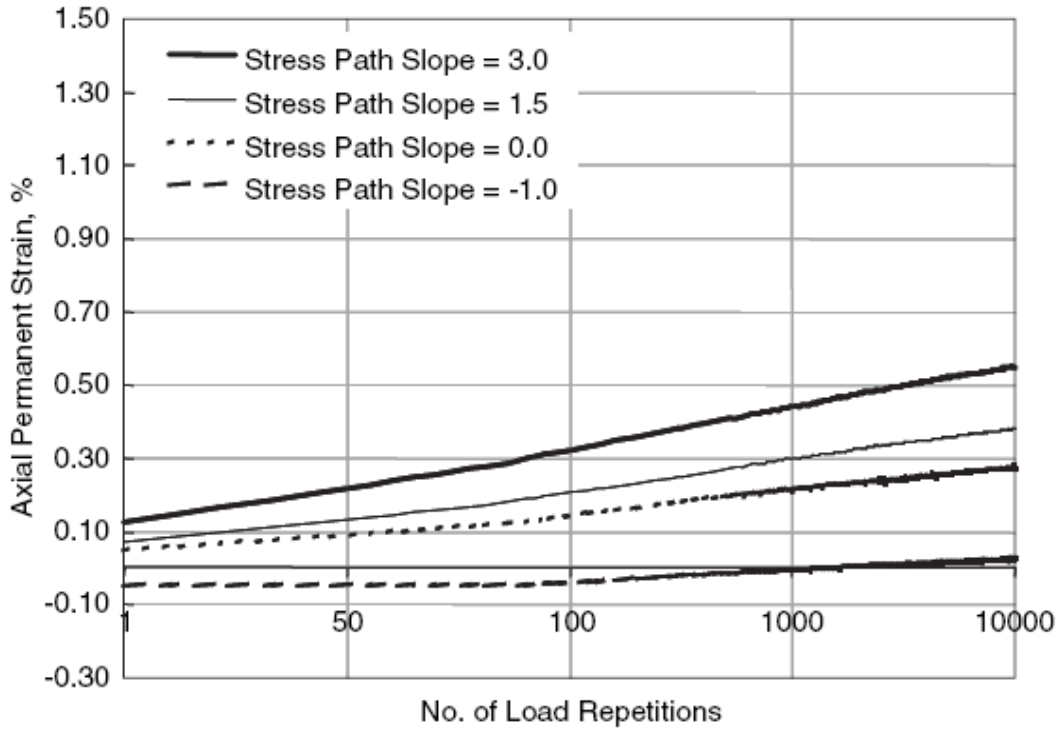

Figure 3-9 Impact of stress path slope on the accumulation of plastic strains (Tutumluer and Kim 2003)

LABORATORY SIMULATION OF MOVING WHEEL LOADS USING STRESS PATH TESTS

As previously discussed in Chapter I, a pavement element undergoes extension-compression-extension stress regimens under moving traffic load. This type of loading results in higher plastic strain accumulation compared to simple plate loading test. Hornych conducted a series of stress path tests to study the effect of stress history and the unique impact of moving wheel loads on the rutting potential in pavement foundations (Hornych et al. 2000). He concluded that such stress history (extension- compression-extension) resulted in an increased rate of nonrecoverable strains, sometimes up to three times greater, when compared to plastic strains measured from repeated plate load tests.

Therefore it is important to understand the nature of moving wheel loads to accurately and realistically simulate the stresses induced by moving traffic loads in the lab.

Figure 3-10 schematically represents the stresses induced by moving wheel load in pavement layers. Two major sections, loading and unloading, are created as the wheel load approaches and departs the reference point (R). Points A and B are in the loading zone as they are impacted by the approaching wheel load while points C and D are in the unloading zone.

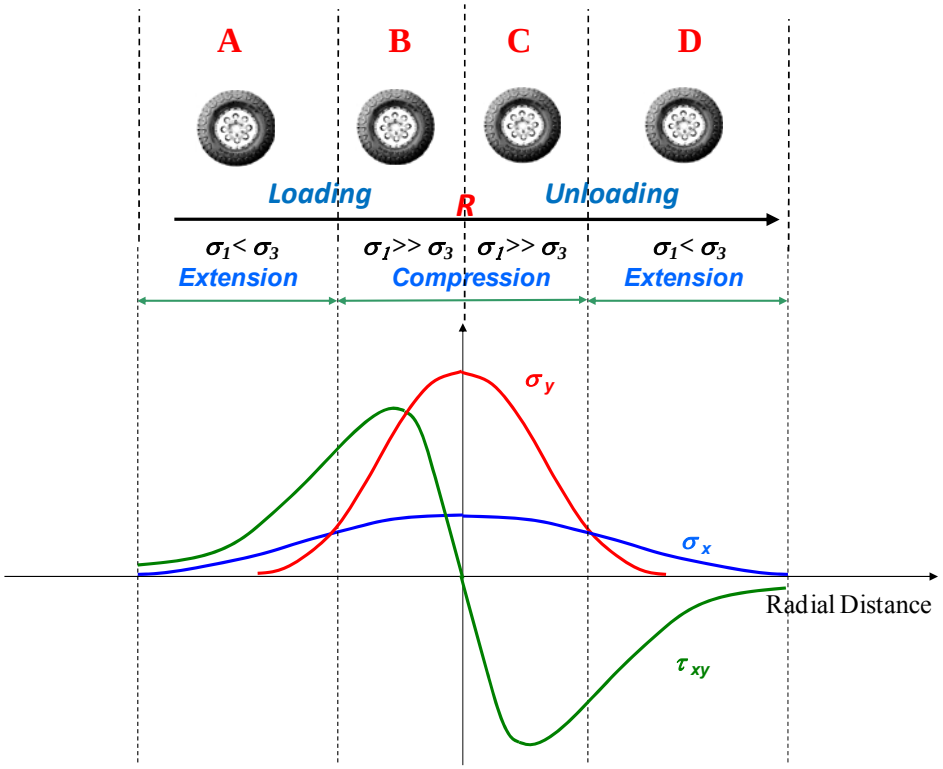

Figure 3-10 Stresses induced on pavement layers by moving wheel load

Each of these points represent different stress states, stress path lengths, and stress path slopes. As the wheel load approaches point A, the magnitude of the horizontal stress is higher than the vertical stress and, therefore, the pavement element at point A is in extension mode. As the wheel load approaches the reference point R and at some radial

distance before reaching the reference point R, the magnitude of the vertical stress becomes higher than the horizontal stress, and consequently the pavement element B is in compression. In the unloading zone, pavement elements C and D experience reduction in both vertical stress and horizontal stress. At some point away from the reference point R, the magnitude of horizontal stress becomes higher than the vertical stress, and pavement element D is in tension.

This variation in stress regimens is plotted in p-q stress space in figure 3-11. A proper stress path test should include both extension and compression regimens to realistically simulate the stresses induced by moving wheel load in the field. The realistic stress history using multiple stress paths is plotted in figure 3-11 (a) where the extension-compression-extension regimens were simulated. However, most of the loading protocols to assess deformation properties of geomaterials use single stress path tests as approximations to multiple stress path tests. This type of stress path test only considers the compression regimen and ignores the effect of stress history and shear stress reversal in pavement layers. As previously discussed in this chapter, CCP stress path test do not create field conditions and typically result in lower plastic deformations.

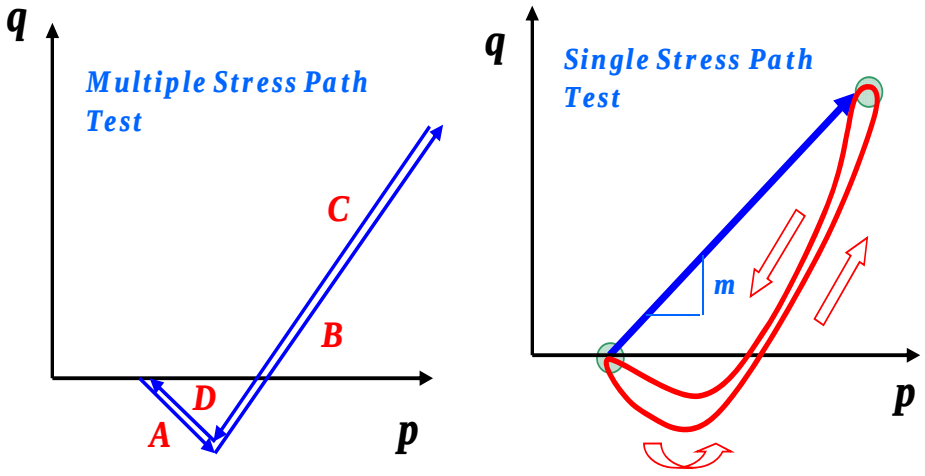

Figure 3-11 Single and multiple stress path testing of geomaterials in the lab (a) multiple stress path induced by traffic load (b) laboratory approximations in single stress path tests

Other Definitions of Stress Paths

As previously discussed in this chapter, the stress-strain responses of geomaterials are highly stress state and stress path dependent. Several researchers studied the effect of stress path on the mechanical behavior of geomaterials. The range of the mechanical models and variations in the prescribed stress path tests shows the complexity of the problem. Along with the physical and mathematical models, it is of outmost importance to establish laboratory stress path testing protocols to realistically simulate field loading.

Lo studied the effect of constant confining pressure stress paths and variable confining pressure stress paths on accumulation of plastic strains using a triaxial device in the lab (Lo and Lee 1990). He employed an extensive stress path protocol to study the behavior of aggregate samples in various conditions. He categorized the stress path tests into three major groups:

- P-tests or constant mean principal stress ($\Delta\sigma_1/\Delta\sigma_3$=constant)
- T-test or constant confining pressure stress path (σ_3=constant)
- R-tests or constant stress ratio tests (σ_1/σ_3=constant)

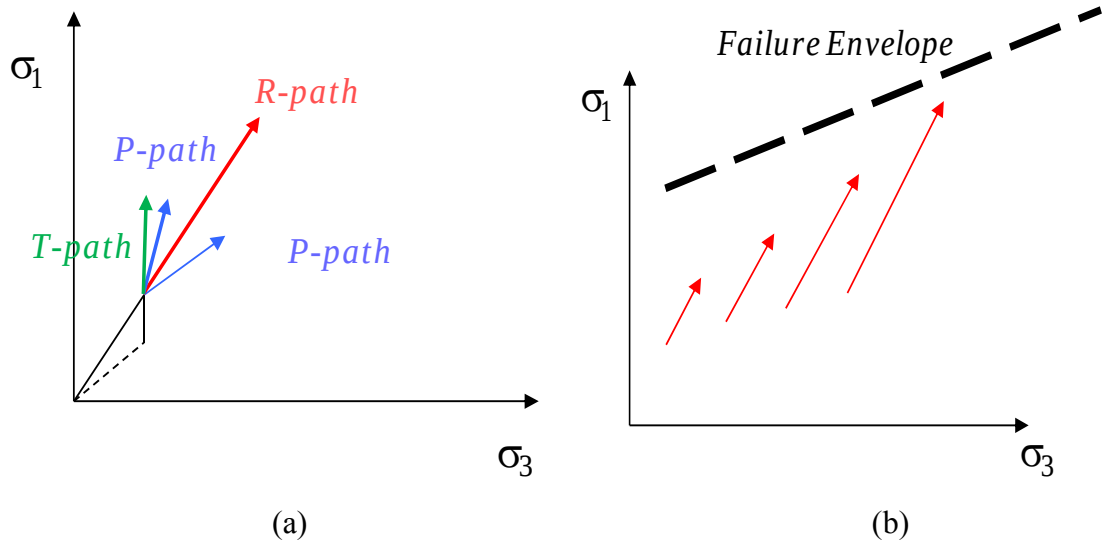

Figure 3-12 Stress path testing of geomaterials

The idea behind constant mean principal stress corresponds to the assumption that the elastic component of the volumetric strain is solely dependent on the mean stress. This type of test is generally used by geotechnical engineers to investigate the stress-dilatancy of geomaterials. Stress dilatancy is central to understanding the anisotropic behavior of aggregate systems.

Lo reported that small strain response of the aggregate systems subjected to p-tests is highly influenced by the boundary conditions such as bedding errors. R-tests, on the other hand, are used to investigate the strength properties of aggregate systems. As we will discuss in this chapter, most of loading protocols employed by pavement engineering such as AASHTO T-307 follow this type of stress path. Figure 3-12 (a) shows this type of stress path.

Lo studied the stress-strain response of aggregate materials along constant stress increment ratio stress paths. He was able to mechanistically demonstrate that the elastic component of the volumetric strains under such stress paths is elastic and anisotropic in nature, and the degree of anisotropy is highly affected by the stress ratio. Figure 3-13 shows the relationship between volumetric strain and the stress ratio. On the other hand the plastic strain increment was found to be significantly influenced by the stress increment ratio.

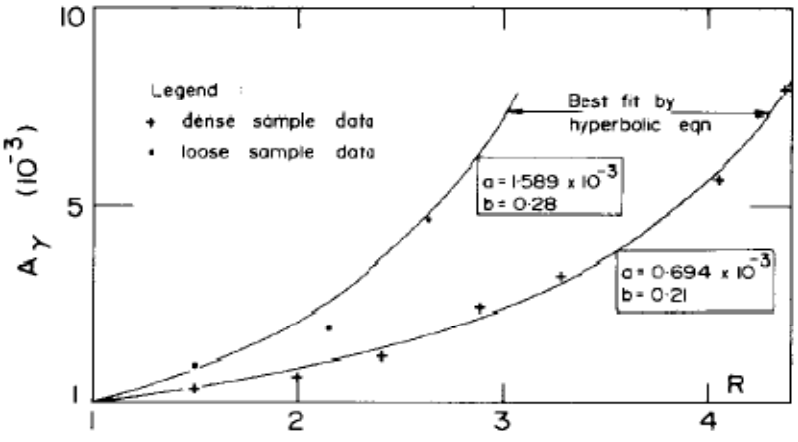

Figure 3-13 Relationship between volumetric strain and stress ratios (Lo and Lee 1990)

STRESS PATHS DUE TO MOVING TRAFFIC LOADS

As illustrated in figure 3-10, the moving traffic loads acting on the pavement induce varying magnitudes of vertical, horizontal, and shear stresses. The loading wave functions are typically follow haversine functions. The magnitude of the vertical stress induced by the wheel load is maximum under the wheel load and decreases in a nonlinear fashion as the wheel load moves away from the centerline of the load. The same pattern is valid for horizontal stresses. Shear stresses, however, are typically maximum at the edge of the tire and are minimum at the centerline of the load where the horizontal and vertical stresses are maximum. The distribution of stresses in the aggregate layer is highly nonlinear. Figures 3-14 and 3-15 represent this nonlinearity of responses in the unbound layer.

Figure 3-14 presents the nonlinear stress distribution in an 8 inch unbound aggregate layer laid over 4 inches of asphalt layer. The asphalt layer was considered to be linear and isotropic with a resilient modulus equal to 400,000 psi. The unbound aggregate layer was considered to be anisotropic with an anisotropy level of 0.3 (E_x/E_y=0.3). The subgrade was considered to be a rather soft subgrade with a modulus of 3,000 psi.

As illustrated in figure 3-14, maximum stress happens at the top of the subgrade right under the wheel load. The stresses gradually dissipate with depth in the aggregate layer. The magnitude of the stresses reduces in a nonlinear fashion as we move away from the wheel load as expected. The results are in conformity with the schematic representation of stresses provided in figure 3-10.

Figure 3-15 shows the distribution of the confining pressure or horizontal stresses in a pavement section with above mentioned layer configurations and material properties. This plot shows the column of confinement induced by the wheel loads on the aggregate layer is maximum under the wheel load and nonlinearly reduced with depth and radial distance. It is worth noting here that the use of anisotropic solutions resulted in very low (less than one psi) tensile stresses at the bottom of the aggregate layer. It is commonplace to use 2 to 3 psi residual stress, mainly induced by compaction, to eliminate the tensile

stresses at the bottom of the aggregate layer. The results in this plot also show very small amounts of tensile stresses occurring at some radial distances away from the load centerline. This confirms the predicted behavior of responses under moving wheel load as presented in figure 3-10.

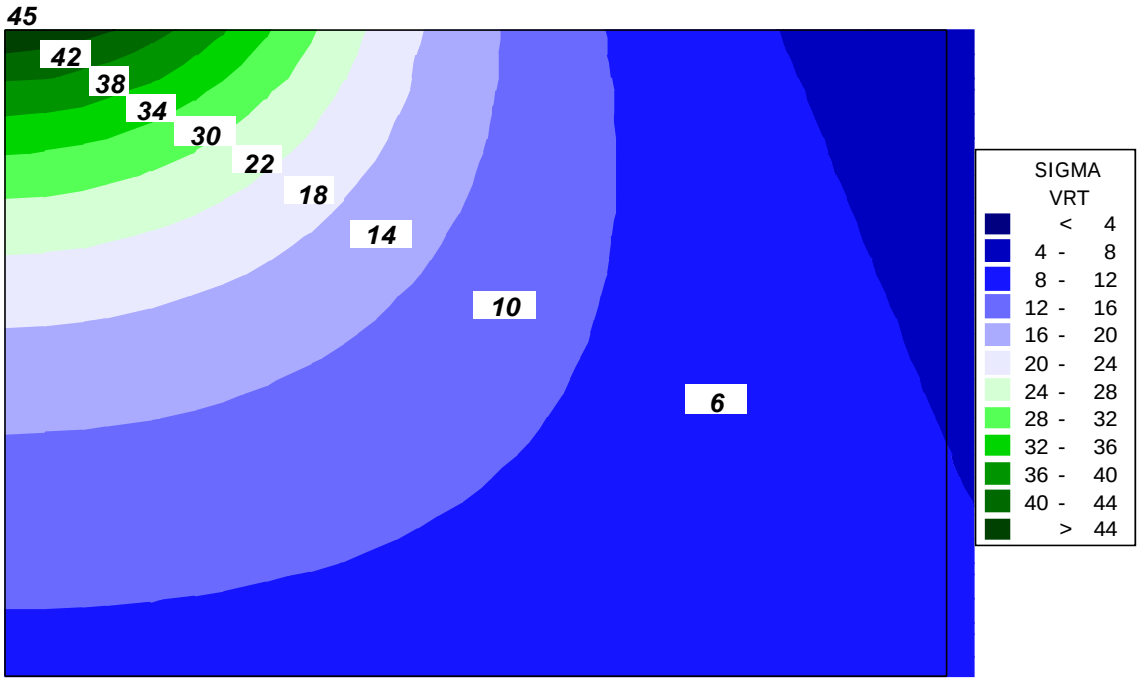

Figure 3-14 Distribution of vertical stresses in the aggregate layer using anisotropic solutions

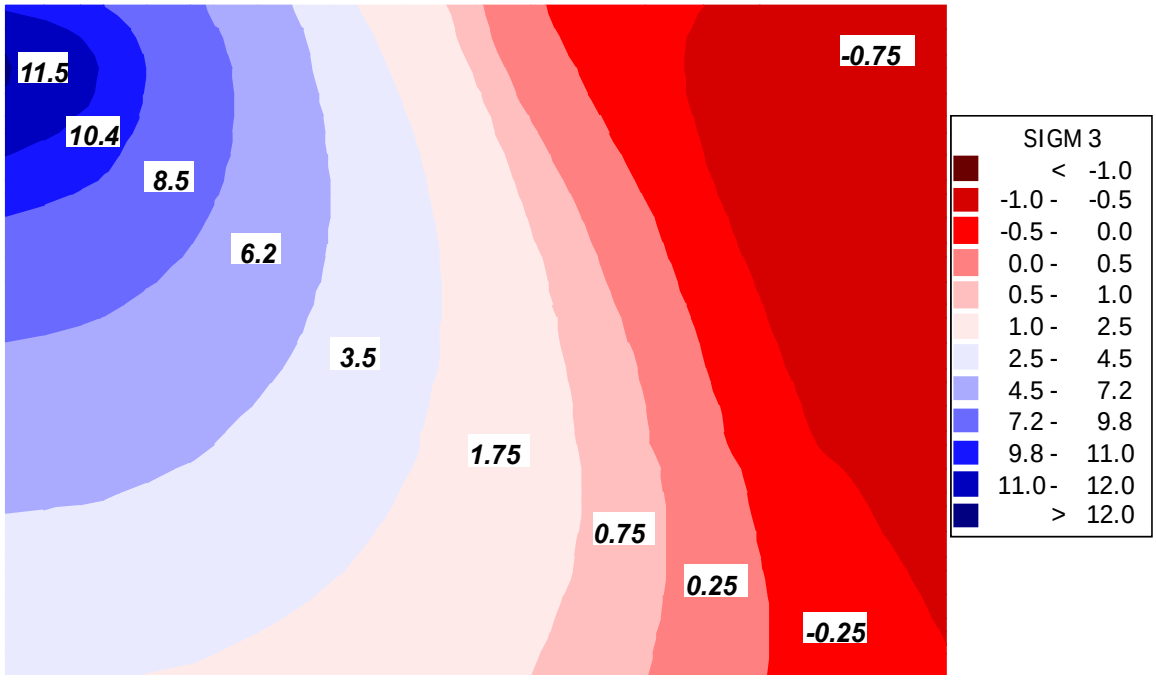

Figure 3-15 Distribution of radial stresses in the aggregate layer using anisotropic solutions

As a result of varying magnitudes of stress states and stress regimens in the aggregate layer, pavement foundations experience variable dynamic confining pressure stress paths. In order to better explain the stress paths that best simulate the response of the aggregate layers under the wheel loads, stress paths are classified based on the nature of confining pressures applied on the samples. It is commonplace in stress path testing of the geomaterials to classify the prescribed stresses based on the confining pressure experienced by the soil particles. Here major categories of stress paths can be identified:

a) Constant Confining Pressure stress paths are also known as CCP tests. In this type of loading protocol, the confining pressure in stress path stays constant. In other words in each stress path the confinement is constant, and the vertical stress changes. AASHTO T-307 loading protocol for determination of the resilient and

permanent deformation properties of aggregate layers is an example of this type of loading protocol.

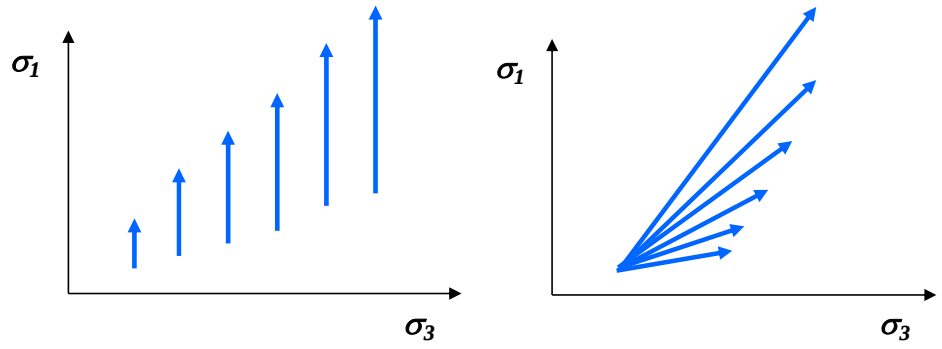

(a) (b)

Figure 3-16 Stress path testing of geomaterials (a) CCP stress path (b) VCP stress path

b) Variable Confining Pressure stress paths are also known as VCP tests. In this type of loading protocol, the confining pressure changes along with dynamic vertical pressure at each stress state in each stress path. Therefore, the deviatoric stress and the bulk stress applied on the aggregate system are different at each stress state and stress path. This would also result in different stress path slopes in the q-p diagram. NCHRP 1-28A loading protocol is an example of this type of stress path testing of geomaterials. Shaw's work on comparing CCP and VCP stress path tests showed that VCP type tests typically result in higher plastic strains when compared to CCP stress path tests (Shaw 1980).

c) Variable Dynamic Confining Pressure stress path tests also known as VDCP tests. Variable dynamic confining pressure stress path tests are basically a denomination of VCP type tests with this difference that the confining pressure is applied dynamically in phase with vertical pressure. This type of stress path testing is closest to the stress states felt by soil particles when subjected to traffic loads. The loading protocol considered in this dissertation is of this kind.

PARAMETERS OF STRESS PATH PROTOCOLS

The rationale behind stress path testing of geomaterials has evolved tremendously during the past 20 years. The parameters that describe the loading protocols and characterization of unbound aggregate systems can be categorized as:

- Classification of materials refers to particle size distribution, maximum aggregate size, percent passing sieve #200 (particles smaller than 75μ), and the method of characterization of the activity of the fine portion of the mix such as plasticity index (PI).
- Sample conditioning refers to method and duration of moisture conditioning of the samples.
- Compaction methods refer to the method of applying compaction energy to aggregate samples. Static compactors are typically characterized by number of blows, weight of the hammer, and height of the drop whereas dynamic compactors are typically characterized by contact pressure, number of gyration, and the angle of gyration.
- Specimen size is based on the maximum aggregate size and, different protocols allow different sample sizes. Aspect ratio (the ratio of sample diameter to sample height) is an important factor in determination of resilient properties as well as deformation of aggregate specimens.
- Loading shape, loading frequency, and rest period between pulses refer to the shape of the loading function applied on the samples. Loading shapes can be square, triangular, or haversine. Behavior of geomaterials are highly influenced by the loading shape function and rest period between the pulses. Best loading shape, loading frequency, and rest period is the one that closely simulate the dynamic behavior of stresses induced by moving wheel load on the aggregate layers.
- Preconditioning of the samples refers to subjecting the aggregate samples to a stress state that reproduces residual stress history induced by compaction in the field and minimizes the bedding effects. The other objective of preconditioning of

the samples is to ensure that large strains will not occur while applying stress paths.

- Stress magnitudes and stress ratio refer to the magnitude of prescribed stresses in the lab and are selected as though they reflect the stresses induced by traffic loads in the field. As previously discussed in this chapter, ascend to the unstable conditions in geomaterials is highly influenced by the stress ratios applied on the samples. The selected stress ratios in the loading protocols must be representative of the stresses induced by moving traffic loads.
- Stress sequence; refers to the method of applying stresses and the stress history. In most protocols designed for good quality aggregates to be used in the bases, samples were initially subjected to small stress states, and gradually more taxing stress paths will be applied on the samples. In some protocols designed for fine grained soils, the samples were initially subjected to stress states with high confining pressure to prevent premature failure, and later the confinement is reduced to create more critical conditions.
- Type of the stress path refers to the stress path type as CCP (Constant Confining Pressure), VCD (Variable Confining Pressure), and VDCP (Variable Dynamic Confining Pressure) stress path tests. The dynamic nature of stresses induced in the pavement (both vertical and horizontal) necessitates selection of stress path type that closely mimics this situation.
- Number of load cycles refers to the number of load repetitions at each stress state in each stress path. The number of load repetitions should be large enough to ensure that the plastic component of the strain tensor is negligible, and the equilibrium is reached in that stress state. The number of load cycles is also related to the type of the loading protocol. In small strain protocols the number of load cycles is significantly smaller than protocols designed to damage the samples in taxing stress paths.
- The following section provides more detail on the loading protocols and standard specifications used to determine the resilient properties as well as deformation potential of the aggregate samples in the lab.

REVIEW OF THE EXISTING STRESS PATH PROTOCOLS

This section will discuss the laboratory loading protocols and procedures for cauterization of unbound aggregate systems in the lab. The following loading protocols will be discussed in this section:

- AASHTO T 292-1991
- AASHTO T 294- 1992
- AASHTO T P46-1994 (Later AASHTO T 307)
- NCHRP 1-28 A 2003 (Harmonized)

AASHTO T 292

This protocol was initially developed in 1991 and employs a series of simplifying assumptions. Materials are first categorized into two groups as “granular” and “cohesive” based on AASHTO classification. The only recommendation on sample size is that it should have a diameter greater than 2.8 inches. The protocol recommends the compaction method that best simulates the field condition (impact, vibratory, kneading, or static) be used based on the technician’s experience and judgment.

The data acquisition process in this protocol is based on readings off of a strip chart. This protocol gives full control to the lab technician and his/her judgment, therefore, the results are highly subjective. In this protocol sample size, compaction method, preconditioning, loading shape, loading frequency, and even the magnitude of stress states applied on samples are decided by a lab technician.

This protocol only requires axial deformation measurements. The axial deformations are measured internally on the samples with clamps. For very soft samples this protocol suggests mounting the LVDTs externally on the loading plate. In conventional triaxial cells, external measurements of deformations will induce significant errors on determination of resilient properties. The main source of this error is due to the

friction between loading system (loading piston) and the cell that induces substantial bedding errors in calculations.

In this protocol three different loading protocols were recommended. This recommendation is based on the aggregate type.

This protocol suggests a fixed load duration of 0.1, 0.15, 0.5, and 1.0 seconds following haversine, rectangular, or triangular loading shape functions. Selection of pulse duration and load shape function is in the hands of the lab technician.

There are two loading protocols suggested for granular materials (base and sub-base) and one loading protocol for cohesive soils (sub grades). There are only five stress states in this loading protocol for Subgrade soils, therefore, the predictions of the resilient properties might not be accurate. The protocol states that the stresses should be selected to cover the expected in-service range of stresses experienced by soil particles. Number of load repetitions is also subjective. In order to determine the number of load repetitions necessary, comparison should be made between recoverable axial deformations at the 20^{th} and the 50^{th} repetitions. If the difference is greater than 5%, the specimen should be subjected to the same stress state for another 50 repetitions.

Resilient modulus of granular aggregates and cohesive soils are calculated using equations 3-14 and 3-15, respectively.

$$M_r = k_1 \, \theta^{k_2} \tag{3-14}$$

$$M_r = k_1 \, \sigma_d^{\,k_2} \tag{3-15}$$

where θ is the bulk stress, σd is the deviatoric stress, and k_1 and k_2 are fitting parameters.

The recommendations in this protocol are very general, and interpretations of the results are highly subjective. This protocol is outdated and currently has no use in the highway design industry.

AASHTO T 294-1992 (SHRP P46)

This protocol was developed in 1992 and was more detailed in providing specifications compared to AASHTO T 292. Aggregates are classified according to AASHTO designation and also particle size distributions. In this protocol geomaterials divided into two categories as coarse-grained and fine-grained aggregates.

Sample size and compaction methods are clearly stated in the AASHTO T 294 protocol. This protocol requires the lab technician to measure the vertical deformations of samples that may cause some errors in the calculations. Load shape function, rest period and load frequency is fixed in this protocol.

Two types of laboratory loading protocols, one for base and sub-base and the other for subgrade, are provided in this approach. Load shape function follows a haversine function with 0.1 second pulse duration and 0.9 second rest period. The tests should be terminated if at any time permanent strain exceeds 10%.

Equations 3-14 and 3-15 are also recommended for determination of resilient modulus of aggregate samples.

Similar to its predecessor AASHTO T 294, this protocol (AASHTO T 294) is outdated and is no longer used for characterization of unbound aggregate systems.

AASHTO T P46-1994 (later AASHTO T 307-1999)

In this protocol aggregate particles are classified based on particle size distributions and plasticity index instead of AASHTO classification.

Aggregate samples were tested in a top loading, closed loop electro-hydraulic testing machine with a loading function generator capable of applying repeated cycles of haversine stress pulses of 0.1 second. Similar to the previously discussed protocols, axial measurements of load and deformations are performed outside the triaxial cell. The

protocol suggests use of 6 inch diameter molds for coarse-grained aggregate soils and 2.8 inch diameter for fine-grained subgrade soils. In order to reduce the variability in measurements, this protocol requires a minimum height to diameter ratio. The aspect ratio is a function of maximum particle size present in the aggregate mixes. Aggregate particles greater than 1.5 inches should be scalped off prior to testing to reduce/eliminate the errors induced by friction between sample and the edges.

Vibratory compaction is recommended in AASHTO T P46 (T 307) for coarse-grained materials and static compaction for preparing the fine-grained soils.

Two loading protocols: one for base and sub-base and the other one for fine-grained subgrade soils have been designated. Load pulse in AASHTO T P46 is haversine-shaped with 0.1 second pulse duration and 0.9 second rest period. The protocol requires collection of at least 200 data points for each of the two LVDTs per load cycle. The stress path test should be terminated any time the permanent strain exceeds 5%. The protocol recommends that if after applying the final stress sequence the total plastic strain was less than 5%, then a quick shear test or repeated load permanent deformation test should be performed on the sample.

This protocol also has provisions to eliminate the possibility of sample miss-alignment. The specimen misalignment is controlled by defining a threshold for lateral deformations measured on the opposite sides of the specimen.

This stress path protocol is based on applying constant confining pressure in each sequence therefore it is a CCP type test. The preconditioning procedure in AASHTO T P46 requires aggregate samples. Therefore, the stress ratio for the preconditioning state is 2. Cylindrical specimens were subjected to 15 stress states and 5 stress paths. Preconditioning stresses, stress path sequences and stress magnitudes are presented in table 3-1.

Figure 3-17 shows the stress path plots for AASHTO T 307. Figure 3-17 (a) clearly illustrates the constant confining pressure nature of this stress path protocol as the confinement is held constant, and the vertical stress increases in each stress state. The

confining pressure jumps into a new level in consecutive stress path sequence. There are five stress paths in this protocol. Confinement ranges from 3.5 psi to 20 psi while the vertical stress ranges from 3.5 psi to 40 psi.

Figure 3-17 (b) shows the AASHTO T 307 stress paths in q-p plane. Stress ratios (σ_1/σ_3) for this stress path protocol ranges from 0.7 to 3, and the slope of the stress path (m) is kept constant as 3 for all the stress sequences. The length of the stress path, which is a measure of stress magnitudes applied on the samples, ranges from 3 psi to 33.3 psi. Table 3-2 shows the calculations for stress ratio, slope of the stress path, and length of the stress path for each stress sequence. This protocol does not suggest any prediction model for resilient modulus.

Table 3-1 Loading Protocol for Base Materials in AASHTO T 307

Sequence Number	Confining Pressure (KPa)	Max. Axial Stress (KPa)	Cyclic Stress (KPa)	Contact Stress (KPa)	No. of Load Applications
Conditioning	103.4	130.4	93.1	10.3	500
1	20.7	20.7	18.6	2.1	100
2	20.7	41.4	37.3	4.1	100
3	20.7	62.1	55.9	6.2	100
4	34.5	34.5	31.0	3.5	100
5	34.5	68.9	62.0	6.9	100
6	34.5	103.4	93.1	10.3	100
7	68.9	68.9	62.0	6.9	100
8	68.9	137.9	124.1	1.6	100
9	68.9	206.8	186.1	20.7	100
10	103.4	68.9	62.0	6.9	100
11	103.4	103.4	93.1	10.3	100
12	103.4	206.8	186.1	20.7	100
13	137.9	103.4	93.1	10.3	100
14	137.9	137.9	124.1	13.8	100
15	137.9	275.8	248.2	27.6	100

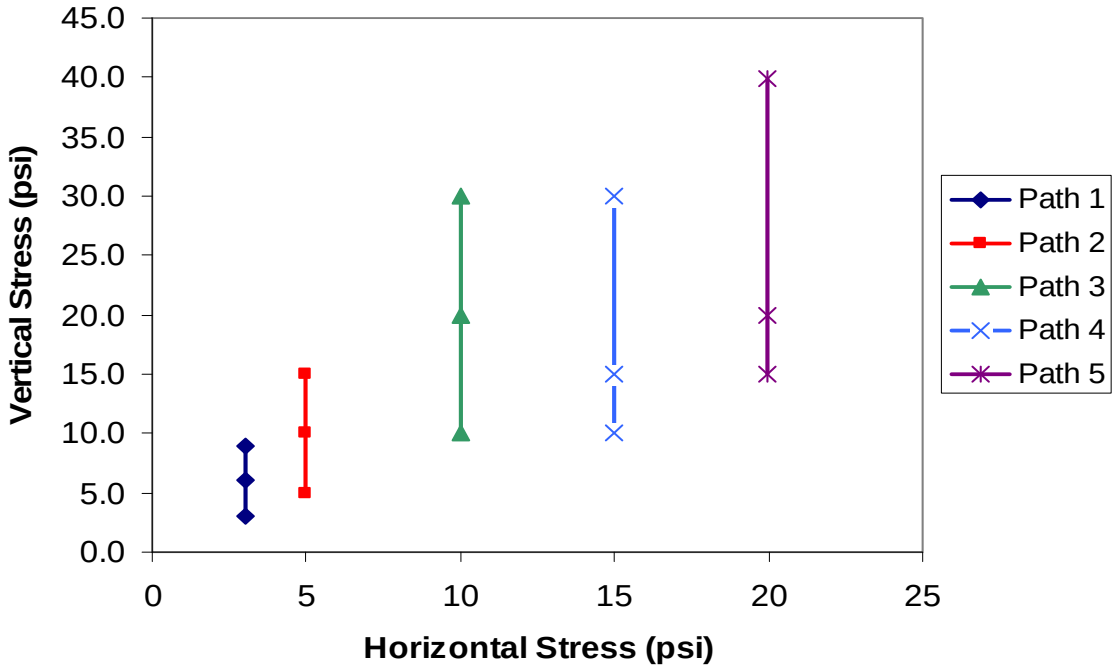

(a)

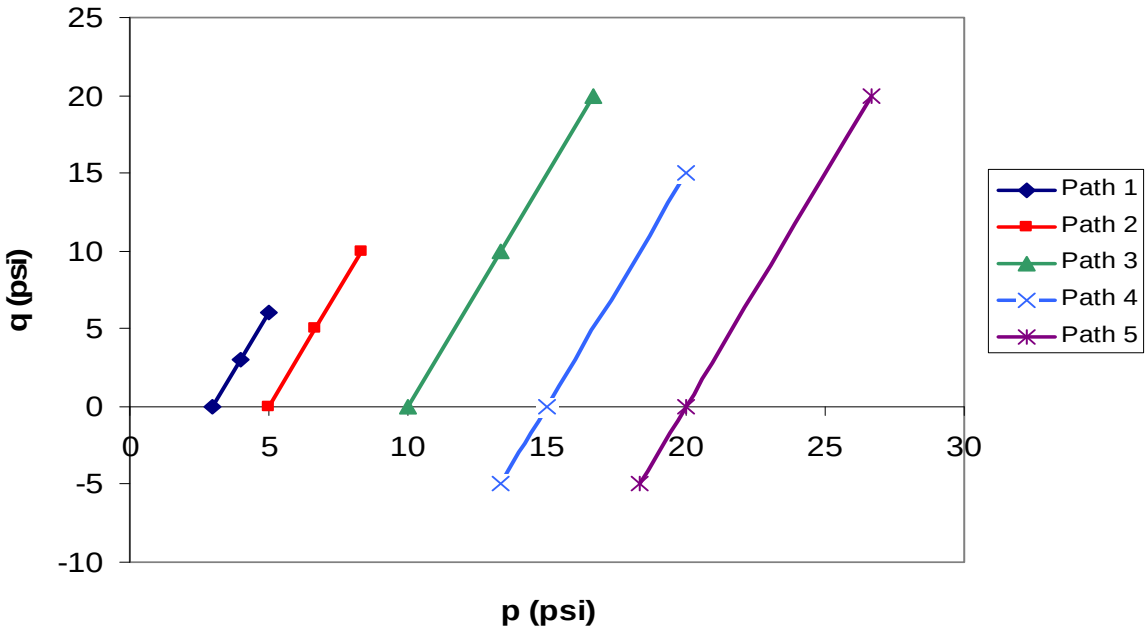

(b)

Figure 3-17 Stress path plots for AASHTO T 307 (a) σ_1-σ_3 stress space (b) q-p stress space

Table 3-2 Stress Path Parameters for AASHTO T 307 Protocol

	p (psi)	q (psi)	SR	m	L (psi)
1	3.0	0.0	1.0		3.0
2	4.0	3.0	2.0	3	5.0
3	5.0	6.0	3.0		7.8
4	5.0	0.0	1.0		5.0
5	6.7	5.0	2.0	3	8.3
6	8.3	10.0	3.0		13.0
7	10.0	0.0	1.0		10.0
8	13.3	10.0	2.0	3	16.7
9	16.6	20.0	3.0		26.0
10	13.3	-5.0	0.7		14.2
11	15.0	0.0	1.0	3	15.0
12	20.0	15.0	2.0		25.0
13	18.3	-5.0	0.7		19.0
14	20.0	0.0	1.0	3	20.0
15	26.6	20.0	2.0		33.3

Stress Ratio at Failure

The rationale behind using constant stress ratio is presented in figure 3-18. As previously stated in this chapter, in constant confining pressure loading protocols, the confining pressure is kept constant, and the axial stress is increased gradually in each stress state. As a result of increasing shear stress on the samples, the stress path points toward the failure state. In order to avoid the failure of the samples, a maximum value of stress ratio (σ_1/σ_3) is defined. This value should be low enough that it does not induce damage to the system. In each sequence, stresses are constantly oscillating between stress states that are close to failure to stress states that induce minimum damage. Weak materials, typically fine-grained soils or aggregate systems at elevated moisture states, fail upon application of initial stress paths. However, strong aggregate systems require more taxing stress states, stress regimens, and higher stress ratios to induce large plastic strains. It is of outmost importance to test the materials on various stress states to gather enough information on the behavior of aggregate systems in both low stress levels as well more demanding stress paths.

Studying the Mohr-Coulomb theory can provide insights used to better understand the relationship between material parameters, stress ratios, and failure of the geomaterials. Equations 3-16 and 3-17 present the relationship between stresses at failure and cohesion (c) and angle of internal friction (ϕ) according to Mohr-Coulomb theory in compression and extension, respectively.

$$\sigma_1 = \sigma_3 \left(\frac{1 + Sin\varphi}{1 - Sin\varphi} \right) + 2c \left(\frac{Cos\varphi}{1 - Sin\varphi} \right) \tag{3-16}$$

$$\sigma_1 = \sigma_3 \left(\frac{1 + Sin\varphi}{1 - Sin\varphi} \right) - 2c \left(\frac{Cos\varphi}{1 - Sin\varphi} \right) \tag{3-17}$$

For non-cohesive geomaterials (c=0), equation 16 can be written as:

$$\left(\frac{\sigma_1}{\sigma_3} \right)_f = \frac{1 + Sin\,\varphi}{1 - Sin\,\varphi} \tag{3-18}$$

Equation 18 shows that the intuitive and obvious points are true in that higher stress ratios are needed to fail the stronger materials, which typically have higher friction angles.

A parametric analysis performed on equation 3-18 is shown in figure 3-19. This plot clearly shows that the probability of failure is lower at low stress ratios. For instance this plot shows a stress ratio of about 4.5 is needed to fail a material with a friction angle of 40 degrees, therefore at stress ratios smaller than 4.5 the stability of the system is preserved, and the aggregate systems is not prone to develop high plastic deformations.

According to this plot selecting stress ratio of 3 in AASHTO T 307 stress path protocol will only be safe for aggregate systems with friction angles larger than 30 degrees. Therefore testing the samples at moisture states higher than the optimum moisture content or unbound aggregate systems with high fines content might result in premature failure of the samples in the initial stress sequences.

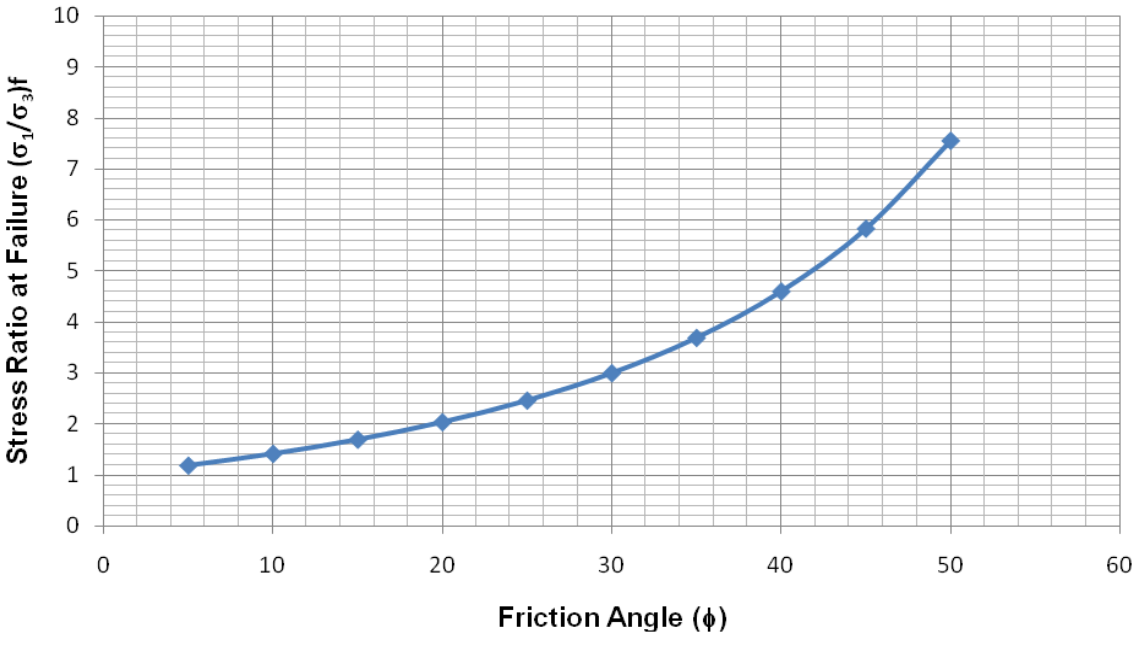

Figure 3-18 Relationship between stress ratio at failure and friction angle

NCHRP 1-28 A (Harmonized Protocol)

This loading protocol was developed for determination of resilient modulus of unbound pavement materials in 2003. Major differences and improvements in this protocol can be summarized as (Andrei et al. 2004):

- New method for defining material type
- Modification and recommendations for specimen size
- New recommendations for compaction method
- Revised stress path (stress states and stress ratios)
- Increase in loading time for subgrade soils
- Revised resilient modulus prediction equation

Harmonized protocol classifies aggregate systems into two groups based on particle size distribution and Atterberg limits. Type (I) materials refer to non-cohesive granular aggregates with low plasticity index (PI<10) whereas type (II) materials are cohesive aggregate systems with high fines content with PI>10. Two different compaction methods have been provisioned for these types of materials.

In NCHRP 1-28 A protocol does not recommend 2.8 inch molds and suggests using 4 inch diameter molds for gradations having a maximum aggregate size of ¾ inch (19 mm). Gradations with a maximum aggregate size larger than ¾ inch must be compacted in 6 inch diameter molds.

This protocol requires compacting type (I) materials using impact or vibratory methods whereas Type (II) aggregate systems should be compacted using a vibratory compactor.

Loading time for subgrade soils has been increased in NCHRP 1 28 A protocol. The analogy for decreasing the loading frequency for type (II) materials is that as one

goes deeper in the pavement layers, the stresses induced by moving wheel load are distributed over a larger area. This implies that the loading wave function has lower frequency. Therefore, this protocol recommends using 0.2 seconds and decreasing the rest period to 0.8 seconds for subgrade soils.

Table 3-3 shows the stress states in NCHRP protocol. This protocol subjects the aggregate systems to six stress paths with five stress states in each sequence, therefore 30 stress combinations will be applied on the specimen.

A major advantage of using NCHRP 1-28 A is that this protocol employs the variable confining pressure (VCP) concept for simulation of traffic loads in the lab. Stress path protocols previously discussed in this chapter use the CCP stress path concept. In other words previously mentioned protocols apply a constant confinement in each stress path and increase the vertical stress in each stress state. Therefore, the stress path applies on the aggregate systems points sharply (stress path slope m=3) toward failure envelope. Aggregate samples with high fines content or specimens compacted at high saturation levels will fail in initial stress states. Few data points can be obtained in this condition and consequently moisture susceptibility of aggregate systems cannot be fully studied. The NCHRP stress path protocol limits the stress ratio applied on samples for initial stress path to a minimum value and further increase this value to gather enough data at both low stress levels (small stress path lengths) and less demanding stress ratios (small stress path slopes). In other words, initial stress states that are farthest from the failure conditions are applied on the samples, followed by more demanding stress paths.

Table 3-4 shows the stress path parameters for the NCHRP 1-28 A stress path protocol. As stated in this table, stress ratios are gradually increased from 1.5 to 8. Stress path slopes range from 0.4 in the first stress path (the least demanding stress path) and increase up to 2.1 in the final stress path (most demanding stress path). It is worth mentioning here that the stress path slopes in this protocol are smaller than stress path slopes in AASHTO T 307. The stress path length ranges from 3.8 psi to 155.1 psi and are significantly higher compared to the other protocols. This provides enough information as

to capture shear softening of the material at high stress combinations. This information is crucial in modeling damage in particulate materials.

Figure 3-19 shows the stress path plots in σ_1-σ_3 and q-p stress states. As illustrated in figure 3-19 (a), axial stress and confining stresses are increased together at each stress in each stress path. This plot also shows the increase in stress ratios (s_1/s_3) in each stress path. Figure 3-19 (b) shows the stress path plot in q-p stress space. This plot shows how the slope and length of the stress path increases in each sequence.

Table 3-3 Loading Protocol for Base Materials in NCHRP 1-28 A

	Confining Pressure		Contact Stress		Cyclic Stress		Maximum Stress	
	KPa	Psi	KPa	Psi	KPa	Psi	KPa	Psi
Conditioning	**103.5**	**15**	**20.7**	**3.0**	**207**	**30.0**	**227.7**	**33**
1	20.7	3	4.1	0.6	10.4	1.5	14.5	2.1
2	41.4	6	8.3	1.2	20.7	3	29	4.2
3	69	10	13.8	2.0	34.5	5	48.3	7.0
4	103.5	15	20.7	3.0	51.8	7.5	72.5	10.5
5	138	20	27.6	4.0	69	10	96.6	14.0
6	20.7	3	4.1	0.6	20.7	3	24.8	3.6
7	41.4	6	8.3	1.2	41.4	6	49.7	7.2
8	69	10	13.8	2.0	69	10	82.8	12.0
9	103.5	15	20.7	3.0	103.5	15	124.2	18.0
10	138	20	27.6	4.0	138	20	165.6	24.0
11	20.7	3	4.1	0.6	41.4	6	45.5	6.6
12	41.4	6	8.3	1.2	82.8	12	91.1	13.2
13	69	10	13.8	2.0	138	20	151.8	22.0
14	103.5	15	20.7	3.0	207	30	227.7	33.0
15	138	20	27.6	4.0	276	40	303.6	44.0
16	20.7	3	4.1	0.6	62.1	9	66.2	9.6
17	41.4	6	8.3	1.2	124.2	18	132.5	19.2
18	69	10	13.8	2.0	207	30	220.8	32.0
19	103.5	15	20.7	3.0	310.5	45	331.2	48.0
20	138	20	27.6	4.0	414	60	441.6	64.0
21	20.7	3	4.1	0.6	103.5	15	107.6	15.6
22	41.4	6	8.3	1.2	207	30	215.3	31.2
23	69	10	13.8	2.0	345	50	358.8	52.0
24	103.5	15	20.7	3.0	517.5	75	538.2	78.0
25	138	20	27.6	4.0	690	100	717.6	104.0
26	20.7	3	4.1	0.6	144.9	21	149	21.6
27	41.4	6	8.3	1.2	289.8	42	298.1	43.2
28	69	10	13.8	2.0	483	70	469.8	68.1
29	103.5	15	20.7	3.0	724.5	105	745.2	108.0
30	138	20	27.6	4.0	966	140	993.6	144.0

Table 3-4 Stress Path Parameters for NCHRP 1-28 A Protocol

	p (psi)	q (psi)	θ (psi)	τ_{oct} (psi)	SR	m	L (psi)
1	3.5	1.5	3.5	0.7	1.5		3.8
2	7.0	3	6.9	1.4	1.5		7.6
3	11.7	5	11.6	2.4	1.5	0.4	12.7
4	17.5	7.5	17.3	3.5	1.5		19.0
5	23.3	10	23.1	4.7	1.5		25.4
6	4.0	3	4.0	1.4	2		5.0
7	8.0	6	7.9	2.8	2		10.0
8	13.3	10	13.2	4.7	2	0.8	16.7
9	20.0	15	19.8	7.1	2		25.0
10	26.7	20	26.4	9.4	2		33.3
11	5.0	6	5.0	2.8	3		7.8
12	10.0	12	9.9	5.7	3		15.6
13	16.7	20	16.5	9.4	3	1.2	26.0
14	25.0	30	24.8	14.1	3		39.1
15	33.3	40	33.0	18.9	3		52.1
16	6.0	9	5.9	4.2	4		10.8
17	12.0	18	11.9	8.5	4		21.6
18	20.0	30	19.8	14.1	4	1.5	36.1
19	30.0	45	29.7	21.2	4		54.1
20	40.0	60	39.6	28.3	4		72.1
21	8.0	15	7.9	7.1	6		17.0
22	16.0	30	15.8	14.1	6		34.0
23	26.7	50	26.4	23.6	6	1.9	56.7
24	40.0	75	39.6	35.4	6		85.0
25	53.3	100	52.8	47.1	6		113.3
26	10.0	21	9.9	9.9	8		23.3
27	20.0	42	19.8	19.8	8		46.5
28	33.3	70	33.0	33.0	8	2.1	77.5
29	50.0	105	49.5	49.5	8		116.3
30	66.7	140	66.0	66.0	8		155.1

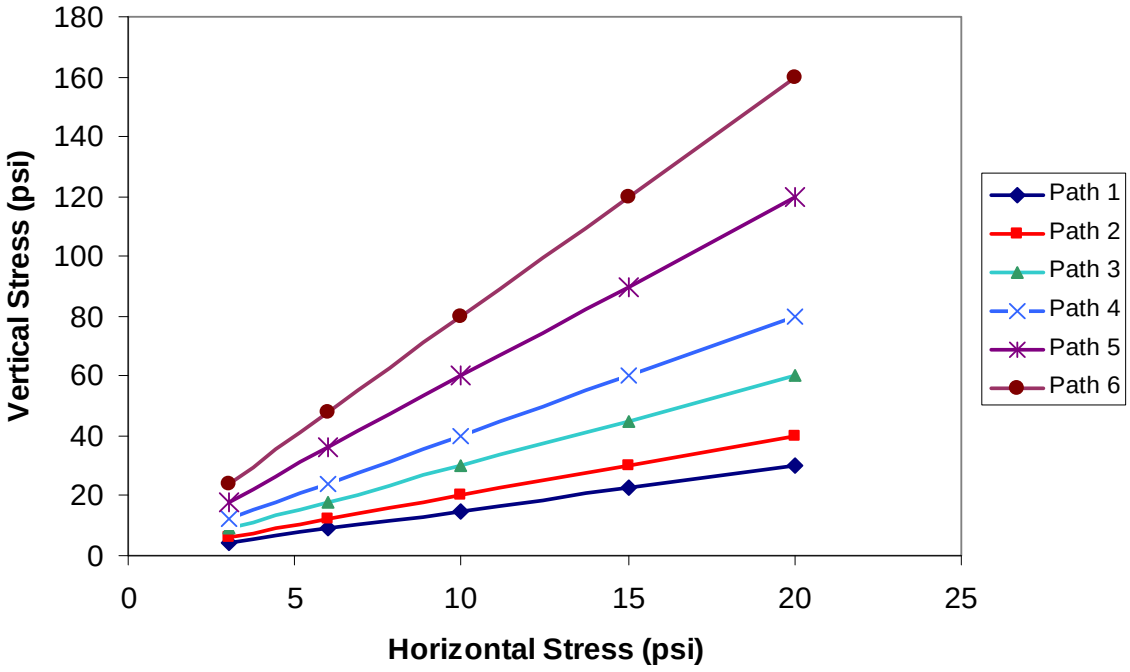

(a)

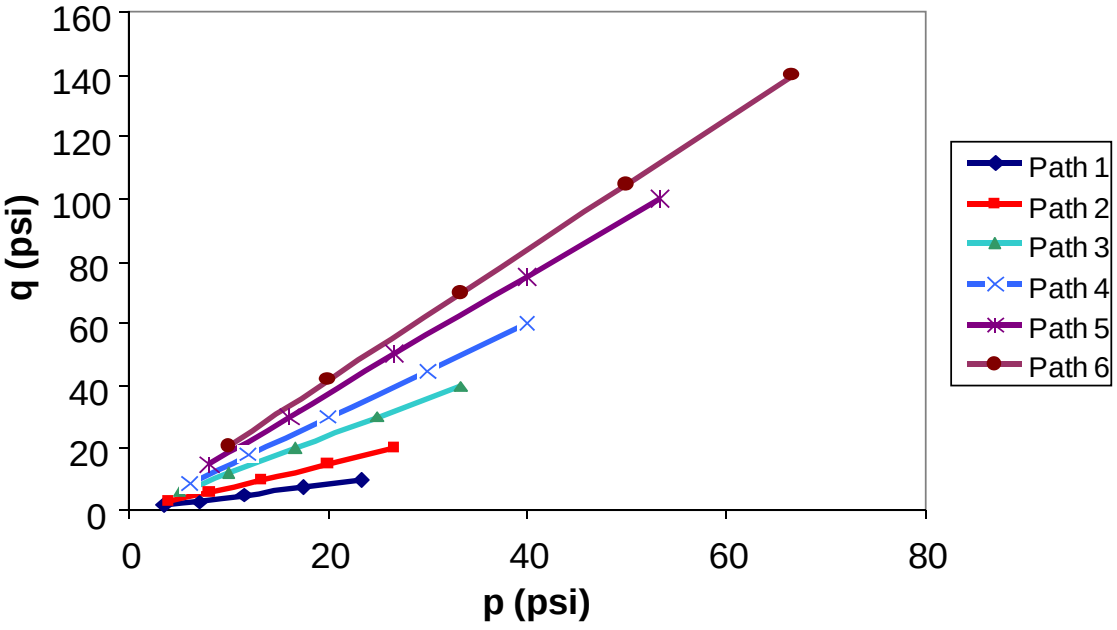

(b)

Figure 3-19 Stress path plots for NCHRP 1-28 A (a) σ_1-σ_3 stress space (b) q-p stress space

Five parameter nonlinear and stress sensitive models are suggested for characterizing the resilient modulus of unbound aggregate systems in this protocol. The general form of the model is presented in equation 3-19 (Andrei et al. 2004).

$$M_R = k_1 \ p_a \left(\frac{\theta - 3k_6}{p_a} \right)^{k_3} \left(\frac{\tau_{oct}}{p_a} + k_7 \right)^{k_3} \quad (3\text{-}19)$$

where:

M_R= resilient modulus

θ = bulk stress

τ_{oct} = octahedral shear stress

k-values = model fitting parameters

COMPARISON OF STRESS PATH PROTOCOLS AND CALCULATED RESPONSES

This section provides comparison of stress states calculated using different material models and stress path tests in the lab through an example.

Stresses developed in unbound aggregate layers for six pavement sections with different material properties and layer configurations are presented in figure 3-21. In this analysis unbound aggregate layers were considered to be stress sensitive and anisotropic. The anisotropy level characterized by the ratio of horizontal to vertical modulus was considered to be 0.3. A previous study at Texas A&M University on the AASHTO road test data showed the best match between measured and calculated responses is obtained when the horizontal stiffness is considered to be 30 % of the vertical stiffness for unbound aggregate layers (Masad 2004). Finite element responses of aggregate layers are grouped with green colors in this plot. The stress envelopes for AASHTO T 307 and NCHRP 1-28 A (harmonized protocol) are also plotted in figure 3-21. As indicated in this plot, the prescribed stress states in harmonized protocol are clearly more demanding than stress states in AASHTO T 307 protocol. This plot also shows that calculated stresses using stress sensitive and anisotropic solutions have more overlap with stress states provisioned in harmonized protocol.

According to figure 3-20, it appears that both protocols fall short to subject the aggregate systems to very low stress levels. Although the behavior of geomaterials at a small strain level can be substantially different compared to intermediate and large strain levels, the probability of transition to critical conditions are not likely at such low strain levels.

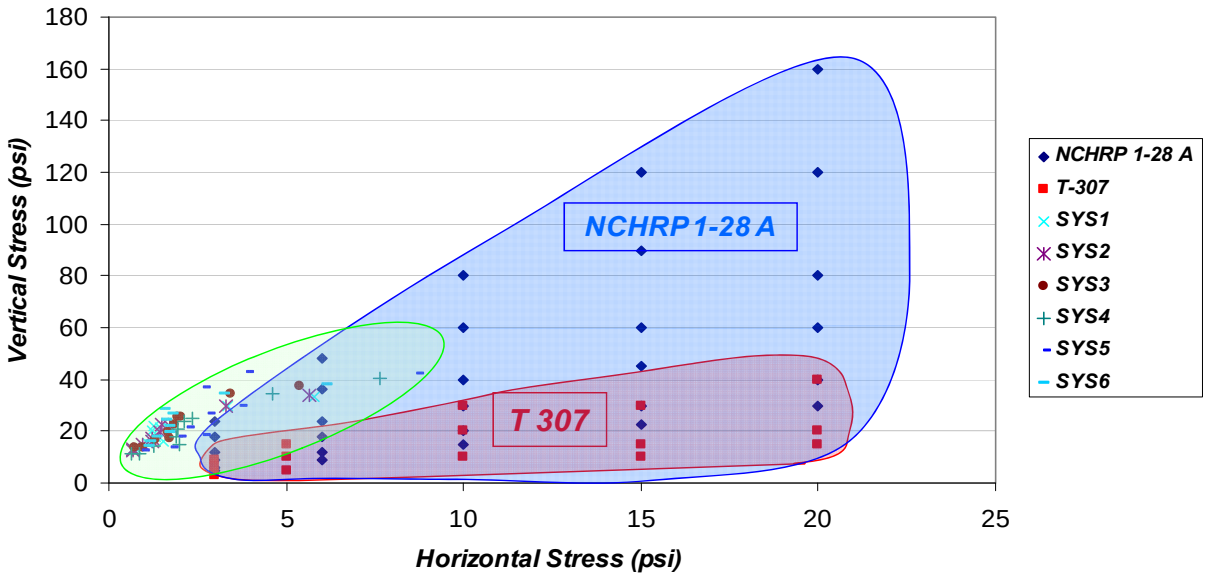

Figure 3-20 Comparison of anisotropic solutions of radial and vertical stresses and laboratory stress path protocols

Figure 3-22 presents another representation of the FE results. As previously shown in figure 3-19, stress ratios play an important role in stability of the geomaterials. Therefore comparison based on stress ratios and a measure stress magnitude provide valuable insight when comparing FE calculated and prescribed lab stresses. Figure 3-22 shows comparison between stress path length and stress ratios (σ_1/σ_3) developed in the aggregate layer with simulated traffic load. Similar to the results presented in figure 3-20, figure 3-21 shows anisotropic solutions have better overlap with NCHRP 1-28 A protocol compared to AASHTO T 307.

A key observation in this plot is the fact that stress ratios provisioned in AASHTO T 307 are significantly smaller than the ones calculated by finite element solutions, which might cause errors when calculating the resilient responses of aggregate layers. It is also worth mentioning here that very high stress ratios that correspond to low stress path lengths typically correspond to stresses calculated at radial distances away from the wheel load.

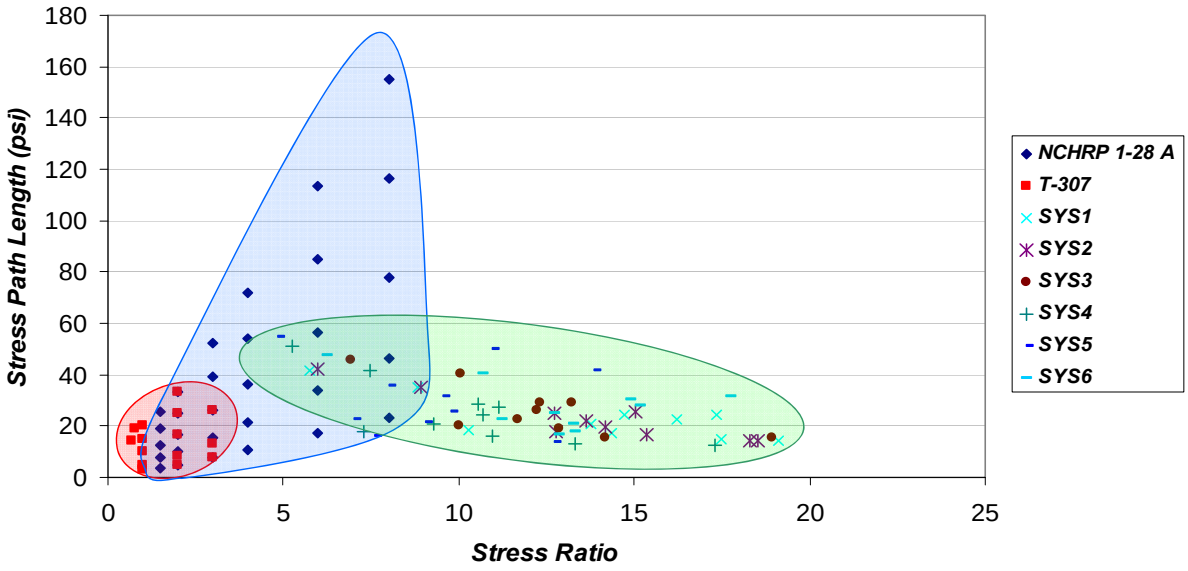

Figure 3-21 Comparison of stress ratios and length of stress path calculated based on anisotropic solutions and laboratory stress path protocols

In another effort, responses of aggregate layers were calculated using linear elastic solutions and compared to nonlinear stress sensitive and anisotropic solutions. Similar to the previous plot, stress path length and stress ratios for calculated responses plotted against prescribed laboratory stress states.

Figure 3-22 shows a significant difference between the results using isotropic and anisotropic material models. Of particular significance in this analysis is the fact that linear elastic solutions resulted in high tensile stresses in the aggregate layer. As illustrated in this figure, absolute value of the stress ratios calculated using layered elastic solutions are smaller than anisotropic solutions; however, the length of the stress path is significantly higher. Negative stress ratios are due to the tensile stresses calculated at mid depth to the bottom of aggregate layer. Unrealistic high tensile stresses calculated using linear elastic solutions at the bottom of the aggregate layer are responsible for such large stress path lengths.

The result presented in figure 3-22 is another testament to the importance of using anisotropic solutions for realistically predicting the stresses induced by traffic loads in the field.

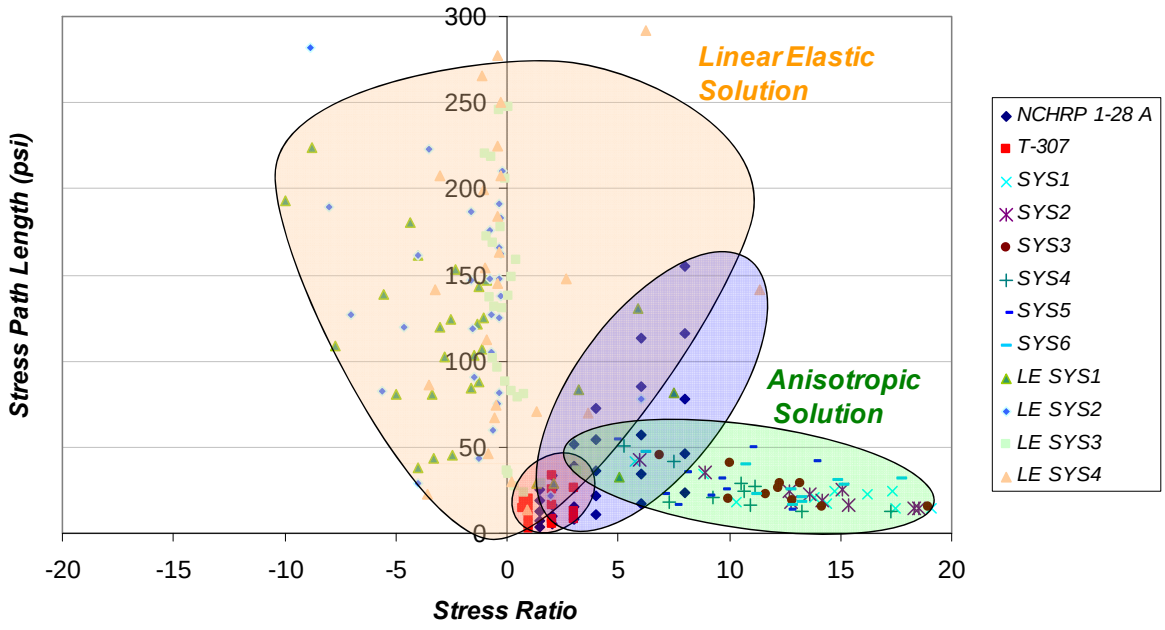

Figure 3-22 Comparison of stress ratios and length of stress path calculated based on anisotropic solutions, linear elastic solutions, and laboratory stress path protocols

TYPICAL STRAIN LEVELS FOR EXISTING STRESS PATH PROTOCOLS

It is well established in the literature that the mechanical response of geomaterials is highly nonlinear and the soil stiffness decays with strain by orders of magnitude. Figure 3-23 shows a classic degradation curve for geomaterials in strain-controlled conditions. This figure indicates that at small strains the magnitude of the modulus is large, and the

stiffness reduces as higher strains induced on the system. The stiffness of geomaterials close to failure is typically very small, and this transition is highly nonlinear.

A triaxial device is commonly used to measure the intermediate to large strain stiffness using various ranges of stress paths. Dynamic methods such as shear wave propagation techniques and resonant columns were used to calculate the stiffness properties of soils at small strains.

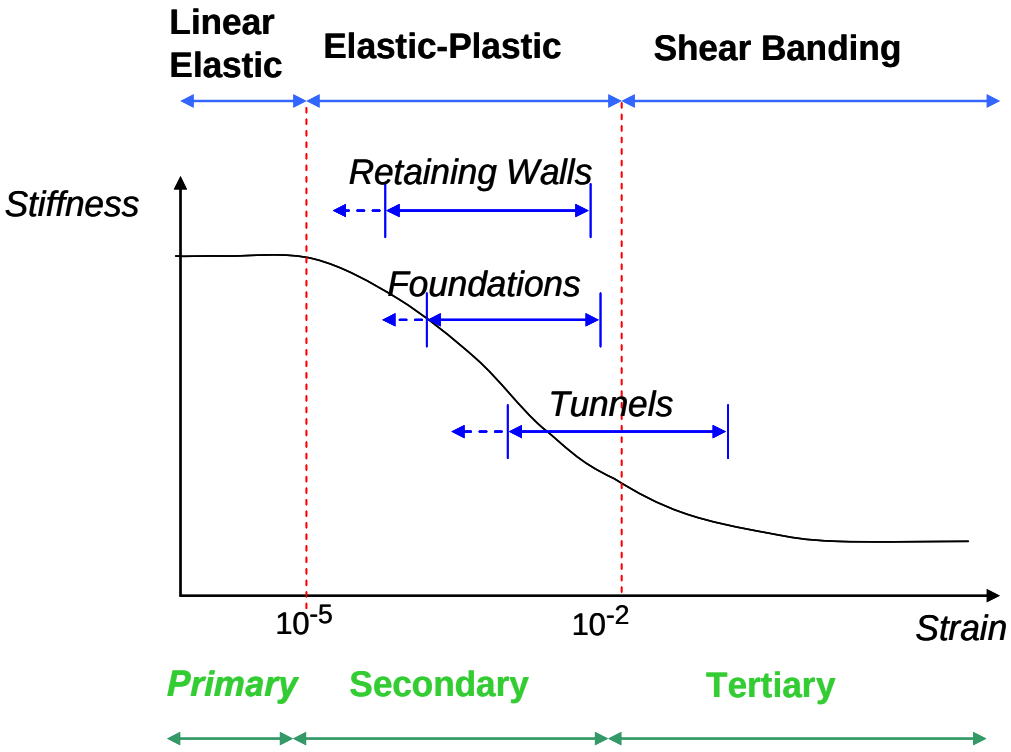

Figure 3-23 Characteristic stress-strain behavior of geomaterials (Atkinson 2000)

Atkinson (2000) argued that at small strains (shear strains smaller than 0.001 percent) the response behavior of soil can be considered as linear. In the small strain region, the stiffness of the unbound aggregate system is constant and is referred to as initial modulus, or E_{max}, in the soil mechanics literature. The modulus value calculated for this region can be considered as the non-damaged stiffness or modulus. However, the stiffness decays in

a nonlinear fashion as the aggregate system is subjected to more demanding stress paths. This will induce non-recoverable plastic strains; the stiffness or the modulus calculated for this region of the stress-strain curve is referred to as damaged stiffness or damaged modulus.

Figure 3-24 shows typical inflicted strains due to application of different stress protocols in the lab. This figure emphasizes the importance of the stress path tests in determination of the design stiffness. As discussed earlier, the NCHRP 1-28A protocol is the most demanding loading protocol among the stress paths tests developed for characterization of pavement foundations. This protocol tests the material up to shear banding to have an estimate of ultimate structural capacity of the systems. Stiffness measured using shear wave propagation techniques is primarily out of the range of strains imposed by traffic loads and results in very high stiffness values. Stiffness values, measured by AASHTO T-307 and ICAR loading protocols, fall somewhere between the shear wave and NCHRP 1-28A modulus values. The nonlinearity of the stress-strain relationship of aggregate systems has a significant impact on the selection of the design parameters of aggregate layers.

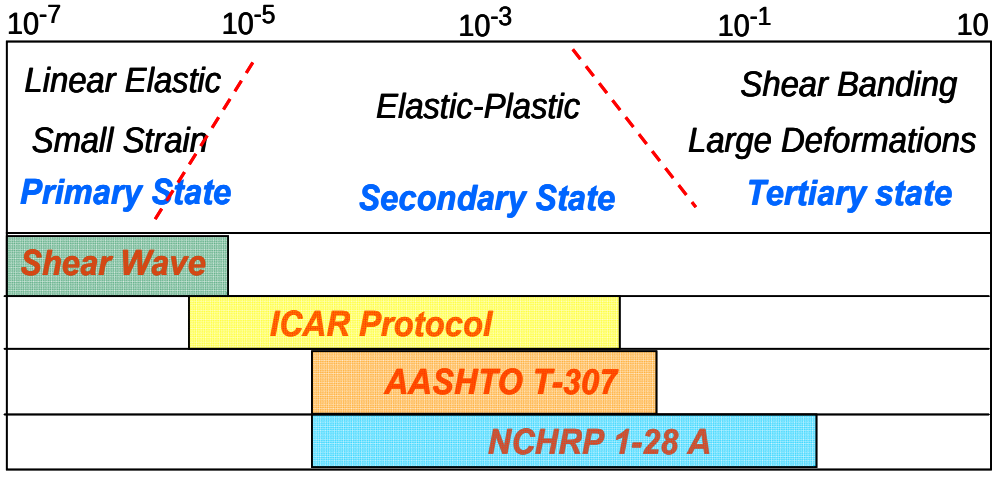

Figure 3-24 Strain level and laboratory stress path protocols

It should be noted here that the measurement of soil stiffness must be performed over the full range of the stress path to determine soil stiffness at both small strains and at large deformations. This information is imperative in the mechanistic design of pavement foundations.

CHAPTER IV

MODELING RESILIENT BEHAVIOR OF AGGREGATE SYSTEMS

BACKGROUND

Small strain resilient properties of unbound aggregate systems are typically characterized by a resilient modulus Poisson ratio in pavement engineering. In mechanistic design of the pavement systems, resilient responses of layers are considered to be the key factors in determination of layer thicknesses and calculation of critical pavement responses under traffic load.

Several researchers worked on the modeling of unbound aggregate systems in pavement foundations. These models are primarily based on isotropic elasticity assumptions, which induce systematic errors in calculation of pavement responses subjected traffic loads. The isotropic models generally require two parameters namely vertical stiffness characterized by elastic modulus and Poisson's ratio to calculate critical pavement responses. Cross-anisotropic models, however, require five material properties: elastic modulus in horizontal direction, elastic modulus in vertical direction, Poisson's ratios in orthogonal directions, and shear modulus to characterize aggregate systems. Due to the advent of powerful computers, nonlinear models and iterative techniques have gained popularity in the mechanistic design of pavement layers. These models have proven to be more physically meaningful, more realistic, and provide a better match with measures stresses and strains in the field compared to their linear and isotropic counterparts. The following section provides discussion on the nonlinear models proposed by pavement scientists to characterize the resilient modulus of unbound aggregate systems. These models are presented in chronological order to emphasize the improvements and complexity of the models.

Confining Pressure Model

This model originally developed by Seed suggests that resilient modulus is exclusively a function of confining pressure applied on the samples in the stress path test. The experiments were performed on both sandy soils and gravels at dry moisture state and saturated conditions. Equation 4-1 presents confining pressure model (Seed et al. 1967).

$$M_R = k_1 (\sigma_3)^{k_2} \quad (4\text{-}1)$$

where σ_3 is confining pressure (psi), and k_1, k_2 are regression constants found from fitting the experimental data to the model.

Bulk Stress (k-θ) Model

This model was developed by Hicks and Monismith in 1977. This model is popular among pavement engineers for calculating pavement responses and thickness design pavement layers. This model considers the resilient modulus of the unbound aggregate layers to be nonlinear and stress sensitive (Hicks et al. 1971). Equation 4-2 presents the bulk stress model.

$$M_R = k_1 (\theta)^{k_2} \quad (4\text{-}2)$$

where:

θ = bulk stress that is the sum of the principal stresses ($\sigma_1+2\sigma_3$)

k_1 and k_2 fitting parameters.

Figure 4-1 and figure 4-2 demonstrate the sensitivity of the resilient modulus to the parameters of the model. Figure 3-1 was developed for constant value of k_2=0.5 while varying the k_1 parameter. As illustrated in this figure, aggregate systems with higher k_1

parameters correspond to stiffer samples. It is commonplace in pavement engineering to plot the bulk stress against resilient modulus in logarithmic scale.

Figure 4-2 shows the sensitivity of the model to k_2, the exponent of the bulk stress term in the model k_2 parameter. As illustrated in this plot, the k_2 parameter captures the nonlinearity of the responses in the bulk stress model. Slopes of the resilient modulus plots presented in figure 4-2 indicate that aggregate systems with a higher k_2 parameter are less stress sensitive whereas aggregate systems with smaller k_2 values show a great variation of stiffness properties throughout the range of induced stresses.

The predictions of the bulk stress model indicate that the stiffness of the unbound aggregate systems increase as the specimens are subjected to higher stress levels. This can be true only if the magnitudes of the stresses are smaller than the characteristic load of the system. By definition, characteristic load is the load the system can withstand without developing plastic strains. Therefore, incorporation of bulk stress as a measure of hardening of the system can only capture the behavior of the unbound systems at small strain levels where most of the strains recover upon unloading.

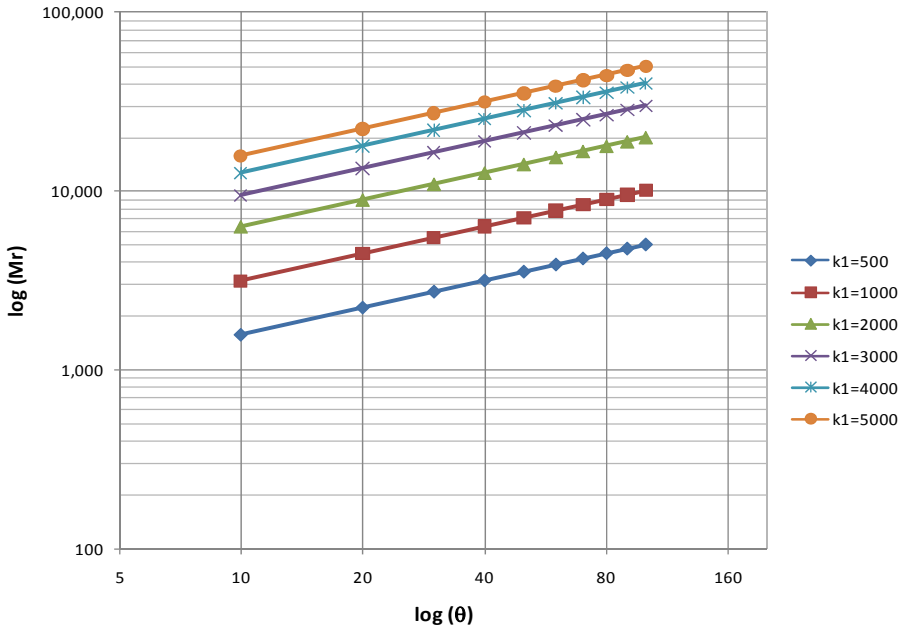

Figure 4-1 Sensitivity of bulk stress model to k_1 parameter (k_2=0)

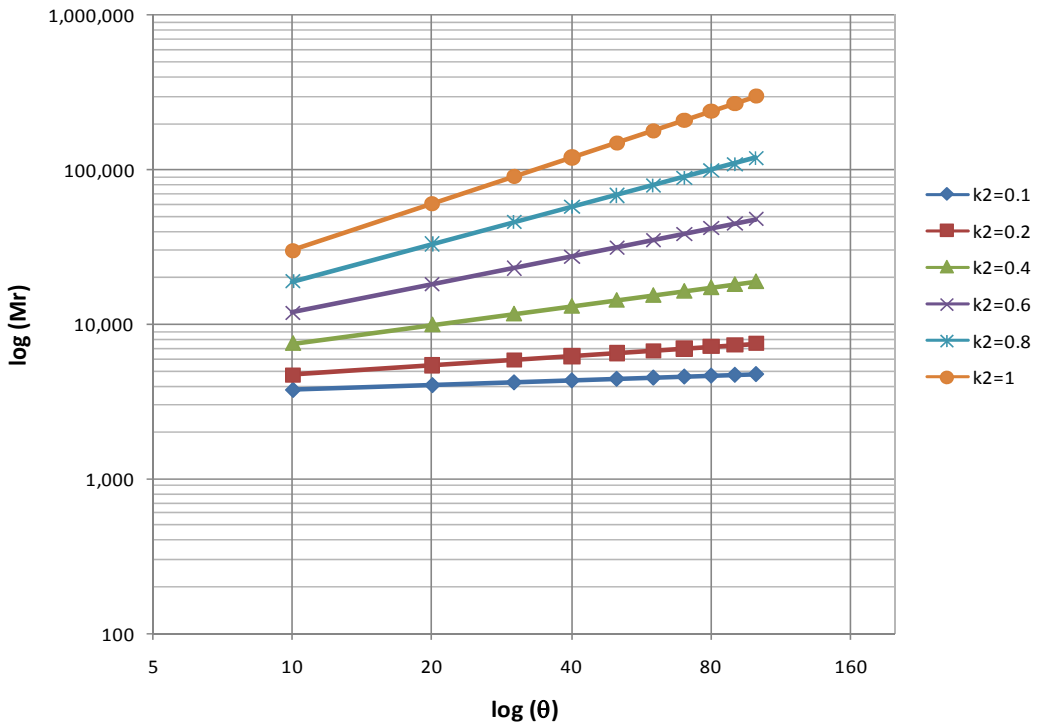

Figure 4-2 Sensitivity of bulk stress model to k_2 parameter (k_1=4000)

Several researchers studied this model and concluded that it is insufficient to account for the shear stresses and shear strains experienced by aggregate layers in the field (Brown 1974), (Moossazadeh and Witczak 1981), (Uzan 1985), and (Kheder 1985).

Brown and Pappin indicated that the bulk stress model falls short in handling volumetric strains correctly and therefore is only valid for a limited range of stress path when the confining pressure is less than the deviatoric stress (Brown and Pappin 1985). Uzan clearly showed the disagreement between the model-predicted resilient modulus values and the lab data (Witczak and Uzan 1988). This analogy is provided in figure 4-3.

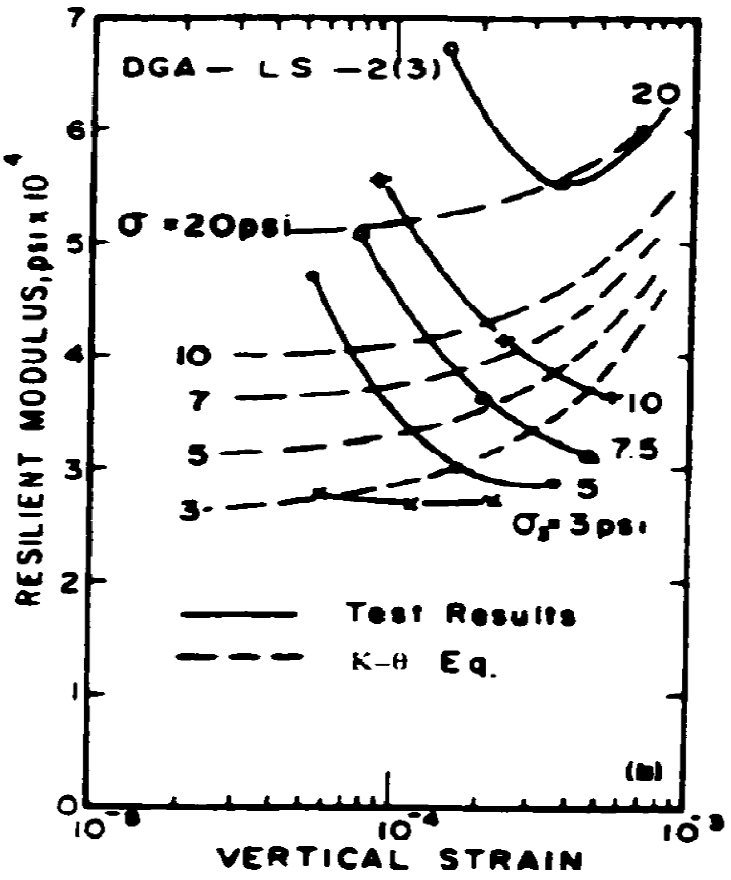

Figure 4-3 Comparison between predictions of bulk stress model and lab test results (Witczak and Uzan 1988)

The predicted resilient modulus values using the bulk stress model increase with increasing values of vertical strain, which contradicts the laboratory test data. The stress path data shows a reduction of resilient modulus when increasing induced strains. This clearly indicates the necessity of softening the component in characterization of unbound aggregate systems. Later, this model was modified by incorporating a softening parameter as a function of shear stress induced on samples to eliminate this limitation. However, due to the simplicity of this model, the bulk stress model is widely used for analysis and design of unbound aggregate layers for the design of pavements.

Uzan Model

Uzan modified the bulk stress model by adding a deviatoric stress term to capture the shear softening behavior in unbound aggregate systems (Uzan 1985). This model is presented in equation 4-3.

$$M_R = k_1 (\theta)^{k_2} (\sigma_d)^{k_3} \quad (4\text{-}3)$$

where:

σ_d= Deviator stress (σ_1-σ_3)

θ = Bulk stress that is the sum of the principal stresses (σ_1+2σ_3)

k_1, k_2, and k_2 =Regression constants

Figure 4-2 shows the comparison between laboratory stress path test results and Uzan model predictions of resilient modulus. Figure 4-2 clearly shows the capability of this model to account for shear softening and degradation of the resilient modulus at high strain levels. Comparisons between figure 4-1 and figure 4-2 also show that experimental data has a better fit to the Uzan model compared to the bulk stress model as expected.

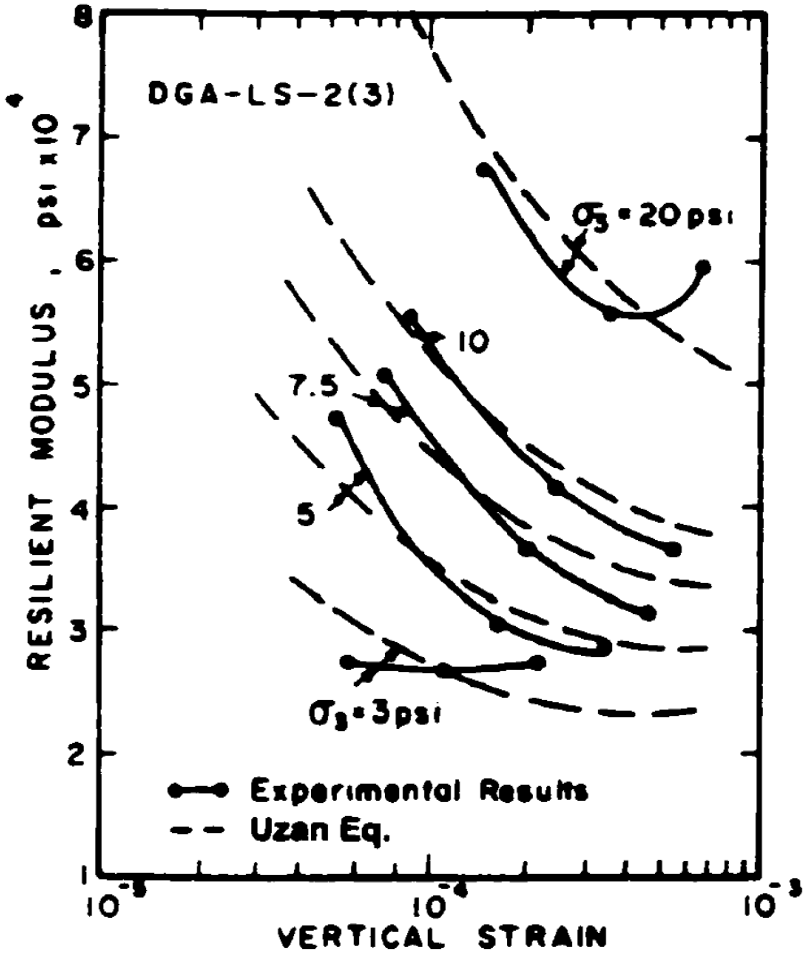

Figure 4-4 Comparison between predictions of Uzan model and experimental results (Witczak and Uzan 1988)

Universal Model

Uzan modified equation 4-3 by replacing the bulk stress with first stress invariant and deviatoric stress with octahedral shear stress (τ_{oct}). They also normalized the stress components to non-dimensionalized the model and to facilitate unit conversion (Uzan 1999). The universal model is presented in equation 4.

$$M_R = k_1 \, Pa \, (\frac{I_1}{Pa})^{k_2} (\frac{\tau_{oct}}{Pa})^{k_3} \tag{4-4}$$

where:

$$I_1 = \frac{1}{3}(\sigma_1 + \sigma_2 + \sigma_3) = \frac{1}{3}(\sigma_1 + 2\sigma_3) \tag{4-5}$$

$$\tau_{oct} = \frac{1}{3}\left[(\sigma_1 - \sigma_2)^2 + (\sigma_1 - \sigma_3)^2 + (\sigma_2 - \sigma_3)^2\right]^{\frac{1}{2}} = \frac{\sqrt{2}}{3}(\sigma_1 - \sigma_3) \tag{4-6}$$

Pa= Atmospheric pressure

k_1, k_2, and k_2 = Model parameters

In this equation $(\frac{I_1}{Pa})^{k_2}$ term is known as the hardening component, and $(\frac{\tau_{oct}}{Pa})^{k_3}$ term is known as the softening component of the resilient modulus model. Hardening component tends to capture the stiffening effect of aggregate matrix when subjected to repeated loading. Stiffness hardening is achieved through re-arrangement of the particles so as to reduce the air voids and achieve higher density. This particle re-arrangement results in more contact points and therefore improves load bearing capacity of the aggregate system. This will be true for the undamaged aggregate systems. As soon as the stresses induced on the system exceed the characteristic load, stiffness of the system reduces or in other words the aggregate system softens. The softening term $(\frac{\tau_{oct}}{Pa})^{k_3}$ tends to capture the damage induced on the system.

Components of the universal model are physically meaningful only when the hardening term $(\frac{I_1}{Pa})^{k_2}$ is greater than unity, and the softening term $(\frac{\tau_{oct}}{Pa})^{k_3}$ is less than one. Therefore it is imperative to choose the material parameters as such that this bond is satisfied. In other words k_2 parameter should be positive, and k_3 parameter should be negative to satisfy this condition. At low shear stress levels, however, the universal model

is not physically meaningful. For instance when octahedral shear stresses acting on an arbitrary aggregate system are less than the atmospheric pressure and knowing that 1<k3<0, the resultant softening term will be greater than one. This result contradicts the physical interpretation of the softening component of the resilient modulus. For this reason, equation 4 was modified by adding another material parameter k_4 to eliminate this error. The modified universal model is presented in equation 4-7. The suggested value for k_4 parameter is unity.

$$M_R = k_1 \left(\frac{I_1}{Pa}\right)^{k_2} \left(\frac{\tau_{oct}}{Pa} + k_4\right)^{k_3} \tag{4-7}$$

Figure 4-3 and figure 4-4 provide comparisons between two softening terms in equations 4 and 7. Figure 4-3 shows the sensitivity of the softening term to varying magnitudes of octahedral shear stresses and k_3 values that are the exponent of the softening term in the resilient modulus equation.

This figure clearly shows that the physical meaning of the softening term in the model has been violated for octahedral shear stresses less than the atmospheric pressure (14.69 psi). As previously noted in this chapter, the softening term is responsible for capturing the loss stiffness due to damage induced to the aggregate matrix. This term needs to be less than one to be physically sensible. Both the trend and the values of the softening term $\left(\frac{\tau_{oct}}{Pa}\right)^{k_3}$ at octahedral shear stresses less than atmospheric pressure are not physically sensible. Since the octahedral shear stresses are typically positive, the exponent of the softening term needs to be negative. Softening exponent (k_3) values were found to range from -0.3 to -0.1 for good quality aggregate systems when subjected to harmonized protocol in the NCHRP 1-28 study. As illustrated in this figure, for positive values of the k_3 exponent, the model predicts higher stiffness properties with increasing shear stresses acting on the continuum, which is not physically meaningful. This discrepancy is also shown in figure 4-4. Therefore it is crucial to select proper model parameter values (negative k_3 values) to be able to simulate the behavior of aggregate systems throughout the range of stresses induced by traffic loads.

Figure 4-4 shows the sensitivity of the softening term to shear stresses for varying k_3 values. This model predicts higher reductions in the stiffness of the aggregate systems when the system is subjected to higher shear stresses. The sensitivity analysis on the softening parameter $(\frac{\tau_{oct}}{Pa}+1)^{k_3}$ shows that aggregate systems with more negative values of k_3 are more sensitive to the shear stresses applied on the aggregate matrix.

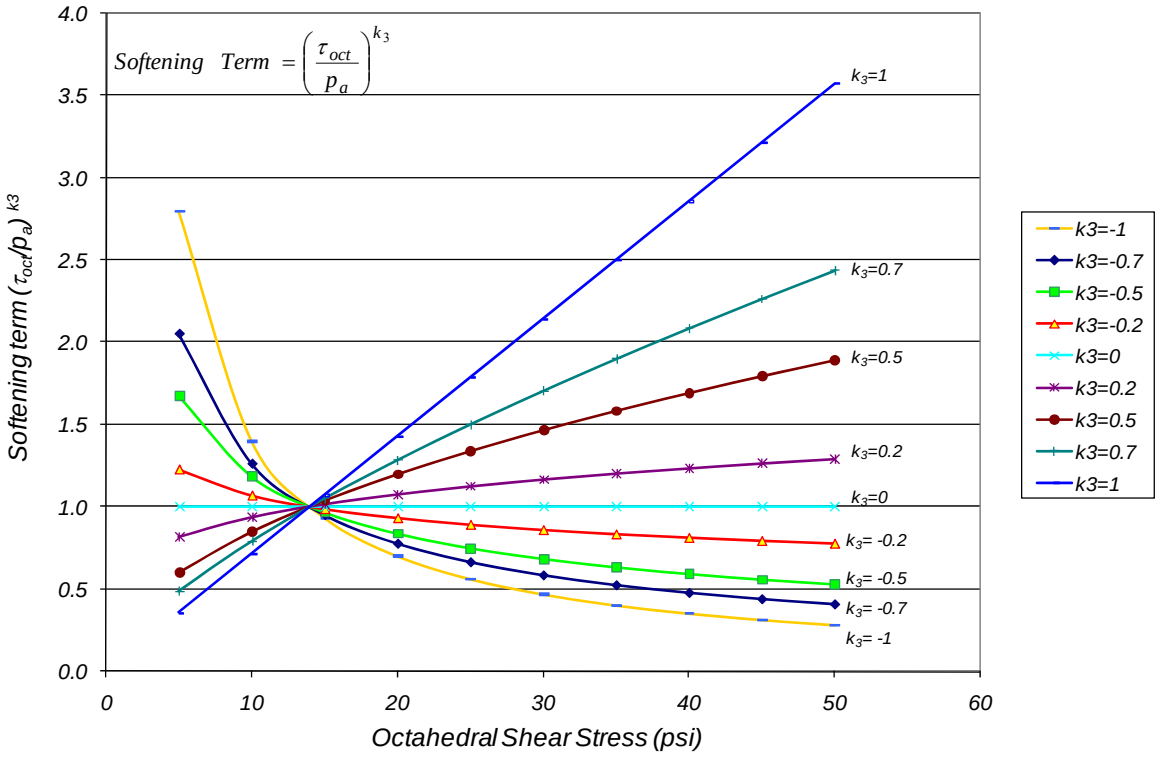

Figure 4-5 Sensitivity of the softening term $(\frac{\tau_{oct}}{Pa})^{k_3}$ of the universal model

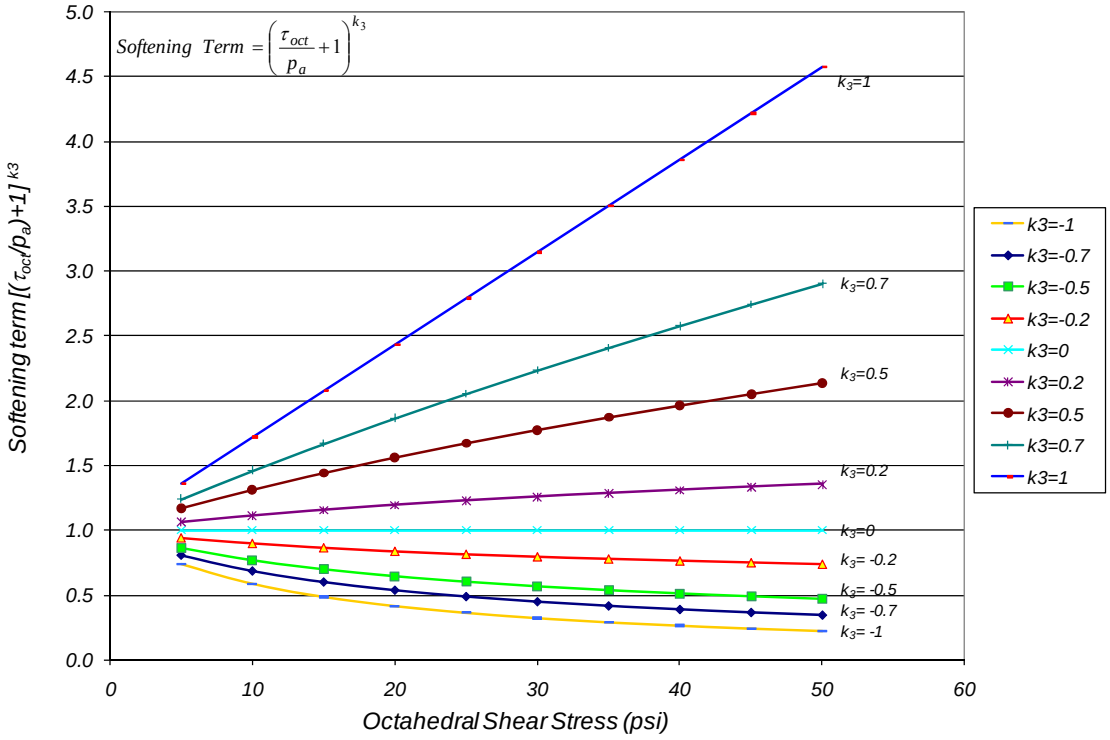

Figure 4-6 Sensitivity of the softening term $(\frac{\tau_{oct}}{Pa}+1)^{k_3}$ of the modified universal model

The universal model collapses into the bulk stress model when k_3=0. Figure 4-3 and figure 4-4 show the stiffness of the matrix is invariant to the magnitude of shear stresses experienced by the aggregate continuum.

Figure 4-5 shows the sensitivity of the modified universal model to varying k_2 and k_3 values, exponents of hardening and softening terms, respectively. This plot shows aggregate increasing the hardening parameter (k_2) results is stiffer aggregate matrix while increasing if softening parameter (k_3) results in reduction of the resilient modulus of the system.

Figure 4-6 shows the sensitivity of the model to k_1 and k_3 parameters. As illustrated in this plot, higher k_1 parameters correspond to stiffer aggregate systems.

Softening parameter k_3 is an indicator of damage due to shear softening in the system; therefore higher negative values of k_3 correspond to softer materials.

Figure 4-7 presents the sensitivity of the universal model to k_1 and k_2 parameters. In both cases, higher values of k_1 and k_2 correspond to a stiffer system.

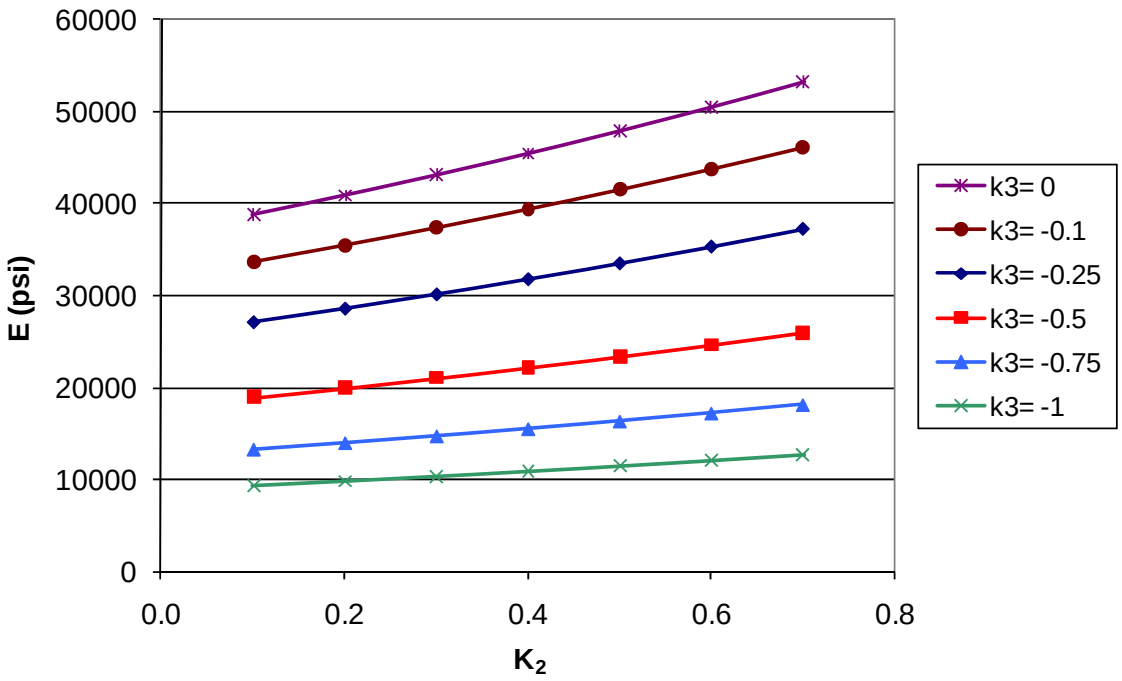

Figure 4-7 Impact of hardening exponent (k_2) and softening exponent (k_3) on the resilient modulus for constant values of k_1=2500

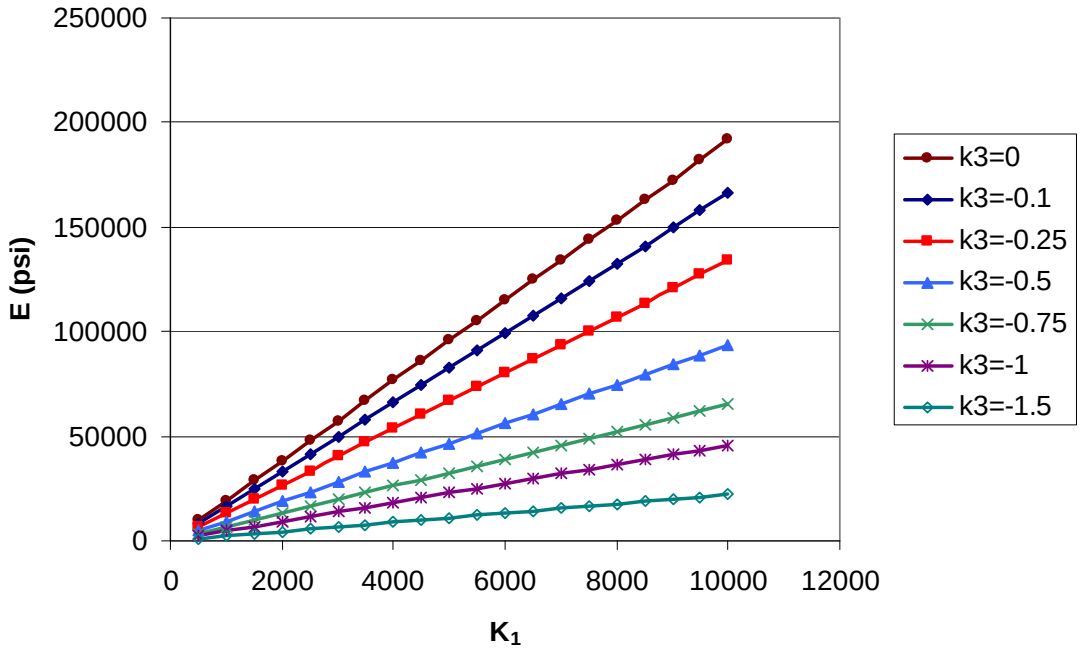

Figure 4-8 Impact of multiplier (k_1) and softening exponent (k_3) on the resilient modulus for constant values of k_2=0.5

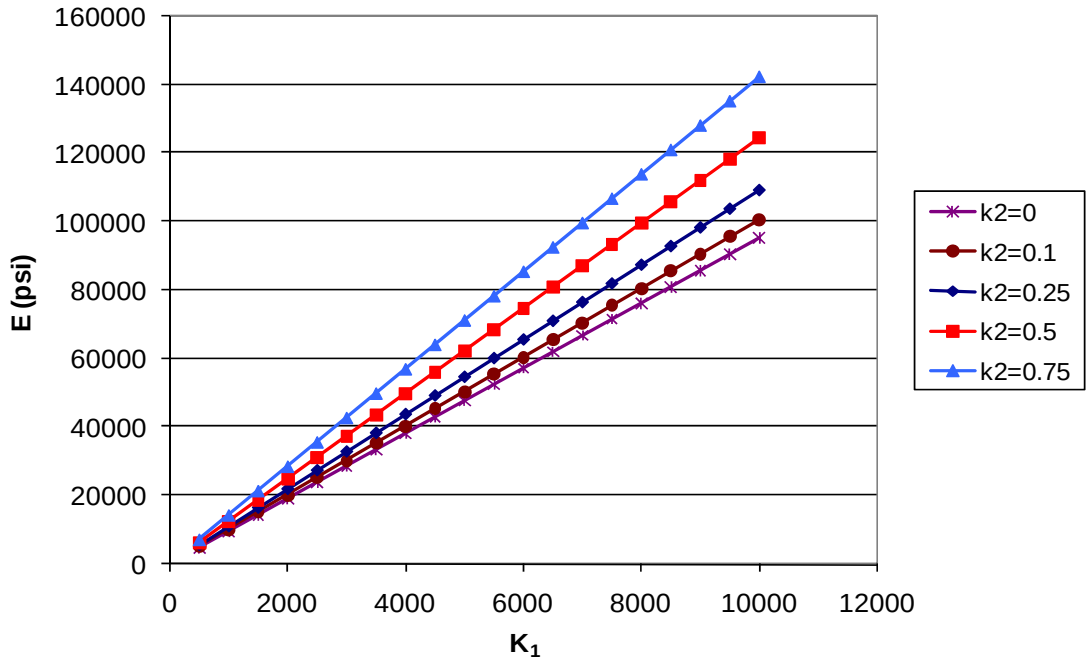

Figure 4-9 Impact of multiplier (k_1) and hardening exponent (k_2) on the resilient modulus for constant values of k_3= -0.3

Sensitivity of Model Parameters (k-values) to Stress States

Model parameters (k-values) capture the stress sensitivity and nonlinearity of the resilient modulus in the aggregate system. Therefore the responses of the aggregate system under the load are also functions of k-parameters. The main objective of the sensitivity analysis of the universal model with respect to model parameters (k-values) presented in the previous section was to illustrate the physical sense of the model parameters as well as their impact on the stiffness properties of the aggregate matrix. This section presents a discussion on the impact of stress states and stress history on the parameters of the universal model.

In order to illustrate the stress sensitivity of model parameters, a stress path test was performed on well-graded Texas limestone. The aggregate sample was subjected to NCHRP 1-28A loading at optimum moisture state. The reason for choosing the harmonized stress path protocol was the fact that stress states are substantially higher than AASHTO T-307 protocol, and therefore the probability of inducing damage to the system will be higher. In order to show the stress sensitivity of k-values to state of stresses and stress ratios, the k-parameters were calculated for five stress combinations at each stress path. The results were in turn plotted for six stress paths and presented in figures 4-10 and 4-11.

Figures 4-10 and 4-11 show the evolution of k-parameters in each stress path. Figure 4-10 shows the sensitivity of the k_1 parameter to stress paths applied on the sample in the lab. As indicated in this figure, the calculated k_1 parameter was lower in the initial stress path and gradually stabilized as the prescribed stress states and stress ratios were increased.

Exponent of the softening term k_3 however, was calculated to be positive in the first stress path, which is due to application of less taxing stress paths and is not physically meaningful. With increasing magnitudes of stress states and stress ratios, the k_3 parameter became negative as expected. The increasing value of the k_3 parameter in each stress path is a testament to shear softening of the aggregate system when subjected to more demanding stress paths. This emphasizes the need for testing the geomaterials

throughout the range of stress states that is expected in the field. The softening in granular materials initiates with slippage and rotation of particles, which leads to initiation of shear banding in the aggregate systems.

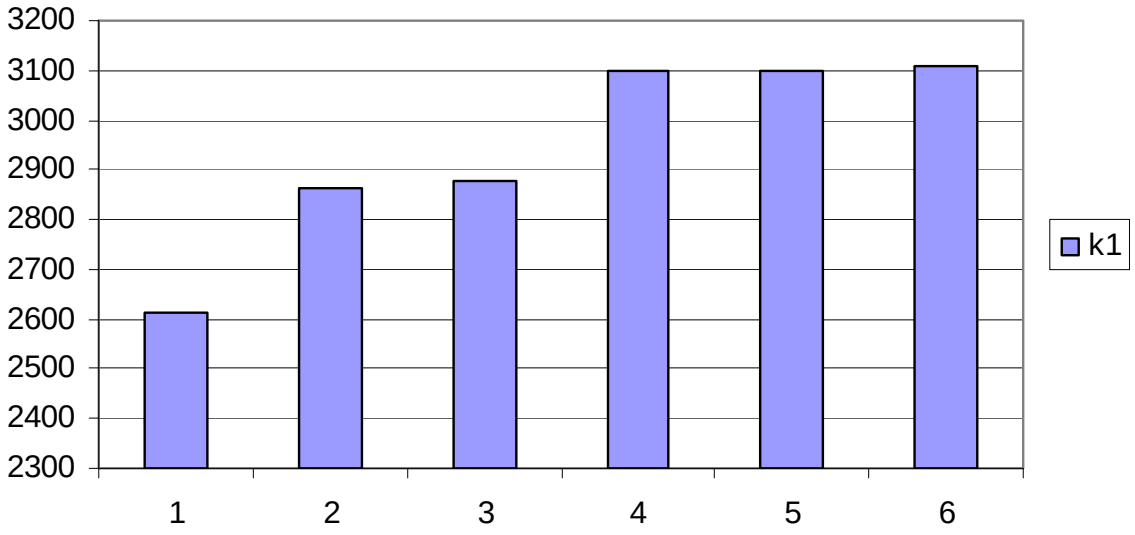

Figure 4-10 Stress sensitivity of k_1 parameter, multiplier in the universal model

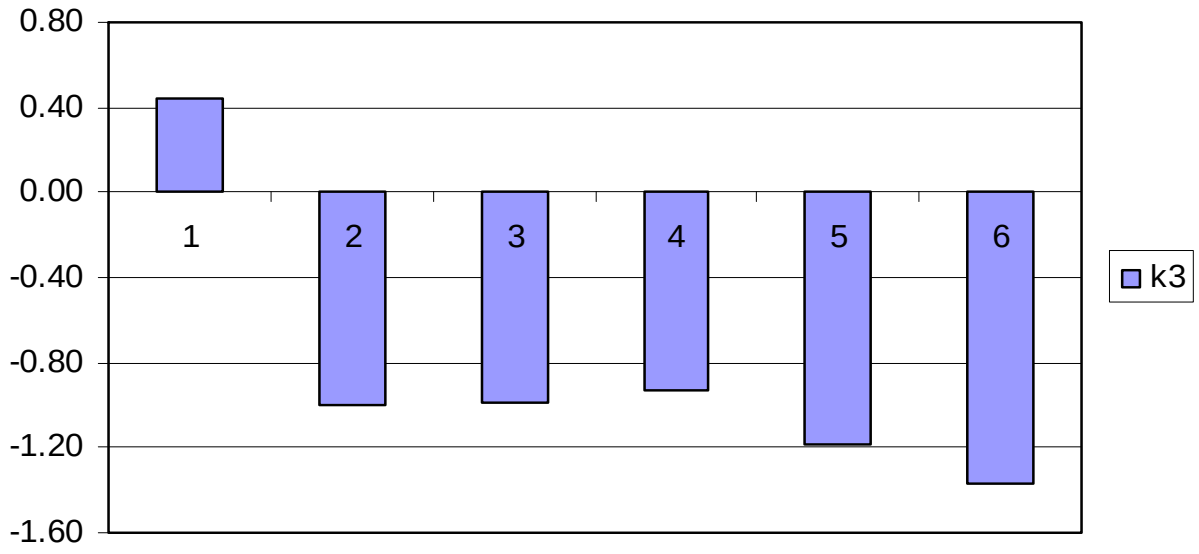

Figure 4-11 Stress sensitivity of k_3 parameter, exponent of the softening term in the universal model

Lade and Nelson Model

Lade and Nelson developed a prediction model for elasto-plastic modulus based on elastic work potential. This model was originally developed based on isotropic assumptions and later modified for anisotropic granular soils. The stiffness properties E, G, and K, elasto-plastic modulus, shear modulus, and bulk modulus, respectively, were formulated as stress dependent properties while Poisson's ratio was considered to be constant at a certain void ratio (Lade and Nelson 1987).

Considering the conservation of energy for an elastic material in a closed loop path, the work completed on the system can be written as:

$$W_{total} = \oint dW = \oint \left[\frac{I_1}{9K} dI_1 + \frac{dJ_2}{2G} \right] = 0 \tag{4-8}$$

where:

I_1= First invariant of the stress tensor

J_2=Second invariant of the deviatoric stress tensor

G=Shear modulus

K=Bulk modulus

Lade showed a partial differential equation can be derived from equation 4-8 as:

$$\frac{I_1}{9K^2}\frac{\partial K}{G^2} = \frac{\sqrt{J_2}}{G^2}\frac{\partial G}{\partial I_1} \tag{4-9}$$

In order to write equation 4-9 in terms of elastic modulus (E) we can use equations 4-10 and 4-11 from general elasticity:

$$K = \frac{E}{3(1-2\upsilon)} \tag{4-10}$$

$$G = \frac{E}{2(1+\upsilon)} \tag{4-11}$$

Now by substituting equations 4-10 and 4-11 into equation 4-9 we have:

$$\frac{1}{J_2}\frac{\partial E}{\partial \sqrt{J_2}} = \frac{6(1+\upsilon)}{(1-\upsilon)}\frac{1}{I_1}\frac{\partial E}{\partial I_1} \tag{4-12}$$

Lade and Nelson proposed equation 4-13 for calculation of elasto-plastic modulus of granular materials (Lade and Nelson 1987).

$$E = M\,Pa\left[\left(\frac{I_1}{Pa}\right)^2 + R\frac{J_2}{Pa}\right]^{\lambda} \tag{4-13}$$

where M and λ are model parameters found from stress path testing, and R is a function of the non-stress dependent Poisson ratio presented in equation 4-14.

$$R = \frac{6(1+\upsilon)}{(1-\upsilon)} \tag{4-14}$$

Table 4-1 presents model parameters for several geomaterials tested for validation of Lade's yield criterion. As indicated in this table, λ values have a narrow range while M values vary significantly for different types of materials.

Table 4-1 Lade Parameters for Different Geomaterials (Abelev and Lade 2003)

Soil Type	**Lade's Parameters**	
	M	**λ**
Santa Monica Beach Sand	1270	0.23
Monterey Sand	1120	0.33
Fine Silica Sand	440	0.22
Mohawk Model Soil	630	0.27
Niagara Type 1	670	0.26
Niagara Type 2	570	0.29
Sacramento River Sand	500	0.28

Figure 4-12 shows the sensitivity of the modulus prediction model to model parameters M and λ. The sensitivity of the model was performed on the stress states within the range of NCHRP 1-28A loading protocol. Figure 4-12 indicates the M value closely related to the magnitude of the resilient modulus as higher M values correspond to stiffer aggregate systems, as expected. The λ value however is more related to the slope of the E-M plots. Figure 4-12 was specifically plotted for a constant value of Poisson's ratio (μ) of 0.3.

Figure 4-13 shows the impact of Poisson's ratio (μ) for different M values. This plot shows that the slope of the curve increases as the Poisson ratio increases. In other words the resilient modulus predicted by the Lade model becomes more sensitive to μ values for aggregate systems with higher Poisson ratios.

Figure 4-14 and figure 4-15 provide the sensitivity of the model toward the state of the stresses experienced by aggregate continuum in pavement foundations. The stress combinations were selected so as to be within the range of harmonized loading protocol.

Figure 4-14 shows the impact of first stress invariant and confining pressure on the predicted resilient modulus values. As illustrated in this figure, first invariant of the stress tensor acts as a hardening parameter in the Lade's model and captures the stiffening effect of aggregate systems under the load. The increase in the stiffness

properties of the aggregate continuum is due to the re-arrangement of the particles in a way that they form more contact points are created which result in stronger force chains. The stress hardening effect, which is primarily due to the reduction of air voids, results in better load distribution capability and therefore stronger aggregate matrix. This figure also shows the impact of confining pressure (σ_3) on the predictions of the model as higher confinement levels resulted in higher resilient modulus values.

Figure 4-15 shows the impact of increasing shear stresses on the resilient modulus values. The resilient modulus values were plotted at five confinement levels for comparison. Shear stresses experienced by soil particles were characterized by second deviatoric invariants of the stress tensor. As indicated in equation 2-16 this value is a function deviatoric stress σ_d in the triaxial test. As illustrated in figure 4-15, J_2 parameter acts as the softening term in the resilient modulus prediction model and therefore increasing values of J_2 resulted in a reduction of the stiffness properties of the aggregate systems.

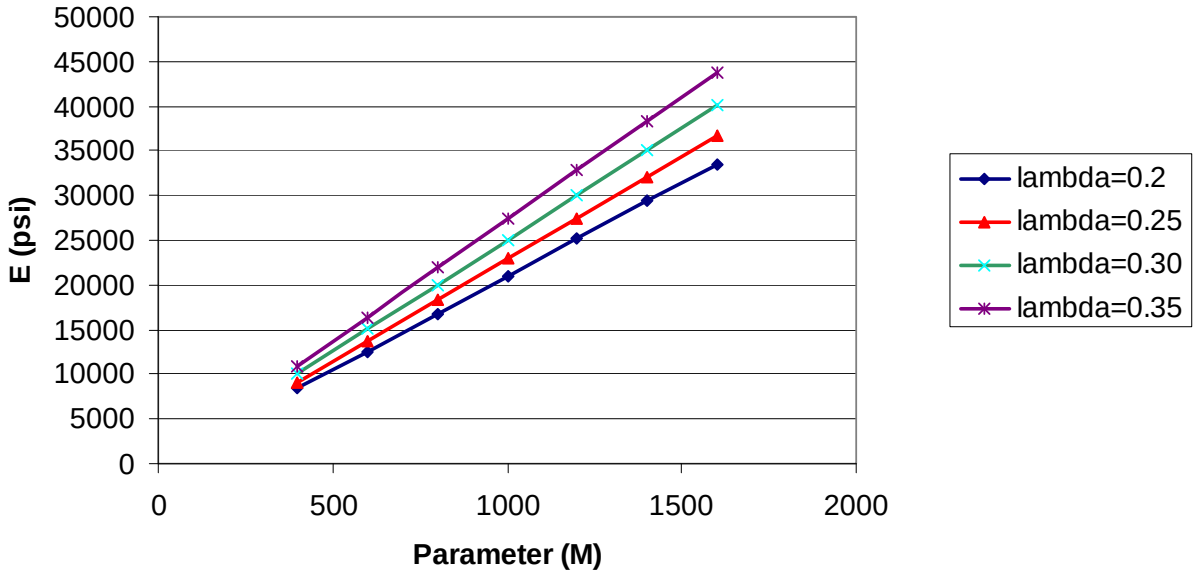

Figure 4-12 Sensitivity of modulus values (E) to parameters of the Lade's model for constant values of Poisson ratio (μ=0.3)

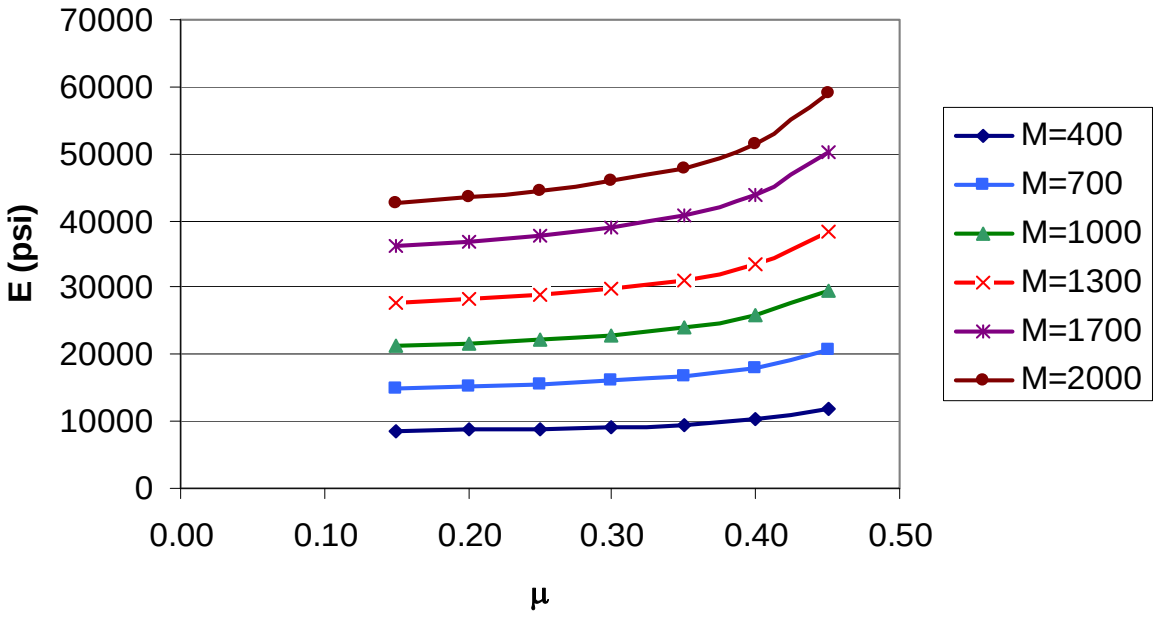

Figure 4-13 Sensitivity of modulus values (E) to parameter M and Poisson ratio (μ) for constant values of (λ=0.25)

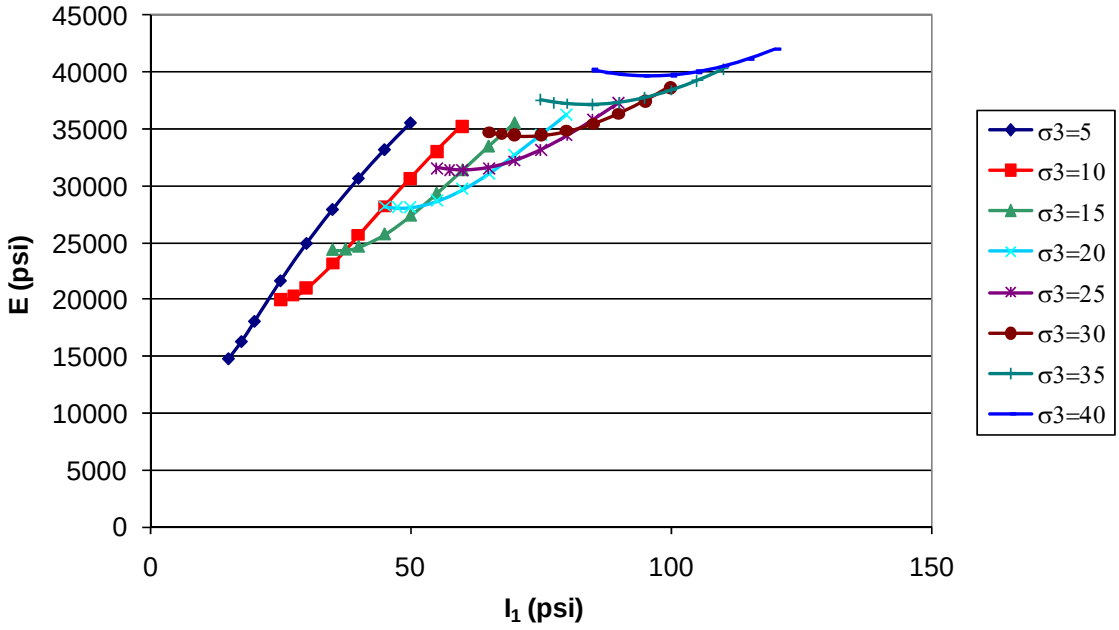

Figure 4-14 Impact of confining pressure (σ_3) and the first stress invariant (I_1) on the Lade's model

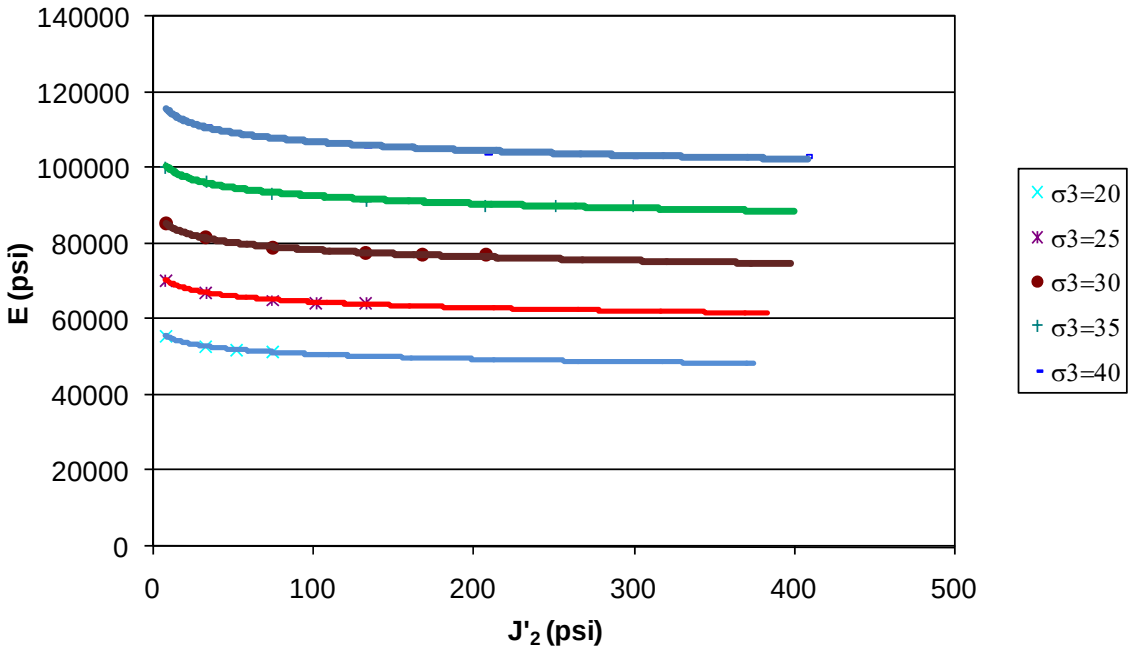

Figure 4-15 Impact of confining pressure (σ_3) and second deviatoric stress invariant (J'_2) on the Lade's model

Lytton's Model

Lytton used the principals of unsaturated soil mechanics and modified the Uzan model. This model considers the impact of moisture state on the stiffness properties of the aggregate systems (Lytton 1995). The degradation of the resilient modulus in this model is captured through adding volumetric water content and a suction term to the Uzan. The Lytton resilient modulus prediction model is presented in equation 4-15.

$$E = k_1 Pa\left(\frac{I_1 - 3\theta f h_m}{Pa}\right)^{k2}\left(\frac{\tau_{oct}}{Pa}\right)^{k3} \quad (4\text{-}15)$$

where:

I_1= First stress invariant

Pa= Atmospheric pressure

θ= Volumetric water content

h_m= Matric suction

f= Function of volumetric water content

The impact of considering the moisture state and pore water pressure is shown through an example presented in figure 4-16. This plot presents the influence of pore water pressure on the resilient modulus predicted by equation 14 for an arbitrary pavement profile. Figure 4-16 clearly indicates the shift and reduction in the hardening component of the predicted resilient modulus as the pore water pressure parameters were considered in the formulations.

Lower hardening parameters correspond to less stiff aggregate systems, therefore taking into account the influent of the pore water pressure enables the pavement designer to better judge the stiffness of the aggregate layer and prevent him from overestimating the modulus of the base layer particularly at wet cycles. The results in this figure indicate that hardening component is approximately 20% smaller when the influence of soil suction is considered in formulations.

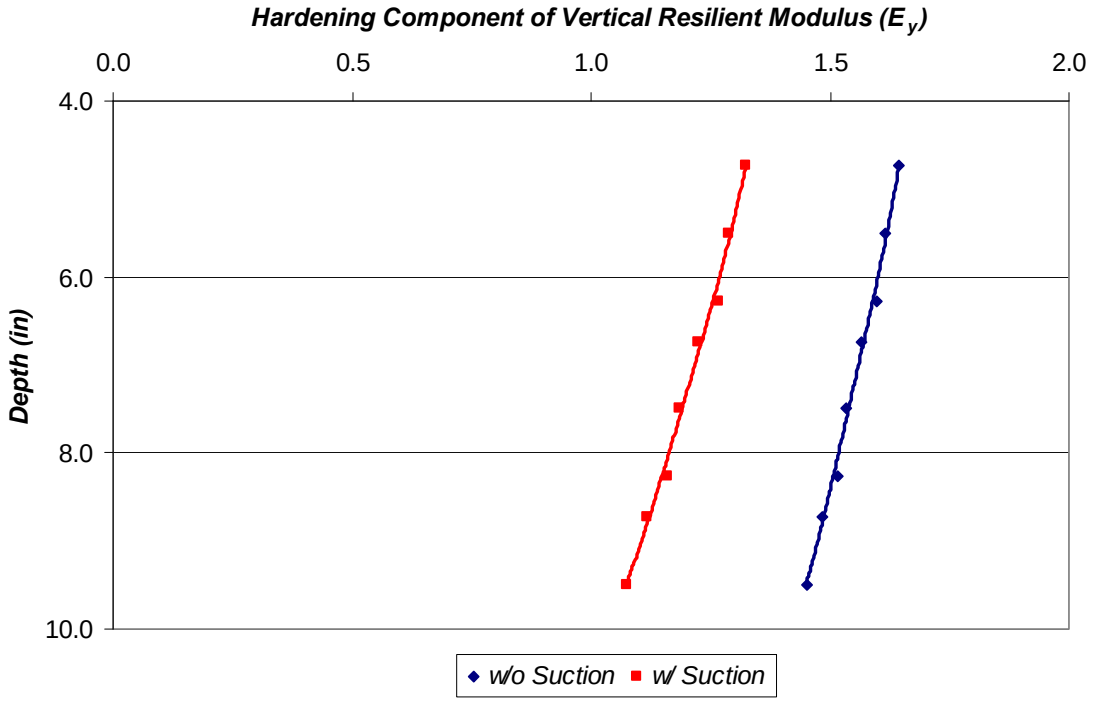

Figure 4-16 Impact of pore water pressure on the hardening parameter of resilient modulus

Figure 4-17 through 4-19 presents the sensitivity of the Lytton's model to parameters of the model. The sensitivity was performed for varying values of moisture states to demonstrate moisture sensitivity of the aggregate systems. The main advantage of this model is that the degradation of the stiffness properties with increasing moisture content can be predicted in the aggregate system.

Figure 4-17 shows the impact of multiplier parameter k_1, on the resilient modulus of the aggregate systems at various moisture states. Higher k_1 parameters correspond to stiffer aggregate systems, and increasing volumetric water content degrades the stiffness of the matrix.

Figure 4-18 shows the impact of hardening exponent k_2 on the resilient modulus of the aggregate systems. Aggregate systems with a higher k_2 parameter showed more stiffening effect under the load and have higher resilient modulus values. The stiffness of the aggregate systems was reduced when the volumetric water content passed beyond the

optimum moisture content of the mix. For the hypothetical case of k_2=0, at which the hardening effect and degradation due to moisture was not considered, the stiffness of the matrix remains constant as shown in figure 4-17.

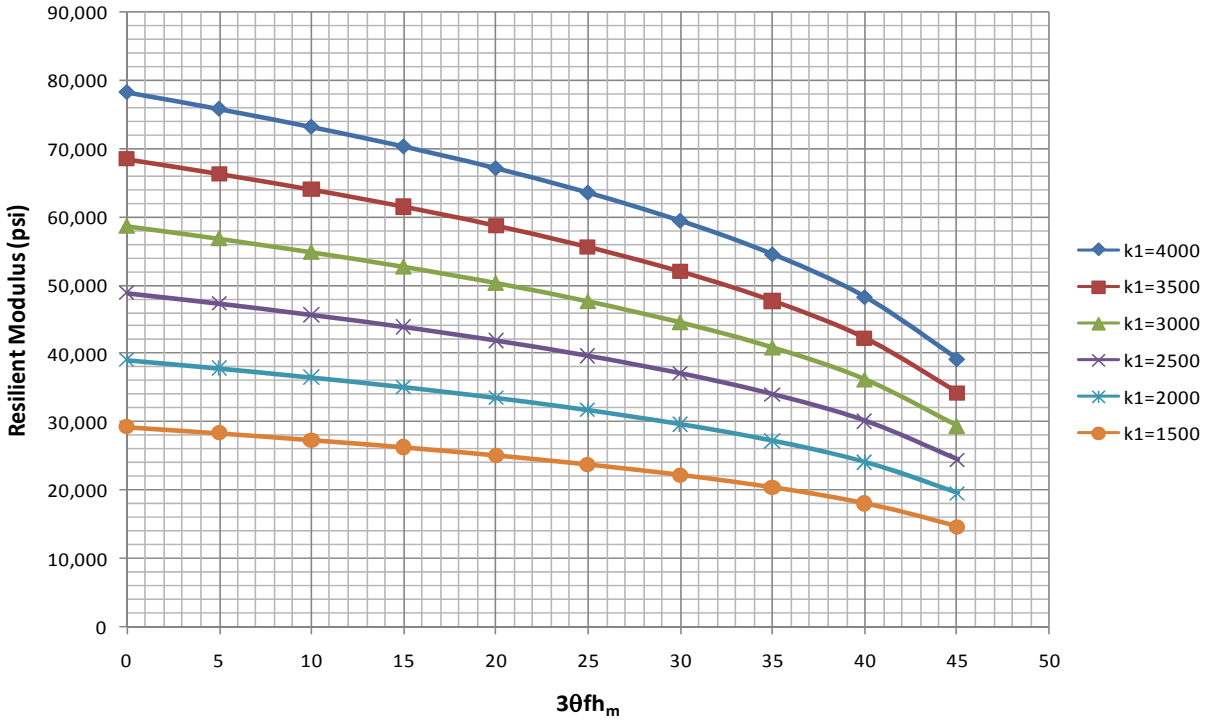

Figure 4-17 Sensitivity of the resilient modulus predicted by Lytton's model to k_1 parameter

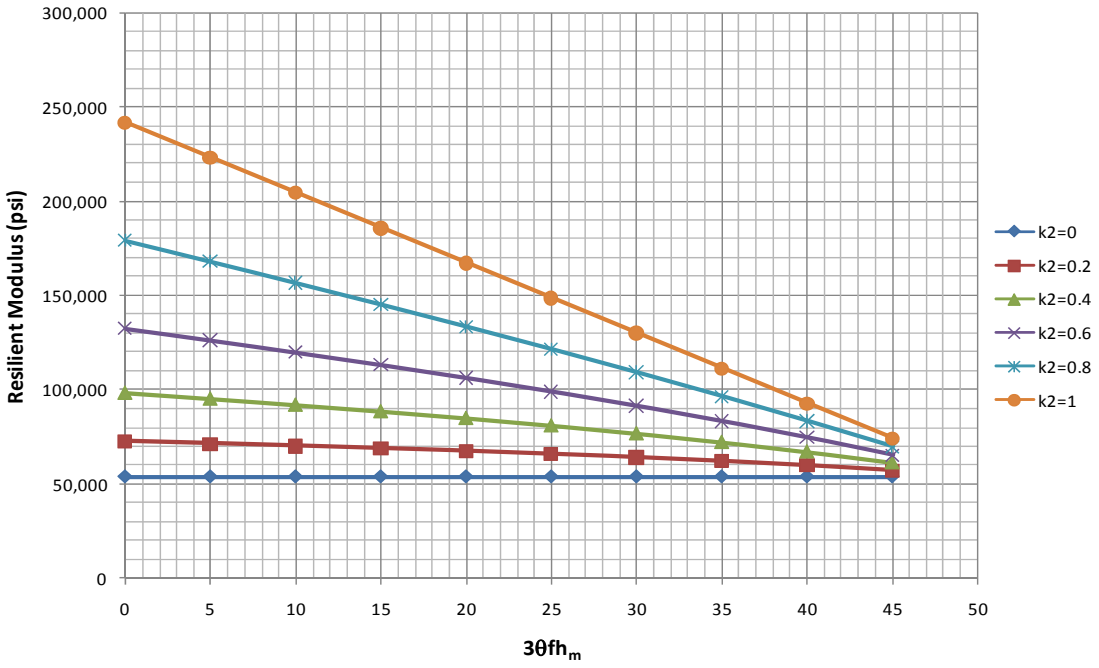

Figure 4-18 Sensitivity of the resilient modulus predicted by Lytton's model to k_3 parameter

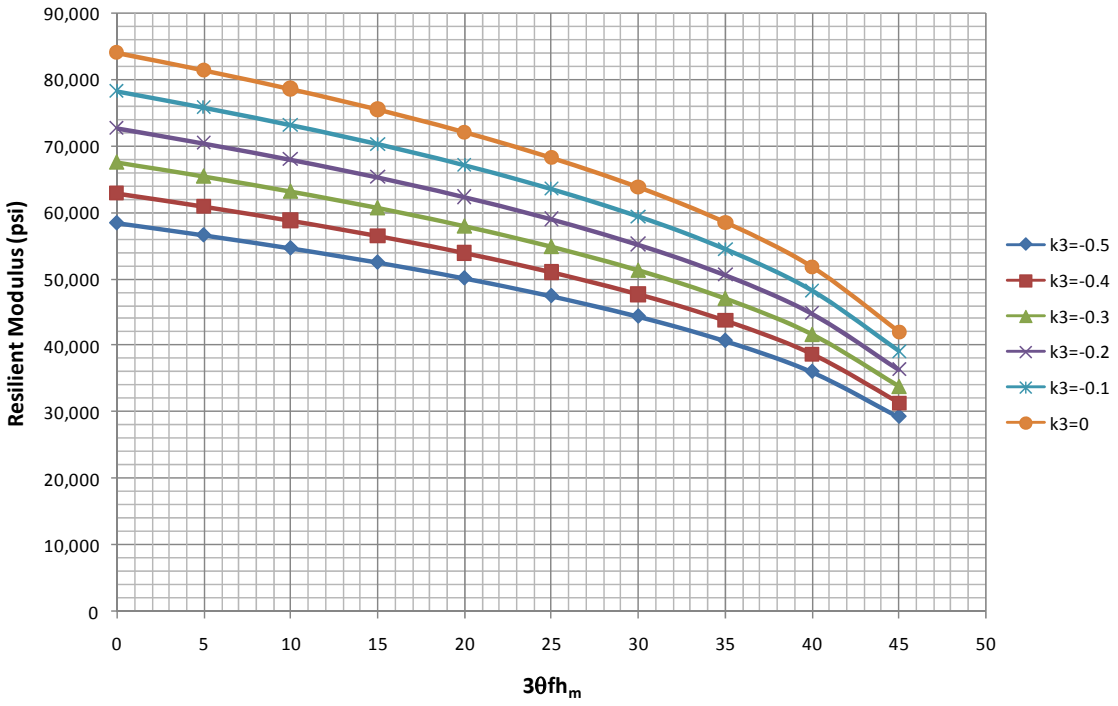

Figure 4-19 Sensitivity of the resilient modulus predicted by Lytton's model to k_2 parameter

Figure 4-19 shows the synergistic impact of increasing moisture content and softening component k_3 on degradation of the resilient modulus of the aggregate systems. This plot clearly shows the loss of stiffness of the mix due to shear softening in geomaterials. The degradation of the modulus is exacerbated by increasing moisture contents as shown in this plot. The slope of the degradation curves tends to increase as the saturation level of the mix increases, which is more evidence of increasing moisture susceptibility when the effect of shear stresses and saturation levels are considered simultaneously.

CHAPTER V

PATTERN RECOGNITION TECHNIQUES AND NEURAL NETWORK MODELING

INTRODUCTION

Non-traditional mathematical techniques such as neural networks have gained huge popularity among scientists as a means to unfold the complex relationships between the features of data sets. The main focus of this chapter is directed toward reviewing several of these mathematical techniques and seeks their application in materials science. Among these methods we will discuss Artificial Neural Networks as an approach for modeling the anisotropic behavior of aggregate systems. Neural networks are basically multi-variable applications, where, if trained properly, they can accurately identify the interactions and patterns between the input and the output of the system. Pattern recognition techniques and dimensionality reduction methods such as principal component analysis and Fisher's discriminant analysis will be discussed in this chapter. These techniques were performed on the aggregate database to identify the aggregate features that contribute most to the level of anisotropy of unbound aggregate systems.

SELECTED PREVIOUS WORK

During the past two decades, several pavement researchers have used non-traditional mathematical methods such as neural networks as their classification technique or function approximation method to predict the performance of pavement systems and the response behavior of highway materials under traffic loads. Owusu-Ababio used neural networks as a pavement performance prediction tool (Owusu-Ababio 1998). He used several topologies to predict top down cracking in flexible pavements. Khazanovic successfully trained a neural network-based model to predict the elastic properties of

asphalt overlays used in rigid pavements. He reported excellent agreement between the FWD data and the neural network-calculated elastic properties of the asphalt overlay (Khazanovich and Roesler 1997). Meier augmented the conventional pavement layer moduli backcalculation program WESDEF by four neural network-based models to compute the pavement surface deflections for a wide range of three-layered flexible pavements. He concluded that the addition of these models significantly reduced computation time, and that the enhanced software was capable of back calculating the pavement layer moduli forty two (42) times faster than original WESDEF program (Meier et al. 1997). Ceylan used neural networks as a pavement structural analysis tool for rapid and accurate prediction of nonlinear layer responses and surface deflections under traffic loads. He used the nonlinear stress-dependent finite element program ILLi-Pave to generate the training dataset for developing the neural network model (Ceylan et al. 2005). In another research initiative, Ceylan used the same model in a validation study of the TRB Nonlinear Pavement Analysis Project data sets. He reported reasonable agreements between the field strain measurements and the calculated strains from the neural network model (Bayrak and Ceylan 2008).

The following sections provide theoretical discussion on non-traditional mathematical techniques used in this study. The analysis of the aggregate database using these techniques was documented in Chapter IX.

DESCRIPTION OF THE NEURAL NETWORKS

A neural network consists of a number of nonlinear computational processing elements called neurons arranged in one or more layers connected by weighted connections between these layers. A schematic representation of a neural network is presented in figure 5-1.

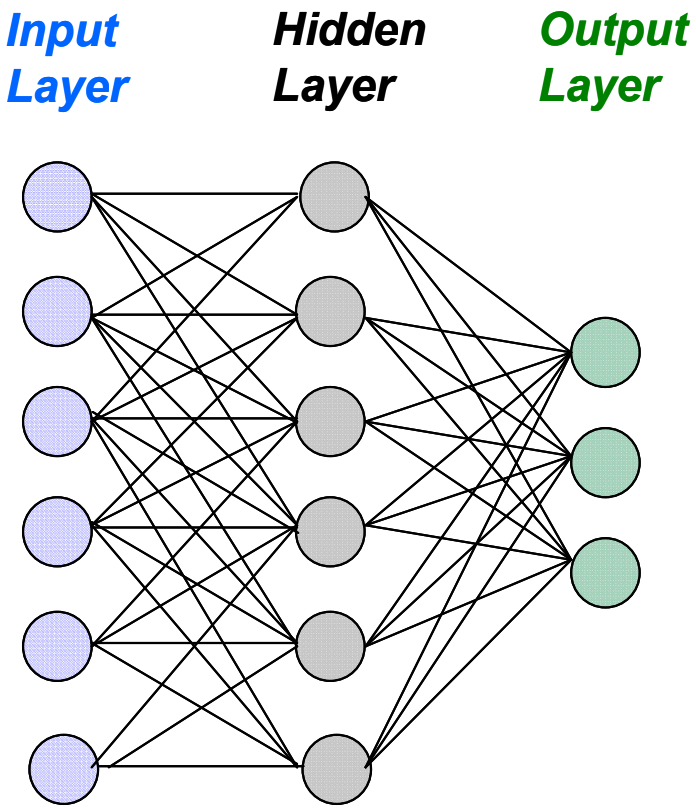

Figure 5-1 General topology of a neural network

As shown in Figure 5-1, there are three primary layers in a neural network: an input layer, hidden layer(s), and an output layer. The input layer is where the data are fed to the neural network, and the output layer holds the responses of the network to the input of the system. An intermediate component is present in the neural nets called the hidden layer(s), which enables the network to provide nonlinear mapping of the data and which accurately predicts the output of the system.

Different neural network topologies provide more flexibility and a powerful means to capture more information and to unfold the underlying relationships between input features and the output of the system. Two types of neural network topologies, namely multilayer perceptrons (MLP) and generalized feed forward (GFF), were studied. Multilayer perceptrons (MLP) are layered feed forward networks typically trained with static back propagation. These networks have found their way into countless applications requiring static pattern classification. Their main advantage is that they are easy to use and can approximate any input mapping of data. Generalized feed forward networks are the generalization of the MLP such that connections can jump over one or more layers. In theory, an MLP can solve any problem that a generalized feed forward network can solve. In practice, however, generalized feed forward networks more efficiently converge to an acceptable error tolerance level. In other words a standard multilayer perceptron requires more training iterations compared to the generalized feed forward network with the same number of processing elements (Bishop 1995).

The main issue in using the neural network techniques involves regularization or adjusting the complexity of the selected network to avoid poor training or over fitting of the data. This is done by selecting the number of weights or parameters in the network. If too many free parameters such as the number of hidden layers are used, generalization will be poor. On the other hand, if too few parameters are used, the model cannot be trained adequately, and the trained model will give a poor estimation of the desired output. Therefore, in this study, the authors considered different neural network topologies with various free parameters to address the overfitting issue while maintaining acceptable performance.

The training of the ANN model is an iterative process. The basic approach is to start with a random set of weights and adjust them by minimizing the error or the criterion function. In each iteration, output is compared with actual target values and the weights are adjusted accordingly to minimize the error function. The output of each unit in the hidden layer is multiplied by the weight of each layer and then passed on to the next hidden layer. The output, Q_j^m , of unit *j* of layer *m* can be written as (Duda and Hart 1973):

$$O_j^m = f(I_j^m) \tag{5-1}$$

In equation 5-1 I_j^m is the input value of unit *j* of layer *m*, and *f* presents the excitation function, which is generally adopted as a sigmoid function as suggested by Rumelhart:

$$F(I_j^m) = \frac{1}{1+\exp(-I_j^m)} \tag{5-2}$$

For the input values ranging from -∞ to +∞, the $f(I_j^m)$ will result in values ranging from 0 to 1. In general by considering B_j^m as the bias of the model, the relationship between input variables, outputs, and the weights of the system (w_{ij}) can be defined as:

$$I_j^m = \sum O_j^m w_{ij} + B_j^m \tag{5-3}$$

The performance of the model is determined by the root mean squared error (RMSE) calculated at the end of each epoch and presented in equation 1:

$$RMSE = J(w) = \sqrt{\frac{\sum_{j=1}^{n} \left[t_j - O_j\right]^2}{n}} \tag{5-4}$$

where *t* is the target output value, and *n* is the number of training input vectors presented to the system for training.

The propagation learning rule adopted in this study is based on gradient decent. The weights in the network are initialized by random values and modified in the direction that reduces the error function. Equation 5-5 shows the expression used for adjusting the weights in the training process.

$$\Delta w = -\eta \frac{\partial J}{\partial w} \tag{5-5}$$

In equation 5-5, *w* represents all the weights in the network, and η is the learning rate. A smooth learning curve was achieved by selecting the learning rate (η) as 0.001 as will be discussed later in this paper.

Duda showed that the relative sensitivity of the output of the neural network model to the feature *k* of the database can be found from equation 5-6:

$$\delta_k = \frac{-\partial J}{\partial t_k} \tag{5-6}$$

where δ_k is the sensitivity of the model to feature k, and t_k is the units' net activation. In general, the sensitivity analysis of the model investigates the overall changes in the output of the system when the feature of the database increases by one unit. This equation was further used to calculate the relative sensitivity of the neural network model to the features of the aggregate system (Duda and Hart 1973).

PATTERN CLASSIFICATION AND DIMENSIONALITY REDUCTION

Background

Study of the anisotropic behavior of unbound aggregate systems and investigation of aggregate features that influence the orthogonal load distribution capacity in unbound layers was performed on a high dimensional aggregate database. The aggregate database consists of 65 aggregate systems with different gradations and tested at different saturation levels. Twenty-seven features for each system were determined and used as input to the aggregate database. This high dimensional aggregate matrix (65x27) was in turn used to identify the underlying patterns among aggregate features as well as impact of each aggregate feature on anisotropic behavior of aggregate systems. Analysis of a database with this magnitude deems necessary to employ dimensionality reduction techniques to eliminate correlated features and select the features with highest significance.

Dimensionality reduction methods were developed as a way of identifying and unfolding the hidden patterns within the data and expressing them in a way that highlights the similarities and differences within the data structure. Since underlying patterns in high dimensional data are hard to decipher, where the luxury of graphical visualization is not available, dimensionality reduction techniques come in handy in analyzing the data. In other words, dimensionality reduction deals with transformation of the data from high dimensional space to low dimensions space, while maintaining most of the useful structure in the original data. Once the underlying patterns of the data were identified, the compressed data exhibits the same pattern without much loss of information.

In principle, the more information we gather about a phenomenon, the better a learning algorithm is expected to perform and more accurately capture the behavior of the phenomenon. Therefore in this study we gathered as many aggregate features as we could and employed mathematical techniques to find the features with the highest impact on the anisotropic behavior of aggregate systems. However, the time and cost of obtaining the features of the data suggest the use of features that best explain the pattern of the data. On

the other hand, many learning algorithms perform poorly in datasets with high features and few samples.

The difficulty in analyzing a dataset with a high number of features and few samples is called the curse of dimensionality (Duda and Hart 1973). The dimensionality reduction can circumvent this problem by reducing the number of features before the training process. Models with less parameter (features) are more desirable because they are easier to interpret and explain. Dimensionality reduction is also a valuable method as a visualization tool, where the high dimensional data set is transformed into two or three dimensions for graphical demonstrations.

The main drawback of dimensionality reduction according to Duda is its dependency on the algorithm used to reduce the irrelevant features. He stated that in feature selection and feature extraction processes, if improper algorithm is used, useful instead of irrelevant information will be discarded, and no matter what the subsequent process is, the useful and lost information cannot be retrieved (Duda and Hart 1973).

Dimensionality Reduction Techniques

One approach to consider with high dimensional data is to reduce the dimensionality by combining the features. Linear combinations are particularly attractive because they are easier to compute, and the physical interpretation of the data is easier. In effect, linear methods project the high dimensional data onto a lower dimensional space.

There are two classical methods for finding the effective linear projection of the data:

- Principal Component Analysis (PCA): seeks a projection of the data along the direction of highest variance.
- Multiple Discriminant Analysis (MDA): seeks a projection that best separates classes of data by minimizing a least squares objective function.

The above mentioned techniques were applied to the aggregate database to identify the underlying relations between aggregate features. The results, which will be presented in Chapter VI, also investigate the class separability information in the aggregate database. These techniques provide a means to assess the contribution of aggregate features to anisotropic behavior of aggregate systems purely from a mathematical standpoint and without introducing any prior knowledge on the physical sense of the data.

Principle Component Analysis (PCA)

Principle Component Analysis (PCA) is commonly used in high dimensional datasets as a dimensionality reduction tool. It is designed to capture the variance in a dataset in terms of principle components. In effect, one is trying to reduce the dimensionality of the data by summarizing the most important patterns of the data while simultaneously filtering out noise.

Duda defined the principal components as a set of variables that define a projection that encapsulates the maximum amount of variation in a dataset and is orthogonal (and therefore uncorrelated) to the previous principle component of the same dataset. Figure 5-2 shows an arbitrary example of projection the data on first and second principle components.

The major components act as Cartesian axes in the PC-Space. Hence, there is reduction in directionality of the dataset. Any direction that is not captured by the first principle component will be captured by the subsequent orthogonal PCs. By determining the eigenvectors of the covariance matrix, we are able to extract the lines (vectors) that characterize the data. The eigenvector with the highest eigenvalue is the principle component of the data set. This is similar to the process for determination of principal stresses in continuum mechanics where the principal stresses were found in the place where shear stress is zero (Duda et al. 2001).

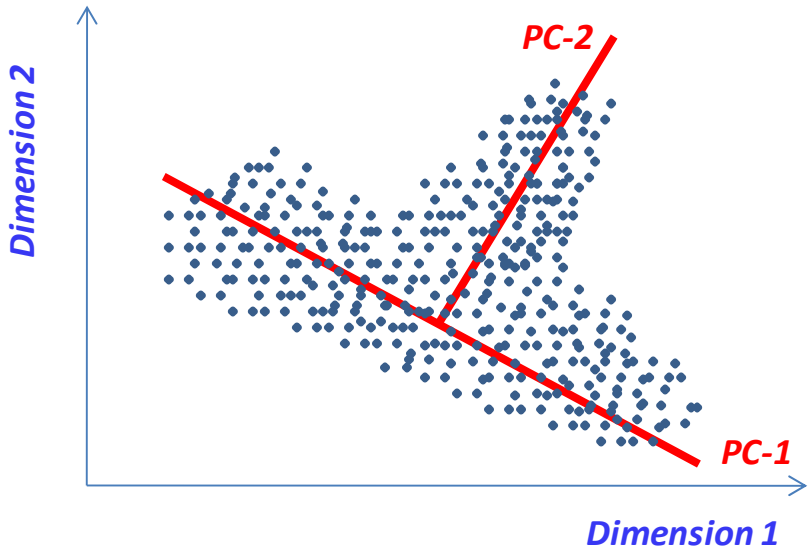

Figure 5-2 Projection of the data onto the first and second principle components

As illustrated in figure 5-2, major variation of the data (direction of the highest variance) is captured by PC-1 the first principle component that is the component with the highest eigenvalue and PC-2 the second principle component with second largest eigenvalue. These two components capture the dominant orientation of the dataset in two dimensional feature spaces. These two major directions are orthogonal.

Typically we are not aware of which features of the database best reflect the dynamics of the system, therefore we have to measure/calculate more features and therefore more dimensions, and consequently we need to consider measurement errors of extra dimensions. The objective of principal component analysis is to determine the most meaningful basis to re-express a noisy data set. The hope is that the new basis will filter out the noise of the data and reveal the structure of the dataset.

Determination of Principal Components

We consider the problem of representing all the vectors in a set of n d-dimensional samples x_1, ..., x_n by single vector x_0. In other words, we want to find a vector x_0 such that the sum of squares distances between x_0 and the various x_k is as small as possible. The least square objective function $J_0(x_0)$ is presented in equation 5-7 (Duda and Hart 1973).

$$J_0(x_0) = \sum_{k=1}^{n} \|x_0 - x_k\|^2 \tag{5-7}$$

We tend to find the value of x_0 that minimizes the objective function. Sample mean *m* presented in equation 5-8 is a potential candidate to minimize the least square objective function.

$$m = \frac{1}{n} \sum_{k=1}^{n} x_k \tag{5-8}$$

This can be verified by substituting the m value into objective function:

$$J_0(x_0) = \sum_{k=1}^{n} \|(x_0 - m) - (x_k - m)\|^2$$

$$= \sum_{k=1}^{n} \|(x_0 - m)\|^2 - 2\sum_{k=1}^{n} (x_0 - m)^T - (x_k - m) \; + \sum_{k=1}^{n} \|(x_k - m)\|^2$$

$$= \sum_{k=1}^{n} \|(x_0 - m)\|^2 - 2(x_0 - m)^T \sum_{k=1}^{n} (x_k - m) \; + \sum_{k=1}^{n} \|(x_k - m)\|^2$$

$$= \sum_{k=1}^{n} \|(x_0 - m)\|^2 + \sum_{k=1}^{n} \|(x_k - m)\|^2 \tag{5-9}$$

In equation 5-9 since the second term is independent of x_0, this expression is minimized by choosing x_0=m. The sample mean is a scalar value and will not provide information

about the direction of the scatter of dataset. Therefore, we tend to project the data onto a line that runs through the sample mean. Considering *e* to be the unit vector in the direction of this line, the general form of this equation can be written as:

$$x = m + ae \tag{5-10}$$

where *a* is the distance of any point from mean of the sample *m*. Now by replacing x_k into equation 5-9 we can find an optimal set of coefficients a_k that minimizes the least square objective function presented in equation 5-7.

$$J_1(a_1,...,a_n,e) = \sum_{k=1}^{n} \left\| (m + a_k e) - x_k \right\|^2 = \sum_{k=1}^{n} \left\| a_k e - (x_k - m) \right\|^2$$

$$= \sum_{k=1}^{n} a_k^2 \left\| e \right\|^2 - 2\sum_{k=1}^{n} a_k e^t (x_k - m) + \sum_{k=1}^{n} \left\| x_k - m \right\|^2 \tag{5-11}$$

Duda showed that by considering $\left\| e \right\| = 1$, differentiating with respect to a_k, and setting the derivative to zero we get:

$$a_k = e^T (x_k - m) \tag{5-12}$$

The geometric meaning of the equation 5-12 is that we found a solution for the least square objective functions. This solution represents a line that is the projection of the vector x_k onto a line in the direction of *e* that passes through the point *m* the mean of the dataset.

Duda showed the procedure for finding the best direction *e* for the solution line. He used the scatter matrix to find the direction of maximum variance. The definition of scatter matrix is presented in equation 5-13. As can be seen in equation 5-13, the scatter matrix is essentially the covariance matrix times (n-1).

$$S = \sum_{k=1}^{n} (x_k - m)(x_k - m)^T \tag{5-13}$$

Now by substituting a_k found from equation 5-13 into equation 5-9 we have:

$$J_1(e) = \sum_{k=1}^{n} {a_k}^2 - 2\sum_{k=1}^{n} {a_k}^2 + \sum_{k=1}^{n} \|x_k - m\|^2$$

$$= -\sum_{k=1}^{n} \left[e^T (x_k - m)\right]^2 + \sum_{k=1}^{n} \|x_k - m\|^2$$

$$= -\sum_{k=1}^{n} e^t (x_k - m)(x_k - m)^T e + \sum_{k=1}^{n} \|x_k - m\|^2$$

$$= -e^T S\, e + \sum_{k=1}^{n} \|x_k - m\|^2 \qquad (5\text{-}14)$$

Equation 5-14 suggests that in order to minimize the objective function we need to maximize the term $e^T Se$. Duda (2001) suggested the method of Lagrange Multipliers for maximizing $e^T Se$.

The Lagrange method suggests that we need to form the Lagrangian function presented in equation 5-15 to optimize function f(x) subject to constraint function g(x):

$$L(x, \lambda) = f(x) + \lambda\, g(x) \qquad (5\text{-}15)$$

In equation 5-15, λ is called the Lagrange undetermined multiplier. Taking the derivative of equation 5-15 with respect to x, the problem converts from constrained to unconstrained optimization.

$$\frac{\partial L(x, \lambda)}{\partial x} = \frac{\partial f(x)}{\partial x} + \lambda \frac{\partial g(x)}{\partial x} = 0 \qquad (5\text{-}16)$$

The Lagrange approach requires solving the above equation for λ and calculating the value of x that optimizes f(x).

Applying the above mentioned methodology we can maximize the term $e^T Se$ subject to constraint $\|e\| = 1$.

$$u = e^T Se - \lambda(e^T e - 1) \tag{5-17}$$

Differentiating with respect to *e* we have:

$$\frac{\partial u}{\partial e} = 2Se - 2\lambda e \tag{5-18}$$

Setting this gradient to zero we have:

$$Se = \lambda e \tag{5-19}$$

Equation 5-19 suggests that *e* must be the eigenvector of the scatter matrix. Therefore in order to maximize $e^T Se$ we need to select the eigenvector corresponding to the largest eigenvalue of the scatter matrix. In other words, to find the best projection of the data, we project the data onto a line that passes through the sample mean in the direction of the eigenvector of the scatter matrix with largest eigenvalue.

Duda showed that this analogy can be extended from one dimensional to d-dimensional projection by substituting equation 5-7 by equation 5-16 and the objective function as equation 5-18 (Duda et al. 2001).

$$x = m + \sum_{i=1}^{d} a_i e_i \tag{5-19}$$

$$J_d = \sum_{k=1}^{n} \left\| (m + \sum_{i=1}^{d} a_{ki} e_i) - x_i \right\|^2 \tag{5-20}$$

The objective function in d-dimensions is minimized when vectors e_1, e_2,…,e_d were considered as eigenvectors of the scatter matrix having the largest eigenvectors. Since the scatter matrix is real and symmetric, the eigenvectors are orthogonal. In d-

dimension, principal component analysis reduces the dimensionality of the feature space and restricts the focus to only those directions along which the scatter of the cloud of data is greatest.

Principal component analysis is a useful technique prior to performing k-means algorithms for pre-processing the data to identify the cluster structure of the aggregate database. More details on k-means clustering will be discussed later in this chapter.

Discriminant Analysis

In the previous section, principle component analysis was introduced as the data representation method. There is no reason to assume projecting the data onto its principle components will result in discriminatory information about the dataset as well. For this reason, discriminant techniques were developed to find the mapping that provides best class reparability between the data. In summary, principle component analysis seeks directions that are efficient for data representation by preserving the maximum variance of the data while discriminant analysis seeks directions that are efficient in identifying classes of data.

In order to find the projection of the data that results in the best classification rate, similar to the case of calculating principle components, we tend to project the d-dimensional data onto a line. Even for the well-compacted cloud of data (with no outliers) in d-space when projected onto a line, the resulted mapping will be confusing and provides poor recognition performance. However by moving and rotating the line around, we might be able to find a direction that provides class separability information among the data. This is the primary goal of performing discriminant analysis (Duda et al. 2001).

Similar to the principle component analysis, we assume that we have a set of n d-dimensional samples x_1 , x_2, …x_n. n_1 in the subset D_1 labeled as w_1, and n_2 in the subset D_2 labeled as w_2. The linear combination of the components of x can be presented as:

$$Y = W^T X \tag{5-21}$$

Equation 5-21 suggests that each y_i is the projection of the corresponding x_i onto a line in the direction of W. It should be noted here that in discriminant analysis the direction rather than the magnitude of W is desired.

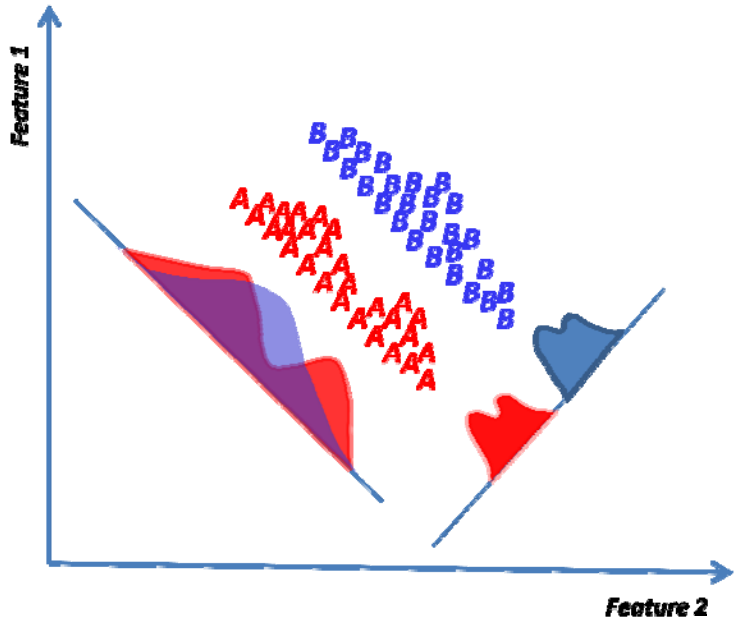

Figure 5-3 Data representation and data classification

Figure 5-3 shows the effect of choosing different directions for *w* to provide class discriminatory information for an arbitrary dataset in two dimensions. The graph on the right shows perfect separation between two sets of data presented with squares and circles.

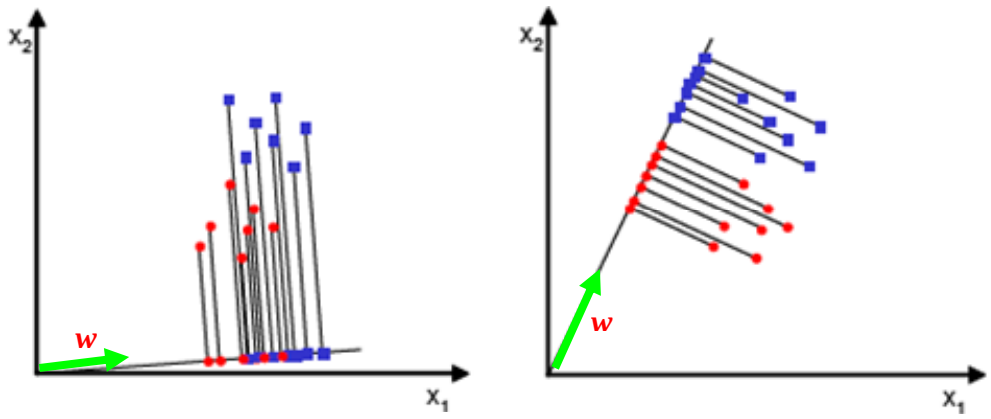

Figure 5-4 Projection of two sets of samples onto two different lines (After Gutierrez-Osana 2006)

Now we are able to find the orientation of *w* that provides the best classification between the data. There are number of methods to pursue this objective depending on the choice of objective function. In this study, we chose Fisher's Linear Discriminant (FDA) approach to find the best linear classifier. FDA uses distance between the means of the datasets as discriminatory criteria. Sample mean *m* in d-dimensions is presented in equation 5-22.

$$m_i = \frac{1}{n}\sum_{x \in D_i} x \tag{5-22}$$

The sample mean for the projected data is given by:

$$\tilde{m}_i = \frac{1}{n_i}\sum_{x \in D_i} y \tag{5-23}$$

$$= \frac{1}{n_i}\sum_{x \in D_i} W^T x = W^T m_i \tag{5-24}$$

The distance between the projected means can be found from equation 5-25.

$$\left|\tilde{m}_1 - \tilde{m}_2\right| = \left|W^T (m_1 - m_2)\right| \tag{5-25}$$

Equation 20 indicates that we can maximize the distance between the means by scaling the W. The objective here is to maximize the distances between the projected means of the data to obtain a good separation with some measure of standard deviations for each class of data. Rather than forming the covariance matrixes, in Fisher's method, two concepts of scatter are employed: within-class scatter and between-class scatter, which will be discussed separately in this chapter.

The scatter for the projected samples with class label w_i is given in equation 5-16:

$$\tilde{s}_i^2 = \sum_{y \in D_i} (y - \tilde{m}_i)^2 \tag{5-26}$$

Therefore, $\frac{1}{n}(\tilde{s}_1^2 + \tilde{s}_2^2)$ is an estimate of the variance within data set. Fisher's linear discriminant analysis tends to minimize the $(\tilde{s}_1^2 + \tilde{s}_2^2)$ which is the within class scatter while maximizing the distance between the projected means (between class scatter) $\left|\tilde{m}_1 - \tilde{m}_1\right|^2$. Therefore, the criterion function in Fisher's Linear Discriminant analysis can be written as:

$$J(w) = \frac{\left|\tilde{m}_1 - \tilde{m}_1\right|^2}{\tilde{s}_1^2 + \tilde{s}_1^2} \tag{5-27}$$

Now we need to find vector (w) that maximizes the criterion function J(w). In order to obtain this vector, we define a scatter matrices S_i as:

$$S_i = \sum (x - m_i)(x - m_i)^T \tag{5-28}$$

Within class scatter, matrix S_w for two classes of data can be presented as:

$$S_W = S_1 + S_2 \tag{5-29}$$

It can be seen that the within class scatter, matrix is proportional to the covariance matrix of the pooled data.

Now by projecting the data along the vector (w), we have:

$$\widetilde{S}_i = \sum (w^T x - w^T m_i)^2 \tag{5-30}$$

$$= \sum w^T (x - m_i)(x - m_i)^T w = w^T S_i w \tag{5-31}$$

The sum of the scatters can be written as:

$$\widetilde{S}_1^2 + \widetilde{S}_2^2 = w^T S_w w \tag{5-32}$$

The same concept can be applied to projected means as:

$$(\widetilde{m}_1 - \widetilde{m}_2)^2 = (w^T m_1 - w^T m_2)^2 \tag{5-33}$$

$$= w^T (m_1 - m_2)(m_1 - m_2)^T w \quad = w^T S_B w \tag{5-34}$$

where S_B is the between class scatter and is always in the direction of $(m_1\text{-}m_2)$,

$$S_B = (m_1 - m_2)(m_1 - m_2)^T \tag{5-35}$$

Now we can re-write the objective function J(w) in terms of within class and between class scatter matrices:

$$J(w) = \frac{w^T S_B w}{w^T S_W w} \tag{5-36}$$

This expression is well known in mathematics as the Rayleigh quotient. The general form of the Rayleigh quotient for the real matrix A and real vector *w* is presented at equation 5-37:

$$R(A, w) = \frac{w^T A w}{w^T w} \tag{5-37}$$

The significance of this measure is that critical values (maximum and minimum of the Rayleigh quotient) happens at eigenvectors of the A matrix (Duda and Hart 1973). The other important property of the Rayleigh quotient is that the maximum of Rayleigh quotient equals the largest eigenvalue of the A matrix, and the minimum of the quotient is the smallest of the eigenvalues of A. In other words, an optimization problem resembling the Rayleigh quotient boils down to finding the eigenvalues and eigenvectors of the A matrix. The largest eigenvalue is the maximum of the Rayleigh quotient while the smallest eigenvalue gives the minimum of the Rayleigh quotient (Duda et al. 2001).

Considering this helpful property, we can now find the vector *w* that maximizes the objective function J(w). Duda showed that according to the Rayleigh quotient for nonsingular S_w, optimization of Fisher's Linear Discriminant function becomes a conventional eigenvalue problem as:

$$S_w^{-1} S_B w = \lambda\, w \tag{5-37}$$

As discussed earlier, in LDA analysis we are only interested in the direction of the *w* to find the projection that provides higher separation between the classes of the data. Considering the fact that $S_B w$ is always in the direction of $(m_1\text{-}m_2)$ as indicated by equation 29 and also the fact that we are only interested in the direction of the vector w, equation 33 can be written as:

$$w = S_w^{-1}(m_1 - m_2) \tag{5-38}$$

Thus, the direction that gives the maximum ratio of between class scatter to within class scatter can be calculated using equation 5-38.

Figure 5-5 schematically illustrates 2D projections of three distributions (clouds of data) onto two subspaces described by normal vectors w_1 and w_2. As evidenced in figure 5-5, the subspace with normal w_1 was able to provide discriminatory information about the datasets.

Fisher's Linear Discriminant is used later in this chapter to identify aggregate features that provide best class separability in supervised and unsupervised analysis of the data.

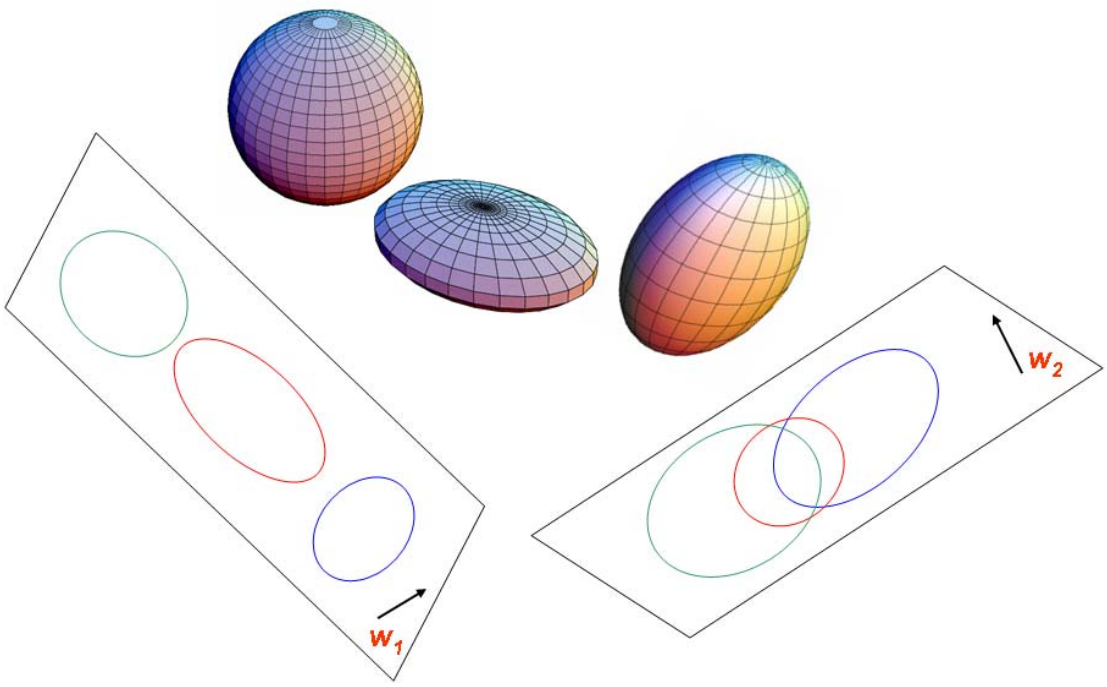

Figure 5-5 Projection of three-dimensional distributions onto two subspaces (Duda et al. 2001)

K Nearest Neighbor (KNN)

Another widely used method for classification of data is k-nearest neighbor algorithm. Osana defined KNN as an intuitive rule that classifies the unlabeled examples based on their similarity in the training dataset. In other words, the class of the data is labeled by a majority vote of its neighbors, for this reason in binary (two class) classification problems; it is helpful to choose *k* to be an odd number as this avoids tied votes. In KNN algorithm, the class of a new data point introduced to the system is identified by the pre-known class of its k-nearest data points. *k* is a positive integer, typically smaller than 10. If $k = 1$, then the data point is simply assigned to the class of its nearest neighbor.

Figure 5-6 illustrates the classification method using k-nearest neighbor. Three classes of data labeled with w_1, w_2, and w_3 were perceived in this figure. The objective was to classify the new data point X_u based on Euclidian distance. The k value is assumed to be 5 for this example, which means the classification determined is based on the pre-labeled class of 5 nearest neighbors. Since 4 of the 5 nearest points shown in figure 5-6 belong to w_1, the new data point X_u is also classified as w_1.

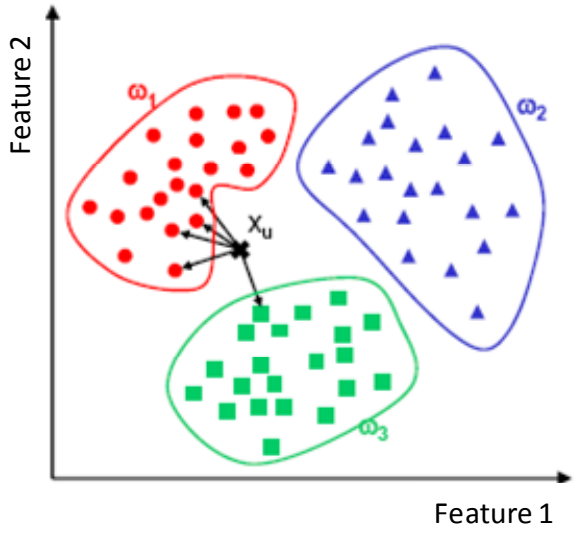

Figure 5-6 Schematic representation of k-nearest neighbor approach (After Gutierrez-Osana 2006)

CHAPTER VI

PLASTIC DEFORMATION AND RUTTING PERFORMANCE OF PAVEMENT FOUNDATIONS

BACKGROUND

The main role of aggregate layers is to protect the subgrade soils from rutting and reduce the bending stresses at the bottom of the hot mix asphalt. Aggregate layers also provide proper platform for construction of the surface layer. Pavement foundations become prone to rutting when the stresses induced by traffic load exceed the characteristic load of the unbound layers. Characteristic load is defined as the load beyond which geomaterials are prone to develop plastic deformations. In other words the characteristic load defines the boundary for stress levels that are within the tolerable range by geomaterials.

The distress identification manual defines rutting as a longitudinal surface depression in the wheel path and states that rutting may have associated transverse displacement (Miller and Bellinger 2003) . Rutting in pavement systems can be caused by non-homogeneous deformation in any or all of the pavement layers, therefore proper protocol needs to be employed to calculate deformations of each layer to determine the total rutting in the pavements.

PLASTIC DEFORMATION MECHANISMS IN PAVEMENTS

The mechanism of permanent deformation can be explained with the concept of energy dissipation in the unbound layers. When the aggregate layer is subjected to traffic loads there is an input flow of energy in the system. For perfectly elastic materials this energy will be recovered when the unloading occurs. For geomaterials however, the remainder of the energy that is not recovered is capable of doing work on the material. This work manifests itself in densification under the load or as transverse movement. In particular,

in the case of geomaterials, most of the work goes into non-recoverable deformations under the traffic load. It is this densification, slippage, and rotation of the aggregate particles that causes rutting in aggregate layers.

In another approach, rutting mechanism and sources of plastic deformations in different pavement layers can be placed in three major categories as:

- Shear rutting: this type of rutting occurs both in unbound layers and hot mix asphalt. Inadequate surface stiffness or surface thickness will result in a lateral spread of HMA. Thin asphalt layers are more prone to develop shear deformations at summertime when the surface temperatures are high. The lateral spread of HMA is exacerbated at the bends where the shear forces induced by tires are typically higher. The other source of high shear forces in pavements is at intersections where the likelihood of rapid deceleration is higher. Overstressing the UAB will also cause deformations due to shear failure in aggregate layers. We will discuss protocols to control the shear stability of the aggregate systems later in this chapter.
- One dimensional densification: this type of rutting manifests itself as a depression at the center of the wheel path without an accompanying heave at the sides of the track. This type of rutting is basically due to inadequate compaction of the unbound layers or excess air voids in the HMA, therefore allowing the layers to compact under the traffic load.
- Transverse spread: this type of rutting is observed along the wheel path when depression at the centerline of the wheel path is accompanied by heaves at the sides. This type of distress is typically due to inadequate shear strength or excess air voids of the surface layer.

CHARACTERIZATION OF PLASTIC DEFORMATIONS

Characterization of unbound aggregate layers has long been a challenge for pavement engineers. In order to mechanistically characterize the rutting potential of unbound layers, we initially need to characterize the resilient properties of the aggregate systems. Repeated load permanent deformation testing is typically used to study the deformation behavior of aggregate layers under the representative stress paths in the lab. The second challenge would be to develop proper plastic deformation models and to adopt suitable protocols to mechanistically characterize the rutting potential and to calculate the plastic deformation in unbound aggregate layers.

In the previous chapter, we extensively discussed the protocols and models for determination of the resilient properties of aggregate systems. In this chapter however, we will discuss the permanent deformation models to determine and identify the likelihood of failure and rutting potential in geomaterials.

There three major techniques identified in the literature to characterize permanent deformation in pavement systems:

The first approach considers calculation of plastic deformation in each layer and then sums the rut depths in each layer to determine the total deformation at pavement surface. The VESYS model uses this approach to calculate the total rut depth in the pavements.

The second technique is to define a threshold and limit the responses under the wheel load such as vertical strain in the unbound granular layers. Pavement life prediction models also known as transfer functions developed by Asphalt Institute uses this approach.

The third approach is to control the stability of the aggregate layers and subgrade. The idea behind this approach is to ensure that stress states are within the tolerable limit. This boundary is typically defined by a failure function. TXDOT uses Mohr-Coulomb

failure function to ensure enough cover is present to protect the subgrade soil subjected to the average of the 10 heaviest wheel loads (ATHWL).

In the following section we will initially discuss selected permanent deformation models and later discuss the protocols to assess the stability of aggregate layers. This type of protocol provides a means as to control the design and assess the likelihood of failure in pavement foundations.

RUT DEPTH MODELS

Mechanistic Empirical Design Guide (MEPDG)

Determination of plastic deformation in the unbound granular materials in the new design guide is based on the Tseng-Lytton model. This expression is presented in equation 6-1.

$$\Delta_a(N) = \beta k_{s_1} \varepsilon_v h \left(\frac{\varepsilon_0}{\varepsilon_r} \right) e^{-\left(\frac{\rho}{N}\right)^{\beta}} \quad (6\text{-}1)$$

where:

$\Delta_a(N)$= Permanent deformation for granular layer

β, ε_0 and ρ = Material parameters

N= Number of load applications

k_{s1}= Global calibration coefficients (k_{s1}=1.673 for granular materials and k_{s1}= 1.35 for fine-grained soils)

ε_v= Average vertical resilient strain found from the primary response model

h= Thickness of the aggregate layer

ε_r= resilient strain imposed in the lab to find the model parameters

Equations 6-2 through 6-7 provide empirical relationships to estimate parameters of the model based on the stress states, moisture states, and resilient properties for granular and fine-grained soils.

$$\log\left(\frac{\varepsilon_0}{\varepsilon_r}\right) = 0.80978 - 0.06626W_c - 0.003077\sigma_\theta + 0.000003E_r \quad (6\text{-}2)$$

$$\log\beta = -0.9190 - 0.03105W_c + 0.001706\sigma_\theta - 0.0000015E_r \quad (6\text{-}3)$$

$$\log\rho = -1.78667 + 1.45062W_c + 0.0003874\sigma_\theta^2 - -0.002074W_c^2\,\sigma_\theta - 0.00000105E_r \quad (6\text{-}4)$$

where:

Wc= Water content,%

σ_θ= Bulk stress, psi

σ_d= Deviator stress, psi

E_r=Resilient modulus, psi

The expressions for fine-grained soils are:

$$\log\left(\frac{\varepsilon_0}{\varepsilon_r}\right) = -1.69867 - 0.09121W_c - 0.11921\sigma_\theta + 0.91219\log E_r \quad (6\text{-}5)$$

$$\log\beta = -0.9730 - 0.0000278W_c^2\sigma_d + 0.017165\sigma_d - 0.0000338W_c^2\sigma_\theta \quad (6\text{-}6)$$

$$\log\rho = 11.009 + 0.000681W_c^2\sigma_d + 0.40260\sigma_d - 0.0000545W_c^2\sigma_{\theta r} \quad (6\text{-}7)$$

Ayres Model for Subgrade Soils and Embankments

Ayres characterized the subgrade soils as elastic half-space material and suggested using equation 6-8 for calculation of plastic strains under the traffic load (Ayres and Witczak 1998).

$$\varepsilon_p(z) = (\varepsilon_{p,z=0})e^{-k\,z} \tag{6-8}$$

where:

ε_p (z) = plastic strain at depth z (measured from the top of the subgrade), in/in

$\varepsilon_{(p,z=0)}$ = Vertical plastic strain at the top of the subgrade, in/in

z= Depth measured from the top of the subgrade

k= Model parameter found from regression analysis

Ayres suggested a limiting value for the model parameter k to be greater than 0.000001 to prevent the assumption that plastic strains decrease with depth from being violated. He reported coefficient of correlations values R^2 greater than 0.97 when using this model. The total permanent deformation due to non-homogeneous settlement of the subgrade soils and embankments can be found from solving integrals presented in equations 6-9 and 6-10.

$$\delta_{SG} = \int_0^h \varepsilon_p(z)\,dz \tag{6-9}$$

$$\delta_{SG} = \varepsilon_{p,z=0}\int_0^h e^{-k\,z}dz = \left[\frac{1-e^{-k\,h}}{k}\right]\varepsilon_{p,z=0} \tag{6-10}$$

where:

δ_{SG}= Total plastic strain at the top of the subgrade, in

h= Depth to the bedrock, in

WesTrack Model

The model resulting from the WesTrack project predicts the rut depth in unbound granular layers as presented in equation 6-11 (Team 2000).

$$RD_{UAB} = \frac{0.14}{\left[1.05\times10^{-9}(\varepsilon_v)_{UAB}^{-4.484}\right]^{0.372}}(N)^{0.372} \quad (6\text{-}11)$$

where:

RD_{UAB}= Rut depth of unbound aggregate base layer

$(\varepsilon_v)_{UAB}$= Vertical plastic strain at the top of granular layer

N= Number of load applications to failure

Layered Plastic Strain Models

In this approach, the plastic strain for each individual layer is calculated as a function of the number of repeated load applications. The calculated plastic strain is in turn multiplied by the layer thickness to determine the permanent deformation in each layer. The permanent deformations of different layers are then summed up to determine the total rut depth for the entire pavement profile.

Barenberg and Thompson studied several models relating the plastic strain and number of load applications and concluded that models relating the logarithm of plastic strain at the top of surface layer to logarithm of number of load applications are most appropriate (Barenberg and Thompson 1992). Equation 6-12 presents the general form of this type of equation.

$$\log(\varepsilon_p) = a + b\,[\log N] \quad (6\text{-}12)$$

where:

ε_p= Plastic strain

N= Number of load applications

a and b= Model parameters

Plastic-Elastic Strain Ratio Models

Similar to layered plastic strain models, plastic-elastic strain ratio models are used to predict the deformation of each layer individually and then add them up to determine the total rut depth at the surface of the pavement. This model is primarily based on the statistical analysis performed on data obtained from repeated load permanent deformation test. This model tends to estimate the plastic strain as a percentage of the resilient strain in each layer. The general form of this model is presented in equation 6-13.

$$\frac{\varepsilon_p}{\varepsilon_r} = a N^b \tag{6-13}$$

where:

ε_p= Plastic strain

ε_r= Resilient strain

a and b= Model parameters

Uzan developed a plastic deformation prediction model for characterization of cumulative rutting in the unbound aggregate layers based on elastic-plastic strain ratio concept (Uzan 2004) . Uzan's deformation model is presented in equation 6-14.

$$\log\frac{\varepsilon_p}{\varepsilon_r}=\left[a_0+a_1\left[\frac{\theta+k_6}{Pa}\right]+a_2\left[\frac{\tau_{oct}}{Pa}\right]\right]+\left[b_0+b_1\left[\frac{\theta+k_6}{Pa}\right]+b_2\left[\frac{\tau_{oct}}{Pa}\right]\right].\log N \quad (6\text{-}14)$$

where:

θ=Bulk stress, psi

τ_{oct}=Octahedral shear stress

Pa=Atmospheric pressure, 14.5 psi

a_i ,b_i, and k= Model parameters

N= Number of load applications

Permanent Strain Rate Approach

An alternative mathematical formulation to calculate the plastic strain developed in individual layers is called strain rate approach. This model tends to calculate the nonrecoverable component of strain tensor in each load cycle. The mathematical model used to calculate the plastic strain per load repetition, ε_{pn}, is presented in equation 6-15.

$$\frac{\partial\varepsilon_p}{\partial N}=\varepsilon_{pn}=\frac{\partial(aN^b)}{\partial N}=a\,b\,N^{b-1} \quad (6\text{-}15)$$

This model assumes that the resilient strain developed in each load cycle is independent of the number of load application N, therefore equation 14 can be written as:

$$\frac{\varepsilon_{pn}}{\varepsilon_r}=\left[\frac{ab}{\varepsilon_r}\right]N^{b-1} \quad (6\text{-}16)$$

Now by assuming $\mu=\frac{ab}{\varepsilon_r}$ and α=1-b we can write equation 6-16 as:

$$\frac{\varepsilon_{pn}}{\varepsilon_r} = \mu\, N^{-\alpha} \tag{6-17}$$

where:

μ= Constant of proportionality between resilient strain and permanent strain at Nth load repetition

α= Permanent deformation parameter indicating the rate of decrease in permanent deformation as the number of load applications increases

This type of formulation became very popular for determination of plastic deformation of HMA as well as unbound aggregate layers. VESYS and Ohio State models were basically developed based on this concept. VESYS model assumes the relationship between number of load applications and plastic strains are linear in logarithmic scales, therefore a general power law such as equation 6-17 will provide proper representation of deformation behavior of pavement layers subjected to cyclic loading.

Figure 5-1 shows the sensitivity of plastic strains to stiffness properties of pavement layers. Twenty permutations of pavement profiles with different asphalt and base layer modulus values were assumed to develop this plot. Resilient strains were calculated using anisotropic solutions and total plastic strains were calculated using the VESYS model. This plot clearly emphasizes the importance of stiffness properties of each layer on the calculated rut depth. This plot shows pavement systems with higher surface modulus values have better performance in terms of lower plastic strains. Same trend is valid for pavement profiles with stiffer unbound aggregate layers.

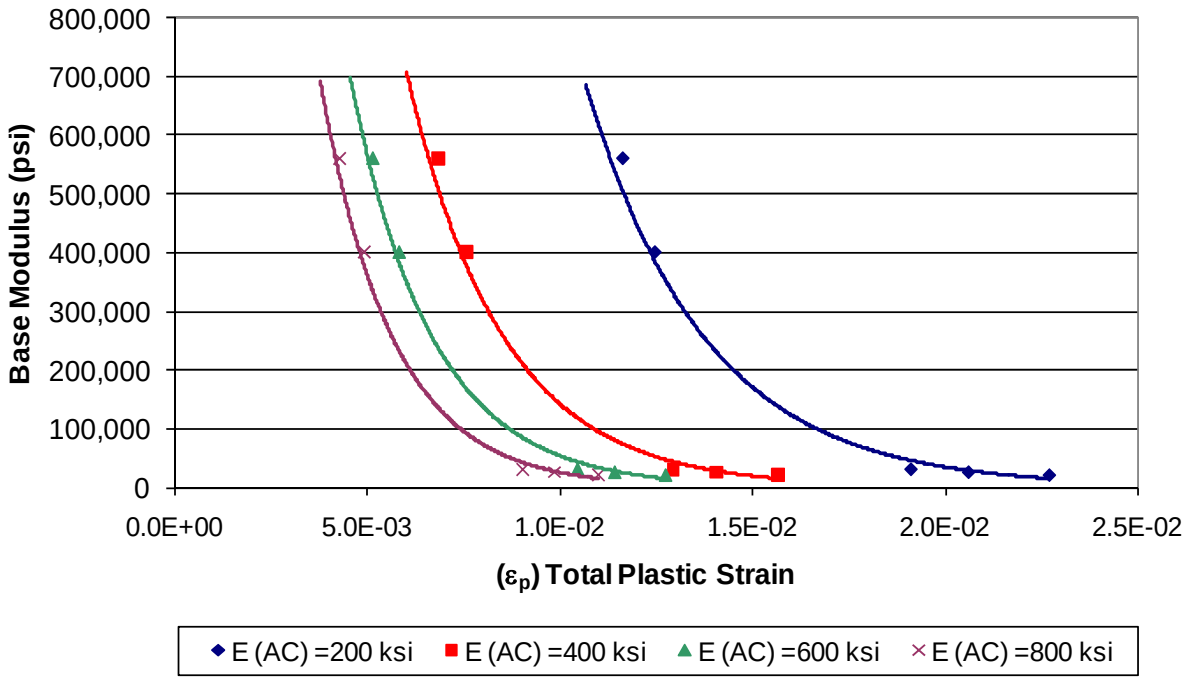

Figure 6-1 Sensitivity of plastic strain to asphalt and base modulus

THRESHOLD METHODS

Limiting Vertical Compressive Strain Approach

This approach relates the number of load applications to failure to stiffness properties and responses of unbound layers subjected to moving wheel loads. The rationale behind these models is to ensure enough cover is present to protect the subgrade layer throughout the expected pavement life. Therefore these models cannot be used to predict the plastic deformations at the top of the subgrade as discussed in previous models.

This type of approach assumes that most of the plastic deformation measured at the pavements surface is due to subgrade deformations, and rutting in structural layers is negligible. The general form of this type of model is presented in equation 6-18.

$$N_d = \beta\, f_1 (\varepsilon_v)^{f_2} (M_R)^{f_3} \qquad (6\text{-}18)$$

N_d= Number of load applications to subgrade failure

f_1, f_2, and f_3=Regression constants

M_R=Resilient modulus of the subgrade soil, psi

ε_v= Plastic strain at the top of the subgrade, in/in

Barker and Brabston used this approach to develop the first generation of limit strain models for the corps of engineers in 1975. In the original formulations, the number of load applications to failure was directly related to the vertical plastic strain at the top of the subgrade (Barker and Brabston 1975). Later Rauhut modified Barkers' equation by considering the effect of subgrade modulus as (Rauhut et al. 1984):

$$N_d = 1.259 \times 10^{-11} (\varepsilon_v)^{-4.082} (M_R)^{0.955} \quad (6\text{-}19)$$

Extensive field studies by several research organizations such as the Asphalt Institute, Belgium Road Research Center, Shell International, and others performed to calibrate this model. The general form of the model that relates the number of load applications to subgrade distortion to vertical compressive strain at the top of the subgrade is presented in equation 6-20.

$$N_d = f_4 (\varepsilon_v)^{f_5} \quad (6\text{-}20)$$

Table 5- 1 presents the model parameters based on deflection tolerance and reliability levels in previous studies.

Table 5-1 Model Parameters and Allowable Rut Depth for Plastic Deformation Models

Organization	Model Parameter		Allowable Rut Depth
	f_4	f_5	(in)
Asphalt Institute	1.365×10^{-9}	4.477	0.5
Shell			0.5
50% reliability	6.15×10^{-7}	4.0	0.5
85% reliability	1.94×10^{-7}	4.0	0.5
95% reliability	1.05×10^{-7}	4.0	0.5
Transport and Road Research Lab (TRRL)	6.18×10^{-8}	3.95	0.4
Belgium Road Research Center	3.05×10^{-9}	3.95	0.4

As previously mentioned in this section, the idea behind this type of model is that the pavement can sustain N_d number of load applications if the plastic strain on the top of the subgrade is smaller than a limited value. This model ignores any deformations in the asphalt and granular based layer, which is not a realistic assumption.

Limiting Modular Ratios

This method assumes a limiting value for the modulus of unbound aggregate layer and the adjacent granular layers. This approach limits the value of the unbound aggregate layer based on the stiffness properties of the supporting layer. The rationale behind this approach is that high tensile stresses are developed at the bottom of the unbound layer when the modular ratios of consecutive layers exceed a limiting value. Corps of engineers' pavement design manual developed by Barker suggests this limiting value to be 3 (Barker and Brabston 1975). The authors argued that if the modular ratios exceed this value the unbound aggregate base will decompact under the traffic load leading to pavement deterioration.

This discrepancy is basically due to modeling the unbound aggregate layers as isotropic materials. As comprehensively discussed in previous chapters, cross anisotropic characterization of aggregate bases will result in a reduction or elimination of high tensile

stresses at the bottom of the granular base layer calculated using isotropic solutions. Therefore assuming isotropic behavior for modeling particulate systems where directional dependency of material properties is significant is not a proper assumption in the first place.

Figure 6-2 presents the design chart developed by Barker for the corps of engineers' design manual based on modular ratios approach.

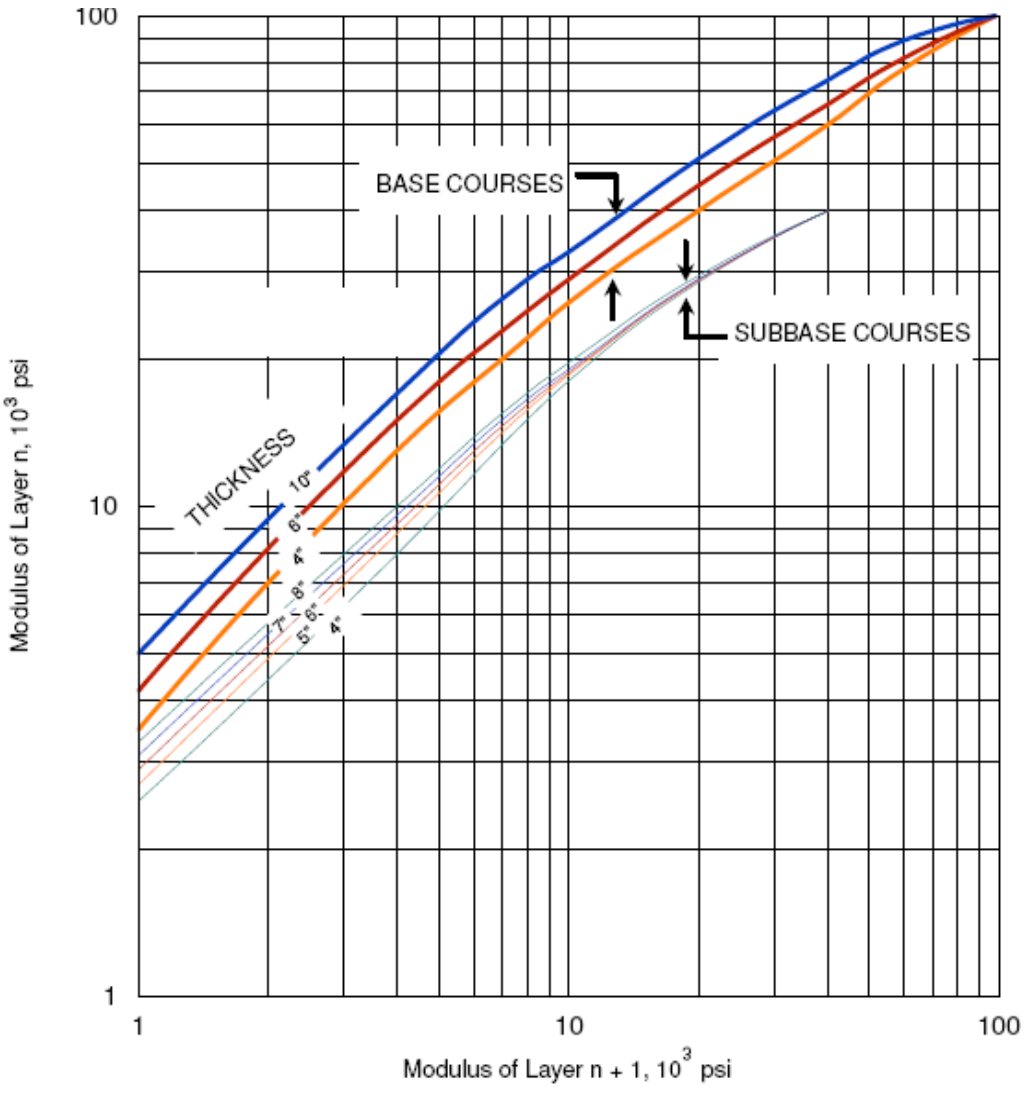

Figure 6-2 Limiting modular ratios concept for successive granular layers (Barker and Brabston 1975)

Safety Factor Method

The rationale behind the safety factor method is to define a limit for the ratio of a measure of shear stresses such as deviatoric stress to a measure of shear strength such as unconfined compressive strength in geomaterials. South Africa and the University of Illinois use this concept to ensure the stability of granular systems, which will be discussed in this section.

South African Approach

Theyse introduced the concept of the safety factor in the South African mechanistic design approach. The safety factor essentially defines a limiting threshold for the ratio shear stresses induced by wheel loads and shear strength of the material determined in the lab. In other words, safety factor is used as a stability control criteria for aggregate layers by limiting the shear stresses induced by traffic loads to a fraction of the shear strength of the aggregate layer (Theyse et al. 1996).

$$SafetyFactor = \frac{ShearStrength}{ShearStress} \tag{6-21}$$

This limit is believed to define a boundary below which the stability of the system is assured. Maree stated that aggregate layers for which the material properties and stress combinations result in safety factors below a certain value, the plastic deformation increases rapidly even under few loading cycles (Maree 1978). On the other hand, when the safety factor is above the cutoff limit, the rate of accumulation of plastic deformation is relatively constant. More explanations on the rate of accumulation of the plastic deformation will be presented in the shakedown section.

The safety factor criteria employed by the South African Design methodology is based on the Mohr-Coulomb theory (Theyse and Transportek 2002). Figure 6-3 is the graphical representation of this approach. Equation 16 presents the relationship for determination of the safety factor in South African Design.

$$F = \left[\frac{\sigma_3 K \left[\tan^2 (\frac{\pi}{4} + \frac{\varphi}{2}) - 1 \right] - 2c K \tan (\frac{\pi}{4} + \frac{\varphi}{2})}{\sigma_1 - \sigma_3} \right] \quad (6\text{-}22)$$

where:

F= Safety factor

c=Cohesion (psi)

ϕ= Angle of internal friction

σ_1= Vertical stress (psi)

σ_3=Horizontal stress (psi)

K= Constant, 0.95 for optimum moisture condition, 0.8 for moderately saturated condition, and 0.65 for fully saturated condition.

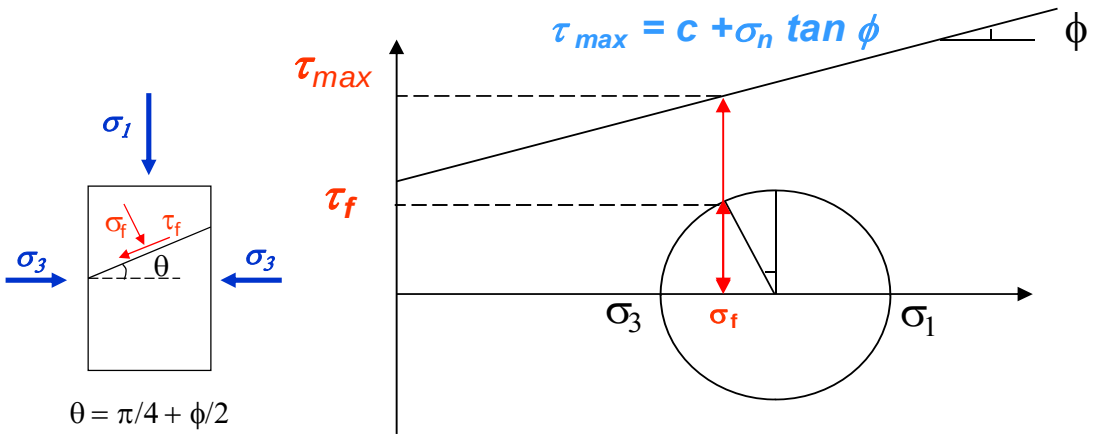

Figure 6-3 Representation of the safety factor approach using the Mohr-Coulomb theory

Thompson reported that the value of the safety factor is also a function of surface temperature (Thompson 1999). Due to the softening effect of temperature, they found that safety factor has its smallest value at summer times when the asphalt surface is softer and therefore granular base layer is subjected to more demanding stress states. Therefore environmental conditions such as surface temperature and moisture state in the granular layer should be considered.

University of Illinois Method

University of Illinois adopted the inverse of the safety factor as a criterion to control the stability of granular layers (Tutumluer and Kim 2003). This ratio is presented in equation 6-23.

$$Shear\ Strength\ Ratio = \frac{Shear\ Stress}{Shear\ Strength} = \frac{\tau_f}{\tau_{\max}} \tag{6-23}$$

This ratio can be found using equations 18 to 20.

$$\tau_{\max} = c + \sigma_n \tan\varphi \tag{6-24}$$

$$\sigma_f = \frac{2\sigma_3 + 2\sigma_3 \tan^2\varphi + \sigma_d + \sigma_d \tan^2\varphi - \sqrt{\sigma_d^2 \tan^2\varphi + \sigma_d^2 \tan^4\varphi}}{2(1+\tan^2\varphi)} \tag{6-25}$$

$$\tau_f = \sqrt{(\frac{\sigma_d}{2})^2 - \left[(\sigma_f - (\sigma_3 + \frac{\sigma_d}{2})\right]^2} \tag{6-26}$$

where:

σ_1 and σ_3 =Vertical and horizontal stresses, respectively, psi

σ_d= deviatoric stress, psi

C=Cohesion, psi

ϕ= angle of internal friction

Kim reported that a limiting value of the ratio of the shear stress to shear strength controls the permanent deformation behavior of aggregate layers (Tutumluer and Kim 2003). This is essentially the same concept employed by Thomson in NCHRP 1-26 to characterize the rutting potential of subgrade soils in 1990. In the NCHRP 1-26 study, Thompson used the deviatoric stress as a measure of shear stress and unconfined compressive strength as a measure of shear strength for fine-grained soils. He showed that rutting performance of pavement systems with a shear strength ratio less than 0.4 was acceptable (Thompson 1990a).

Table 5-2 presents the provisions for range of shear strength ratios in the lab. Four levels of shear strength ratios of 0.3, 0.5, 0.7, and 0.9 at four confinement levels of 3, 5, 10, and 15 psi were considered in the protocol to fully characterize the plastic deformation behavior of unbound aggregate layers in the lab. This means that aggregate samples should be subjected to shear stresses up to 90 percent of their shear strength. The test is essentially a constant confining pressure type stress path test at three confinement levels and for 10,000 load cycles. This protocol recommends performing additional variable confining pressure stress path tests (VCP) with slopes of zero and -1 after completion of the CCP type stress path tests.

Table 5-2 Stress States and Strength Ratios Recommended by UIUC Protocol

Confining Pressure (σ_3), psi	**Shear Strength Ratio (τ_f/τ_{max})**	**Deviator Stress (σ_d), psi**
3	0.3,0.5,0.7,0.9	Found from equation 18 to 20
5	0.3,0.5,0.7,0.9	
10	0.3,0.5,0.7,0.9	
15	0.3,0.5,0.7,0.9	

Shakedown Method

Several researchers applied the shakedown theory to characterize the rutting behavior of unbound geomaterials used in pavement foundations. Figure 6-4 schematically represents behavior of different geomaterials under cyclic loading.

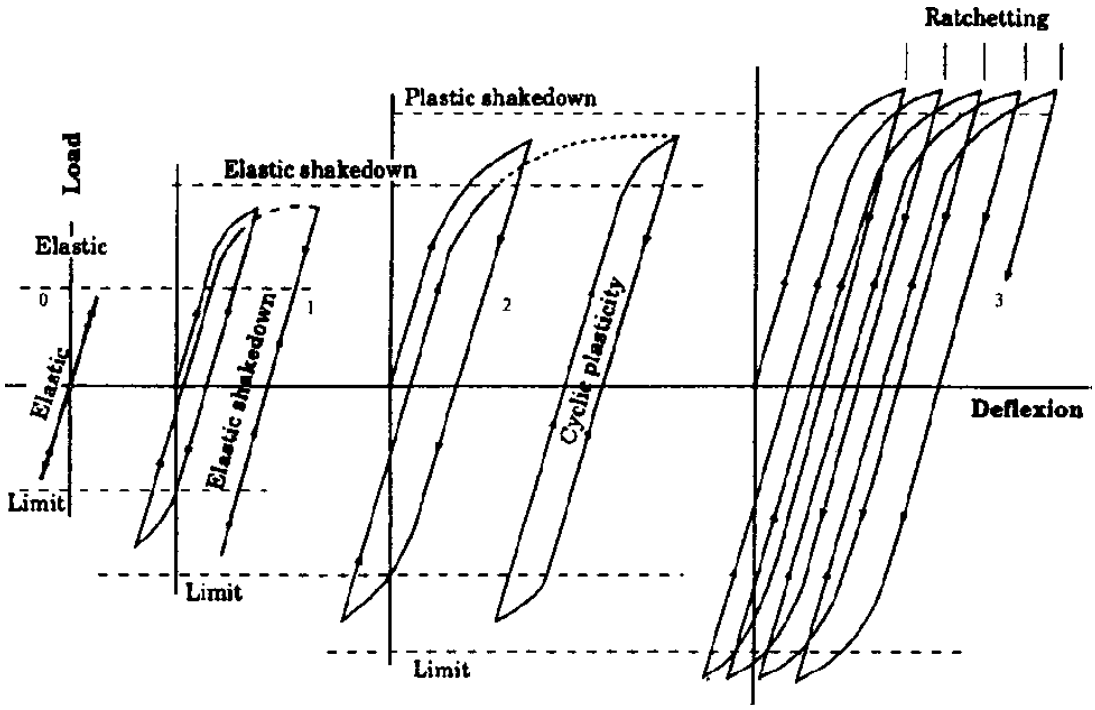

Figure 6-4 Classical elastic-plastic shakedown behavior under cyclic loading (Johnson and Wallis 1986)

According to shakedown theory, permanent deformation behavior of unbound aggregate layers subjected to repeated load testS can be categorized into three major categories as follows:

- Plastic shakedown limit: below this threshold the incremental plastic strain per load cycle decreases with increasing load cycles and finally approaches zero. In other words the deformation-number of load application curve reaches an asymptotic value. As illustrated in figure 6-5, plastic strains rate at this stage is high for initial cycles, and the response behavior becomes fully resilient.

- Plastic creep limit: below this threshold the plastic deformation rate of geomaterials reaches a constant value at high load repetitions. The initial behavior of aggregate systems are the same as plastic shakedowns while in plastic creep after a high number of load applications the slope of the curve becomes constant. This behavior is depicted in figure 6-5. As illustrated in this figure, the plastic creep limit can also be used as a boundary to identify the stress states or number of load applications that causes instability in aggregate layers.
- Incremental collapse limit: above this threshold the incremental plastic strain per load cycle increases significantly as load cycles increase. Aggregate systems at this stage experience an exponential increase in plastic deformation and develop severe rutting.

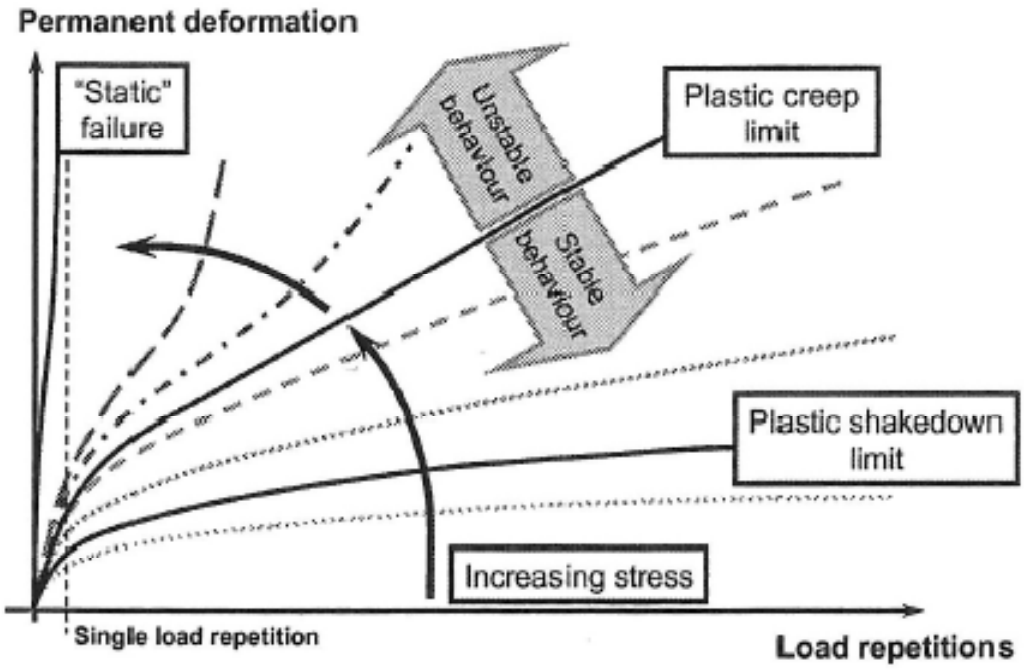

Figure 6-5 Application of shakedown theory for characterization of permanent deformation in unbound aggregate layers (Theyse et al. 2007)

It is worth mentioning that the Shakedown approach in essence is a method for clustering the permanent deformation of geomaterials subjected to cyclic loading based on a plastic strain rate and does not give the rut depth. This method can also be used as a stability control for unbound aggregate layers as well as the subgrade soils.

TXDOT Approach

Texas Department of Transportation (TXDOT) developed a methodology to control the stability of the subgrade soils subjected to super heavy loads. TXDOT considers gross vehicle weights ranging from 1112 KN to above 8896 KN as super heavy loads. These loads include industrial equipment and machinery such as dragline components, off-shore pipe laying equipments, oil pressure vessels, and electric transformers. Due to the fact the supper heavy load permit applications have increased significantly during the recent years, TXDOT needs to check if the existing pavement is structurally adequate to withstand the supper heavy load. The idea behind this approach is to check if enough cover is present above the subgrade so that the stresses are in a tolerable level, and the pavement foundation is protected against rutting (Fernando 1997).

In order to control the stability of the subgrade layer, the pavement response under the super heavy load is calculated. TXDOT procedure employs an incremental, isotropic, nonlinear, layered, and elastic approach to model the unbound aggregate layers. The calculated stresses at the top of the subgrade were in turn used as input to Mohr-Coulomb yield criterion to evaluate the stability of the pavement subjected to a super heavy load. Yield criterion can be expressed as the limit of elastic deformations defined by a combination of stress states (Desai et al. 1987). The Mohr-Coulomb yield function in terms of stress invariants is presented in equation 6-27.

$$f = \frac{I_1}{3}\sin\varphi + \sqrt{J_2}\,\sin(\theta + \frac{\pi}{3}) + \frac{\sqrt{J_2}}{3}\cos(\theta + \frac{\pi}{3})\sin\varphi - c\cos\varphi \qquad (6\text{-}27)$$

where:

$$\cos 3\theta = \frac{3\sqrt{3}}{2}\frac{J_3}{J_2^{3/2}} = \frac{\sqrt{2}J_2}{\tau_{oct}^3} \quad (6\text{-}28)$$

$$J_2 = \frac{1}{6}\left[(\sigma_1 - \sigma_2)^2 + (\sigma_1 - \sigma_3)^2 + (\sigma_2 - \sigma_3)^2\right] \quad (6\text{-}29)$$

$$J_3 = \left[\sigma_1 - \frac{I_1}{3}\right]\left[\sigma_2 - \frac{I_1}{3}\right]\left[\sigma_3 - \frac{I_1}{3}\right] \quad (6\text{-}30)$$

I_1= First invariant of the stress tensor

J_2 and J_3= Second and third invariants of deviatoric stress tensor

θ= angle of similarity, defined in equation 6-28

C=cohesion, psi

ϕ= angle of internal friction

σ_1, σ_2 and σ_3= Principal stresses, psi

As discussed earlier, the potential for damage is assessed based on evaluating the failure function at the top of the subgrade. Several yield criterion are developed by researchers to identify the onset of yielding for different materials. The values of the yield functions can be used as a measure for probability of failure in different materials. Figure 6-6 presents the projection of yield functions on the octahedral plane. As indicated in this plot, Tresca and Von Mises yield functions are symmetrical. In other words, the behavior in tension and compression are similar. This is far from reality in geomaterials. Yield functions, specifically developed for granular soils such as Mohr-Coulomb and Lade yield functions clearly show different behavior in compression and tension as indicated by different slopes in compression and tension zones.

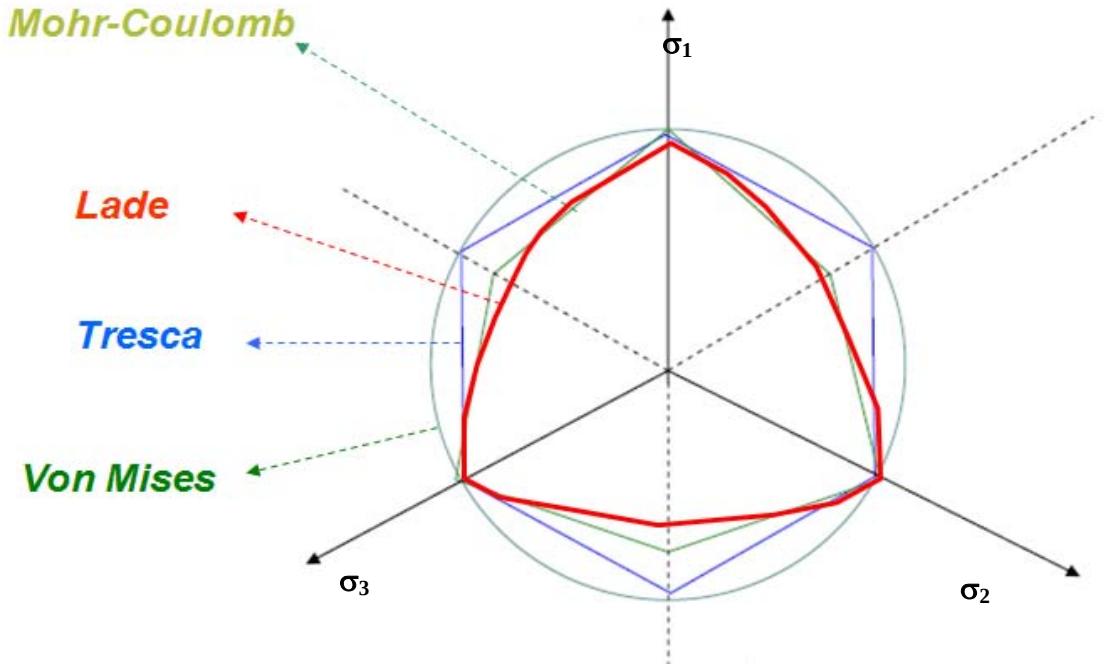

Figure 6-6 Schematic representation of different yield functions on principal plane

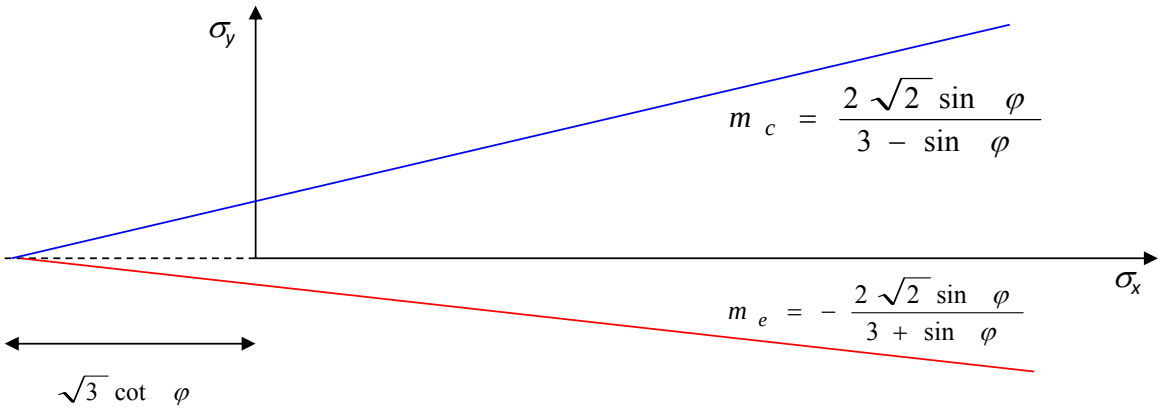

Figure 6-7 Slope of the Mohr-Coulomb failure function in compression and tension

Figure 6-7 shows the difference between the slope of the failure function projected on the principal plane in compression and tension zones. This figure indicates that the yield strength in compression is higher than in the extension regimen. Desai stated that this difference is pertinent to the impact of the third stress invariant present in the yield function (Desai 1984). Therefore it is imperative to employ failure functions that capture the difference in response and therefore the performance under compression and tension stress regimens.

From the mechanics, yielding is signaled when the value of the failure function becomes zero. In other words, if the stress states calculated from the analysis falls inside the yield surface, the value of the yield function is negative and the probability of failure is slim. On the other hand, if the stress states calculated in the analysis part result in positive values of yield function, the pavement system is prone to develop high plastic deformations. This concept is graphically illustrated in figure 6-8.

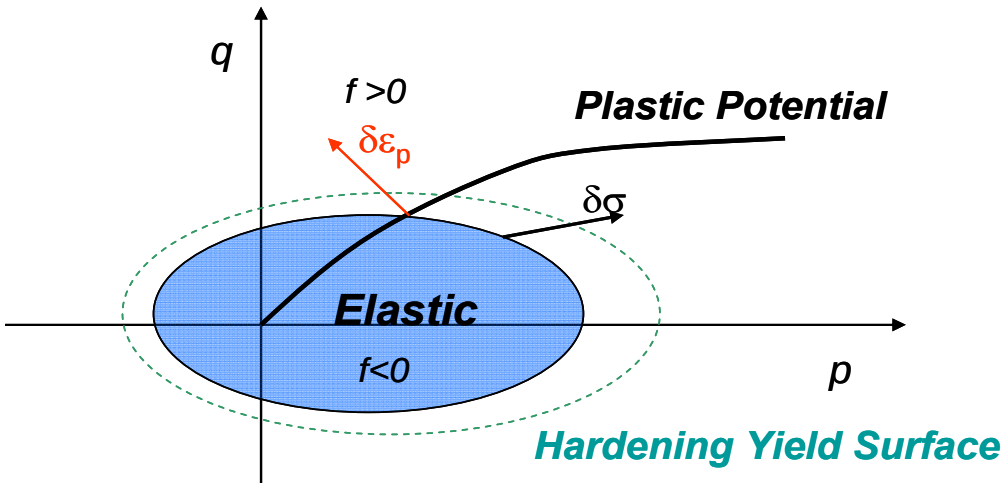

Figure 6-8 Application of yield function in defining the elastic-plastic boundary

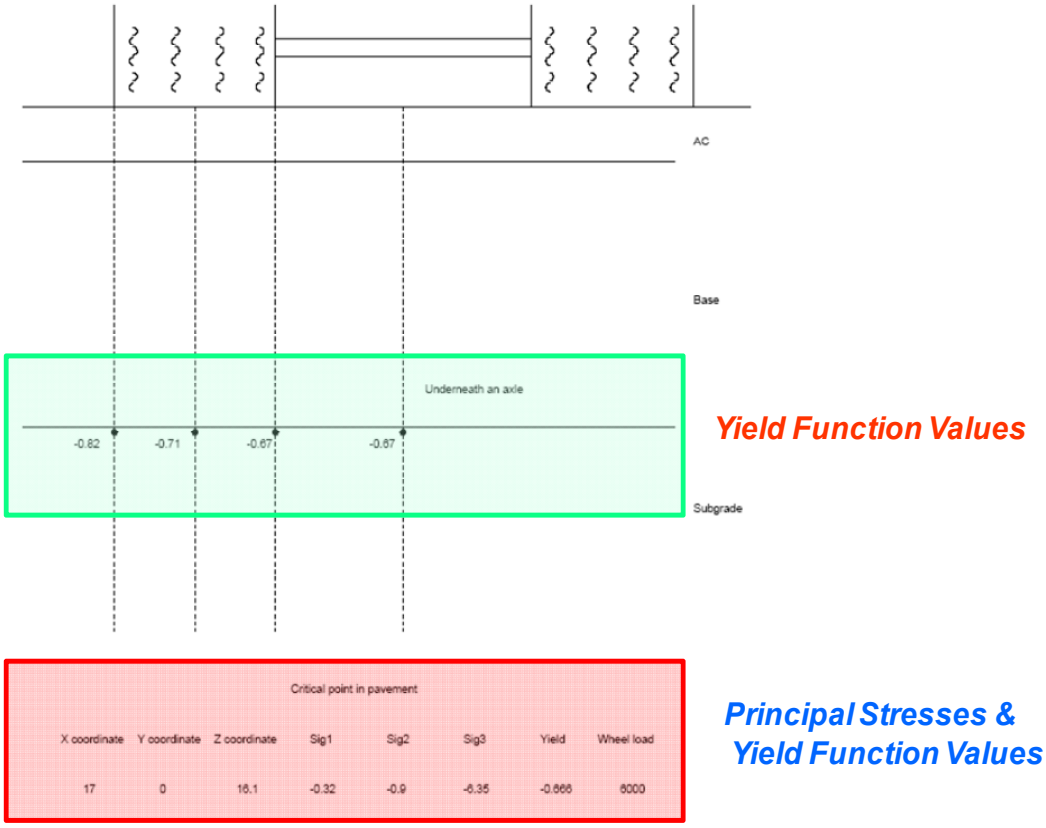

Figure 6-9 Calculation of yield function at critical locations (Fernando 1997)

Figure 6-9 presents our result for an arbitrary pavement configuration using the TXDOT approach for controlling the stability of the subgrade. A three-layer system was assumed and the values of the Mohr-Coulomb failure function calculated at three radial distances namely mid-tire, edge of the tire, and halfway between the two tires. As illustrated in this figure, the values of the yield function at all the critical points were negative, which correspond to conditions of elastic behavior. This indicates that the assumed pavement can sustain the super heavy load without developing plastic deformation.

As indicated earlier in this section, TXDOT employs isotropic solutions to calculate the critical responses under the super heavy wheel loads. In previous chapters we extensively discussed and showed that the stresses calculated using anisotropic solutions are typically higher and more realistic compared to measured values. On the other hand we showed responses calculated using isotropic solutions results in high

tensile stresses at the bottom of the base layer. This value is more negative when the ratio of the base modulus to subgrade modulus is high. It is intuitive and obvious that unbound aggregate layers cannot sustain high tensile stresses, and the calculated stresses are not realistic. Therefore the stresses calculated from isotropic solutions induce a systematic error on the calculated values of the yield function. High tensile stresses and low compressive stresses will result in unrealistic predictions of the stability of the pavement foundation. The proposed methodology that follows tends to eliminate this discrepancy and provide a more conservative assessment of the stability of the subgrade as well as unbound aggregate layers.

Proposed Methodology

Similar to TXDOT approach, the proposed methodology employs the concept of using the failure function to identify the probability of failure in geomaterials. Modifications to the existing methodology can be summarized as:

- Using anisotropic solutions to calculate critical pavement responses
- Using modified Drucker-Prager yield criterion to identify the elastic-plastic boundary
- Employing the same methodology for unbound aggregate layers as well as subgrade soils

As indicated earlier, the stresses and strains calculated using anisotropic solutions are typically higher compared to stresses calculated using isotropic solutions. The unrealistic responses used to calculate the failure function results in inaccuracies in prediction of the rutting performance of pavement foundations. This discrepancy can be eliminated or at least be reduced by using anisotropic solutions to compute responses under the heavy wheel loads. For instance if the stresses at the bottom of the base layer are used in the failure function, depending on the modular ratios of base and subgrade layer, high tensile stresses would signal unstable conditions in the aggregate layer.

On the other hand, stability of the aggregate layers in pavement sections with very thin asphalt layers needs to be checked during the design process. Emerging design techniques such as inverted pavement design that is gaining popularity during recent years is another example of this kind. Inverted sections typically use thin asphalt layers, which might overstress the unbound aggregate layer. Therefore using the failure function approach deems necessary to ensure the stability of the unbound aggregate layer.

In the proposed methodology, the Drucker-Prager yield criterion is used to define the onset of plastic deformation in unbound aggregate layers. The general form of the Drucker-Prager yield function can be written as:

$$q - \xi\, p = k \tag{6-30}$$

where:

q= Deviatoric stress, psi

p= Average of the principal stresses, psi

ξand *k*= Model parameters found from fitting shear test data to the model

Equation 25 represents a straight line on the q-p plane as illustrated in figure 6-10. In the three-dimensional stress pace however, the yield functions plot as a circular cone. The projection of this cone on the octahedral plane is a circle as plotted in figure 6-11. Physically, the average of the principal stresses (p) is associated with volume change in a material under loading, while the deviatoric stress (q) is associated with shear deformation and softening of the material under load.

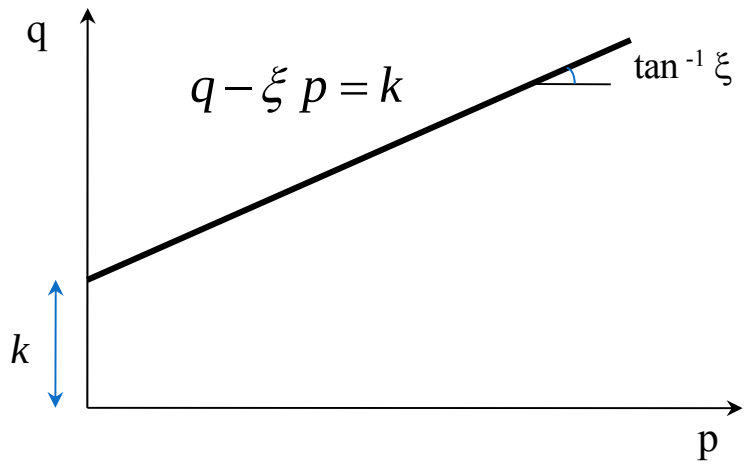

Figure 6-10 Representation of Drucker-Prager yield function in q-p plane

Model parameters ξ and *k* for the Drucker-Prager yield function can be determined from the slope and the intercept of the failure envelope plotted in figure 6-10. This plot can be generated using stress path tests up to the failure conditions. There are several ways to define failure in geomaterials. Some consider the peak in the stress-strain curve as the failure condition. In critical state soil mechanics, the failure refers to the state at which no volume change occurs.

The value of ξ and *k* can be expressed by more familiar concepts such as cohesion and angle of internal friction. Two sets of parameters can be found by finding the intersection of the Mohr-Coulomb failure function with the Drucker-Prager yield function. Model parameters found from fitting the Drucker-Prager yield criterion to the major vertices of Mohr-Coulomb yield function are presented in equation 6-31. Graphical representation of this concept presented in figure 6-11.

$$k=\frac{6c\cos\varphi}{3+\sin\varphi} \qquad \xi=\frac{6\sin\varphi}{3+\sin\varphi} \tag{6-31}$$

Model parameters found from fitting the Drucker-Prager yield function to minor vertices of Mohr-Coulomb yield function are presented in equation 6-32.

$$k = \frac{6c\cos\varphi}{3-\sin\varphi} \qquad \xi = \frac{6\sin\varphi}{3-\sin\varphi} \tag{6-32}$$

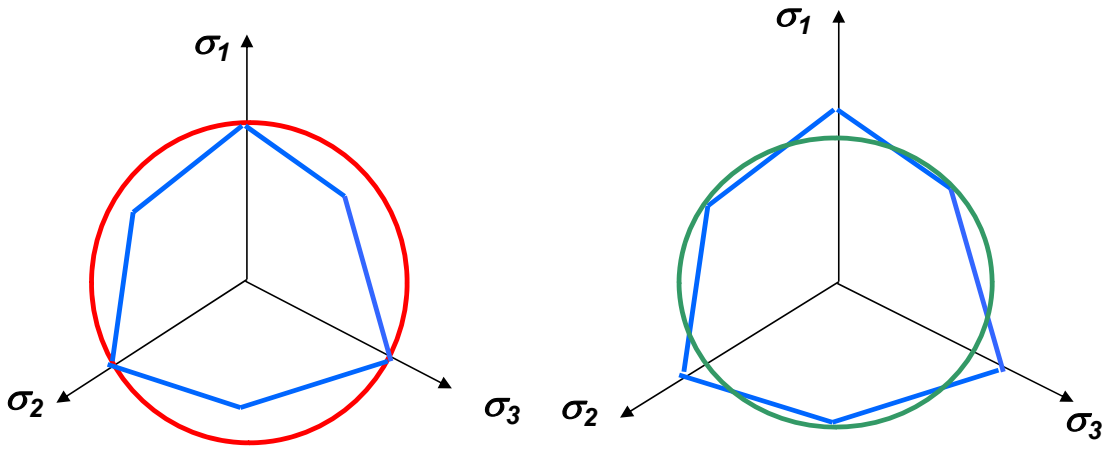

Figure 6-11 Determination of Drucker-Prager model parameters based on Mohr-Coulomb criterion

In the proposed methodology, model parameters pertaining to fitting the Drucker-Prager criterion to minor vertices of Mohr-Coulomb yield function are used to calculate ξ and *k*. As illustrated in figure 6-11, projection of failure surface on π-pale derived from fitting to minor vertices of Mohr-Coulomb yield function provide more conservative conditions. In other words fewer stress combinations will fall within the stable range when ξ and *k* are calculated using equation 6-32. Therefore this methodology recommends using equation 6-32 for calculation of model parameters.

Figure 6-12 shows an implementation of the proposed methodology for determining the stability of unbound aggregate layers. The structural parameters of the pavement system were selected as such that the predictions of the yield function result in unstable conditions. The aggregate layer was considered to be 6 inches and constructed

under a 4 inch asphalt layer with the vertical modulus of 400,000 psi. The level of anisotropy of the aggregate layer was considered to be 0.3.

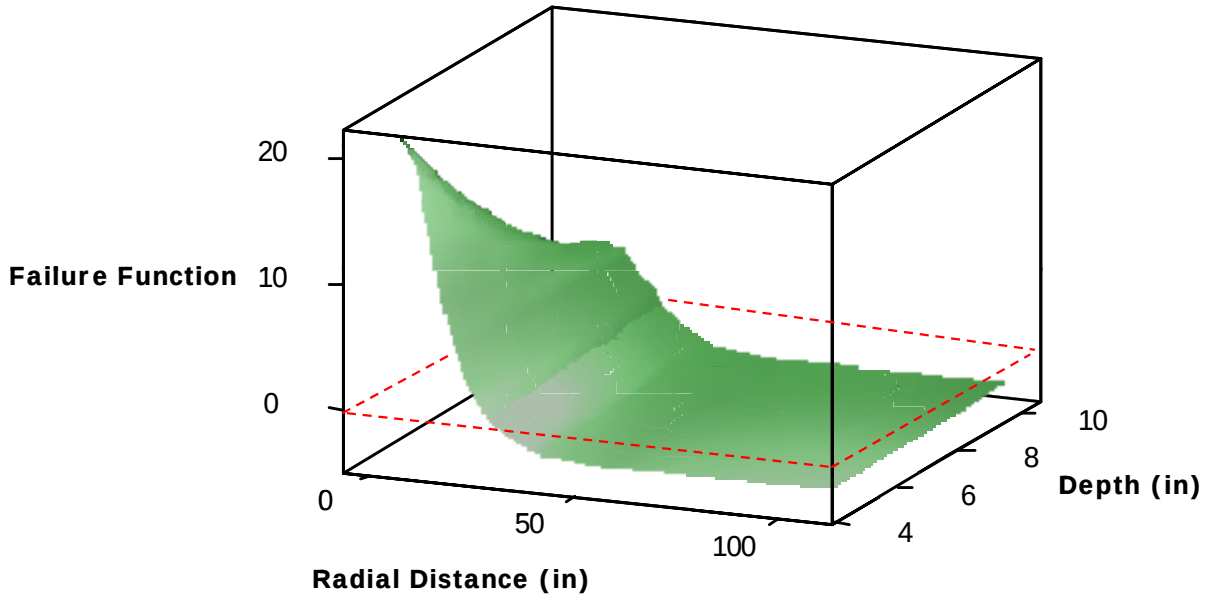

Figure 6-12 Variation of yield function values in the base layer, an example

Figure 6-12 indicates that the highest value of the failure function is calculated at the top of the aggregate layer along the centerline of the wheel load. As stated earlier in this chapter positive values of failure function correspond to more unstable conditions.

The plane at which the value of the failure function is zero is designated with dotted red lines. This plane defines the boundary within which the stress states result in negative values of failure function, which is synonymous with stable conditions. This plot shows as the stresses dissipate through depth of the pavement, the value of the yield function becomes smaller. In other words smaller stress states calculated at the bottom of the base layer result in less critical conditions, which is intuitively true.

The same analogy is valid as we move away from the wheel load. Stress states calculated at radial distances from the wheel load are typically smaller and therefore result in less critical conditions.

In conclusion, the material properties and layer configurations selected for this example will result in unstable conditions and the pavement system is prone to develop plastic deformations when subjected to the assumed load level.

CHAPTER VII

EFFECT OF STRESS PATH AND LOADING DIRECTION ON THE STABILITY OF AGGREGATE LAYERS

INTRODUCTION

This chapter provides a theoretical study of the usefulness of failure function and plasticity theory for stability control of aggregate layers. The general concept behind using failure function is to identify the onset of plastic deformation. In plasticity theory, a mathematical function called failure function defines this boundary. Stress states that fall within this boundary represent stable conditions at which the stability of the system is assured. The design should be modified by selecting better materials or by increasing the depth of the layers if the failure function signals rutting potential.

In this chapter two yield criteria one by Lade and the other one by Pietruszcak and Mroz will be discussed. The yield criterion developed by Lade uses invariants of the stress tensor to formulate the failure function. The failure function developed by Pietruszcak and Mroz, however, employs loading direction and directional stiffness when defining the elastic boundary. The sensitivity performed on the combined failure functions provides valuable information about the parameters that influence the stability of the pavement layers when subjected to traffic loads.

LADE FAILURE CRITERION

Lade initially proposed a failure criterion based on isotropic assumptions in 1977. This failure function is formulated in terms of invariants of the stress tensor as presented in equation 7-1 (Lade and Musante 1977).

$$f = \eta_1 = \left(\frac{I_1^3}{I_3} - 27 \right) \left(\frac{I_1}{Pa} \right)^m \tag{7-1}$$

$$I_1 = \sigma_1 + \sigma_2 + \sigma_3 \tag{7-2}$$

$$I_3 = \sigma_1 \sigma_2 \sigma_3 \tag{7-3}$$

where:

I_1=First invariant of the stress tensor, psi

I_3=Third invariant of the stress tensor, psi

m=Model parameter

Pa=Atmospheric pressure, psi

Figure 7-1 shows the sensitivity of the failure function to model parameters. In principal stress states, the shape of the projection of the failure surface on an octahedral plane resembles an asymmetric bullet with the pointed apex at the origin of the principal stress axes. Parameter *m* in equation 1 controls the curvature of the yield function. For constant values of *m* and increasing values of η_1 the shape of the failure function changes from circular to triangular with rounded corners as illustrated in figure 7-1.

As indicated in equation 1, the yield criterion is only a function of stress states and does not capture the influence of the rotation of the principal plane. The parameter *m* is influenced by the moisture state and particle size distribution of the mix.

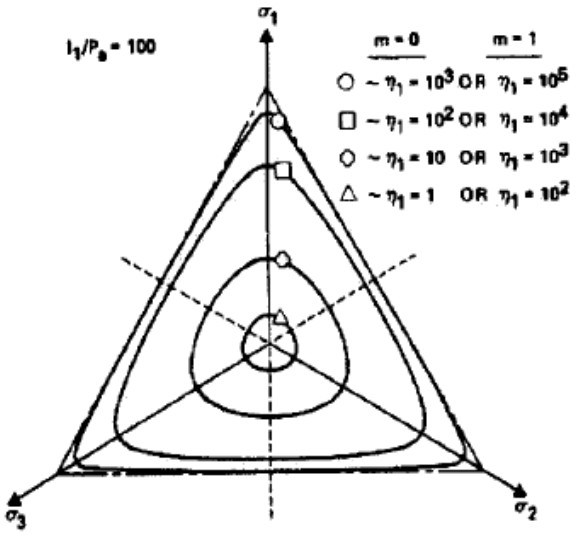

Figure 7-1 Sensitivity of Lade's yield function to parameters of the model (Abelev and Lade 2003)

PIETRUSZCZAK AND MROZ FAILURE CRITERION

Pietruszczak and Mroz developed a failure criterion that accounts for the direction of loading for cross anisotropic materials (Pietruszczak and Mroz 2001). The coordinate systems and general sign convention for formulation of the failure function is presented in figure 7-2. Equations 7-4 through 7-6 can be used to determine (L_i) the magnitudes of the resultant stresses acting on each plane (Lade 2008).

$$L_1 = \sqrt{\sigma_{11}^2 + \sigma_{12}^2 + \sigma_{13}^2} \tag{7-4}$$

$$L_2 = \sqrt{\sigma_{21}^2 + \sigma_{22}^2 + \sigma_{23}^2} \tag{7-5}$$

$$L_3 = \sqrt{\sigma_{31}^2 + \sigma_{32}^2 + \sigma_{33}^2} \tag{7-6}$$

where L_1, L_2, and L_3 are the resultant of stresses in planes 1, 2, and 3, respectively, and σ_{ij} are the stresses acting on ij plane.

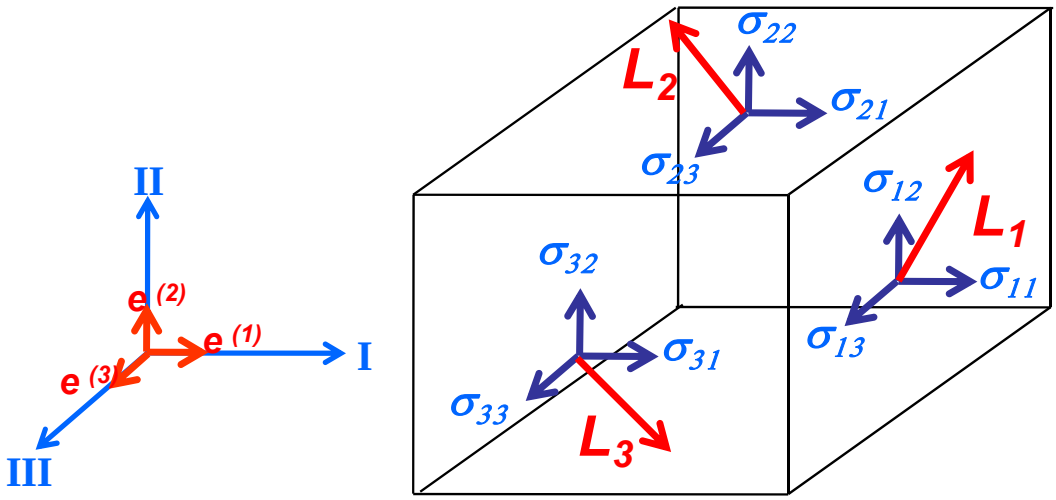

Figure 7-2 Directions of the components of loading vector and general sign convention

The authors proposed the generalized form for loading vector as:

$$L_i = (L_1, L_2, L_3) = L_1.e_i^{(1)} + L_2.e_i^{(2)} + L_3.e_i^{(3)} \tag{7-7}$$

where e_i is the unit vector, and L_i is the resultant stress on plane i.

The loading direction therefore can be determined using equation 7-8 (Lade 2008).

$$(l_1, l_2, l_3) = \frac{(L_1, L_2, L_3)}{\sqrt{L_1^2 + L_2^2 + L_3^2}} \tag{7-8}$$

Pietruszczak and Mroz formulated a yield criterion for cohesive frictional materials based on loading directions and directional stiffness as:

$$f = \eta_o (1 + \Omega_{ij}\, l_i l_j) \tag{7-9}$$

where:

Ω_{ij}= Stiffness in ij plane

η_0= Radius of the sphere defined in figure 7-3

Figure 7-3 schematically presents the spatial variation of Pietruszcak and Mroz yield function in the principal plane. The concept behind Pietruszcak and Mroz yield criterion is that the yield function is essentially a deformed sphere. The radius of the sphere is η_0 as illustrated in figure 7-3.

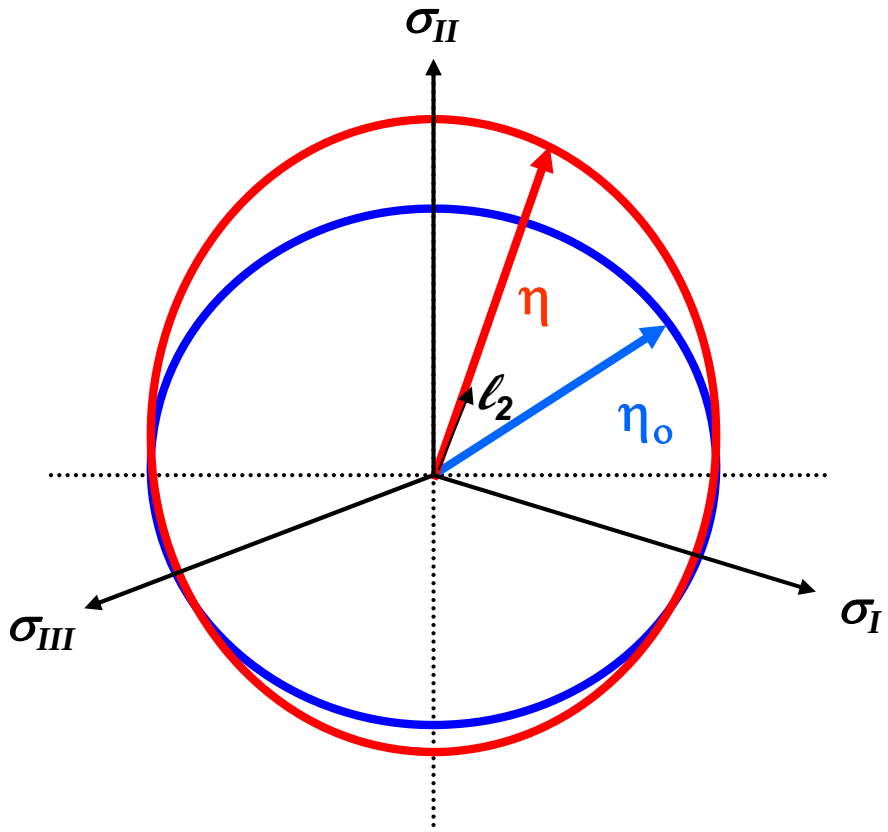

Figure 7-3 Representation of Pietruszczak and Morz yield function

The term $(1+\Omega_{ij}\, l_i l_j)$ describes the deviation in three dimensions from the sphere. This term captures the influence of directional stiffness as well as loading direction in the yield function. The stiffness of an orthotropic cohesive material in ij plane (Ω_{ij}), where the

normal to principal planes coincide with material axes, has two distinct eigenvalues. For cross-anisotropic materials, stiffness in the horizontal plane in two directions is equal ($\Omega_{1=}\ \Omega_3$) therefore Ω_{ij} can be identified by only one scalar value. For isotropic material, where stiffness in three directions is equal ($\Omega_{1=}\ \Omega_{2=}\Omega_3$) the ($\Omega_{ij}$) vanishes and the projection of the yield function on the octahedral plane is a circle with a radius of η_0 (Pietruszczak and Mroz, 2000).

The yield criterion presented in equation 9 can also be written as:

$$f = \eta = \eta_o(1 + \Omega_1 l_1 + \Omega_2 l_2 + \Omega_3 l_3) \tag{7-9}$$

Since in cross-anisotropic materials the stiffness in a horizontal plane (directions 1 and 3) is equal ($\Omega_{1=}\ \Omega_3$) and knowing that $l_1^2+l_2^2+l_3^2=1$, therefore, the general form of the yield function for cross-anisotropic geomaterials can be written as (Lade 2008):

$$f = \eta_o\left[1 + \Omega_1(1 - 3l_2^2)\right] \tag{7-10}$$

where η_0 is the radius of the sphere, and the term $\left[1 + \Omega_1(1 - 3l_2^2)\right]$ controls the deviation of the yield function in three dimensions from a sphere with radius of η_0. The second term in the right-hand side of equation 10, $\left[1 + \Omega_1(1 - 3l_2^2)\right]$ is also known as a perturbation term and is controlled by the scalar material parameter Ω_1 and loading direction l_2. The mathematical representation of equation 7-10 is a rotationally symmetric shape as illustrated in figure 7-3.

Lade showed that the direction of the loading for a conventional triaxial setup can be found from equation 7-11 (Lade 2008). This equation defines the loading direction l_2 as a function of the inclination angle and the stresses applied on the specimen in a triaxial test. The sign convention is according to figure 7-4.

$$l_2 = \sqrt{\frac{\sigma_y^2 \, Sin^2\beta + \sigma_z^2 \, Cos^2\beta}{\sigma_x^2 + \sigma_y^2 + \sigma_z^2}} \qquad (7\text{-}11)$$

where:

β= Angle of load inclination

σ_x, σ_y and σ_z= Principal stresses in x, y, and z directions in stress path test, respectively

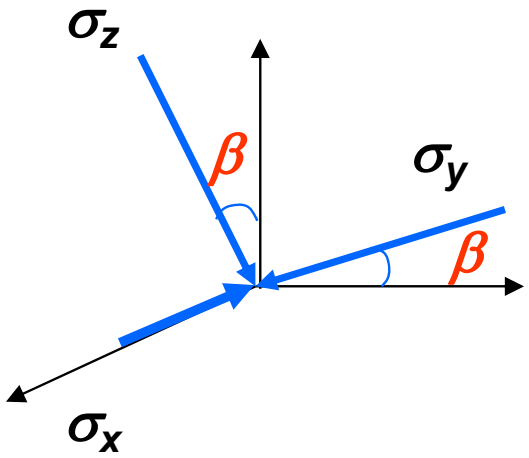

Figure 7-4 Sign convention for determination of loading direction

COMBINING THE YIELD FUNCTIONS

Yield criterion presented by Lade and yield function for cross-anisotropic soils developed by Pietruszczak and Mroz are essentially the same entities and tend to predict the onset of plastic deformation in geomaterials. Therefore we can combine these two equations as:

$$f = \eta_o \left[1 + \Omega_1 (1 - 3l_2^2)\right] = \left(\frac{I_1^3}{I_3} - 27\right)\left(\frac{I_1}{Pa}\right)^m \quad (7\text{-}12)$$

As discussed earlier in this chapter, Pietruszcak and Morz criterion is based on the angle of load inclination and the directional stiffness of the material while Lade's criterion is basically a function of stress invariants. Therefore combining the two failure functions can provide valuable information revealing the relationship between the stress states and the rotation of the principal stresses induced by traffic loads and the performance of the pavement foundations.

PARAMETRIC ANALYSIS

A sensitivity analysis on equation 7-12 was performed to demonstrate the implication of yield criterion approach for stability control of pavement layers under the moving wheel load. Stress states in the range of NCHRP 1-28 protocol were selected to perform the sensitivity analysis. Model parameters pertaining to Santa Monica beach sand derived by Lade were used to generate figures 7-5 through 7-8.

Four confinement levels namely 5, 10, 15, and 20 psi were considered as representative field confinements imparted by wheel loads, and stress ratios up to 10 were used in this analysis. The vertical stresses were in turn calculated based on the confinement levels and stress ratios. As previously discussed in Chapter II, the approaching and departing nature of the wheel loads causes the rotation of the principal plane in pavement layers. The inclination of the orientation of the principal plane under the wheel load is zero right under the wheel load and increases gradually with radial distance as the load moves away from the reference point. In other words the β value, which is the angle between vertical plane and the loading direction, has its smallest value directly under the wheel load. This value increases with the radial distance from the centerline of load. Therefore for the purpose of the sensitivity analysis in this section, smaller β values were assigned to more demanding stress paths to simulate the field conditions.

Figure 7-5 shows the impact of stress ratios and the angle of load inclination on the value of failure function. Negative values of failure function correspond to conditions at which the probability of failure is slim while positive values of failure function represent stress combinations, which results in significant likelihood of failure.

This plot shows that probability of transition to unstable region ($f>0$) increases as the stress ratios induced on aggregate layers increase. This is evidenced in the first and second stress paths (designated with dark and light blue lines) where the value of the failure function is positive at the end of the stress path. This plot also indicates that the critical conditions in terms of transition from an unstable region to stable region happen when the wheel load is directly on the assumed point at which the β value is very small.

Figure 7-6 shows the simultaneous effect of confining pressure and stress ratios on the stability of the pavement systems. This plot shows that higher confinement levels correspond to less critical conditions while lower confining pressures correspond to conditions at which the probability of transition to unstable conditions increases. Confining pressure in geomaterials contributes to particle interlock and results in better orthogonal stiffness properties of the system. Lower confinement levels however resulted in positive values of failure function, which is synonymous with critical conditions. The gradient toward unstable conditions is controlled by the stress ratios. As the stress ratios increase at each confinement level, the slope pointing toward the unstable condition increases.

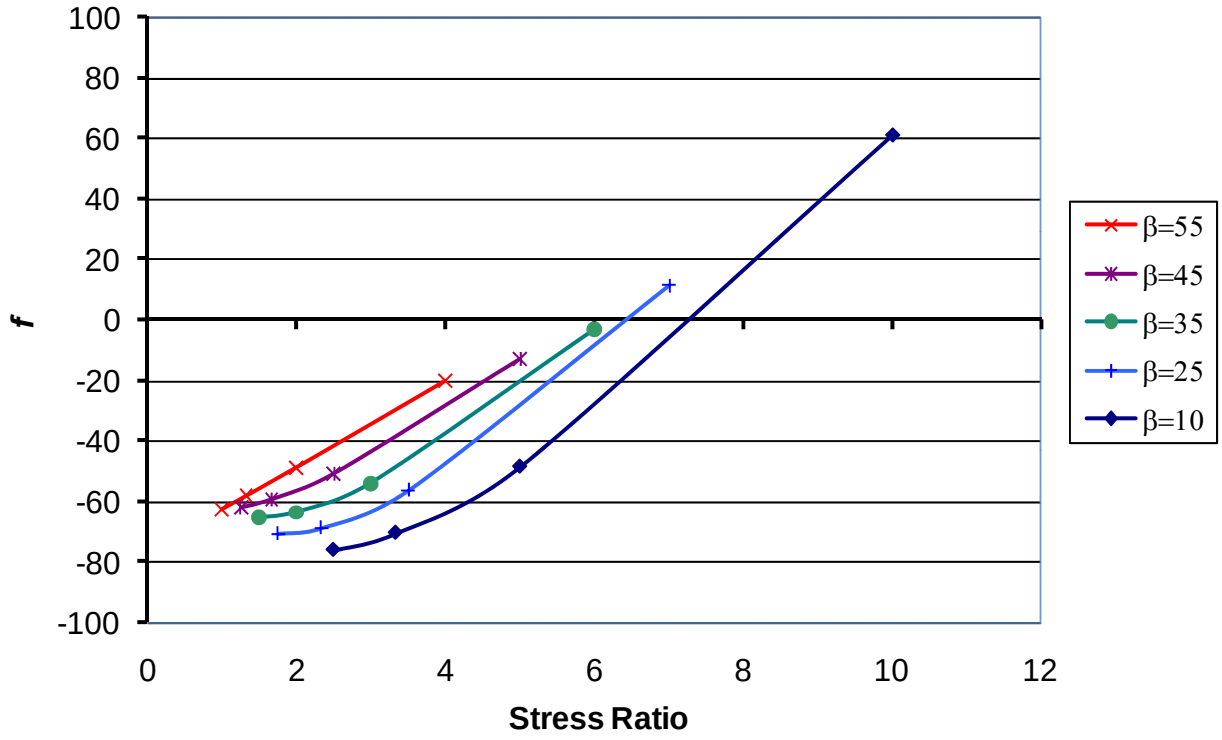

Figure 7-5 Impact of load inclination and stress ratios on the failure function

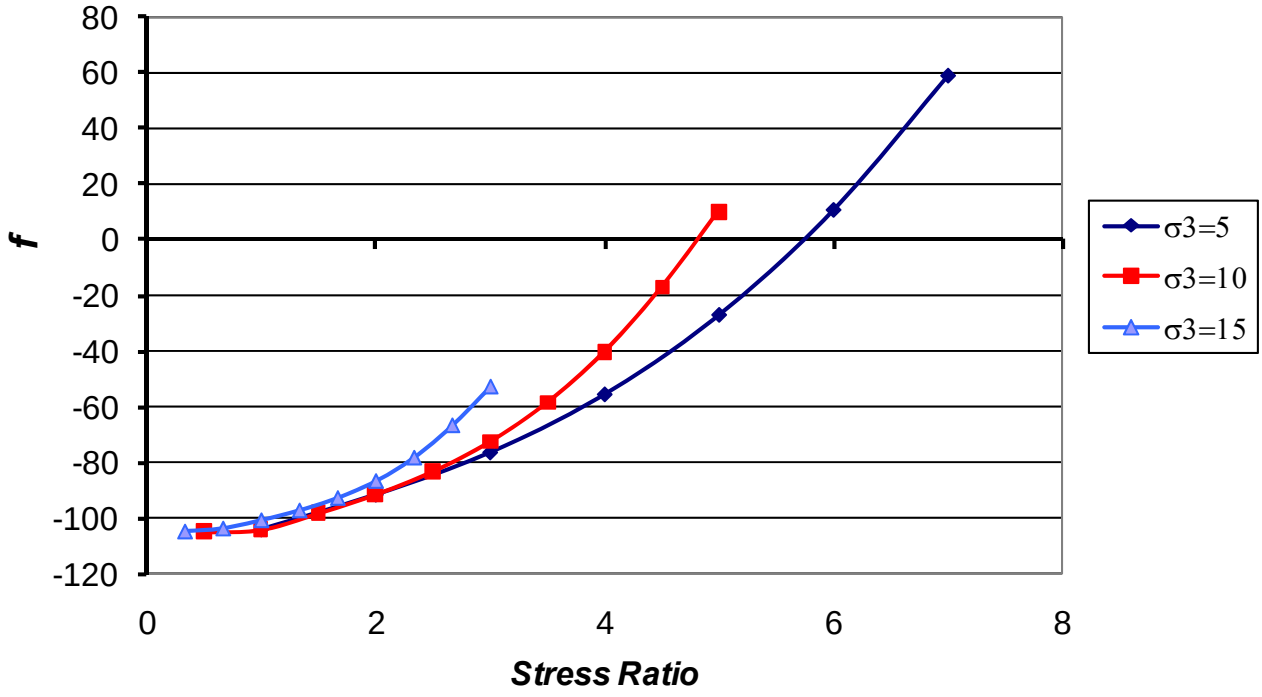

Figure 7-6 Impact of confinement and stress ratios on the failure function

Figure 7-7 shows the synergistic effect of confinement level and shear stresses represented by second invariant of the deviatoric stress tensor (J_2) on the value of failure function.

This figure shows that increasing values of shear stresses point toward the transition phase from elastic to plastic region. The slopes of the curves are controlled by confining pressure. As evidenced in this figure, increasing values of confining pressure resulted in reduction of the slope toward unstable conditions. This plot also shows sharper gradient of assent toward the critical conditions happens at small confinement levels with increasing shear stresses.

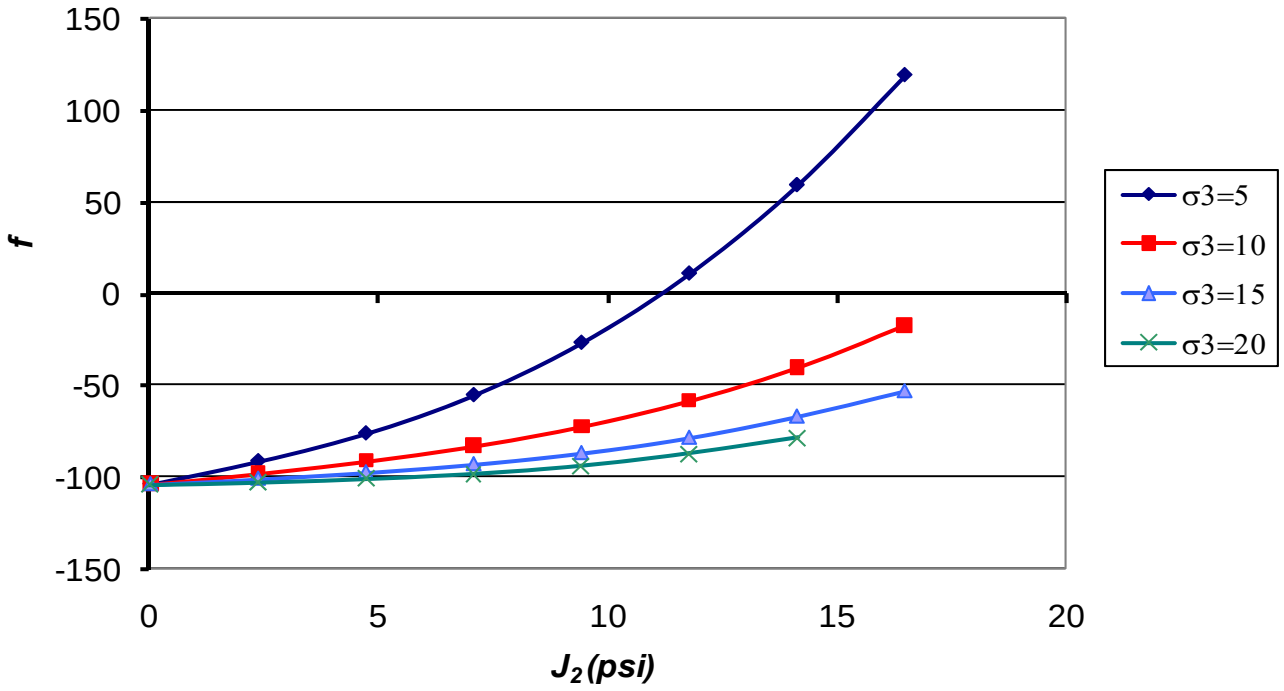

Figure 7-7 Impact of confinement and shear stress on the failure function

Figure 7-8 shows the sensitivity of failure function to combined effect of confinement level and angle of load inclination. As illustrated in this plot, probability of developing plastic deformation is higher when the confinement level is smaller. Higher confining pressure contributes to better aggregate interlocks and therefore a more rigid aggregate matrix, which is in conformity with the results in this plot.

The negative slopes of the plots indicate the inverse relationship between the load angle and the value of the failure function. In other words, the probability of transition from elastic region to plastic region decreases as the radial distance from load increases or the load departs the reference point. As discussed earlier in this section, β value is smallest when the wheel load is directly on the assumed point and increases with radial distance from the centerline of the load.

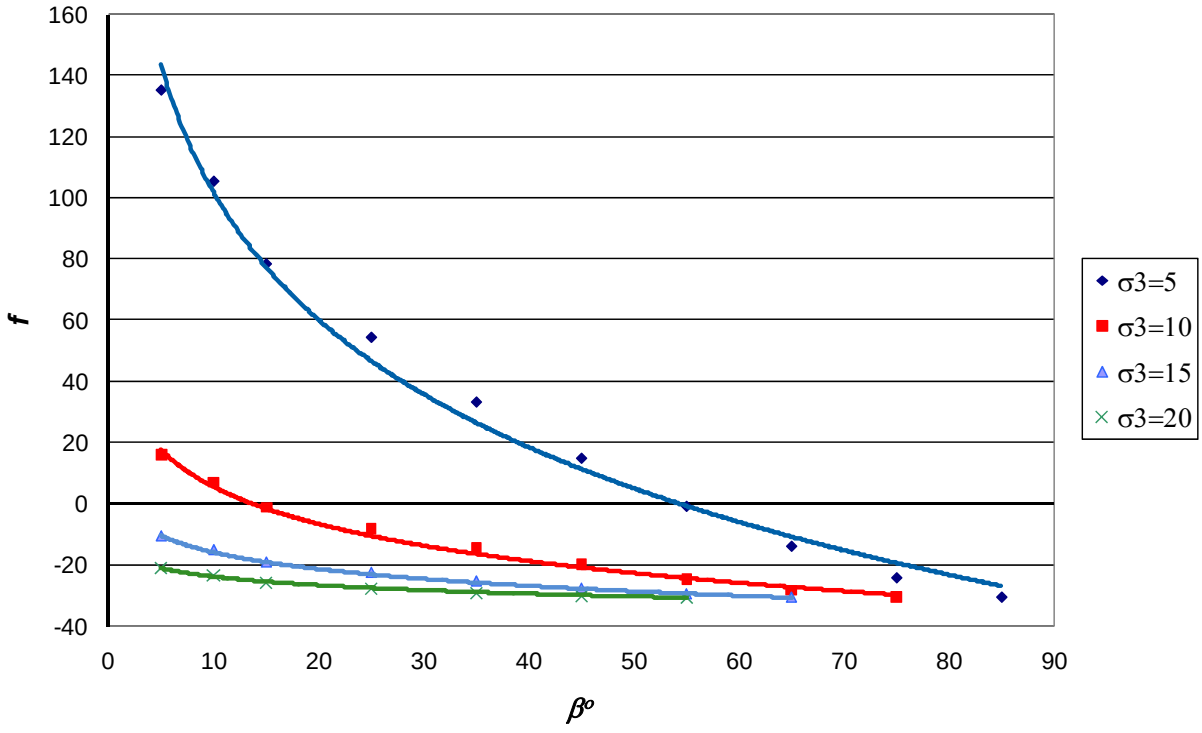

Figure 7-8 Impact of load inclination and confining pressure on the failure function

CHAPTER VIII

UTILIZATION OF QUARRY FINES IN PAVEMENT FOUNDATIONS

BACKGROUND

It is estimated that about 5127 crushed stone quarrying operations and 6000 sand and gravel operations exist in the United States, which produce 2000 million tons of aggregates annually (Bolen et al. 1996) .The aggregate production industry produces a significant amount of byproduct mineral fine materials in the process of rock crushing. The stockpiling, transportation, and disposal of byproduct fines pose several environmental and financial concerns for the aggregate industry. Proper characterization of non-plastic fines for civil engineering applications such as chemically bonded or unbounded pavement layers, soil caps, infiltration layers, and general fill, will maximize their potential as an environmentally friendly alternative for the construction industry.

DEFINITION OF FINES

The definition of fines varies within the aggregate industry. The European Aggregates Standards (ESA) defines the fine aggregates as materials passing sieve #4 for use in concrete, as particles smaller than 2 mm for use in asphalt, and as particles smaller than 0.063 mm for use as filler. The general consensus among the aggregate producers in the United States is that fines are the undersized material from crushing plants that is given no further processing and accumulates over time, or material produced by baghouse installations. The maximum size of fines from crushing plants may be as large as 6 mm, and size fractions below this vary greatly. Baghouse fines, which may later be mixed with fines produced during crushing of the parent rock, are typically below 0.075 mm (passing sieve #200). Typically there are two main particle size fractions, materials smaller than 9.5 mm (particles passing sieve 3/8 inch) and particles smaller than 75 microns (passing sieve #200).

TYPES AND AMOUNTS PRODUCED

(Hudson et al. 1997) wrote a comprehensive report on the status of byproduct mineral fines produced by construction aggregate companies in the United States. The report was based on a survey of 154 companies that operate 362 plants around the country. This report states that these companies produce about 292 million tons of aggregates annually. From this production level, it was estimated that 478 to 508 million tons of smaller than 9.5 mm mineral fines are produced, 91 to 103 million tons of which are not marketed annually in the United States. Additionally, 103 to 112 million tons of particles smaller than 75 microns (passing sieve #200) mineral fines are produced, and about 76 to 81 million tons are not marketed. Besides the annual production of byproduct mineral fines, it is estimated that 305 to 330 million tons of stockpiled materials smaller than 9.5 mm and about 406 million tons of fines smaller than 75 microns (passing sieve #200) in pond or pit storage are available (Hudson et al. 1997).

According to Hudson the byproduct mineral fines can be categorized into three major categories as:

- Fines retrieved from dry screening
- Fines retrieved from wet screening or from settling ponds
- Baghouse fines

The collection of mineral fines varies depending on the facilities that collect the fines in the quarry. The two major types are dry processing and wet processing. Aggregate particles retrieved from dry screenings are usually smaller than 5 mm in size and accumulate during primary and secondary crushing and separation. About 5 to 10 percent of byproduct fines originate from dry-screening operations. The chemical and mineralogical contents of screenings depend on the mineral types in the gravel or parent rock. The physical characteristics of the byproduct fines such as fine particle angularity may vary because of variations in mineralogy, strength, and fracture characteristics of the aggregates or the parent rock as well as the crushing techniques used in the quarries.

Quarries that operate as dry plants retrieve the fines in the screening operations and also from baghouses or cyclones. According to the study by Hudson on the state of fines production in the United States, baghouse fines represent about 5 percent of the mineral fines generated and are typically smaller than 75 microns. Baghouse fines are collected dry; therefore, they pose less handling concern than damp or wet byproduct fines (Hudson et al. 1997).

Sediment fines in ponds or settling pond fines, pond screenings, pond slime, and pond tailings are obtained from washing aggregate as it is wet-processed into a product. These fines represent about 10 to 15 percent of the total aggregate production. Pond fines are usually directed to a settling tank or hydraulic cyclone where the coarser fractions can be removed for further industry use, and the remaining fines are discharged into a series of sequential settling ponds.

Currently, the aggregates and crushed rock industries are moving toward using more wet-processing operations due to environmental and air pollution concerns rather than dry crushing. Therefore, depending on the type of facility and the scope of operation, the byproduct fines can be collected through wet or dry screenings.

The handling, stockpiling, and disposal of aggregate byproduct mineral fines are costly. It has been estimated that the handling and disposal of pond screenings cost the industry about $400 million annually (Machemehl 1996). This cost includes removing, drying, and transporting the pond fines to stockpiles or for further industry use.

A number of industry-sponsored studies have examined the current and potential utilization of mineral fines. According to (Hudson et al. 1997), current uses of mineral fines include:

- Pavement and geotechnical engineering uses such as high fines aggregate bases, asphalt pavement layers with high fines content, high fines concrete, and backfills
- Agricultural uses such as Aglime and fertilizer filler
- Environmental uses of limestone aggregate fines to control SO_2 emissions, pond and watershed liming, acid mine drainage abatement, and landfill layers

- Miscellaneous applications such as industrial fillers and paints

Another study conducted by Wood suggests possible uses of mineral fines include asphalt concrete products, Portland cement products, chemical products, industrial minerals, mineral coatings, fillers and pigments, environmental and pollution control products (such as acid neutralization, landfill daily cover, and sludge dewatering aid), and ceramic products (Wood 1995).

CIVIL ENGINEERING APPLICATIONS OF BYPRODUCT FINES, REVIEW OF LITERATURE

Aggregate bases are a significant potential use of quarry fines. According to Rockliff, the wider use of byproduct quarry fines in unbound aggregate layers in highway pavements may have been held back by insufficient specifications (D. Rockliff 1996).

The study conducted by (Touahamia et al. 2002) indicates that quarry fines can be substituted for primary aggregates used as coarse granular material for backfilling, highway construction, and sub-bases for roads and railway tracks. The authors constructed compacted layers of the dry quarry waste, building debris, and crushed concrete separated by geogrids. The strength and performance of the layers made of waste materials and byproduct fines were evaluated and compared to traditional aggregate layers made of crushed basalt. The authors reported that the quarry waste had a much smaller particle size distribution than the other materials (smaller than 5 mm as opposed to smaller than 13 mm waste materials). The authors reported that the presence of geosynthetic reinforcement layers greatly increased the shear strength (by up to 50 percent) and resulted in smaller plastic deformations.

Parker reported similar results in his study titled as: investigating the advantages of utilizing fines generated in the crushing process as engineered backfill for mechanically stabilized earth walls. Three materials: granite screenings, limestone pond fines, and natural pit run sand, were tested for strength, permeability, and chemical

properties. A 12-foot-high geotextile fabric-stabilized wall was designed using the measured properties, and the author reported that crushed stone fines required less fabric reinforcement than natural sand, resulting in lower construction costs (Parker 1996).

In another study by De Rezende and De Carvalho on the utilization of quarry waste for highway pavements, a test section 240 feet long and 30 feet wide was constructed in a low-traffic zone, and the performance was monitored over a three-year period. Quarry waste with a grain size smaller than 100 mm was used to construct an 8-inch-thick base layer, which was covered by a 2.5-inch asphalt layer. Based on the performance of the tests sections, the authors concluded that the quarry waste can be used successfully as an alternative for base materials in low-volume highway facilities (De Rezende and De Carvalho 2003).

Where soil erosion and land gradients are a problem for land developers, fines can be an attractive alternative to soil backfill. Waste fines are more easily worked than high plastic clay soils, benefiting the contractors. A test project was carried out in Georgia in 1988 by Vulcan Materials Company, using backfill for the building of a large mall (Brown 1996). Brown reported that the fines from Vulcan Materials' Kennesaw quarry could withstand the required bearing pressures of 4000 psf. He also reported that the moisture density, safety factor for bearing capacity, void ratio, and angularity of the waste fines were also suitable and met the specifications.

Several researchers have studied the resilient behavior of high fines unbound systems. These studies reported a decrease in the resilient modulus due to an increase in fines content (Simonsen et al. 2002; Thadkamalla and George 1995) and (Gray 1962). Gray reported that in unbound aggregate bases with 25.4 mm maximum particle size, the highest strength was achieved through the use of a maximum of 8 percent fines. (Tutumluer and Seyhan 1999) evaluated the anisotropic resilient properties of aggregate systems and reported that the aggregate matrix showed significant softening behavior as the percentage of fine particles (materials smaller than 75 microns) exceeded 12 percent. High fines content base layers were shown to be sensitive to moisture variation and susceptible to frost heave. Simonson studied the effect of freeze-thaw cycles on fine-

grained soils. He performed resilient modulus tests on samples frozen at –10°C in triaxial cells, then thawed the samples before testing, and found a 50 percent reduction in vertical resilient modulus values (Simonsen et al. 2002).

Thadkamalla studied the effect of moisture and saturation techniques on the resilient behavior of coarse and fine-grained soils. The authors concluded that the saturation level above the optimum moisture content has a nominal effect (20 percent reduction) on the vertical resilient modulus in coarse-grained soils, whereas it has a substantial effect (50 to 75 percent reduction) on fine-grained subgrades (Thadkamalla and George 1995).

IMPACT OF LITHOLOGY ON FINES GENERATION

The recent study conducted by (Manning and Vetterlein 2004) on exploitation of quarry fines in Great Britain indicates that construction aggregates produced by crushing of limestone rock (including dolomite and chalk) typically produce around 20 to 25 percent fines in the crushing process, whereas sandstone quarries produce up to 35 percent fines.

The authors reported that the strength and physical properties of fine particles generated from sand and gravel pits vary enormously depending on the sand-to-gravel ratio and on the clay content, but are mostly between 5 to 15 percent of production. Igneous rocks are also variable based on the lithology of the aggregates, and the byproduct fines generated in the crushing process range from 10 to 30 percent. Manning reported that according to British geological survey report published in 2003, the total annual production of construction aggregates is around 238 million tons; therefore, the total annual production of quarry fines in Great Britain is estimated to be on the order of 41 million tons (Manning and Vetterlein 2004).

Figure 8-1 and Figure 8-2 show the impact of lithology of the aggregates on the generation of byproduct fines during plant operations in Great Britain. Figure 8-1 summarizes the annual production of construction aggregates based on tonnage of final

products. Figure 8-2 demonstrates the impact of mineralogy and the source of the parent rock on the generation of quarry fines.

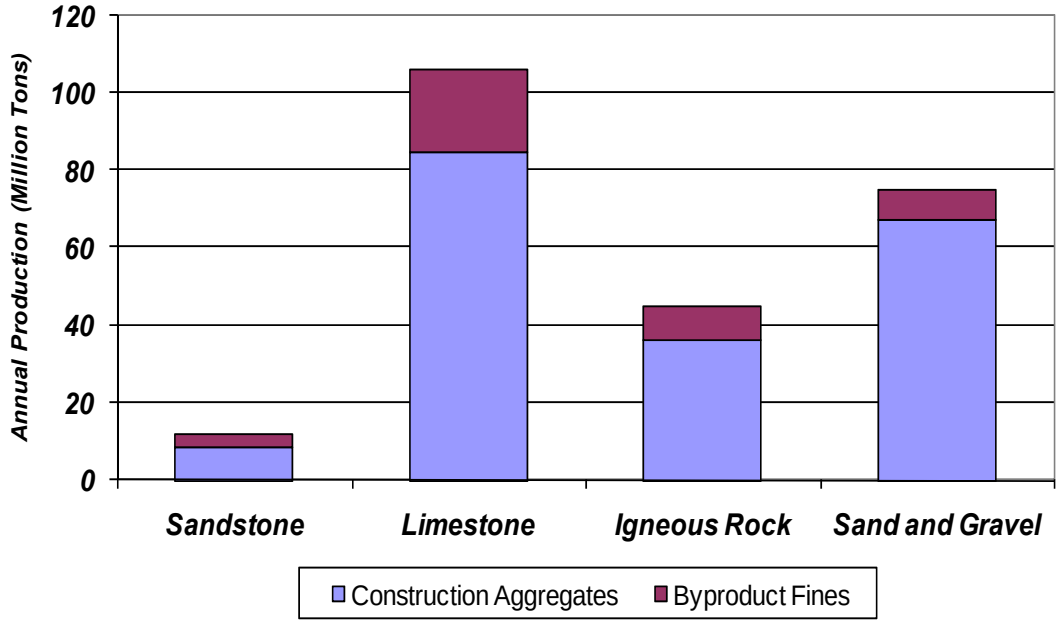

Figure 8-1 Impact of lithology on fines generation based on weight

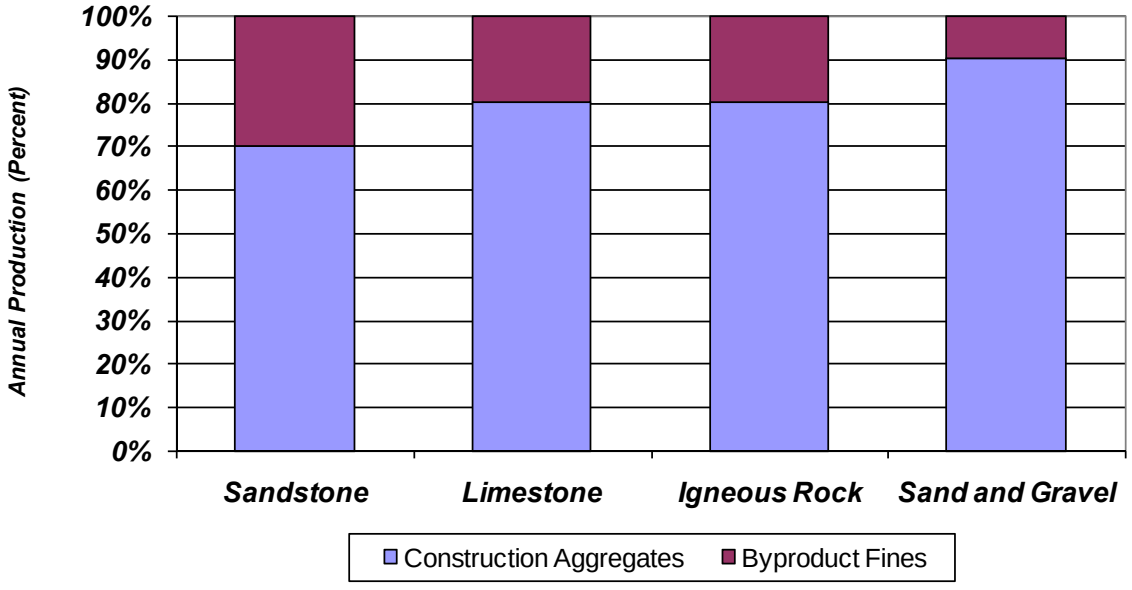

Figure 8-2 Impact of lithology on fines generation based on percentage

The generation of byproduct fines in the operation process is also a function of crushing techniques used in the plant. The next section of this report presents the different types of crushing and their impact on fines generation.

IMPACT OF CRUSHER TYPE IN FINES GENERATION

The quarry operation's final product—construction aggregates—is produced by abrasion/attrition of the parent rock as it comes into contact with other rock particles; this is a result of fracture of the rock in weak planes as the particles smash past each other. In general, method of applying the crushing energy employed in different crushing equipments (such as Jaw, Gyratory, Cone, or Roll crushers) results in different fractured planes and particle characteristics.

For instance in a study by Seberras at Georgian Aggregate's Duntroon Quarry in Toronto, Canada, the authors reported that when the primary crusher had changed from an impact crusher to a jaw crusher, the plant produced 28 percent fines in lieu of 38 percent fines, equivalent to a reduction of 100,000 metric tons per year (tpa) (Seberras 2000).

Bateman reported that when Dufferin Aggregate replaced its vertical shaft impact crusher with a cone crusher, they reduced the byproduct fines production and enhanced the performance of the quarry. He reported that upon this change, they increased their production of single-size aggregates from 40 to 50 percent by weight of the total plant production (Bateman 2003).

Issues with the Crushers

In a report by Manning on the exploitation of quarry fines in Great Britain, the authors summarized the issues with crushers and plant operations that cause an increase in fines generation as follows (Manning and Vetterlein 2004):

- The proportion of filler-grade material produced by an impact crusher ranges from 5 to 20 percent. This proportion increases as the operation speed in the plant increases (Ahn and Fowler 1999).
- Feeding the crusher too fast will cause a significant increase in fines generation due to the elevated probability of rock-on-rock interaction in the crushing chamber.
- Scalping off the primary crushed material increases the capacity of the subsequent crushing stages and reduces the likelihood of material becoming wedged in the crushers (known as “packing”). Packing can lead to excess fines being produced due to the greater rock-on-rock interaction.

CHAPTER IX

LABORATORY TESTS AND MATERIALS

BACKGROUND

Four gradations of limestone aggregates sourced from Brownwood, Texas, were selected to study the synergistic impact of fines, moisture, and light stabilization of aggregate systems. Table 9-1 summarizes the percent passing on each sieve for each gradation variant. This table also provides the ASTM D2940 specification for base and sub-bases for comparison. Gradation variants for the unbound study are presented in table 9-2.

Aggregate gradations were selected to have different percentages of fines as defined by particles passing sieve #40 (smaller than 425 microns). It is important to note that the gradations were designed so as to provide enough intermediate particles in fine gradations to maintain proper packing and aggregate interlock.

Gradation V1, which follows the ASTM D2940-03, that is The Standard Specification for Graded Aggregate Material for Bases or Sub-bases for Highways or Airports, designation, was selected as the reference gradation in this study. The impact of fines and stabilizers as well as moisture state on the mechanical properties of the aggregate systems were later determined and compared to the V1 gradation. The fine aggregate fraction was increased incrementally to form gradations V2 (20 percent fines), V3 (30 percent fines), and V4 (40 percent fines).

The percentages of intermediate particle sizes were adjusted to maintain appropriate density in each gradation variant. The gradations of the systems evaluated in particle size distributions for gradation variants for stabilization study is presented in Figure 9-1.

Table 9-1 Particle Size Distribution of Variants for Stabilization Study

Sieve Opening (mm)	Sieve No.	***Percent Passing (%)***				
		ASTM D-2940	***V1***	***V2***	***V3***	***V4***
37.5	1.5	95-100	100	100	100	100
19	3/4	70-92	85	85	85	90
9.5	3/8	50-70	60	65	75	80
4.75	4	35-55	40	50	60	65
2.36	8	…	25	35	50	55
1.18	16	…	20	30	40	50
0.600	30	12-25	…	…	…	…
0.425	40	…	15	20	30	40
0.15	100	…	10	15	20	30
0.075	200	0-8	5	10	15	20

Table 9-2 Particle Size Distribution of Variants for Unbound Study

Sieve Opening	*Percent Passing (%)*		
(mm)	*Fine*	*Intermediate*	*Coarse*
25	100	100	100
19	85	85	85
12.5	74	74	72
9.5	70	66	62
4.75	67	54	40
2.36	62	41	25
1.18	52	30	18
0.6	42	23	14
0.3	34	18	10
0.15	28	14	8
0.075	20	10	7

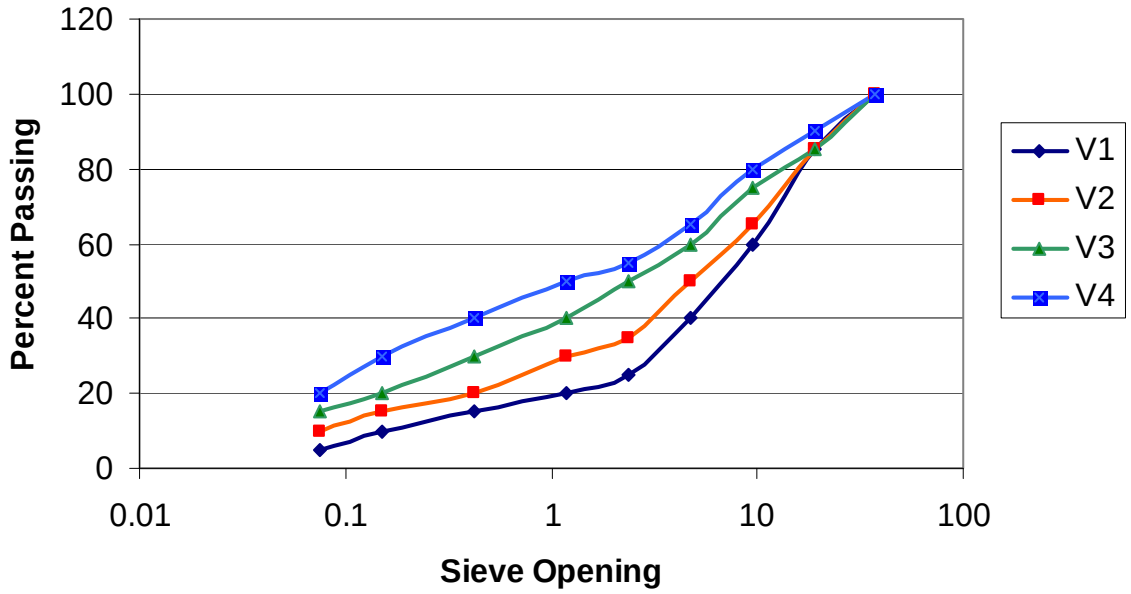

Figure 9-1 Particle size distributions

SPECIMEN CONDITIONING

Resilient properties and permanent deformation properties were measured on specimens compacted at optimum and wet of optimum (optimum + 2 percent) volumetric water contents. The compressive strength was measured on specimens compacted at optimum moisture content but subjected to moisture conditioning as described later in this report. The variation in water content was used in order to study the moisture susceptibility of aggregate systems containing excess amounts of low-plasticity fine particles. The Plasticity Index (PI) of the Texas limestone used in this study was 8 percent. In order to study the effect of moisture on the mechanical response of the aggregates, the materials were tested in three moisture conditions: optimum moisture content, dry of optimum moisture content, and wet of optimum moisture content. A compaction test (ASTM D1557) was performed on the aggregates to determine the optimum water content of each gradation variant.

Table 9-3 Material Variables and Testing Matrix

Test	Material Condition		
	Gradation (Percent Fines Passing Sieve #40)	**Stabilizer Content (%)**	**Moisture State**
Resilient Properties	V1 (15%) V2 (20%) V3 (30%) V4 (40%)	0% 1% 2%	Optimum, Wet of Optimum (Optimum + 2%)
Permanent Deformation	V1 (15%) V2 (20%) V3 (30%) V4 (40%)	0% 1% 2%	Optimum, Wet of Optimum (Optimum + 2%)
Compressive Strength	V1 (15%) V2 (20%) V3 (30%) V4 (40%)	0% 1% 2%	Optimum & Moisture Conditioning

As shown in Table 9-3, testing was conducted on different permutations of material conditions in order to evaluate the synergistic effect of fines content, moisture state, and stabilizer content on the engineering properties of high fine aggregate systems.

The main mode of stabilization of the fines with low levels of Portland cement (1 and 2 percent) is to develop a cement matrix primarily of calcium silicate hydrate (CSH) among the fine aggregate. However, since the concentration of calcium due to the addition of Portland cement is high in the fines matrix of limestone particles, it is probable that a calcium carbonate matrix may also be developed *(9)*. Major strength improvements can be achieved through time-dependent soil-cement and pozzolanic reactions. This objective was investigated with the strength gain process in samples tested for unconfined compressive strength.

With the intention of simulating the early and critical stages of performance, aggregate systems were tested for anisotropic resilient properties and permanent deformation potential immediately after compaction. Substantial further improvements in resilient response and rutting potential of stabilized systems are expected through time-

dependent strength gain reactions by forming CSH and Calcium Aluminate Hydrate (CAH) products.

LABORATORY TESTS

The following tests were performed on the samples to investigate the synergistic effect of fines, moisture, and stabilizer on the performance of high fine aggregate systems:

- Atterberg limits
- Moisture density test
- Variable confining pressure stress path test
- Repeated load permanent deformation test
- Unconfined compressive strength test
- Aggregate shape properties using AIMS
- Visual inspection of fines with electronic light microscope
- Methylene blue test
- Dry compacted fines (Rigden voids) test

In order to evaluate the impact of low levels of stabilization, either 1 or 2 percent of type I cement was added to the selected aggregate systems in the factorial. Samples were prepared using the impact compaction method following AASHTO T-180 using a 4.54 kg hammer and a 457 mm drop. Samples were compacted in rigid cylindrical molds 150 mm in diameter and 150 mm in height, in three 50 mm thick layers, by applying 25 blows per layer.

Stress Path Test

In order to assess the complex behavior and directional dependency of the response of aggregate bases under a moving wheel load, aggregate samples were tested following the Texas A&M small strain stress path protocol. Detailed description of the stress path testing is provided in Chapter II.

As discussed earlier in Chapter II, stress path tests have been widely used to simulate the stress states applied by traffic load on aggregate layers. The standard triaxial test protocols were only suitable for simulating the state of the stresses under stationary load. A proper test protocol should be used to capture the extension-compression-extension stress regimens induced by moving wheel load on the aggregate layer. As illustrated in figure 2-9 in chapter II, as the wheel approaches the reference point, more confinement is induced on the pavement, and as it departs the reference point, the magnitude of confinement decreases. The same behavior is valid for the vertical stresses. The pavement experiences the highest vertical stress when the wheel load is directly on the reference point, and as it departs, the magnitude of the vertical stress diminishes in a nonlinear fashion. This constant change in the vertical and horizontal stresses causes rotation of the direction of principal stresses. Therefore, using triaxial loading protocols that use a constant confining pressure (CCP) stress path does not realistically simulate the stresses induced by moving traffic load. Variable dynamic confining pressure (VDCP) type stress path tests offer the possibility of applying dynamic vertical pressure as well as dynamic confinement on the samples in the lab. VDCP type stress path tests were performed on the unbound and stabilized aggregate samples to better simulate the field stresses.

In this study, the RaTT (Rapid Triaxial Test) cell developed by Industrial Process Controls (IPC) in Australia was used for stress path tests. RaTT cell device is controlled by a multi channel data acquisition system that is capable of applying both vertical and dynamic confining pressures. The general setup for the stress path test using the RaTT cell device. The setup, as shown in figure 9-2, is consisted of RaTT cell mounted in universal testing machine (UTM), data acquisition system, and a computer for control

and storage of the data. The RaTT cell can apply both static and dynamic loadings individually in horizontal and vertical directions. The IPC system supports automated cell movement and displacement measurement with linear variable differential transducers (LVDT) for both directions.

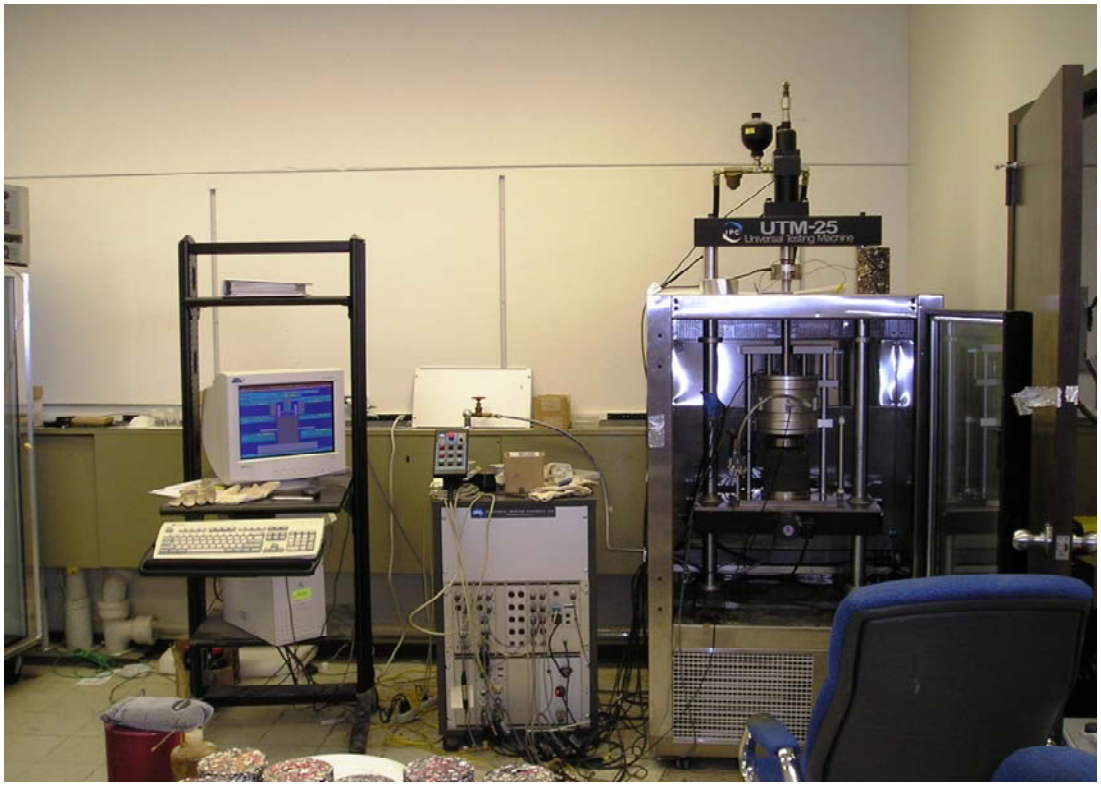

Figure 9-2 Stress path test set-up

Repeated Load Permanent Deformation Test

Repeated load permanent deformation tests were performed to evaluate the laboratory performance of aggregate systems. The samples were tested at a 50 kPa confining pressure and under a 250 kPa dynamic axial stress using a haversine-shaped loading function with 0.1-second load pulse and 0.9-second rest period. The repeated load testing was conducted using a confining pressure of 50 kPa, which is less than the pressure (103.5 kPa) recommended by the NCHRP 1-27 protocol. The reason for designing the

experiment with lower confining pressure was to subject the aggregate systems to more demanding conditions. Lower confining pressure at constant vertical stresses corresponds to less rigid matrixes. Therefore the aggregate systems are more prone to develop larger plastic deformations, and the rate of accumulation of this plastic strain is higher. On the other hand, field measurements of lateral pressure induced by wheel loads on instrumented pavement sections resulted in lateral pressures in the range of 35 kPa to 56 kPa in the base layer (Tutumluer et al. 2003).

Permanent deformation tests continued for 10,000 cycles, until the specimens failed, or until permanent strain reached 10 percent, whichever occurred first. The unbound high fine aggregate systems (V3 and V4) at wet conditions reached the maximum strain criterion, so these tests were terminated before completion of the 10,000 load repetitions.

The permanent deformation test was performed on the aggregate samples approximately 2 hours after compaction without allowing the full strength gain process to take place through the process of pozzolanic reactions and formation of CSH and CAH.

Unconfined Compressive Strength Test

As opposed to the resilient modulus and permanent deformation tests, the unconfined compressive strength test was performed on specimens that were compacted at optimum moisture content. However, these specimens were subjected to capillary soak and conditioned in the moisture room at 32^{o}C and 95 percent relative humidity for 48 hours to ensure moisture equilibrium throughout the entire sample. Capillary soak and moisture conditioning of the samples probably triggered some hydration of cement and added to strength gain.

The test was performed in accordance with ASTM D1633-00. Specimens were tested in the strain-controlled mode with the strain rate equal to 1 percent per minute.

The test was terminated if a sample experienced 5 percent strain or softening occurred to a point where the stress level decreased to about 80 percent of the peak strength.

Aggregate Geometry

Aggregate geometry was characterized in terms of particle form, angularity, and texture using the Aggregate Imaging System (AIMS). Aggregate form defines the flat or elongated nature of aggregate particles. Angularity refers to the sharpness or degree of roundness of aggregate corners. Finally, texture relates to small asperities at the surface of particles that defines surface roughness. More details regarding the AIMS device and testing method can be found in (Kim et al. 2005). Fifty-six (56) aggregate particles from three aggregate sizes of each source were tested with the AIMS device. It is intuitive that aggregate shape, angularity, and texture should affect level of anisotropy as these geometric properties impact the interaction among aggregate particles, especially under compaction and loading induced stresses.

Methylene Blue Test

Methylene blue test was performed on the fine fraction of the aggregate systems to assess the moisture susceptibility of the samples. One of the methods of identifying the deleterious fine particles in the mix is the Methylene blue test. This can be done through quantification of soil suction or by some, simpler surrogate test. In this study we sought to find a simpler index test for this purpose and selected the methylene blue test.

This test (ASTM C832-2003) was adopted to provide a measure of the activity of fine particles in the mix. Several studies showed that the deleterious effect of plastic fines, particularly shrink-swell potential, is strongly correlated with the methylene blue value (Cokca and Birand 1993).

Methylene blue is a large polar organic molecule that is adsorbed onto the negatively charged surfaces of clay minerals. The amount of methylene blue adsorbed by

a given mass of clay depends on the relative concentration of negatively charged sites on the clay particle surfaces as well as surface area of the clay per unit mass.

Several researchers reported that the cation exchange capacity of fine particles can be measured by the absorption of methylene blue dye from an aqueous solution (Fityus et al. 2000) and (Nevins and Weintritt 1967). Figure 9-3 shows experimental relationship between the absorbance and cation exchange capacity. Nevins showed a strong relationship exists between methylene blue value and cation exchange capacity of clay particles. Cation exchange capacity of clay particles were in turn used as a measure of deleterious activity of fine particles manifested as volumetric expansion in geomaterials.

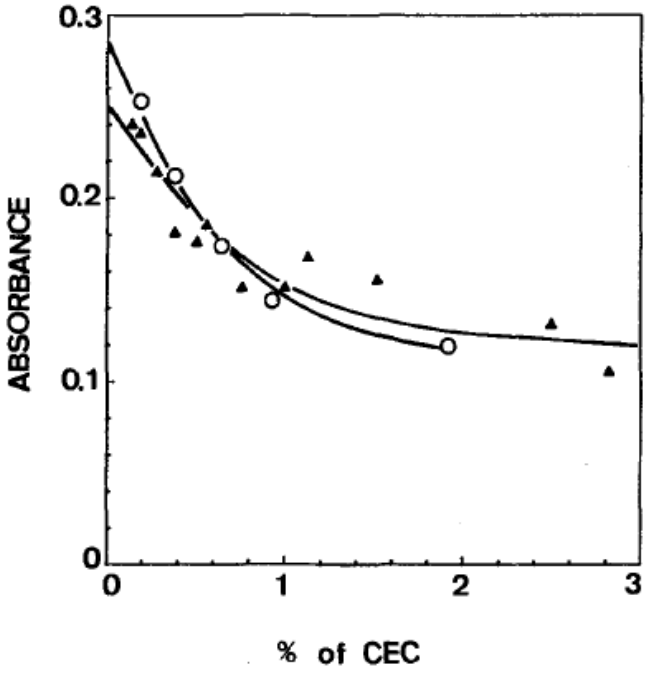

Figure 9-3 Variation of methylene blue absorption with cation exchange capacity (CEC) for two clay sources (After Cenens and Shoonheydt 1988)

According to Gouy-Chapman equation, thickness of water layer adsorbed to the clay surface is proportional to the cation exchange capacity of the clay particles present in the aggregate mix. Equation 9-1 presents the parameters that influence the thickness of the adsorbed water layer adsorbed to clay surface. The thickness of the absorbed water layer controls the swell potential of aggregates and their susceptibility to attract and hold moisture. In general, the thicker the diffused water layer, the less the tendency for particles to folliculate and the higher the swelling pressure in expansive soils.

$$\frac{1}{K} = \left(\frac{D\,k\,T}{8\pi n_o e^2 \nu^2} \right)^{0.5} \tag{9-1}$$

where:

$\frac{1}{K}$ = Thickness of adsorbed water later to the clay surface

n_o = Electrolyte concentration

ν =Cation valance

D = Dielectric constant of the medium

T = Temperature

E = Charge of an electron ($1.60217646 \times 10^{-19}$ c)

k = Boltzmann's constant (1.3807×10^{-16} erg/K)

Since Methylene blue molecules are preferentially adsorbed onto the negatively charged sites on clay surface, titration with Methylene blue can provide a good indication of the cation exchange capacity of clay particle (Fityus et al. 2000). Hence, in this study methylene blue test was adopted as a measure of moisture susceptibility and swell potential in aggregates systems.

The ASTM C832-2003 procedure was used to determine the methylene blue value for 10 aggregate sources. The concept behind the methylene blue test is that a certain amount of materials smaller than 75 microns titrated with Methylene blue dye, and a spot is tested on a filter paper. The addition of more dye to the solution continues until the spot of material absorbs no more dye. This could be evidenced by a lighter blue ring around the spot tested. Figure 9-4 shows a schematic representation of dye absorption by fine particles.

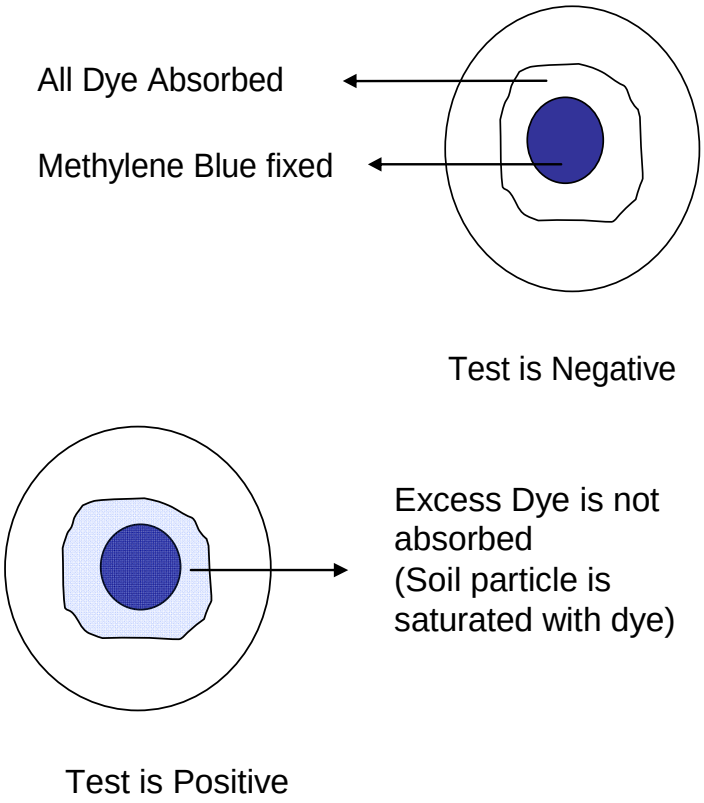

Figure 9-4 Schematic representation of Methylene blue absorption test

Initially, as illustrated in figure 9-4 a faint blue spot of solids was observed surrounded by a transparent ring of clear solution. As the process of addition of methylene blue solution continued, the color of the inner circle became darker due to the fact that the fine particles absorbed more dye. The surrounding solution remained distinct at this stage.

Eventually, the end point is reached when the outline boundary of the inner blue spot breaks down into a light blue-green circle.

Once the blue-green circle appeared, titration was stopped, and the drop test on the filter paper was then repeated five times. If the green-blue circle persists, the end point has been reached; otherwise more methylene blue is added to the solution and titration continued. Once the end point has been reached, equation 9-2 was used to calculate the methylene blue value for each aggregate sample.

$$MBV(gr/100gr) = \frac{[V_{cc}(ml) \times 10(gr) \times 100(gr)]}{1000(ml) \times Ws(gr)} \quad (9\text{-}2)$$

where:

MBV= Methylene blue value

V_{cc} = the volume of methylene blue injected to the soil solution (ml)

W_s = the dry weight of fine particles used (gr)

Dry Compacted Fines

As with the methylene blue test, the authors sought to find a relatively simple and reliable test to assess the impact of the compacted fines on anisotropy. It is intuitive that the level of frictional interaction among the particles of the fines matrix will impact larger aggregate particle interaction and thus anisotropy. In order to characterize the shape properties of the fine portion of the aggregate matrix, a modified Rigden test was performed on particles smaller than 75μ in the aggregate mix. The dry compacted fines test (Rigden voids tests) provides a measure to relate the maximum packing of fine particles to the geometry of particles as well as the uniformity of particle size distribution in the fines portion of the aggregate systems. It is assumed that higher density and tighter packing between fine particles will be achieved in samples with more uniform size

distribution. MODOT-T73 Volume of Voids in Compacted Filler test procedure was followed in this study to calculate the density and void contents of fine particles of 10 aggregate sources.

The test method is based upon the assumption that the densest packing (maximum bulk density) of fines can be obtained by compacting the dry fines in a mold by a 100 gram compaction hammer. More details on sample mold and hammer is presented in figure 9-5. Equations 9-3 through 9-5 were then used to determine the dry compacted air void content in fine aggregate samples. The calculated air void contents were used as inputs to the anisotropy level prediction model.

$$V_{fb} = \frac{\pi D^2 t}{4} \tag{9-3}$$

$$V_{fs} = \frac{W_{fs}}{\gamma_w Gs} \tag{9-4}$$

$$\%DCF = \frac{V_{fb} - V_{fs}}{V_{fb}} \times 100 \tag{9-5}$$

where:

V_{fb} = bulk volume of compacted fines (gr/cm^3)

V_{fs} = volume of the fine solids (cm^3)

t = change in the thickness of the sample (t1-t2) (cm)

d = diameter of the mold (cm)

Wfs= weight of compacted fines (gr)

Gs = specific gravity of solids (gr/cm^3)

%DCF = percentage of voids in dry compacted fines

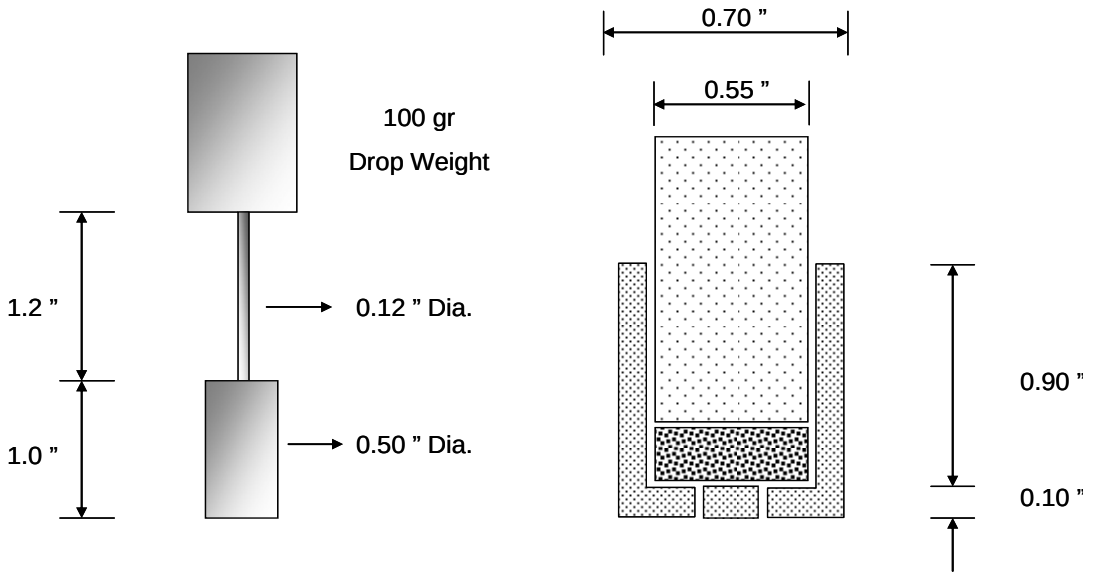

Figure 9-5 Compaction hammer and sample mold used in determination of dry compacted fine aggregates

CHAPTER X

ACCEPTABILITY CRITERIA FOR LIGHTLY STABILIZED HIGH FINE AGGREGATE BASES

INTRODUCTION

This chapter presents the results pertaining to the study of the synergistic effect of fines content and moisture state of unbound as well as lightly stabilized aggregate systems.

Four gradation variants of limestone with fines content (particles smaller than 75 microns) ranging from 5 to 20 percent sourced from Brownwood, Texas, were used in this study. Aggregate specimens were tested in three moisture states, namely dry of optimum, optimum, and wet of optimum. Small percentages of type I cement were incrementally added to the aggregate blends. The aggregate systems were tested as unbound (no stabilizer), with 1 percent and 2 percent type I cement. Specimens were molded at different moisture contents to investigate the impact of saturation level on the performance of aggregate systems.

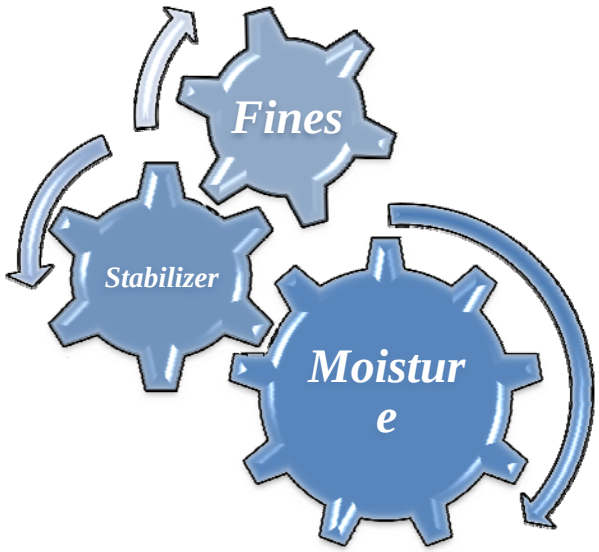

Figure 10-1 Schematic representation of synergistic interaction of stabilizer, moisture content, and fines content

VOLUMETRIC RELATIONS

Aggregate systems were molded according to AASHTO T-180 specification in this study. This method uses a 4.45 kg hammer and a 457 mm drop to simulate field compaction in the lab. Samples were compacted in aluminum cylindrical molds 150 mm in diameter and 150 mm in height, in three 50 mm thick layers, by applying 25 blows for each layer.

After the samples were extruded from the aluminum molds, the samples' weight, diameter, and height were measured and used for calculating the density of the samples after compaction.

Upon completion of the stress path tests, specimens were weighed again and placed in the oven for 48 hours. The dry weights were in turn used to calculate the dry density and void ratio of the specimens. These results are presented in tables 10-1 through 10-6. The following relations were used to calculate the dry density and void ratio of the samples:

$$\gamma_{dry} = \frac{\gamma_{total}}{1+\omega} \tag{10-1}$$

$$S_r = \frac{V_v}{V_s} \tag{10-2}$$

$$e = \frac{G_s \omega}{S_r} \tag{10-3}$$

where:

γ_{dry} = dry density (kg/m^3)

ω = water content (%)

γ_{total} = total density (total weight/total volume) (kg/m^3)

V_v = volume of voids in the sample (total volume – volume of soil) (m^3)

V_s = volume of soil in the sample (m^3)

e = void ratio

G_s = specific gravity

Table 10-1 Moisture Content and Dry Density of Unbound Systems Compacted at Optimum Moisture Content

Unbound @ Wet of Optimum

	Gradation V1	*Gradation V2*	*Gradation V3*	*Gradation V4*
Achieved Moisture Content(%)	7.8	8.3	8.8	9.1
Dry Density(kg/m^3)	1891	1886	1948	1851
Void Ratio(%)	0.40	0.40	0.36	0.43

Table 10-2 Moisture Content and Dry Density of Unbound Systems Compacted at Wet **of** Optimum Moisture

Unbound @ Wet of Optimum

	Gradation V1	*Gradation V2*	*Gradation V3*	*Gradation V4*
Achieved Moisture Content(%)	7.8	8.3	8.8	9.1
Dry Density(kg/m^3)	1891	1886	1948	1851
Void Ratio(%)	0.40	0.40	0.36	0.43

Table 10-3 Moisture Content and Dry Density of 1 Percent Cement Stabilized Systems Compacted at Optimum Moisture Content

1% Cement Stabilized @ Optimum Target Moisture

	Gradation V1	*Gradation V2*	*Gradation V3*	*Gradation V4*
Achieved Moisture Content(%)	6.5	7.4	8.1	9.0
Dry Density(kg/m^3)	2198	2159	2119	2123
Void Ratio(%)	0.21	0.23	0.25	0.25

Table 10-4 Moisture Content and Dry Density of 1 Percent Cement Stabilized Systems Compacted at Wet of Optimum Moisture Content

1% Cement Stabilized @ Wet of Optimum

	Gradation V1	*Gradation V2*	*Gradation V3*	*Gradation V4*
Achieved Moisture Content(%)	10.0	11.4	13.6	10.4
Dry Density(kg/m^3)	1934	2082	2181	2065
Void Ratio(%)	0.37	0.27	0.22	0.28

Table 10-5 Moisture Content and Dry Density of 2 Percent Cement Stabilized Systems Compacted at Optimum Moisture Content

2% Cement Stabilized @ Optimum Target Moisture

	Gradation V1	*Gradation V2*	*Gradation V3*	*Gradation V4*
Achieved Moisture Content(%)	5.8	8.1	7.7	8.8
Dry Density(kg/m^3)	2065	1875	2003	2000
Void Ratio(%)	0.28	0.32	0.32	0.33

Table 10-6 Moisture Content and Dry Density of 2 Percent Cement Stabilized Systems Compacted at Wet of Optimum Moisture Content

2% Cement Stabilized @ Wet of Optimum

	Gradation V1	*Gradation V2*	*Gradation V3*	*Gradation V4*
Achieved Moisture Content(%)	9.9	11.0	13.5	15.0
Dry Density(kg/m^3)	2158	2117	1997	1855
Void Ratio(%)	0.23	0.25	0.33	0.43

RESILIENT PROPERTIES

The influence of fines and moisture content on the properties of the unbound systems was different than on the stabilized systems. Table 10-7 shows the percentage change in the horizontal and vertical moduli for a given gradation with respect to V1 gradation at the same stabilizer content and moisture condition. For the unbound systems, the resilient moduli of V3 and V4 were either the same or slightly higher than that of V1 under the optimum moisture condition. However, under wet of optimum conditions, the increase in fines content had a detrimental effect on the anisotropic resilient moduli of V3 and V4. The horizontal and vertical moduli of V4 were 87 percent and 70 percent less than their V1 counterparts, respectively. Table 3-4 shows that for the stabilized systems, V3 and V4 had higher resilient moduli than V1 under optimum and wet of optimum conditions. In fact, with 1 percent stabilizer, V3 and V4 significantly outperformed V1 under wet of optimum conditions.

Table 10-8 presents the percentage increase in the moduli of the stabilized systems with respect to the unbound systems at the same fines content.

As expected, the addition of the stabilizer increased the resilient properties. The high fines content systems benefited from the stabilizer much more than the low fines content systems. It is interesting to note that V4 gradation stabilized with 1 percent cement significantly outperformed V4 stabilized with 2 percent cement under wet of optimum conditions.

During the laboratory experiments, it was noticed that the V4 system with 2 percent cement molded at wet of optimum condition was much more rigid than the other systems and resulted in initiation of micro-cracks developed during the stress path tests. A plausible explanation for the reduction of the stiffness properties of V4 gradation with 2 percent cement can be associated to initiation and propagation of micro-cracks. As will be discussed later, this behavior was also noticed in the permanent deformation and unconfined compressive strength tests.

Another observation was that higher resilient modulus values were calculated for the stabilized V3 and V4 aggregate systems molded at wet of optimum moisture contents compared to specimens molded at optimum moisture content. This might be due to the fact that the excess water in mix took part in the soil-cement strength gain reactions and further enhanced the resilient properties of lightly stabilized aggregate systems.

Table 10-7 Percent Changes in Anisotropic Resilient Moduli of V3 and V4 with Respect to V1 at the Same Conditions

	Unbound				*1% Cement Stabilized*				*2% Cement Stabilized*			
	Optimum		*Wet*		*Optimum*		*Wet*		*Optimum*		*Wet*	
	V3	***V4***	***V3***	***V4***	***V3***	***V4***	***V3***	***V4***	***V3***	***V4***	***V3***	***V4***
Ex	3	19	-48	-87	32	103	62	288	19	51	7	34
Ey	-3	11	-13	-70	43	32	10	85	25	89	3	9

Table 10-8 Percent Changes in Anisotropic Resilient Moduli of Stabilized Systems with Respect to Unbound Systems

	1% Cement Stabilized						*2% Cement Stabilized*					
	Optimum Moisture			*Wet of Optimum*			*Optimum Moisture*			*Wet of Optimum*		
	V1	***V3***	***V4***	***V1***	***V3***	***V4***	***V1***	***V3***	***V4***	***V1***	***V3***	***V4***
Ex	*-10*	*15*	*54*	*20*	*276*	*3442*	*6*	*22*	*35*	*31*	*171*	*1231*
Ey	*-20*	*18*	*-5*	*12*	*42*	*599*	*-17*	*8*	*42*	*6*	*25*	*289*

ANALYSIS OF THE DEGREE OF ANISOTROPY

Structural capacity of particulate systems depends on stiffness properties in orthogonal directions. The ratio of horizontal modulus to vertical modulus is referred to as modular ratios, and the level of the anisotropy of aggregate systems was characterized by this ratio in this study. When this ratio equals one, the system is fully isotropic. The level of anisotropy increases as the modular ratio decreases.

Figure 10-2 shows that increase in the fine content slightly reduced the level of anisotropy of the aggregate systems at optimum moisture contents. At high saturation levels however, the modular ratio dramatically decreased as more fines were introduced to the systems as illustrated in figure 10-2. Figures 10-3 and 10-4 present modular ratios for stabilized systems.

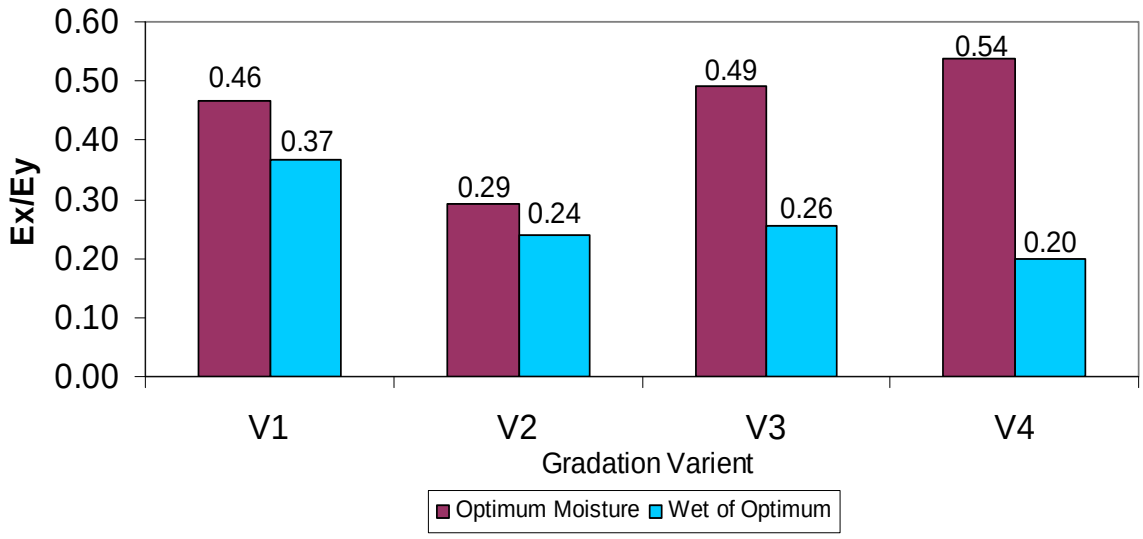

Figure 10-2 Average modular ratios for unbound aggregate systems

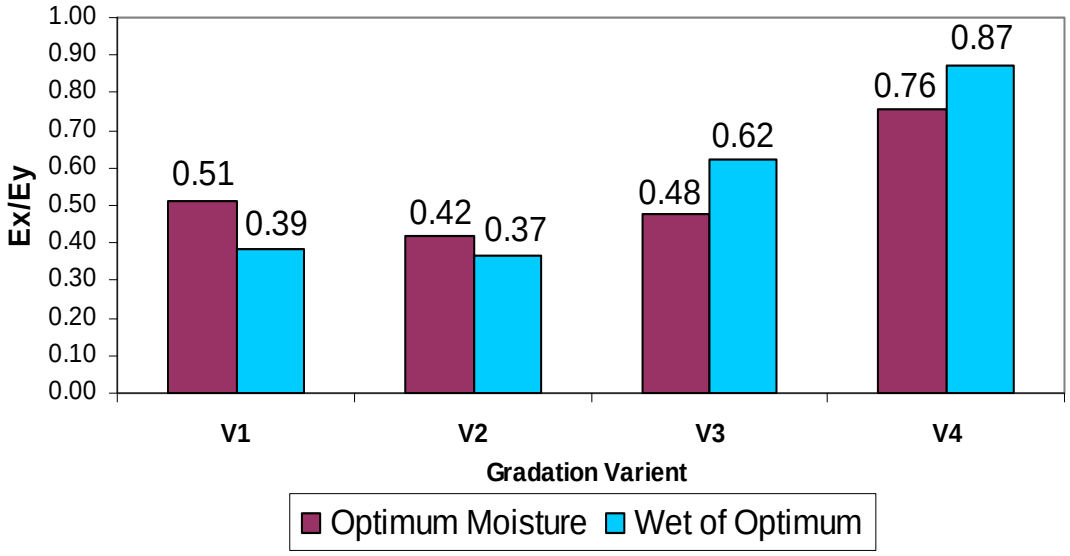

Figure 10-3 Average modular ratios for 1 percent cement stabilized aggregate systems

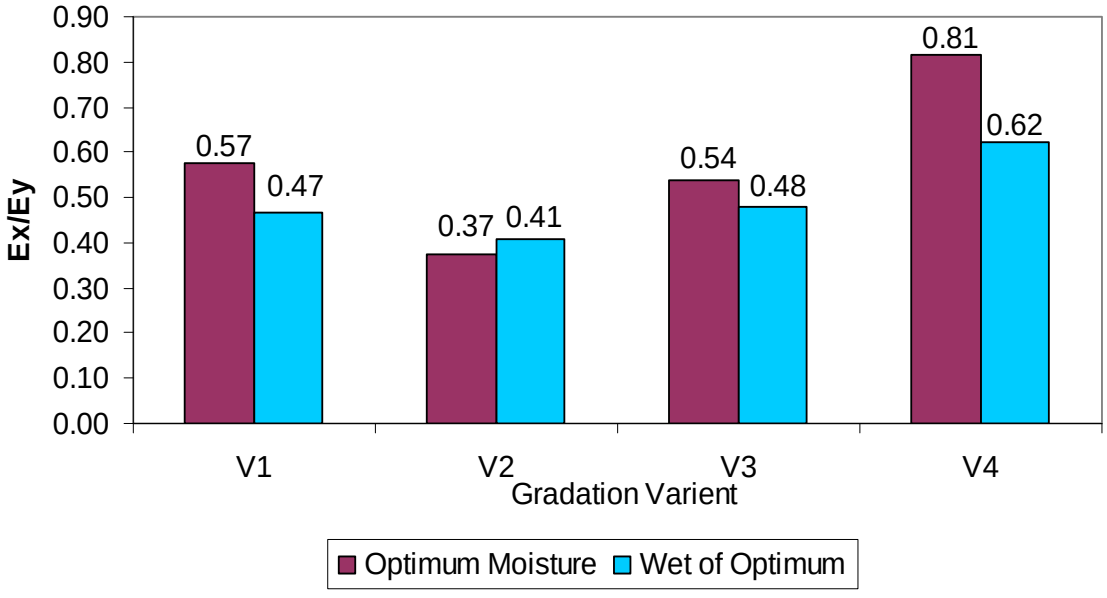

Figure 10-4 Average modular ratios for 2 percent cement stabilized aggregate systems

Figure 10-3 shows the anisotropy of the systems decreases as low levels of stabilizer is added to the system. Aggregate systems molded at optimum moisture condition and at wet of optimum moisture conditions showed the same trend. Aggregate systems with more fine contents benefited more from the low level of stabilizer when compared to control system V1.

Using modular ratios as a measure of the level of anisotropy revealed that even a small percentage of stabilizers significantly reduced the level of anisotropy of aggregate systems. When this result is combined with the stress path test result, it is revealed that low levels of stabilization not only improved the stiffness in orthogonal directions but reduced the anisotropy of the system and hence improved load distribution capacity of lightly stabilized aggregate systems.

It is important to note here that level of anisotropy or modular ratios cannot be exclusively considered as a measure of the performance of aggregate systems.

ANALYSIS OF DEGREE OF NONLINEARITY

Detailed discussion on methodology for determination of the level of anisotropy in geomaterials was presented in Chapter II. Figure 10-5 through 10-6 presents the plots for analysis of nonlinearity of unbound and stabilized systems.

Figure 10-5 shows the variation of the degree of nonlinearity based on the deviatoric stress ratios in the aggregate samples. Figure 10-4 clearly shows that using (q_f/q_r) resulted in a physically meaningful plot of the data. As illustrated in Figure 10-4, adding fines to the mix in unbound systems (0 percent stabilizer) resulted in a significant increase in the degree of nonlinearity of the aggregate samples. Figure 10-4 also shows the drastic reduction in the level of nonlinearity of the aggregate systems when small percentages of stabilizer were added to the system. Figure 10-5 and Figure 10-6 are another representation of the analysis of nonlinearity in aggregate samples. Figure 10-7 illustrates the change in the degree of nonlinearity characterized by (q_f/q_r) as the stabilizer content increases in the mix. A nonlinearity characterizer ($\varepsilon_f/\varepsilon_r$) was used to study the impact of stabilizer content on the reduction of the level of nonlinearity in the aggregate blends. Both figures show that the aggregate samples with low percentages of stabilizer were significantly less nonlinear than their unbound counterparts.

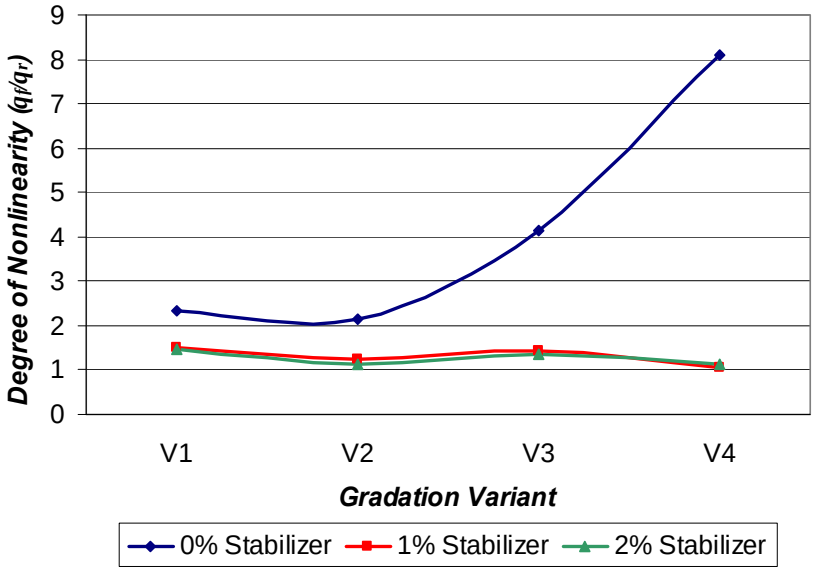

Figure 10-5 Variation of the degree of nonlinearity based on deviatoric stress ratios

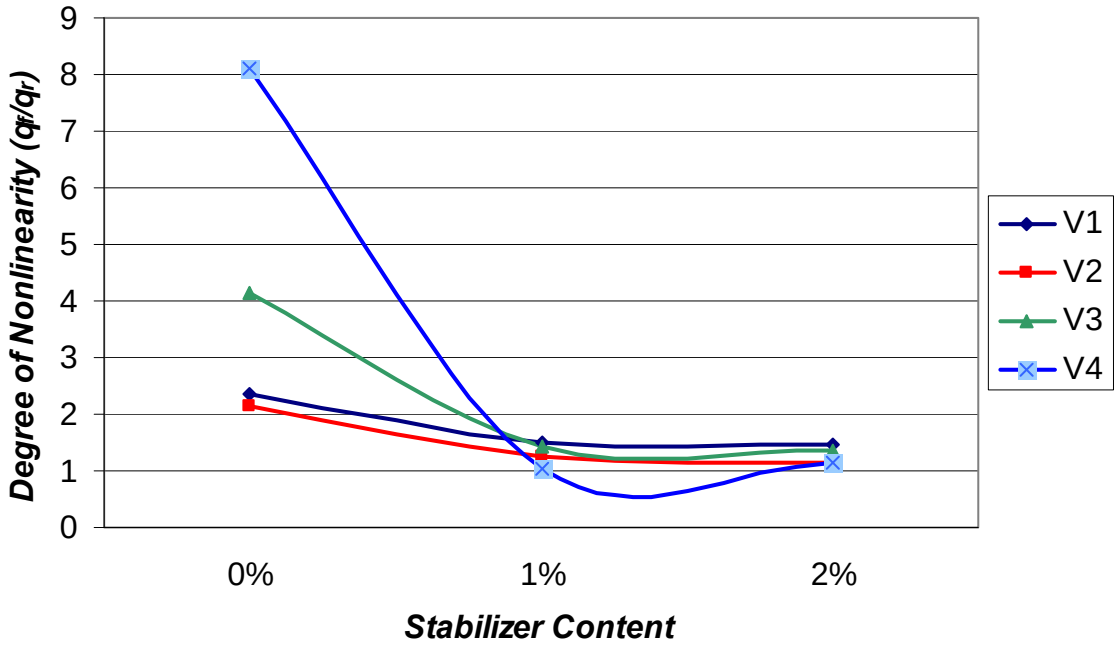

Figure 10-6 Analysis of the degree of nonlinearity based on deviatoric stress ratios

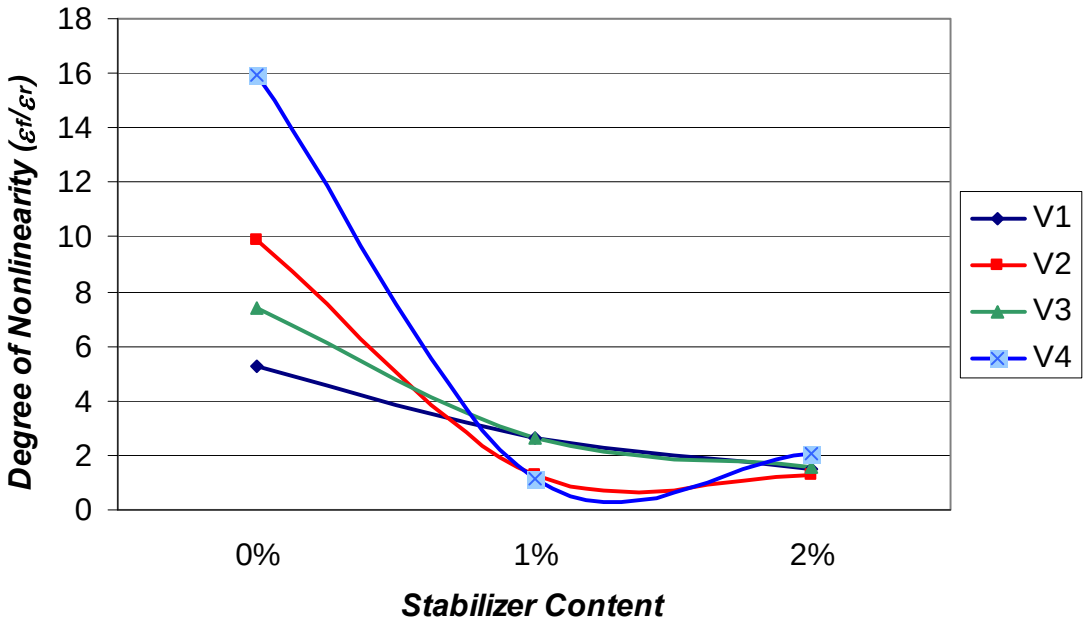

Figure 10-7 Analysis of the degree of nonlinearity based on strain ratios

PERMANENT DEFORMATION TEST RESULTS

The repeated load permanent deformation test was performed to assess the laboratory performance of aggregate systems. The aggregate samples were subjected to 10,000 load cycles with a 0.1 second loading pulse and a 0.9 second rest period. The samples were tested at 35 psi dynamic axial stress and 7 psi constant confining pressure.

Figures 10-8 through 10-12 present the plots showing accumulation of plastic strains under constant confining pressure stress path tests for various aggregate systems.

Figure 10-8 shows a permanent deformation result for gradation V1 at wet of optimum and at different stabilizer contents. This plot clearly shows that gradation V1 significantly benefited from low levels of stabilizer in the mix in terms of lower plastic deformations at the end of 10,000 loading cycles.

This plot also shows that adding low levels of stabilizer reduced the nonlinearity of the aggregate systems. In other words, the plastic strain curves for the stabilized systems reached an asymptotic value after around 1500 load cycles while the slope of curve for the unbound system was still increasing after 10,000 load repetitions.

These phenomena can be explained based on the Shakedown theory. More details on the shakedown theory and concept behind categorizing the aggregate systems based on this approach have been provided in Chapter VII.

Based on the Shakedown concept, the stabilized systems plotted in this figure can be categorized as systems below the plastic shakedown limit while the unbound system falls into the plastic creep category. Shakedown approach suggests that the stabilized systems are less prone to develop plastic deformations in the field compared to the unbound system at elevated saturation levels.

Figure 10-9 shows the accumulation of plastic strains as a function of number of load applications for gradation V3 with high fine contents molded at optimum moisture content.

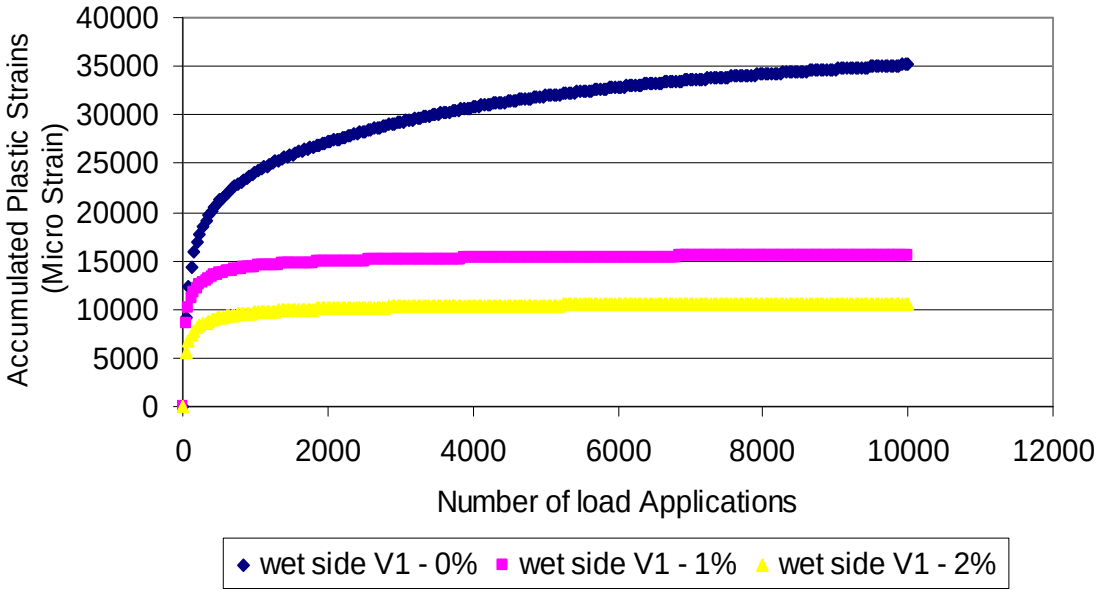

Figure 10-8 Permanent deformation results for gradation V1 at wet conditions

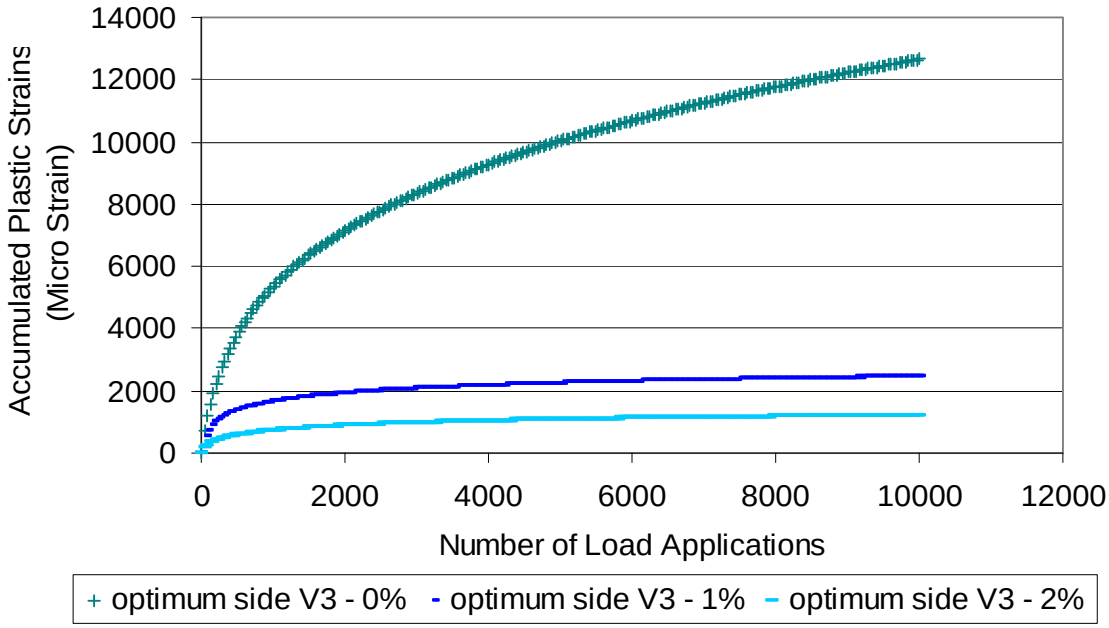

Figure 10-9 Permanent deformation results for gradation V3 at wet conditions

This plot shows an increasing rate of accumulation of plastic strains with the number of load applications for the unbound system V3. Figure 10-9 also indicates the beneficial effect of adding small percentages of stabilizer to high fines content aggregate systems. As illustrated in this plot, stabilized aggregate systems significantly outperformed the unbound system in terms of accumulated plastic deformation developed in the end of the test. This plot also shows a light level of stabilizer reduced the nonlinearity of the aggregate systems.

Figure 10-10 shows the cumulative permanent deformation curves for high fines content gradation V4 with 20 percent passing sieve #200 at optimum moisture content. As illustrated in this plot, unstabilized gradation V4 developed high nonrecoverable deformations compared to stabilized systems at the end of the test. The rate of the accumulation of plastic deformation was observed to be much higher compared to stabilized systems. The results for V4 stabilized systems showed that the rate of accumulation of plastic deformation for 1 percent and 2 percent stabilized systems were very close at optimum moisture state. However, the rate of accumulation of plastic strains and magnitude was found to be significantly different. More discussion on this will be presented later in this section.

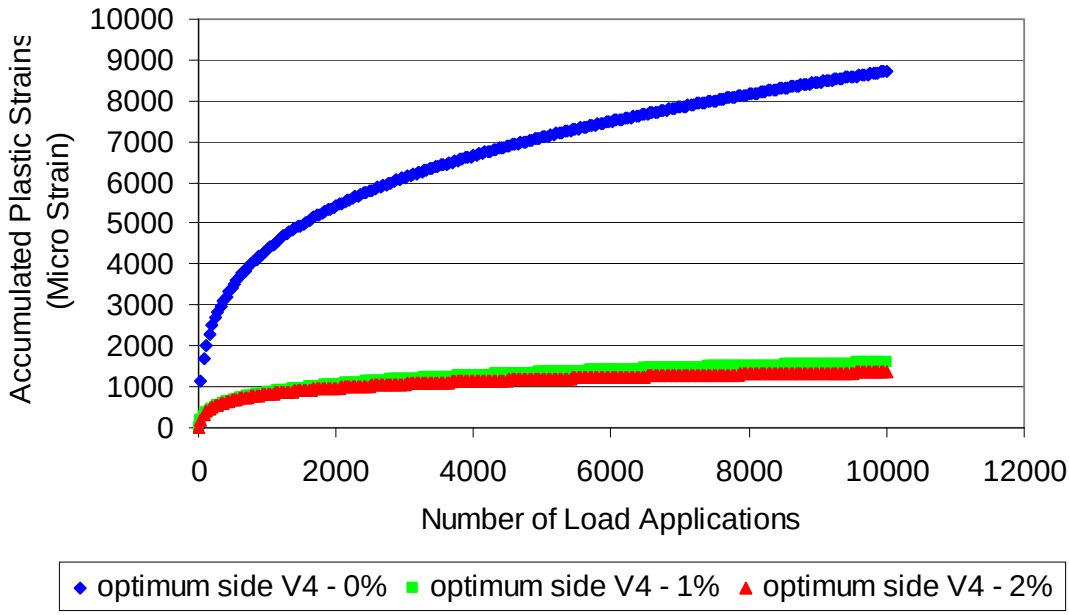

Figure 10-10 Permanent deformation results for gradation V4 at wet conditions

Figure 10-11 and figure 10-12 present comparison plots for plastic deformation curves for 2 percent Portland cement stabilized systems with varying fine contents.

Figure 10-11 shows that the magnitude of plastic deformation measured at the end of 10,000 load cycles was significantly higher for control gradation V1 compared to gradations V3 and V4 with high fines contents molded at optimum moisture. In other words high fines content systems were found to benefited more from small levels of stabilization at optimum water content.

Figure 10-12 shows the permanent deformation test results for two percent Portland cement stabilized systems with different fines content molded at wet of optimum moisture content. This plot shows that gradation V3 with 15 percent fines content and two percent stabilizer content outperformed the control gradation V1 with two percent stabilizer.

This plot indicates that gradation V4 performed the poorest in terms of plastic deformation compared to gradations V1 and V3 at wet conditions. This might be due to the synergistic effect of fines content and moisture content in the mix. In other words using low levels of stabilization in gradations containing high amounts of fines does not seem to be a favorable solution to mitigate rutting in pavement foundations at wet climatic cycles.

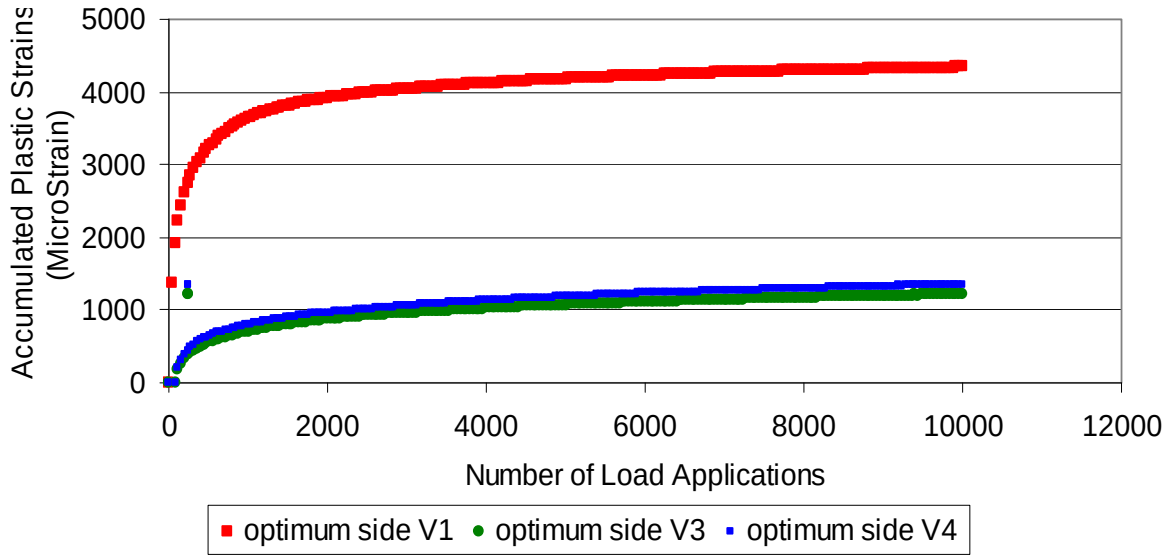

Figure 10-11 Permanent deformation results for 2 percent cement stabilized systems at optimum moisture conditions

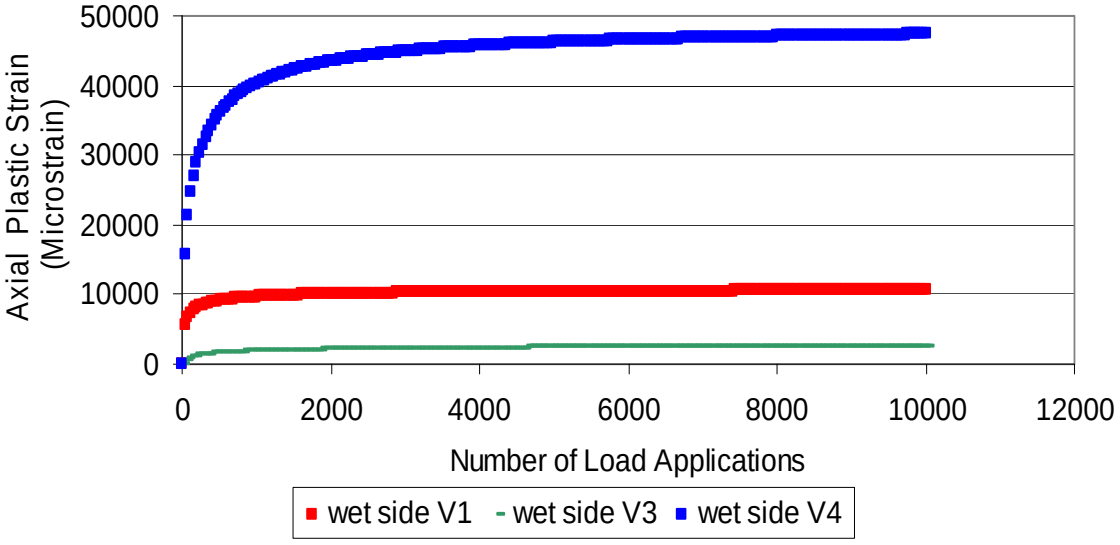

Figure 10-12 Permanent deformation results for 2 percent cement stabilized systems at wet conditions

Figures 10-13 and 10-14 present the summary of the plastic deformation measures at the end of 10,000 load cycles or as the aggregate systems reached failure.

The unbound aggregate systems with high fines content (V3 and V4) under wet of optimum conditions reached the maximum strain criterion of 10 percent, and consequently these two tests were terminated before the completion of the 10,000 cycles. The results in Figure 10-13 confirm the deleterious effect of high fines content under wet of optimum conditions on aggregate systems. In the systems with 1 percent Portland cement, adding more fines resulted in a general trend of a lower plastic strain regardless of the moisture content. The same trend was observed for the systems with 2 percent Portland cement at optimum moisture content (figure 10-13), but it differed for the wet of optimum moisture content since V4 performed poorest at 2 percent stabilizer (figure 10-14). A plausible explanation for this result is that when both the fines content and cement content are high, a more rigid fines matrix results. Such a matrix is likely to be more susceptible to the development of cracks and, therefore, more prone to base layer damage that is reflected in plastic deformation. This finding is in agreement with the analysis of resilient properties.

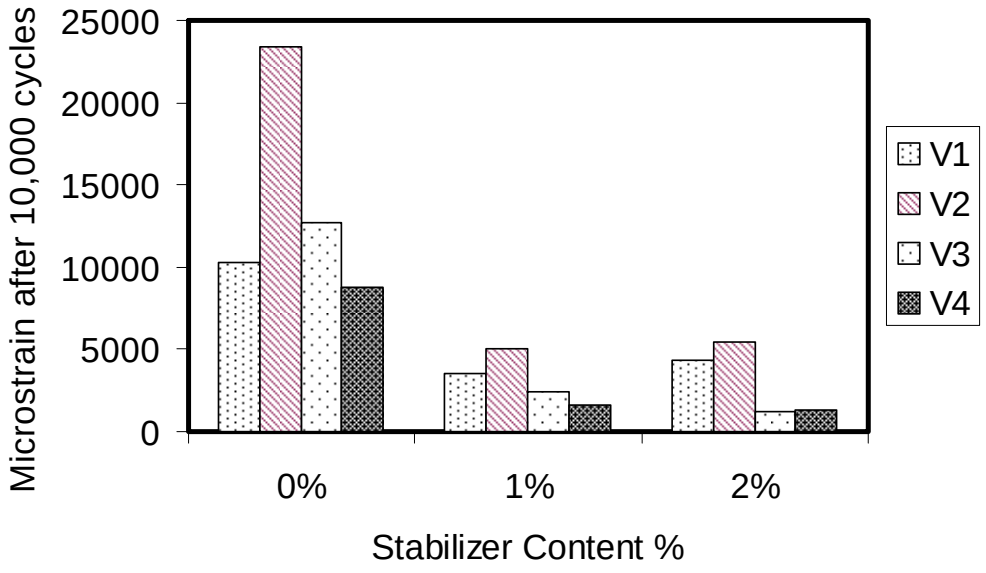

Figure 10-13 Comparison of permanent strain after 10,000 load cycles at optimum moisture content

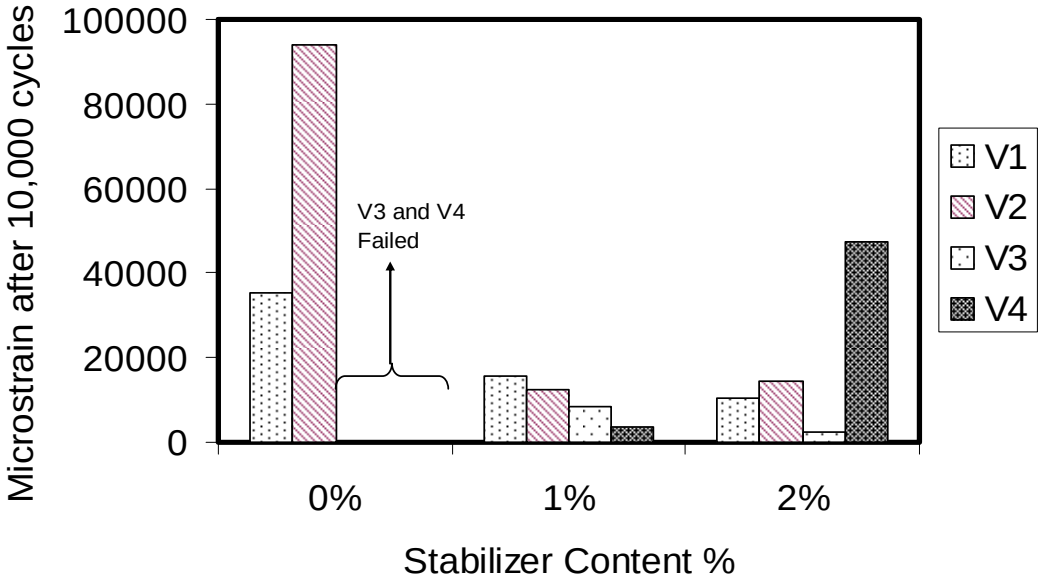

Figure 10-14 Comparison of permanent strain after 10,000 load cycles at wet of optimum moisture content

UNCONFINED COMPRESSIVE STRENGTH

Unconfined compressive strength tests were performed on specimens compacted at optimum moisture content and then subjected to moisture conditioning. The conditioning time allowed moisture to reach the top of the samples through capillary pores. The diffused water not only provided moisture for cement hydration but also provided moisture that impacted the strength and stability of the fines fraction.

The trends in figure 10-15 clearly demonstrate the beneficial effect of light levels of stabilizers on the unconfined compressive strength of the samples tested. Strength properties of unbound aggregate systems were observed to be lower than the stabilized systems as expected. Among the stabilized systems at each stabilizer content, gradation V4 typically demonstrated lower strength compared to other stabilized gradations.

Figure 4-3 shows that the highest strength value was achieved in gradation V3 with 2 percent stabilizer. This figure also shows that the unconfined compressive strength

value can be used as a controlling measure to set limits on the amount of fines used in lightly stabilized aggregate systems.

The trends in figure 10-15 show a tendency toward an asymptotic value for unconfined compressive strength values with increasing stabilizer content for each gradation. This suggests that there probably exists an optimum stabilizer content for each gradation at which the gradient of the curves becomes zero. This point probably corresponds to a stabilizer-fines content ratio that results in maximum unconfined compressive strength.

Figures 10-16 and 10-17 show the micro-cracks and the damage induced by shear stress test on the samples.

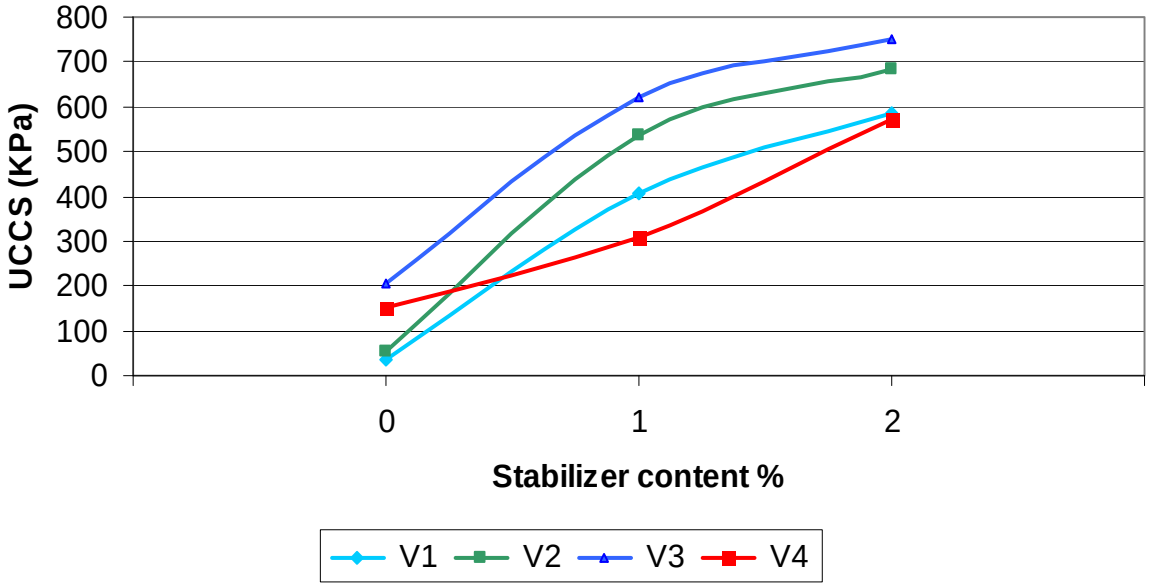

Figure 10-15 Unconfined Compressive Strength for Conditioned Aggregate Systems

Figure 10-16 Integrated cracking in 2 percent cement stabilized high fines system V3

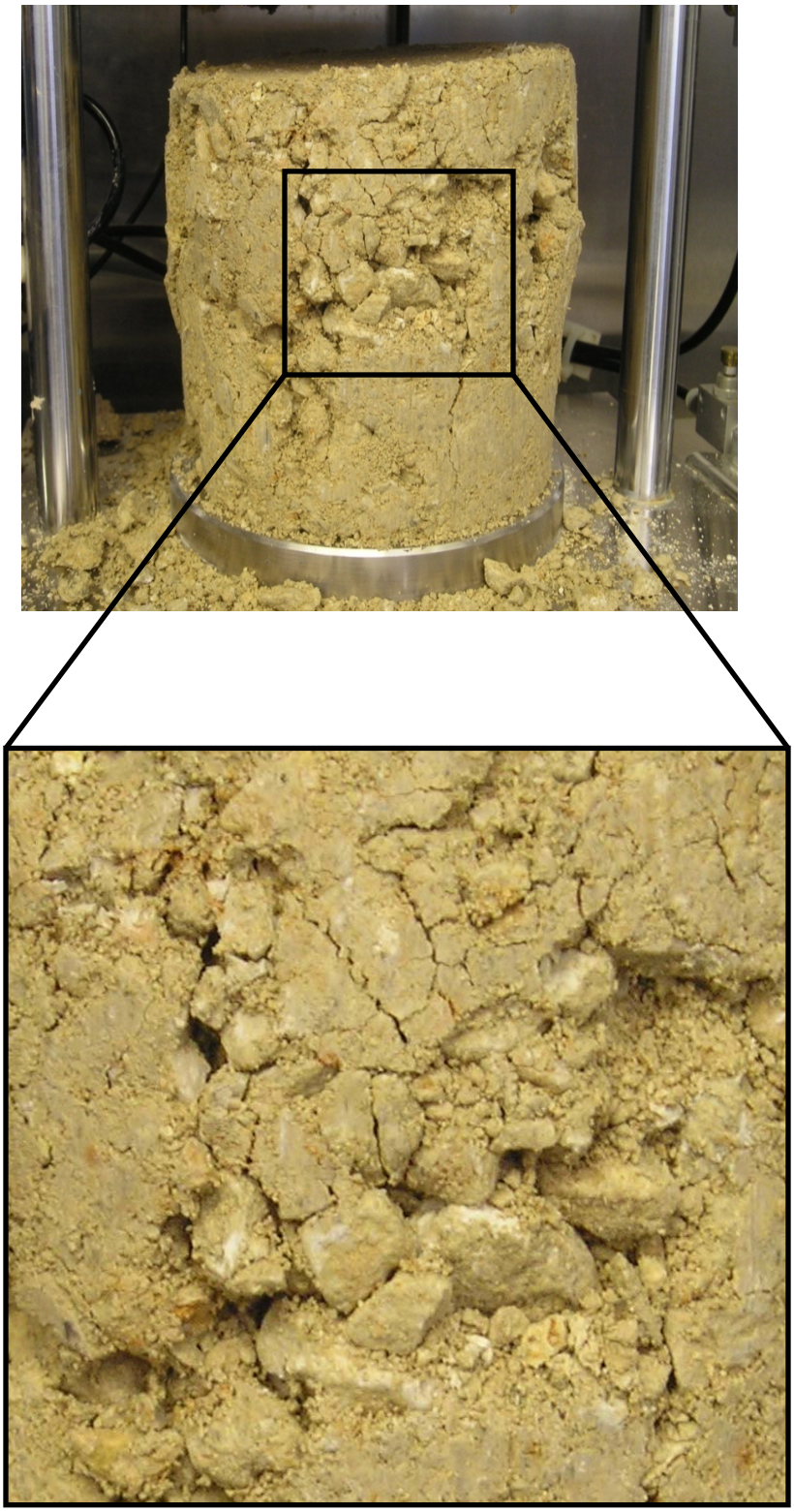

Figure 10-17 Degradation of particles for coarse gradation V1 at dry conditions

VISUAL INSPECTION OF FINES UNDER LIGHT MICROSCOPE

A qualitative visual investigation of the geometry of the fine portion of the gradations were performed on materials passing sieve #100 (particles smaller than 15 mm) and materials passing sieve #200 (particles smaller than 75 microns). The fine particle was placed in the oven for 48 hours and the samples were in turn placed under light microscope. The pictures of the fine portion of the mixes taken under light microscope are presented in Appendix C of this dissertation.

Figures C-1 through C-10 indicate that the crushed siliceous gravel and crushed granite materials have more angular edges compared to limestone materials. It was also observed that surface microstructure for granite materials were more distinct compared to limestone materials.

Figure 10-18 Light microscope image of siliceous gravel (A6) smaller than 0.15 mm (Passing Sieve #100)

FINITE ELEMENT ANALYSIS

Anisotropic material properties calculated in this study were used in a finite element program to investigate the synergistic effect of stabilizer content, moisture state, and fines content on the response of aggregate layers in the field. The finite element analysis was performed using the TTI-PAVE software to analyze a pavement structure. Anisotropic material properties presented in equations 10-4 to 10-6 in conjunction with k-values presented in equation 2-23 were used as input to the finite element program.

$$n = \frac{E_x}{E_y} \tag{10-4}$$

$$m = \frac{G_{xy}}{E_y} \tag{10-5}$$

$$\mu = \frac{\nu_{xx}}{\nu_{xy}} \tag{10-6}$$

E_x and E_y= Modulus in horizontal and vertical directions, respectively

G_{xy}=Shear modulus in xy plane

ν_{xx}=Poisson ratio in horizontal direction when loading is in horizontal direction

The analysis was conducted using an axisymmetric finite element mesh with eight node elements in three layers. Nonlinear anisotropic solutions were used to calculate the response of the aggregate layers under simulated wheel load. A tire pressure of 100 psi acting on a circular area with a radius of 5.5 inches was used in the analysis.

The pavement section consisted of a 6 inch linear isotropic asphalt layer with a modulus of 400,000 psi and a Poisson's ratio of 0.35 resting on a 16 inch thick nonlinear anisotropic aggregate base layer was considered in this study. The base layer was modeled using the material properties of the aggregate systems listed in Table 10-9. The

pavement was assumed to be supported by a soft subgrade with a modulus of 6000 psi and Poisson's ratio of 0.45.

Table 10-9 Material Parameters of the Aggregate Systems

Gradation	Stabilizer Content (%)	Moisture Content (%)	$\gamma_{d\ max}$ (kg/cm^3)	$n=E_x/E_y$	$m=G_{xy}/E_y$	γ_{xx}/γ_{xy}
V1 (Wet)	0	7.8	2142	0.37	0.16	1.51
	1	9.9	2181	0.39	0.23	1.79
	2	5.8	2065	0.47	0.29	1.62
V3 (Optimum)	0	7.9	1948	0.49	0.24	2.36
	1	8.1	2119	0.48	0.33	2.49
	2	7.8	2100	0.54	0.39	2.25
V3 (Wet)	0	8.8	2054	0.26	0.2	1.76
	1	10.4	2032	0.62	0.25	1.55
	2	7.7	2102	0.48	0.35	1.56
V4 (Wet)	0	9.3	1851	0.2	0.12	0.77
	1	10.7	2064	0.87	0.34	1.95
	2	9.1	2084	0.56	0.28	2.04

Analysis of Critical Strains

Table 10-10 presents the critical pavement responses, namely vertical strain at the top of the subgrade and horizontal strain at the bottom of the asphalt layer.

As tabulated in table 10-10, critical pavement responses in stabilized systems were calculated to be lower than the critical strains in unbound systems, which is synonymous with greater pavement life in stabilized systems.

Table 10-10 shows an aggregate layer with parameters pertaining to gradation V3 with 2 percent stabilizer performed better in terms of lower critical strains at wet of optimum moisture conditions compared to its counterpart molded at optimum moisture conditions. As discussed earlier, this could be the result of additional water in the stabilized system triggering additional cement hydration reactions.

Table 10-10 Finite Element Results of Critical Pavement Responses

	Stabilizer(%)	*Strain @ Bottom of Asphalt*	*Strain @ Top of Subgrade*
	0	5.683E-04	1.680E-03
V1 *(Wet)*	*1*	2.613E-04	1.332E-03
	2	2.562E-04	9.113E-04
	0	4.62E-04	1.05E-03
V3 *(Optimum)*	*1*	4.43E-04	1.12E-03
	2	6.70E-04	1.11E-03
	0	8.015E-04	1.890E-03
V3 *(Wet)*	*1*	6.623E-04	1.525E-03
	2	1.546E-04	7.956E-04
	0	9.922E-04	2.205E-03
V4 *(Wet)*	*1*	3.437E-04	1.199E-03
	2	2.195E-04	1.047E-03

Figure 10-19 and Figure 10-20 show comparisons of the critical pavement responses when the material parameters pertaining to wet conditions were considered for the base layer. For the case of stabilized systems, the high fines content systems V3 and V4 performed either similar to or in some cases better than the control system V1. The greatest improvement was observed for gradation V3 with 15 percent passing sieve #200 when 2 percent stabilizer was added to the mix.

It is interesting to note that finite element analysis results were in conformity with the laboratory results of permanent deformation and unconfined compressive strength tests.

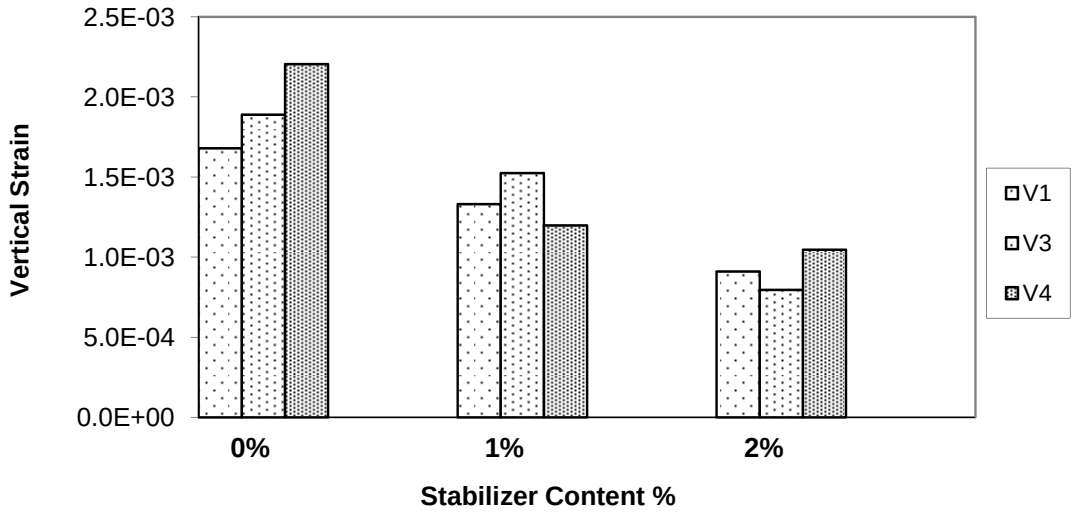

Figure 10-19 Comparison of vertical strains at the top of the subgrade for a pavement structure with different aggregate systems tested under wet conditions

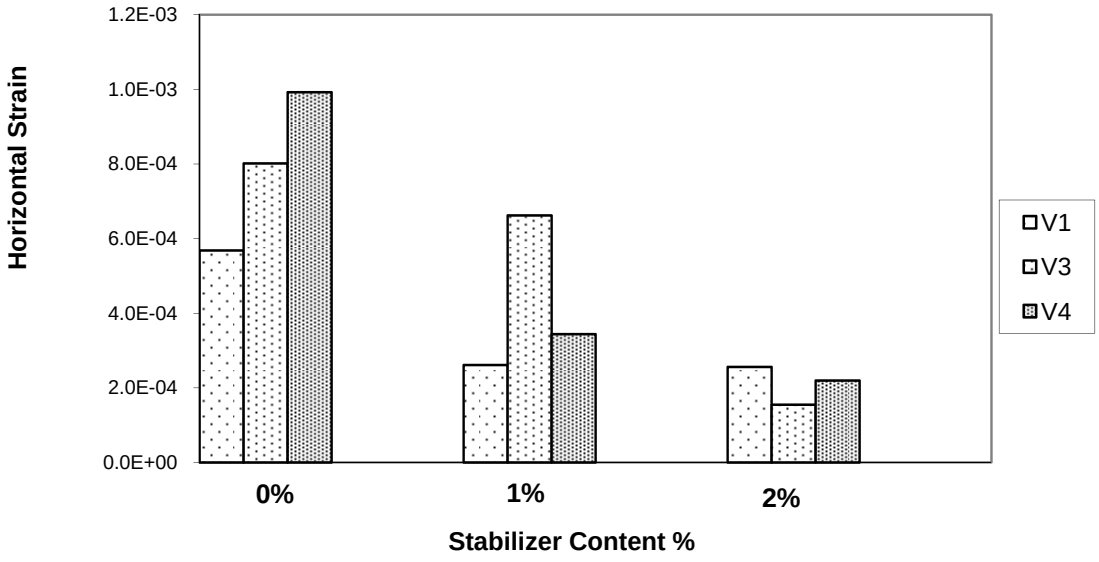

Figure 10-20 Comparison of tensile strains at the bottom of the asphalt for a pavement structure with different aggregate systems tested under wet conditions

Analysis of the Shear Stresses Developed in the Base Layer

Nonlinear and anisotropic solutions were used to calculate the shear stresses developed in the base layer under simulated traffic load for unbound and stabilized systems. Figure 10-21 through figure 10-23 present the contour plots of shear stresses in the base for selected systems. The significance of shear stresses is the fact that several measures of the stability of aggregate layers were based on the ratio of a measure of shear stress to a measure of strength determined in lab. Detailed discussion on the stability control of pavement foundations was presented in Chapter VII.

Figure 10-21 presents the shear stress distribution in base layer using material parameters pertaining to gradation V1 at optimum moisture conditions. Figure 10-21 shows that maximum shear stress occurred at the top of the base layer and aligned at the edge of the tire. The magnitude of shear stress was calculated to be 17.3 psi for the controlled system with gradation V1.

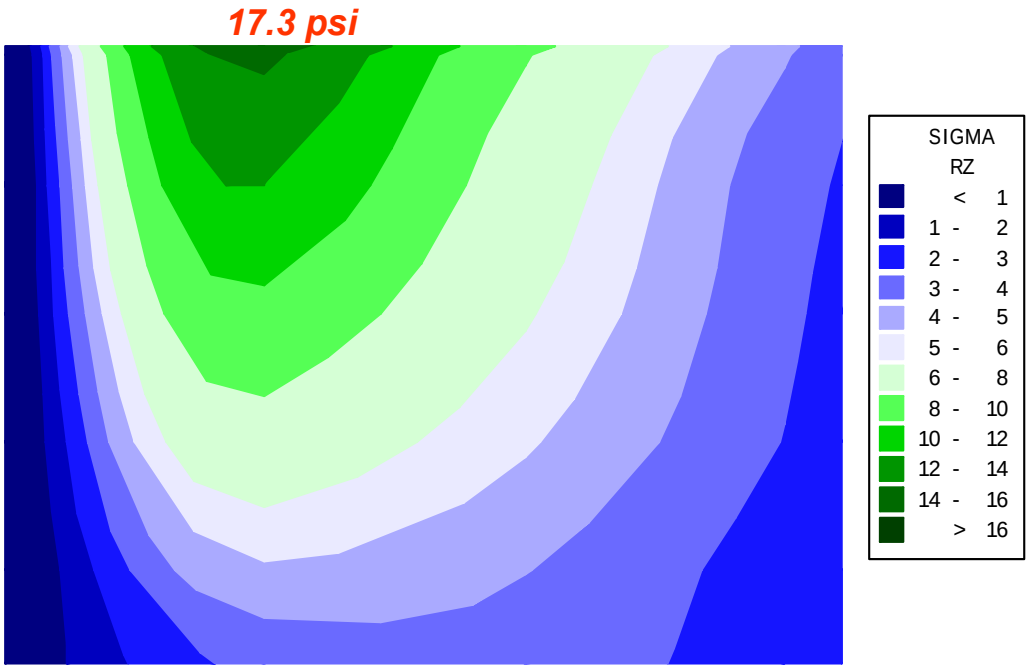

Figure 10-21 Shear stress distribution in the base layer for controlled system V1

Figure 10-21 and Figure 10-22 show the shear stresses developed in the base layer with material parameters pertaining to gradation V3 with 30 percent passing sieve #40 and 15 percent passing sieve #200. Figure 10-22 shows the shear stress distribution in an unbound V3 system whereas figure 10-23 shows the contour plot of shear stresses throughout the 2 percent Portland cement stabilized base layer. Material parameters for both systems were selected at wet of optimum moisture conditions to reflect the impact of moisture state on the mechanical responses of aggregate layers.

Figure 10-22 shows the shear stress distribution in the base layer for gradation V3 under wet conditions. Maximum shear stress developed in the aggregate layer was 24.6 psi. Comparing the maximum shear stress developed at wet conditions in fine system V3 and control system V1, it was observed that moisture intrusion in unstabilized high fines systems results in 29 percent higher shear stresses, which might translate into instability of the aggregate layer.

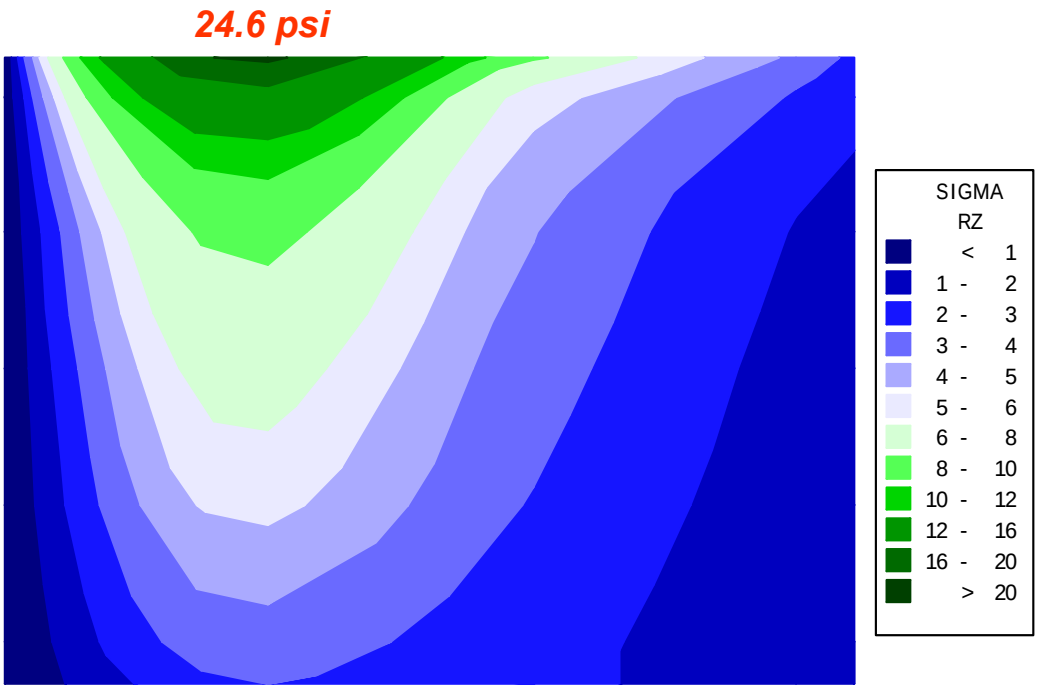

Figure 10-22 Shear stress distributions in the base layer for unstabilized V3 system under wet conditions

Figure 10-23 shows the shear stresses developed in the base layer for a lightly stabilized system. V3 system anisotropic material properties for gradation V3 stabilized with 2 percent Portland cement and molded at wet of optimum moisture conditions were used as inputs to a finite element program to calculate shear stresses and generate Figure 10-23.

Maximum shear stress was calculated to be 8.2 psi for this variant. The results clearly indicate significant reduction in the shear stresses developed in the base layer when 2 percent type I cement was added to the high fine aggregate system. The maximum shear stress was reduced by 200 percent at the top of the subgrade for the 2 percent cement stabilized V3 system when compared to the same unstabilized system V3 at equal moisture states.

The lightly stabilized high fines content gradation V3 has performed better in terms of lower shear stresses developed in the base layer. Analysis of the shear stresses calculated in the unbound and stabilized systems indicates that light stabilization of the high fines content system can significantly reduce the shear stresses developed in the pavement foundations.

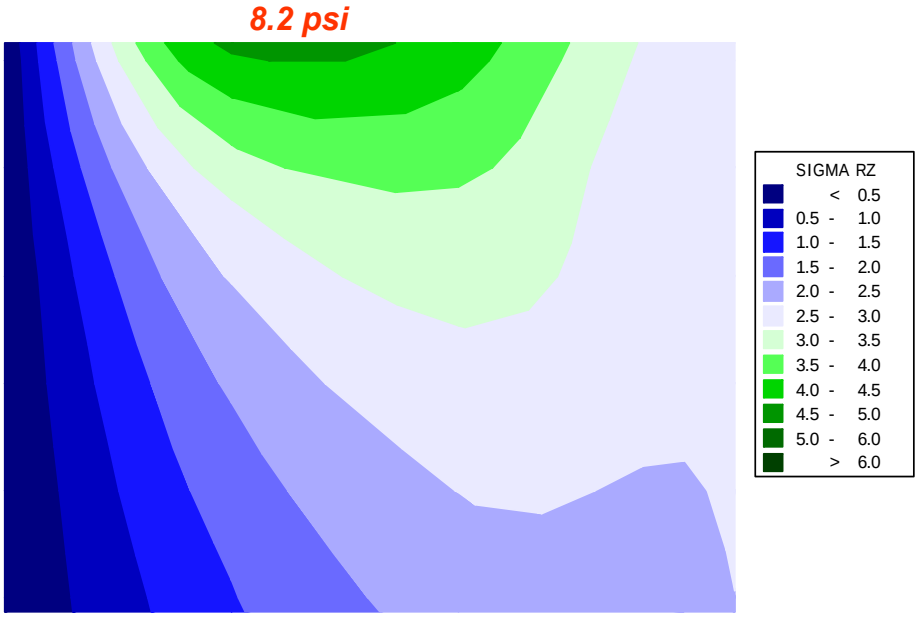

Figure 10-23 Shear stress distribution in the base layer for 2 percent cement stabilized system V3 under wet conditions

ANALYSIS OF PERFORMANCE

General

Several researchers suggested the shear strength ratio as a measure of the performance of aggregate layers. Shear strength ratio is basically the ratio of a measure of shear stress to a measure of strength in the aggregate systems. This concept was primarily developed by (Thompson 1990b) for NCHRP 1-26 for the stability control of subgrade soils. He used the ratio of deviatoric stress to unconfined compressive strength of the subgrade soils (σ_d/UCCS) as a measure of performance of subgrade soils. Thompson also showed that a reasonable relationship exists between field rutting data and the shear strength ratio of subgrade. He concluded that there is a limiting value for (σ_d/UCCS), above which the subgrade is prone to permanent deformation. He suggested a limiting value for the stress ratios to be below 0.4 to ensure the stability of subgrades subjected traffic loads. More discussion on this is presented in Chapter XI.

Based on this concept, the ratio of maximum octahedral shear stress $(\tau_{oct})_{max}$ calculated in the base layer to the unconfined compressive strength of the aggregate systems determined in lab was used as a performance indicator in this study, as seen in equation 10-7. The value of $(\tau_{oct})_{max}$ was calculated using anisotropic solutions and used as input to equation 5-5.

$$Shear\ Strength\ Ratio\ (SSR) = \frac{Octahedral\ Shear\ Stress\ at\ Top\ of\ \ Base\ Layer}{Unconfined\ Compressive\ Strength} \qquad (10\text{-}7)$$

It should be noted here that the shear stresses calculated due to traffic loads found from the anisotropic solutions are typically higher than shear stresses found from the isotropic solutions, which ultimately results in higher stress ratios. As mentioned earlier in this chapter, higher shear stress ratios correspond to situations in which the stability of the pavement is in jeopardy, and the base layer is prone to develop non-recoverable plastic deformations.

Analysis of Shear Strength Ratios

Anisotropic solutions were used to calculate the octahedral shear stresses in the base layer. Equation 10-7 was in turn used to generate the shear strength plots. Figure 10-24 and Figure 10-25 show the distribution of the shear strength ratios developed in the base layer. As mentioned earlier, the position of maximum shear stresses and consequently maximum shear strength ratios were found to be aligned with the edge of the tire and occur at the top of the base layer.

Figure 10-24 presents the contour plot for the distribution of shear strength ratios for a high fines content system V3 at wet conditions. As evidenced in these figures, shear strength ratios vary in a nonlinear fashion throughout the aggregate layer. The maximum shear strength ratio was calculated to be 0.43 at the top of the aggregate layer.

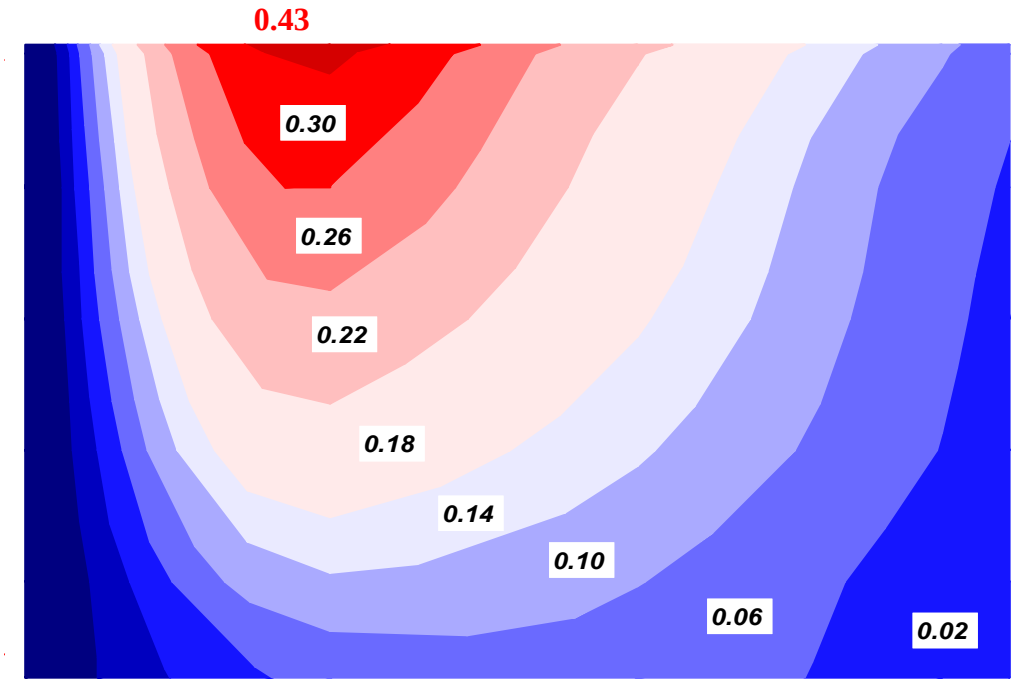

Figure 10-24 Shear strength ratios for high fines content system V3 with no stabilizer and at wet conditions

Figure 10-25 illustrates the distribution of shear strength ratios in the base layer for a stabilized system V3. Anisotropic material properties for 2 percent cement stabilized gradation V3 at molded at wet of optimum moisture conditions were used as inputs to the nonlinear and cross-anisotropic finite element program to calculate the octahedral shear stresses throughout the base layer. The maximum shear strength ratio was calculated to occur at the top of the base layer aligned with the edge of the tire. The magnitude of the maximum shear strength ratio in this simulation was calculated to be 0.12.

As discussed earlier in this chapter, lower shear strength ratios are synonymous to less probability of failure for aggregate layers. In other words, aggregate bases with lower shear strength values are less prone to develop plastic deformations and rut under traffic loads.

A comparison between the two cases discussed earlier shows that adding 2 percent cement to the high fine aggregate system V3 under wet conditions resulted in significant reduction (about 258 percent) in the shear strength ratio.

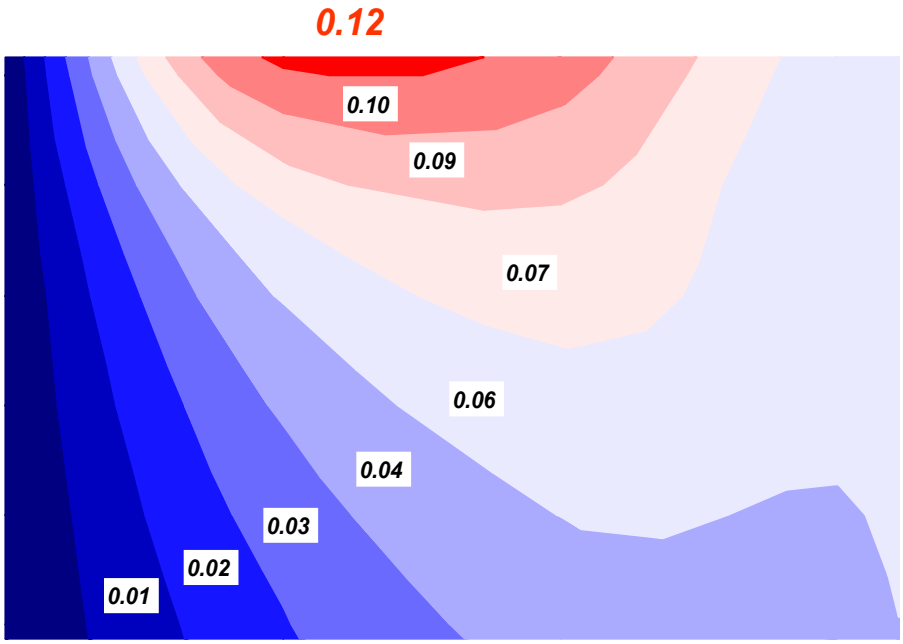

Figure 10-25 Shear strength ratios for 2 percent cement stabilized high fines system V3 under wet conditions

Considering the argument presented by (Thompson 1992) in NCHRP 1-26 that lower shear strength ratios correspond to lower rut potential in the pavement systems, it can be concluded that the performance of the lightly stabilized V3 gradation with 15 percent passing sieve #200 will be superior to its unbound counterpart. These systems can be considered for potential use in sustainable highway systems.

CHAPTER XI

PREDICTION MODEL FOR THE LEVEL OF ANISOTROPY OF AGGREGATE SYSTEMS

INTRODUCTION

The focus of this part of the study was to establish a procedure to determine the level of anisotropy of aggregate systems based on simple aggregate properties. Several features of aggregates were determined and used as input to the aggregate database. Various gradations and saturation levels were considered for each aggregate source. Stress-induced directional dependency of material properties were evaluated based on multiple variable dynamic confining pressure stress path tests for 10 aggregate sources. The cross-anisotropic modular ratios were used as indicators of the level of anisotropy.

Dry density and water content at the time of stress path testing was also used in the aggregate database to study the effect of saturation level on the anisotropic behavior of aggregate systems.

Inherent anisotropy, which is controlled by the geometry of particles, was characterized using the Aggregate Imaging System (AIMS). Cumulative Weibull distribution function was in turn fitted to the data to determine distribution parameters of particle size and aggregate geometry.

The fine portion of the gradation was characterized by two tests: Rigden voids test and methylene blue test were performed on the fine portion of the gradation to account for fine particle shape properties and deleterious effect of plastic fines on volumetric stability of aggregate layers.

This chapter initially provides a brief description of the parameters of the aggregate database. Then the anisotropy model developed in this study will be presented. This study also provides a sensitivity analysis on the model accompanied by a finite

element study to investigate the impact of modular ratios on the performance of aggregate systems.

DISTRIBUTION FUNCTIONS

Various two parameter and three parameter mathematical models have been used to describe aggregate particle size and shape distributions *(3, 9)*. However, widespread applications of some of these functions have been limited due to the complexity in physical interpretations regarding each distribution parameter.

In developing the first generation anisotropy model, Kim used the three parameter Fredlund model presented in equation 11-1 to fit the cumulative distribution functions of gradation and geometry of aggregates (Kim et al. 2005).

$$P_p = \frac{100}{\ln\left[\exp(1) + \left(\frac{g_a}{d}\right)^{g_n}\right]^{g_m}} \tag{11-1}$$

where Pp is the percent passing a particular sieve; d is sieve opening; and g_a ,g_n, and g_m are fitting parameters that correspond to an initial break in the curve, maximum slope, and curvature of the distribution function, respectively.

The Rosin-Rammler distribution function described by Djamarani has long been used to describe the particle size distribution of powders of various natures and sizes. The function is particularly suited to representing particles generated by grinding, milling, and crushing operations (Djamarani and Clark 1997). The Rosin-Rammler function is represented by two parameters: mean particle size (D_m) and n that is a measure of the spread of particle size distribution. Rosin-Rammler function is presented in equation 11-2.

$$Q(D) = 1 - \exp\left[-\left(\frac{D}{D_m}\right)^n\right] \tag{11-2}$$

The two parameter Weibull cumulative distribution function is very similar to the Rosin-Rammler distribution commonly used by researchers working in the area of powder technology and cement industry.

Several two parameter and three parameter distributions were fitted to the data and the goodness of the fit was determined through least square error criteria. It was observed that the two parameter Weibull distribution provides a reasonable fit to both particle size and shape properties data at a 95% confidence level. Equation 11-3 presents the general form of the two parameter Weibull cumulative distribution function.

$$Q(d) = 1 - \exp\left[-\left(\frac{d}{\alpha}\right)\right]^{\beta} \tag{11-3}$$

where:

d=Aggregate size,

α =Scale parameter of cumulative Weibull distribution

β=Shape parameter of cumulative Weibull distribution

Figure 11-1 and figure 11-2 show the impact of scale parameter and shape parameter on the overall shape function of the two parameter cumulative Weibull distribution function. Figure 11-1 shows that as the scale parameter α increases, the distribution becomes more spread out and small values of the scale parameter α correspond to more condensed distributions. Gradations with larger particle sizes have higher α values. In terms of angularity distribution, a higher α value indicates a higher number of particles with crushed faces when compared with a sample with a lower α. The same analogy is valid for aggregate texture properties; an increase in the α value in texture distribution corresponds to an increase in the number of particles with a rougher microstructure at the surface of particle while distributions with a lower α value correspond to more smooth and polished particles.

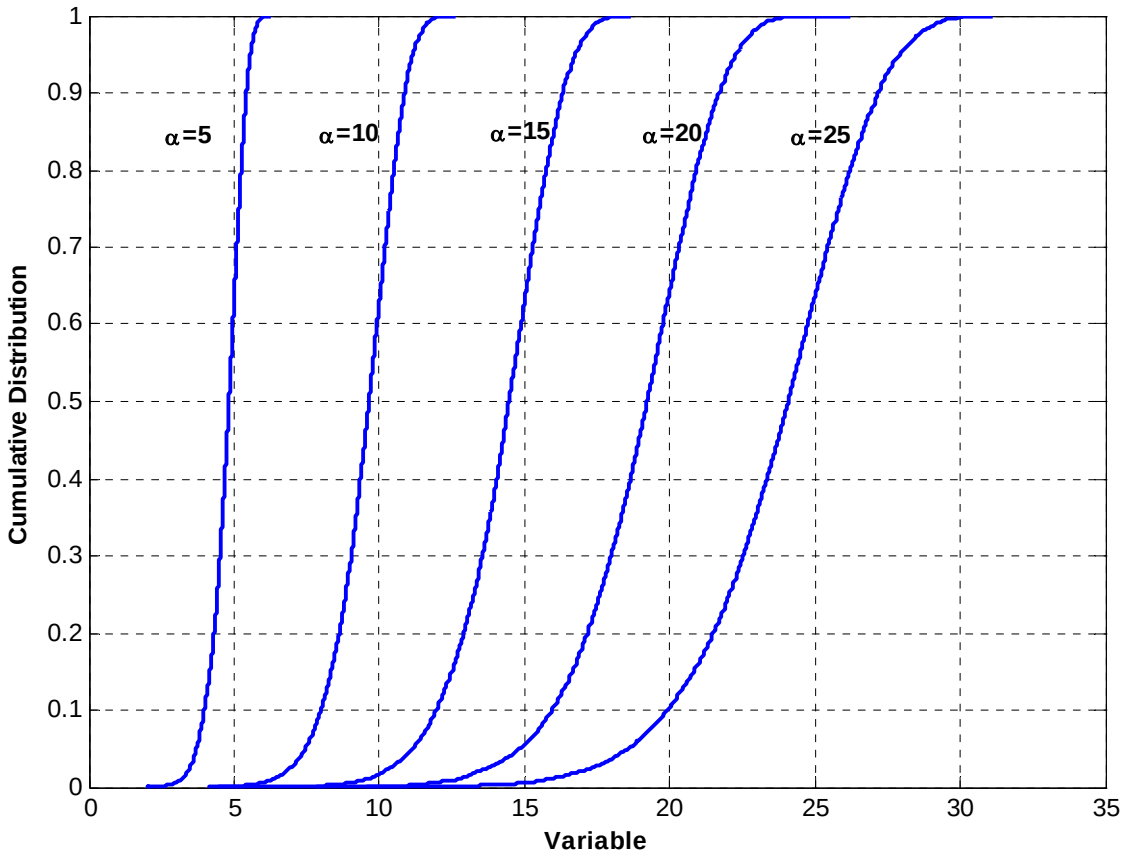

Figure 11-1 Effect of variation of scale parameter (α) on Weibull distribution

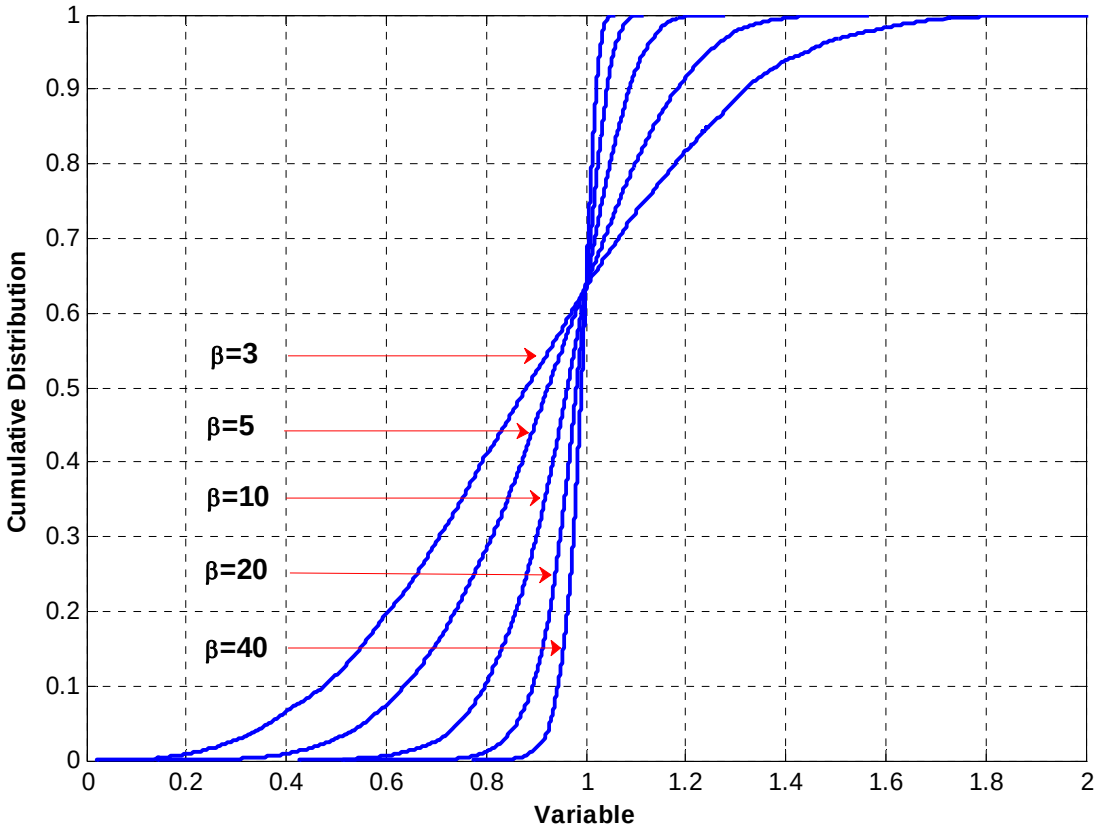

Figure 11-2 Effect of variation of shape parameter (β) on Weibull distribution

Figure 11-2 shows that the shape parameter, β, relates to the uniformity of the distribution. For instance, a lower β value corresponds to an aggregate gradation that spreads over a wide range of particle sizes. This figure also suggests that finer gradations with longer tails exhibit a lower β value.

The fact that the Weibull distribution is a well-established statistical function, and the sensitivity of the distribution parameters fits the physical characteristics of aggregates such as particle size, and geometry made it our popular choice of fitting distribution.

The distribution parameters determined from fitting the particle size distribution and aggregate shape properties data to the Weibull distribution were later used as input to the aggregate database for the purpose of developing the anisotropy model.

Parameters of the Aggregate Database

Characterization of Particle Geometry

Geometry of particles was characterized by angularity, form, and texture using Aggregate Imaging System (AIMS).

Fifty-six (56) aggregate particles from three aggregate sizes for each aggregate source were tested using the AIMS device, and the distributions were fitted to two parameter cumulative Weibull distributions. The parameters of the Weibull distributions, Scale parameter (α) and shape parameter (β), were used as input to the neural network model.

Table 11-1 Distribution Parameters for Form, Angularity, and Texture

		Angularity		***2D Form***		***Texture***	
	Representative Seive	*Shape Parameter*	*Scale Parameter*	*Shape Parameter*	*Scale Parameter*	*Shape Parameter*	*Scale Parameter*
	3/8	3.89	3268.88	5.20	7.96	2.93	183.31
A1	*1/4*	4.87	3265.30	4.15	9.02	2.27	145.03
	#4	2.99	3687.82	4.19	10.28	2.14	153.92
	3/8	4.41	2890.97	3.08	8.02	2.64	175.54
A2	*1/4*	4.62	3098.77	3.85	8.69	2.01	150.54
	#4	4.33	3212.57	4.74	8.27	2.49	126.48
	3/8	5.57	3367.00	3.92	8.45	5.18	315.27
A3	*1/4*	4.98	3409.33	3.46	9.15	3.85	230.16
	#4	3.29	4104.53	4.78	9.55	3.30	228.49
	3/8	6.11	3553.05	4.36	7.97	3.64	190.64
A4	*1/4*	5.80	3747.33	4.82	8.43	2.78	164.98
	#4	4.82	4135.84	4.95	8.70	3.18	138.91
	3/8	4.82	3212.25	4.96	7.73	2.71	170.19
A5	*1/4*	4.78	3762.92	5.10	8.36	2.61	130.95
	#4	3.92	3875.11	5.49	8.50	2.43	135.78
	3/8	3.36	2918.71	4.21	7.31	2.00	108.82
A6	*1/4*	4.03	3074.21	5.87	7.56	1.86	89.80
	#4	5.89	3311.84	5.18	8.73	1.75	88.26
	3/4	3.37	3310.31	4.72	6.91	3.06	236.40
A7	*3/8*	2.95	3681.64	3.46	8.47	2.65	178.66
	#4	3.24	3591.91	4.29	7.85	2.15	109.75
	3/8	4.82	3212.25	4.96	7.73	2.71	170.19
A8	*1/4*	4.78	3762.92	5.10	8.36	2.61	130.95
	#4	3.92	3875.11	5.49	8.50	2.43	135.78
	3/8	3.36	2918.71	4.21	7.31	2.00	108.82
A9	*1/4*	4.03	3074.21	5.87	7.56	1.86	89.80
	#4	5.89	3311.84	5.18	8.73	1.75	88.26
	3/8	5.65	3231.94	4.45	8.08	3.76	391.17
A10	*1/4*	4.78	3828.53	5.04	8.34	3.06	327.13
	#4	3.24	4223.22	6.20	8.32	2.26	240.40

Moisture Content and Density of Aggregate Systems

Dry density and moisture state of aggregate systems were used in the aggregate database to account for the effect of moisture on directional dependency of material properties. Table 11-3 presents the water content and dry density of aggregate systems.

Deleterious Effect of Fines

In this study, methylene blue test (ASTM C832-2003) was adopted to provide a measure of activity of the fine particles in the matrix. Several studies have shown that the deleterious effect of plastic fines, particularly shrink-swell potential, has a strong correlation with the methylene blue value.

Methylene blue is a large polar organic molecule that is adsorbed onto the negatively charged surfaces of clay minerals. The amount of methylene blue adsorbed by a given mass of clay depends on the relative concentration of negatively charged sites on the clay particle surfaces as well as surface area of the clay per unit mass (Fityus et al. 2000).

Since Methylene blue molecules are preferentially adsorbed onto the negatively charged sites on clay surface, titration with methylene blue can be considered to provide a relative measure of the cation exchange capacity of a clay soil (Cokca and Birand 1993).

Hence, in this study the methylene blue test was adopted as a measure of moisture susceptibility and swell potential in aggregates systems. The ASTM C832-2003 protocol was used to determine the methylene blue value for 10 aggregate sources. More details on the calculation of Methylene blue value was presented in Chapter V.

Table 11-2 Dry Density and Moisture States of Aggregate Systems

Aggregate ID	*Moisture State*	*Gradation*	*Dry Density* (Kg/m^3)	*w* (%)
A1 Limestone (Fort Worth, Texas)	Dry of Optimum	Coarse	2144	4
	Optimum	Coarse	2192	4.5
	Dry of Optimum	Intermediate	2148	4.6
	Optimum	Intermediate	2214	4.8
	Wet of Optimum	Intermediate	2181	5.2
	Optimum	Fine	2130	5.6
	Wet of Optimum	Fine	2106	6.6
A2 Limestone (Wichita Falls, Texas)	Dry of Optimum	Coarse	1980	4.1
	Optimum	Coarse	2020	4.6
	Dry of Optimum	Intermediate	2068	5
	Optimum	Intermediate	2008	5.5
	Wet of Optimum	Intermediate	2014	5.7
	Optimum	Fine	1958	6.8
A3 Granite (El Paso, Texas)	Optimum	Coarse	2060	4.5
	Wet of Optimum	Coarse	1977	4.9
	Dry of Optimum	Intermediate	2069	4.8
	Optimum	Intermediate	2111	6.4
	Wet of Optimum	Intermediate	2107	7
	Dry of Optimum	Fine	1968	5.6
	Optimum	Fine	2021	7
	Wet of Optimum	Fine	1985	7.2
A4 Granite (Paris, Texas)	Optimum	Coarse	2040	4
	Optimum	Intermediate	2005	3.8
	Wet of Optimum	Intermediate	2052	4.6
	Optimum	Fine	2015	4.1
A5 Gravel (Amarillo, Texas)	Optimum	Coarse	2143	4
	Dry of Optimum	Intermediate	2087	3.3
	Optimum	Intermediate	2199	4.5
	Dry of Optimum	Fine	2140	4.9
	Optimum	Fine	2118	4.7
	Wet of Optimum	Fine	2013	5.2
A6 Gravel (Waco, Texas)	Dry of Optimum	Coarse	2116	3
	Dry of Optimum	Intermediate	2124	3
	Optimum	Intermediate	2238	4.4
	Wet of Optimum	Fine	2036	5
	Optimum	Fine	2032	4
A7 Limestone (Brownwood, Texas)	Optimum	Coarse	2144	2.8
	Dry of Optimum	Intermediate	2260	3.5
	Optimum	Intermediate	2350	4.1
	Wet of Optimum	Intermediate	2315	4.9
	Dry of Optimum	Fine	2251	4.7
	Optimum	Fine	2302	5.4
	Wet of Optimum	Fine	2234	5.9
A8 Gravel (Reavis, Texas)	Optimum	Coarse	2020	5.5
	Dry of Optimum	Intermediate	2062	5.5
	Optimum	Intermediate	2240	7.7
	Dry of Optimum	Fine	2075	5.4
	Optimum	Fine	2210	7.5
A9 Gravel (Minnesota)	Dry of Optimum	Intermediate	2139	4.5
	Optimum	Intermediate	2167	6.2
	Wet of Optimum	Intermediate	2240	7.7
	Dry of Optimum	Fine	2159	4.7
	Optimum	Fine	2296	7.6
A10 Granite (Mill Creek, Oklahoma)	Dry of Optimum	Intermediate	2179	3.5
	Optimum	Intermediate	2218	4
	Wet of Optimum	Intermediate	2192	4.6
	Dry of Optimum	Fine	2177	4.1
	Optimum	Fine	2215	4.6
	Wet of Optimum	Fine	2278	5.9

Geometry of Fine Particles

In order to characterize the geometry of particles smaller than 75 μ, a modified Rigden test was used. The dry compacted fines test (Rigden voids tests) provides a measure by which to relate the maximum packing of fine particles to the shape and size distribution of particles. It is assumed that higher density and tighter packing of fine particles will be achieved in a sample with size distribution that spreads over a larger range of particle sizes.

MODOT-T73 specification, Volume of voids in compacted filler test procedure developed by Missouri Department of Transportation (MODOT), was followed in this study to determine the density and void content of the fine portion of unbound aggregate samples. This test method is based on the assumption that the densest packing or maximum bulk density of fines can be obtained by compacting the dry fines in a mold using a 100 gram compaction hammer. More details on this method is presented in Chapter V.

Characterization of the Anisotropic Response of Aggregate Systems

In order to assess the directional dependency of the response of aggregate bases under a moving wheel load, aggregate samples were tested following the Texas A&M stress path protocol. Figure 11-3 schematically illustrates the stress paths applied to aggregate samples in σ_1-σ_3 plane. Figure 11-3 is the representation of the stress paths in q-p plane.

This protocol provides a means to determine cross-anisotropic material properties: E_x and E_y (elastic modulus in the horizontal and vertical directions, respectively), ν_{xy}, ν_{xx} (Poisson's ratio in the horizontal direction due to vertical loading and Poisson's ratio in the horizontal direction due to horizontal loading, respectively) and G_{xy}, shear modulus.

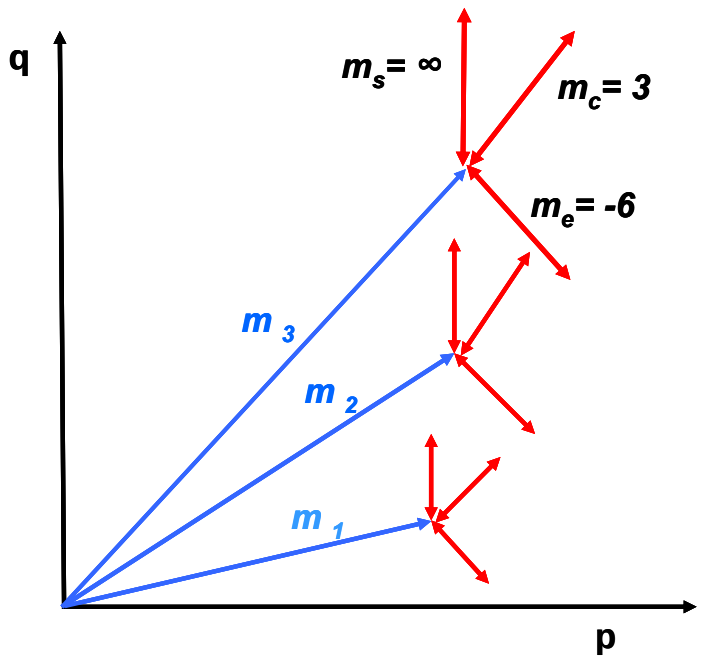

Figure.11-3 Schematic representation of variable dynamic confining pressure stress paths in the Texas A&M protocol

Applied stresses and measured strains are then input into an iterative error minimization technique called the system identification method to simultaneously solve for four of the five anisotropic material properties (E_x, E_y, ν_{xx}, and ν_{xy}).

$$\begin{bmatrix} \frac{1}{E_x} & -\frac{\nu_{xy}}{E_x} & -\frac{\nu_{xx}}{E_x} \\ -\frac{\nu_{xy}}{E_x} & \frac{1}{E_y} & -\frac{\nu_{xy}}{E_x} \end{bmatrix} \begin{bmatrix} \sigma_x \\ \sigma_y \\ \sigma_x \end{bmatrix} = \begin{bmatrix} \varepsilon_x \\ \varepsilon_y \end{bmatrix} \tag{11-4}$$

The fifth material property, G_{xy}, is directly determined using equation 2, which is derived using elastic work potential relationships derived specifically for the shear stress regime. Details regarding the derivation of equation 2-2 can be found in Chapter II.

$$G_{xy} = \frac{3}{4} \frac{\Delta\sigma_y}{(\Delta\varepsilon_y - \Delta\varepsilon_x)} \tag{11-5}$$

In cross-anisotropic materials, a plane of isotropy exists such that material properties in the x and z directions are equal. Since the horizontal plane is the plane of isotropy, the term G_{xx} is related to v_{xx} and E_x by equation 11-6.

$$G_{xx} = \frac{E_x}{2\,(1+\nu_{xx})} \tag{11-6}$$

The values of vertical (E_y), horizontal (E_x), and shear (G_{xy}) moduli were fitted to the bulk stress (θ) and octahedral shear (τ_{oct}) stress using nonlinear functions as shown in Equations 11-7 through 11-9.

$$E_y = Pa\; k_1\left(\frac{\theta}{Pa}\right)^{k_2}\left(\frac{\tau_{oct}}{Pa}+1\right)^{k_3} \tag{11-7}$$

$$E_x = Pa\; k_4\left(\frac{\theta}{Pa}\right)^{k_5}\left(\frac{\tau_{oct}}{Pa}+1\right)^{k_6} \tag{11-8}$$

$$G_{xy} = Pa\; k_7\left(\frac{\theta}{Pa}\right)^{k_8}\left(\frac{\tau_{oct}}{Pa}+1\right)^{k_9} \tag{11-9}$$

where k_1 through k_9 are fitting parameters, and Pa is the atmospheric pressure (101 kPa). The k-values calculated from stress path tests were used as input to aggregate database to characterize stress sensitivity, nonlinearity, and cross-anisotropic behavior of unbound aggregate systems.

Figure 11-4 and figure 11-5 show the accumulation of plastic strains for two aggregate systems. Figure 11-4 presets axial strain plot for well-graded granite materials molded at optimum moisture content. Figure 11-5 shows the accumulation of axial strains with respect to time for the same gradation of granite material molded at 2 percent above the optimum moisture content. Comparison between the two plots clearly demonstrates the time-dependency of response in the fine gradation. In other words, measured strain is decomposed into instantaneous recovery (elastic), time-dependent rebound (visco-elastic), and permanent (plastic) strains.

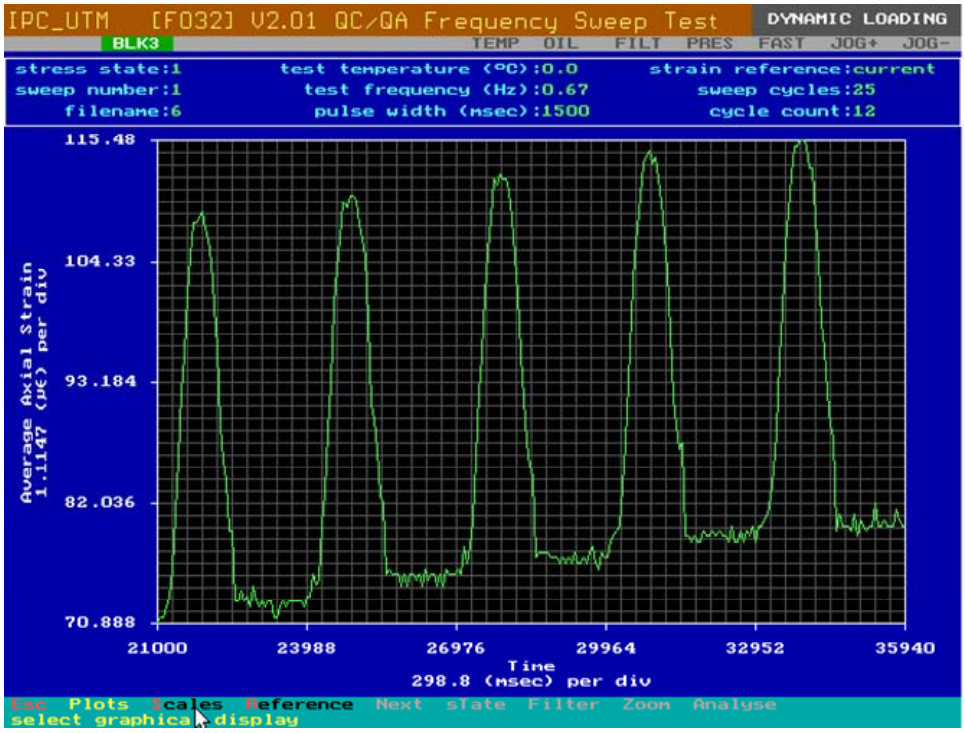

Figure 11-4 Axial strain plot for well-graded granite materials at optimum moisture content

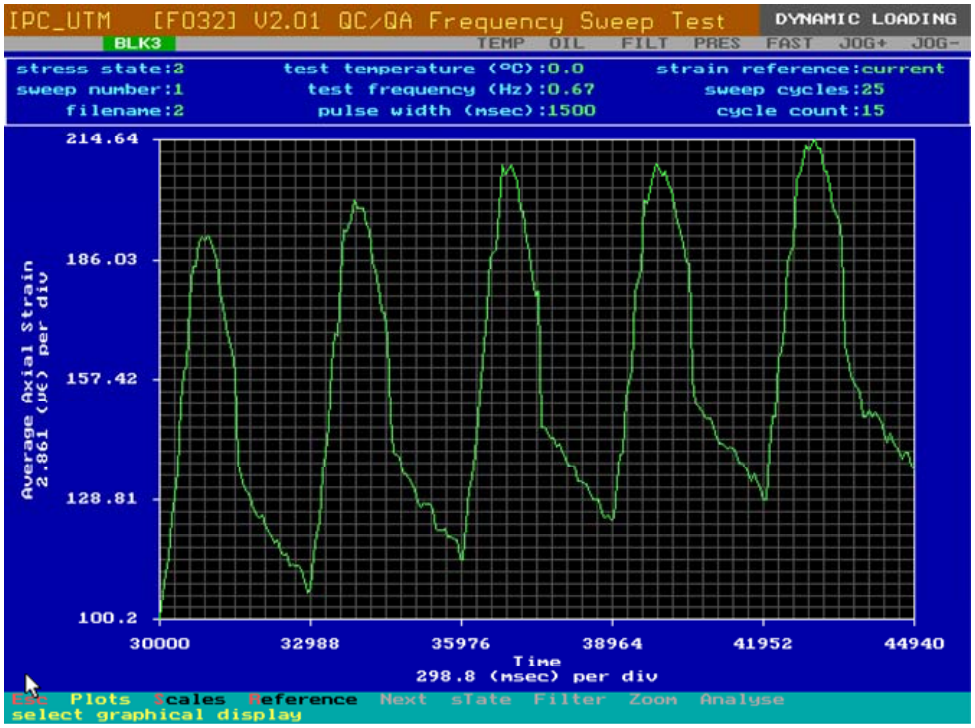

Figure 11-5 Axial strain plot for well-graded granite materials at wet conditions

Characterization of the Level of Anisotropy

Kim used equations 11-7 through 11-9 to derive several measures for the level of anisotropy of aggregate systems as functions of k parameters (Kim et al. 2005):

$$\frac{E_x}{E_y} = \frac{k_4}{k_1}\left(\frac{I_1}{Pa}\right)^{k_5-k_2}\left(\frac{\tau_{oct}}{Pa}\right)^{k_6-k_3} \tag{11-10}$$

$$\frac{G_{xy}}{E_y} = \frac{k_7}{k_1}\left(\frac{I_1}{Pa}\right)^{k_8-k_2}\left(\frac{\tau_{oct}}{Pa}\right)^{k_9-k_3} \tag{11-11}$$

Kim stated that these functions define the level of anisotropy in aggregate systems. These functions are: k_4/k_1, k_7/k_1, k_5-k_2, k_6-k_3, k_8-k_2, and k_9-k_3. Figure 11-6 presents the matrix plot of anisotropy characterizers based on k parameters.

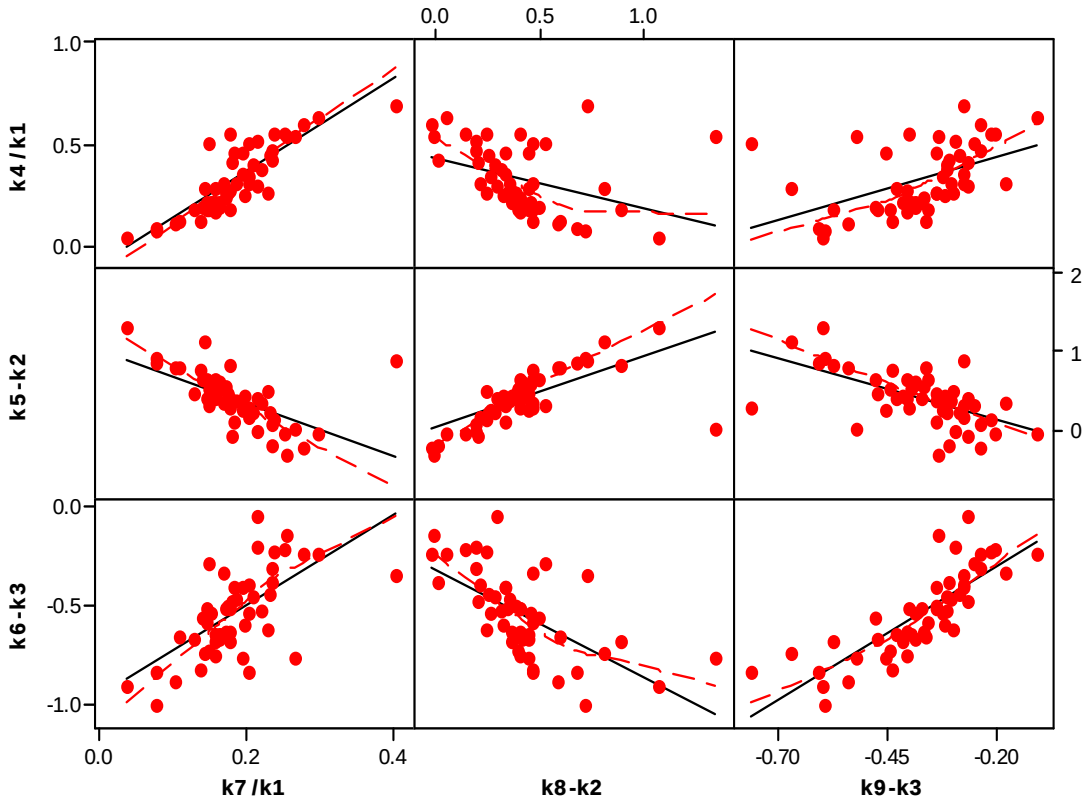

Figure 11-6 Matrix plot for measures of anisotropy as functions of k-values

As illustrated in this figure, characterizers of the level of anisotropy do not vary in the same direction therefore interpretation of the results based on these measures is cumbersome. For instance figure 11-6 suggests that more anisotropic systems have small values of k_4/k_1, k_7/k_1, k_6-k_3, and k_9-k_3 and high values of k_5-k_2 and k_8-k_2.

To eliminate this problem, average modular ratio E_x/E_y, G_{xy}/E_y, and G_{xx}/G_{xy} were considered as the characterizer of the level of anisotropy for unbound aggregate systems in this study.

Figure 11-7 presents the cross correlation of modular ratios in this study. Small values of modular ratios correspond to more anisotropic systems while modular ratios close to unity represent aggregate systems with less directional dependency of material properties. As evidenced in this figure, characterizers of the level of anisotropy vary in the same direction, and therefore interpretation of the data would be easier.

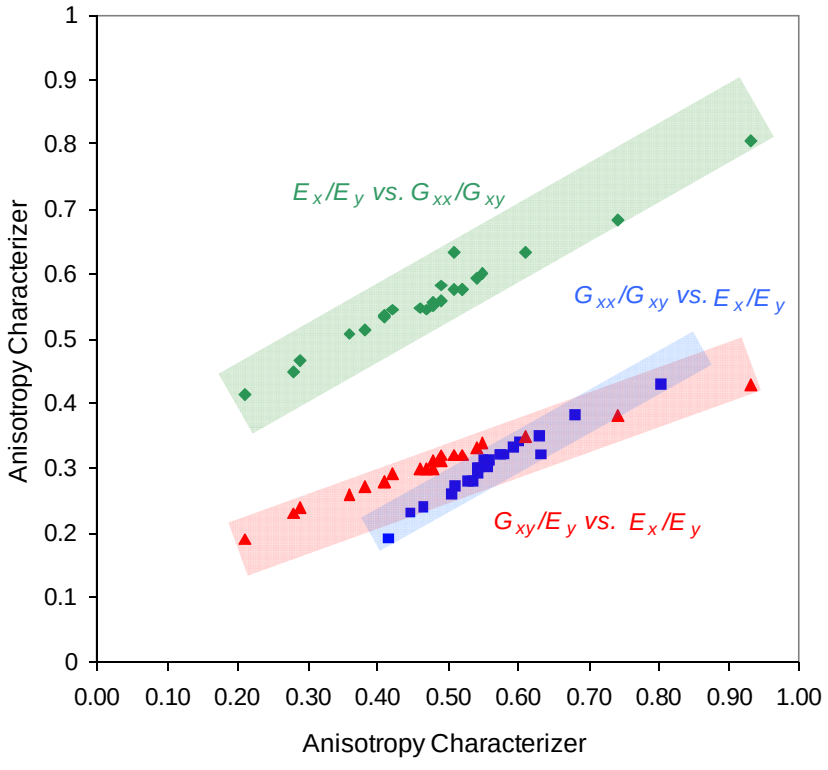

Figure 11-7 Cross correlation of characterizers of anisotropy based on modular ratios

Analysis of the Aggregate Database

Anisotropic material properties of 10 aggregate sources were determined using multiple variable dynamic confining pressure stress paths. Then, Equations 4-6 was fitted to the stress levels and measured material properties in order to calculate the k parameters. The k parameters capture the stress sensitivity, nonlinearity, and anisotropic behavior of the aggregate systems in the lab.

As discussed earlier, aggregate shape parameters were determined using the Aggregate Imaging System (AIMS). The measured shape features of particles were then fitted to the Weibull distribution function presented in equation 11-3. Statistical parameters of cumulative Weibull distribution namely the shape parameter and scale parameter were then used as input data for the aggregate database. Particle size distributions were also fitted with the Weibull distribution equation, and the corresponding parameters were determined and used in the aggregate database.

The moisture content at the time of testing, dry density, dry compacted air voids in fines, and the methylene blue value of the aggregates were also determined and used as input to the aggregate database.

Figures 11-8 and 11-9 show the relationship between degree of anisotropy and aggregate shape characteristics measured using AIMS. The results clearly demonstrate the influence of aggregate shape features on the degree of anisotropy in unbound aggregate systems. Figure 11-8 shows the effect of aggregate texture and aggregate form on the level of anisotropy as characterized by the shear modular ratio (G_{xx}/G_{xy}). Aggregate sources with more cubical particles and rougher texture demonstrated higher shear modular ratios (G_{xx}/G_{xy}), which are synonymous with less anisotropic systems as evidenced in figure 11-8. Less anisotropic unbound systems perform better in terms of load distribution characteristics throughout the aggregate layer and are less prone to develop shear deformation. Finite element analysis, which will be presented in the performance prediction section of this chapter, substantiates this assessment.

Figure 11-9 demonstrates the impact of particle texture and aggregate angularity on the level of anisotropy characterized by modular ratios (i.e., E_x/E_y). Figure 11-8 shows that aggregate systems containing particles with rougher texture, and more crushed surfaces (more angular) result in less anisotropic systems. Particle surface texture and angularity contribute to inter-particle frictional forces and affect aggregate interlock. Aggregate systems with rougher texture and more angular particles result in systems that more efficiently distribute load and are less prone to plastic deformation under traffic.

Figure 11-8 and Figure 11-9 emphasize the importance of lithology as well as rock crushing techniques used by the aggregate producers in the pavement industry. These graphs indicate that because the aggregate properties of angularity and texture impact anisotropy, which in turn impacts performance, they can be used as quality control/quality assurance tools for aggregate producers.

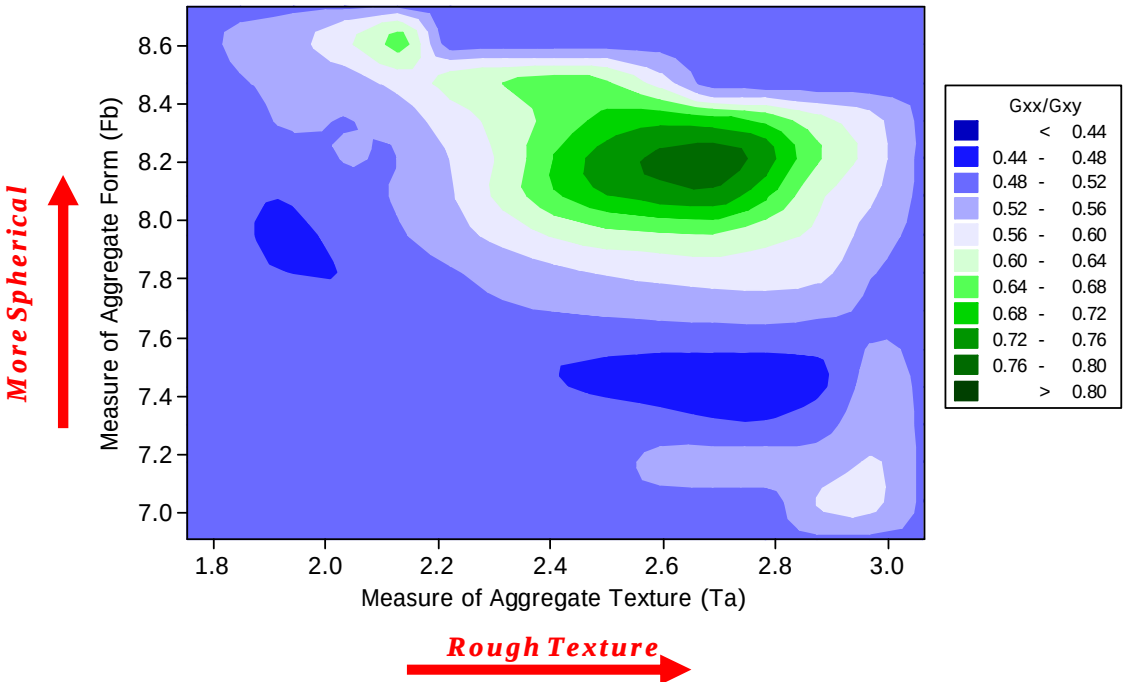

Figure 11-8 Impact of Aggregate Texture and Form on Anisotropy Level Assessed Using the Shear Modulus Ratio (G_{xx}/G_{xy})

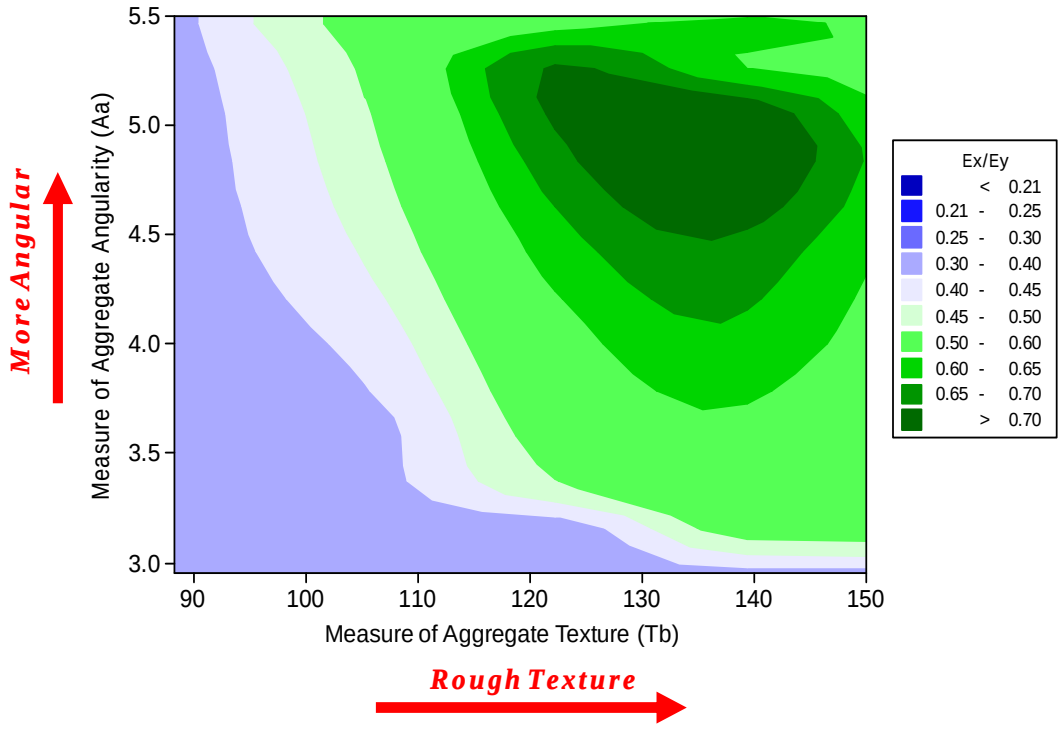

Figure 11-9 Impact of aggregate angularity and texture on anisotropy level assessed using the axial modulus ratio (E_x/E_y)

ANISOTROPY MODEL

Aggregate parameters discussed in the materials testing section of this paper were used as input data to an aggregate database that was in turn used to develop a model to predict the level of anisotropy. In this study, modular ratios (G_{xx}/G_{xy}), (E_x/E_y), and (G_{xy}/E_y) were used to characterize the level of anisotropy for sixty two (62) aggregate systems. The inputs to the model are:

- The stiffness properties in the vertical direction represented in terms of k_1, k_2, and k_3
- The scale (α) and shape (β) parameters of the Weibull distribution equation fitted to aggregate form, angularity, and texture

- The shape and scale parameters of the Weibull distribution fitted to aggregate size distributions
- The moisture content at the time of testing
- Dry density
- Percent air voids in dry compacted fines
- The methylene blue value

Equation 8 presents the regression model that was established using a stepwise regression analysis with a 95% confidence level. The stepwise regression performs variable selection by adding or deleting predictors from the existing model based on an F-test. This method is a combination of a forward and backward feature selection and elimination process.

The shear modular ratio (G_{xx}/G_{xy}) was found to have a superior goodness of fit (R^2= 95%) when compared to the other two anisotropy level characterizers, i.e., (E_x/E_y) and (G_{xy}/E_y), that had coefficients of correlation (R^2) of 0.75 and 0.79, respectively.

$$\begin{bmatrix} \frac{G_{xx}}{G_{xy}} \\ \frac{E_x}{E_y} \\ \frac{G_{xy}}{E_y} \end{bmatrix} = \begin{bmatrix} -2.4 \\ -4.29 \\ -0.51 \end{bmatrix} + \begin{bmatrix} -0.00003 & 0.221 & 0.369 & -0.042 & 0.042 & 0.023 & 0.100 & -0.0022 & 0.24 & -0.005 & 0.016 \\ 0.00006 & 0.316 & -0.362 & -0.084 & 0.050 & 0.022 & 0.156 & -0.0023 & 0.18 & 0.017 & -0.011 \\ 0.00002 & 0.0721 & -0.137 & -0.028 & 0.017 & 0.008 & 0.042 & -0.0006 & 0.05 & 0.004 & -0.003 \end{bmatrix} \begin{bmatrix} k_1 \\ k_2 \\ k_3 \\ w \\ A_\alpha \\ F_\beta \\ T_\alpha \\ T_\beta \\ G_\beta \\ DCF \\ MBV \end{bmatrix} \quad (11\text{-}12)$$

where

k_1, k_2, and k_3 : Fitting parameters presented in equation (11-7),

w: Percent moisture content at the time of testing,

A_α : Shape parameter of angularity cumulative distribution function,

F_β : Scale parameter of form cumulative distribution function,

T_α: Shape parameter of texture cumulative distribution function,

T_β: Scale parameter of texture cumulative distribution function,

G_β: Scale parameter of gradation cumulative distribution function,

MB: Methylene blue value and

DCF: Air voids in dry compacted fines (percent)

This model provides a simple and cost effective mean to determine the anisotropy level of aggregate samples with a few simple and routine tests. The anisotropy model also offers the opportunity to investigate the impact of aggregate features on the performance of unbound aggregate systems. This approach can be used as a quality control tool for aggregate producers and pavement material engineers.

Improvements over the first generation of the anisotropy model developed by Kim can be summarized as:

- The number of specimens that populate the database was increased from 36 (in the previous model) to 62 aggregate samples from 10 aggregate sources with three gradations and tested at various moistures states.
- Representations of the level of anisotropy are now based on three modular ratios (G_{xx}/G_{xy}), (E_x/E_y), and (G_{xy}/E_y).
- The Weibull distribution was used to fit the distributions of both characterizers of aggregate geometry and gradations in lieu of the empirical fitting model presented in equation 1.
- The representative sieve concept was used with the motivation that particle shape properties are functions of particle size as well as crushing techniques and the mineralogy of the parent rock. Furthermore, based on the analysis of the

distribution functions of aggregate shape properties for several sieve sizes of the same source, it was observed that different particle sizes exhibit different shape properties, which is evidenced in Table 11-2. Therefore, averaging shape parameters over different sieve sizes will induce systematic error in developing an anisotropy prediction model. Hence instead of reporting only one set of shape parameters for an aggregate source regardless of gradation, the representative sieve concept allocates a set of shape parameters for each gradation variant. In other words, aggregate shape parameters pertaining to the #3/8 sieve were used for coarse gradation, values pertaining to the #1/4 sieve were used for intermediate gradation, and values pertaining to the No. 4 sieve were used for fine gradation.

- The Rigden voids test was used as a measure of fine particles (particles smaller than 75 μ) shape features.
- The methylene blue value (MBV) test was used as a measure of the deleterious effect of plastic fines (particles smaller than 75 μ) in terms of moisture susceptibility of aggregate systems.

Sensitivity Analysis of the Anisotropy Model

A parametric analysis was conducted to evaluate the proposed anisotropy model presented in equation 8 and specifically to evaluate the level of contribution of each selected feature. As with most regression-based models, it is not necessarily realistic to hold selected parameters within the model constant and arbitrarily change only one parameter. For instance, change in the gradation parameter will result in a change in the optimum moisture content, dry density, and mechanical responses of the aggregate system (k parameters). Despite the inter-correlation of aggregate parameters, it is instructive to monitor the impact of each variable on the level of anisotropy of aggregate systems.

Figure 11-10 through figure 11-13 provide the sensitivity of the model with respect to aggregate parameters. Figure 11-10 shows the impact of (k_2) in equation 4 on the level of anisotropy as quantified using the modular ratios. An increase in k_2 results in a higher modular ratio, which is synonymous with less anisotropic behavior. This can be explained by the fact that an increase in k_2 means that the modulus is more sensitive to confinement level. An increase in confinement level improves particle interlock and load distribution in orthogonal directions and reduces the anisotropy of the system.

Figure 11-11 through Figure 11-13 illustrate the impact of aggregate geometry on level of anisotropy. Figure 11-11 shows the impact of aggregate angularity on level of anisotropy. This plot demonstrates that aggregate systems with more angular particles have higher modular ratios or less anisotropy. This is primarily due to better aggregate interlock in the matrix.

Figure 11-12 shows the effect of aggregate texture on anisotropy. Aggregate particles with higher surface texture are less anisotropic as surface micros-structure contributes to inter-particle friction.

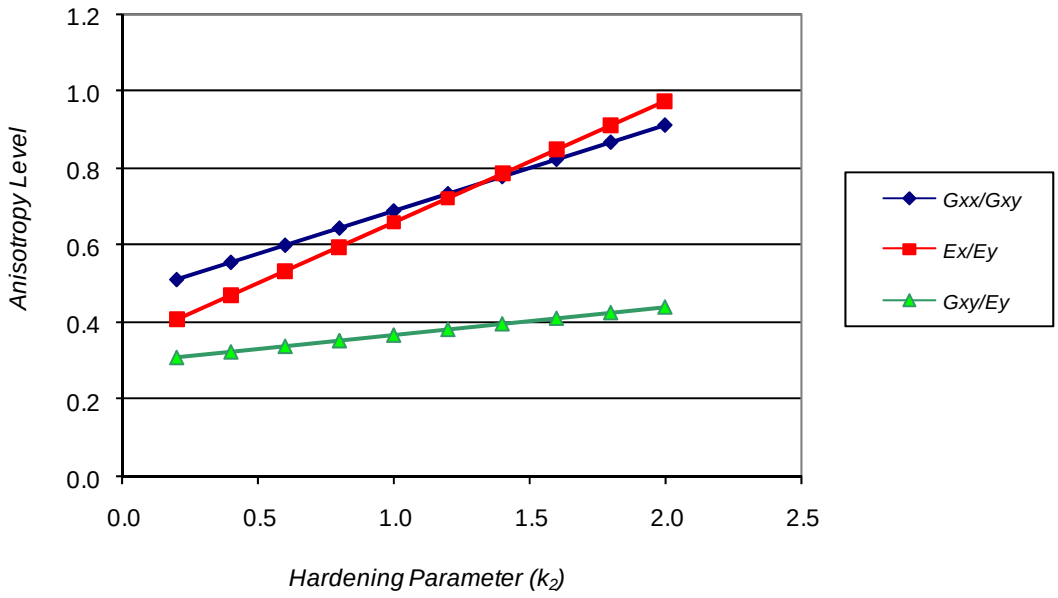

Figure 11-10 Influence of hardening parameter k_2 on the anisotropy level of aggregate systems characterized by modular ratios

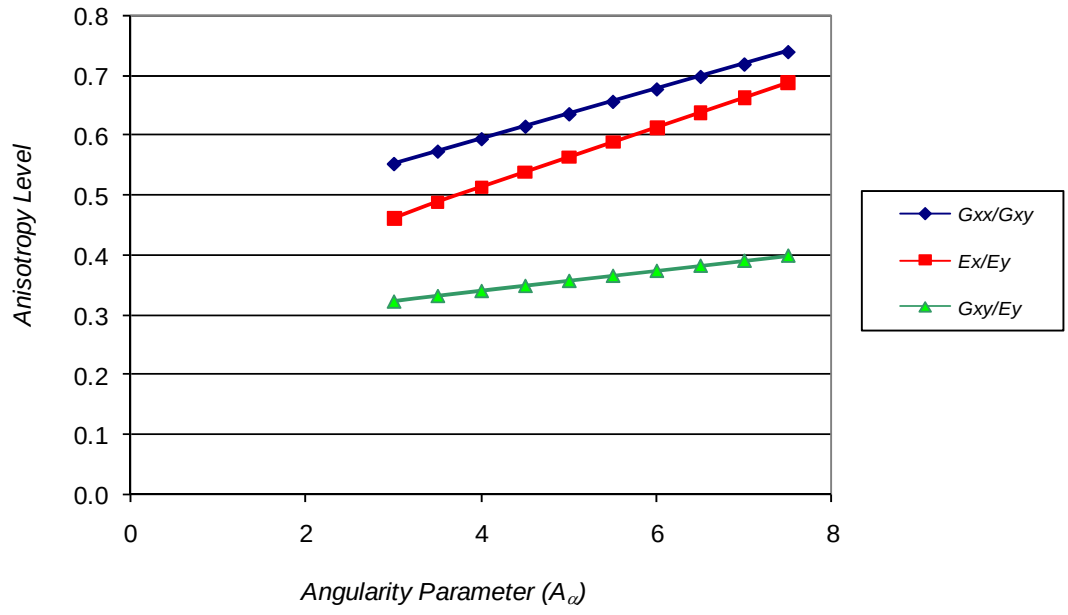

Figure 11-11 Influence of angularity parameter A_α on the anisotropy level of aggregate systems characterized by modular ratios

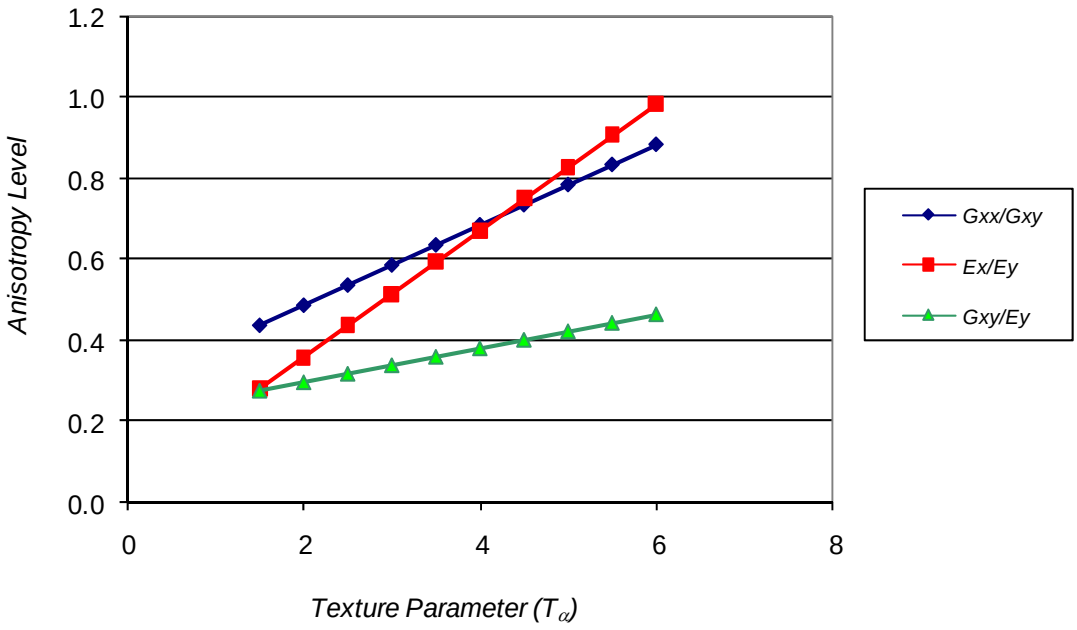

Figure 11-12 Influence of texture parameter T_α on the anisotropy level of aggregate systems characterized by modular ratios

Contribution of Aggregate Features to Anisotropic Behavior of Aggregate Systems

The slopes of the lines plotted in figure 11-10 through figure 11-13 were used to assess the sensitivity of modular ratios to the selected features. The slopes of curves are summarized in Table 11-3. A higher slope absolute value indicates more sensitivity of the level of anisotropy to the aggregate feature.

Table 11-3 Sensitivity of modular ratios to aggregate features

Modular ratio	Slope			
	k_2	T_a	A_a	F_b
G_{xx}/G_{xy}	0.22	0.10	0.04	0.02
E_x/E_y	0.32	0.16	0.05	0.22
G_{xy}/E_y	0.07	0.04	0.02	0.01

Among the particle geometry features in the aggregate database, modular ratio (E_x/E_y) was found to be most sensitive to the degree of elongation of the aggregate particles or how cubical the aggregate particles are. This is in conformity with the fact than upon field compaction, elongated materials tend to re-orient themselves to the horizontal plane, which results in significant differences in material properties in orthogonal directions. The modular ratio (G_{xy}/E_y) was found to be less sensitive to aggregate features compared to the other two anisotropy level characterizers (G_{xx}/G_{xy}) and (E_x/E_y). Modular ratio (E_x/E_y) was found to be most sensitive to the level of confinement characterized by the hardening parameter. As stated earlier, increasing confining pressure contributes to better aggregate interlock, improves orthogonal stiffness properties of aggregate systems, and therefore reduces the level of anisotropy of unbound systems.

ANISOTROPY LEVEL AND PERFORMANCE

The relationship between level of anisotropy and performance of unbound aggregate systems was investigated by conducting finite element analysis of a typical pavement section. The analysis was conducted using TTI-PAVE software, which is an axisymmetric finite element program that was developed at Texas A&M University. The pavement section consisted of 4 inches of a linear isotropic asphalt layer with a vertical modulus of 400,000 psi and a Poisson's ratio of 0.35; a cross-anisotropic and nonlinear unbound aggregate base layer with a thickness of 12 inches; and a natural subgrade with a vertical modulus of 7,000 psi and Poisson's ratio of 0.45. A wheel load with 100 psi pressure acting on a circular area with a radius of 5.5 inches was used in this analysis. The inputs for the unbound layer cross-anisotropic model are k_1, k_2, k_3 in equation 4; and n, m, and μ coefficients according to equations (4-1) to (4-3) presented in the previous chapter.

The unbound layer's inputs were determined from the results of stress path testing aggregate systems using the Texas A&M small strain protocol.

Performance of the aggregate systems was evaluated based on the shear strength ratio concept discussed in the previous chapter. Thompson (1991) showed that a reasonable relationship exists between field rutting data and shear strength ratio of aggregate base layer. Therefore, the shear strength ratio (SSR) defined in equation 11-13 was the same as performance criteria in this study.

$$Shear\ Strength\ Ratio\ (SSR) = \frac{(\tau_{oct})_{MAX}}{UCCS} \tag{11-13}$$

The unconfined compressive strength (UCCS) was determined from laboratory testing following the ASTM D2166 procedure. The octahedral shear stress was calculated using nonlinear and anisotropic solutions at three points on the top of base layer: centerline, edge, and 2 inches away from the prescribed circular load. Consequently, SSR was determined at the three points at the top of the base layer. The analysis was limited to four aggregate systems as shown in Table 11-4.

Table 11-4 Materials and Input Parameters Used in Finite Element Analysis

	Aggregate Type	*Moisture State*	k_1	k_2	k_3	E_x/E_y	G_{xy}/E_y	ν_{xx}/ν_{xy}	*UCCS (psi)*
Case 1	Texas Limestone	Wet	2815	0.50	0.15	0.25	0.32	1.3	28.5
Case 2	California Granite	Dry	3179	0.299	0.316	0.5	0.35	1.5	51.7
Case 3	Texas Limestone	Optimum	3839	0.37	0.34	0.6	0.35	1.5	62.6
Case 4	Texas Gravel	Optimum	4152	0.329	0.372	0.75	0.37	1.2	68.7

Nonlinear cross-anisotropic material parameters were determined by subjecting aggregate samples to the small strain Texas A&M protocol. k parameters determined during laboratory testing were used to calculate the modulus values using equations 11-7 through 11-9. Modular ratios as an indicator of anisotropy level of the aggregate systems at the top of the base layer were then calculated.

Table 11-5 summarizes modulus values in two directions (E_x and E_y), anisotropy characterizers (E_x/E_y and G_{xy}/E_y) as well as shear strength ratio (SSR) found from the finite element analysis. Nonlinear and stress sensitive modulus values were calculated at the specified locations. The modulus values along with anisotropy ratios were reported in this table. Shear strength ratio for each system also calculated and presented in table 11-5.

The finite element analysis results indicate that shear strength value had its maximum value for case 1 where material properties of Texas limestone at wet conditions were selected for the base layer. Higher shear strength value corresponds to conditions at which the probability of developing plastic deformation and lateral movement of the pavement foundation is higher.

Table 11-5 Cross-Anisotropic Material Properties

		E_y (psi)	E_x (psi)	G_{xy} (psi)	E_x/E_y	G_{xy}/E_y	SSR
Case 1	*@ Centerline of load*	30527	3345	6430	0.120	0.196	0.44
Case 2		43699	15914	10885	0.36	0.25	0.28
Case 3		44921	16435	11613	0.393	0.261	0.27
Case 4		48518	20998	13441	0.433	0.277	0.24
Case 1	*@ Loading Edge*	29478	3158	6086	0.137	0.206	0.43
Case 2		41345	13937	9821	0.34	0.24	0.30
Case 3		43842	14622	10039	0.33	0.23	0.25
Case 4		45970	18147	12033	0.395	0.262	0.22
Case 1	*@ 2" away from load*	28296	2956	5709	0.139	0.202	0.42
Case 2		38513	11761	8610	0.31	0.22	0.29
Case 3		40127	13798	9824	0.34	0.24	0.24
Case 4		42170	14351	10073	0.340	0.239	0.23

Figure 11-13 shows the contour plot for the analysis of four unbound layers. Aggregate systems with less anisotropy (higher modulus ratio) and higher vertical modulus values performed better in terms of the shear strength ratio criterion at the top of the unbound aggregate base layer.

The authors emphasize the fact that modular ratios cannot be considered solely as a performance measure in aggregate systems. For instance, a very fine-grained soil can have a high modular value (less anisotropic) with low modulus values in orthogonal directions. Therefore, the results should be analyzed considering all material properties as well as shear strength ratio.

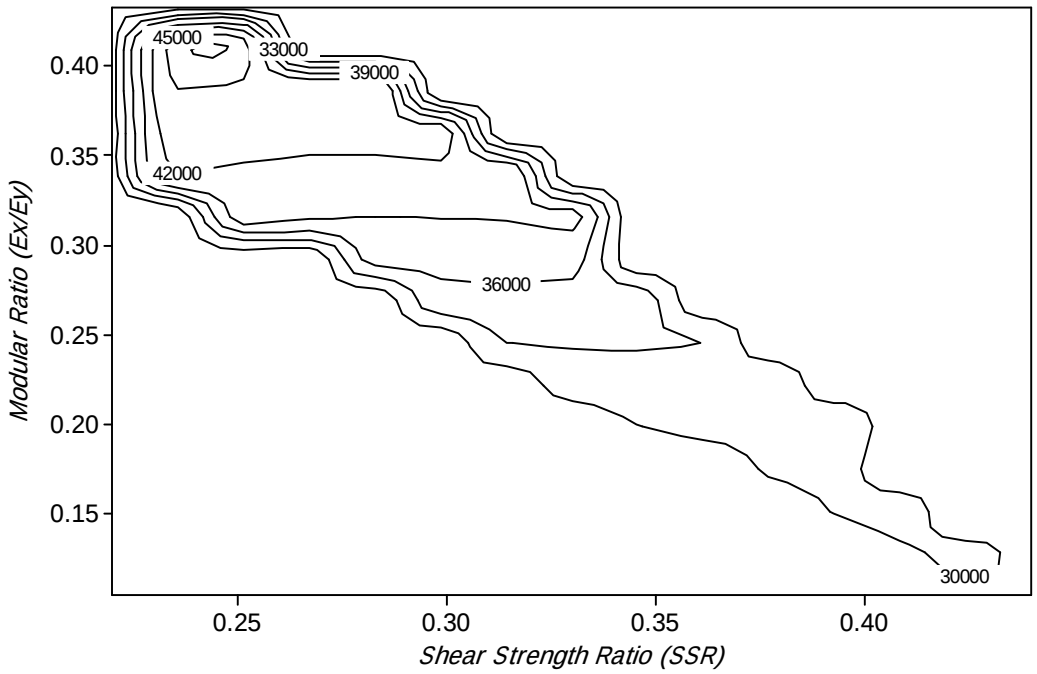

Figure 11-13 Contour plot of shear strength ratio (τ_{oct}/UCCS), anisotropy level (E_x/E_y), and vertical modulus (E_y)

CHAPTER XII

APPLICATION OF PATTERN RECOGNITION TECHNIQUES AND NEURAL NETWORKS IN CHARACTERIZATION OF UNBOUND AGGREGATE SYSTEMS

INTRODUCTION

This study investigates the capability of pattern recognition techniques and artificial neural networks to predict cross-anisotropic material properties of unbound aggregate base materials. The analysis was performed on the comprehensive database of 10 aggregate sources with different gradations and tested at different saturation levels. Nonlinear and cross-anisotropic material parameters (k_1 through k_9 values) were determined using variable dynamic confining pressure stress paths. Particle geometry was characterized using the Aggregate Imaging System (AIMS). Scale parameters and shape parameters of the characterizers of the aggregate geometry (form, angularity, and texture of the particles) were in turn used as inputs to the model to account for the impact of shape-induced anisotropy in aggregate systems. Moisture content and dry density of the aggregate specimens at the time of testing as well as Weibull parameters of particle size distributions were determined and used as inputs to the neural network model.

Several neural network models with different architectures were developed, and the performances of the models were assessed based on an unseen set of data. Dimensionality reduction techniques and discriminant analysis were also performed to identify features of the aggregate systems that have the most impact on the anisotropic behavior of aggregate systems.

First part of this chapter deals with neural network modeling and sensitivity analysis on the model. Second part of this chapter presents the results applying dimensionality reduction techniques and discriminant analysis on the aggregate database.

DESCRIPTION OF INPUT AND OUTPUT FEATURES

In total eighteen (18) input parameters and three output parameters for sixty five (65) aggregate systems were determined and were used to train several neural network-based models. The general architecture of the neural network model is presented in figure 12-1. Particle shape parameters were determined using the aggregate imaging system. Stress and strain levels corresponding to that produced by actual traffic-induced loading were simulated by state of the art equipment capable of simulating cross-anisotropic loading called the RaTT (Rapid Triaxial Tester). Dry density and moisture content at the time of testing were used as inputs to the model to capture saturation level dependency of the material parameters. Modular ratios (E_x/E_y and G_{xx}/G_{xy}) and the ratio of the Poisson ratios (ν_{xx}/ν_{xy}), which are the input data for the anisotropic solutions in the finite element program (TTI-PAVE), were considered as the output of the model. Details regarding the input and output of the database were presented in Chapter IX.

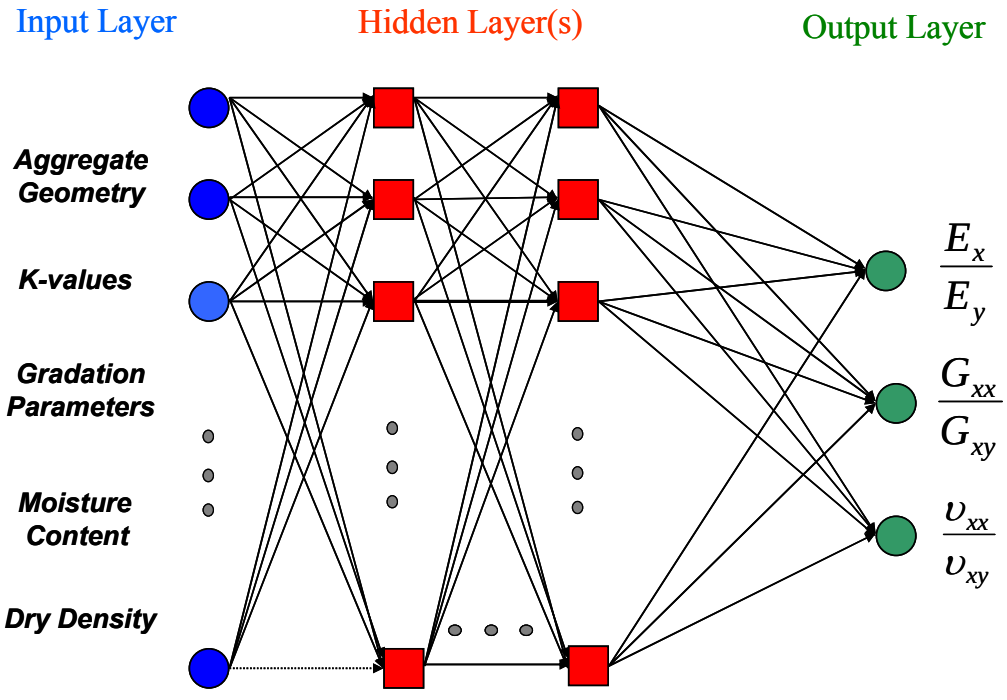

Figure 12-1 Representation of inputs and outputs of the neural network-based model

(Yu 1993)Yu (1993) showed the infinitesimal strain increment for cross-anisotropic particulate medium can be found from equations 12-1 through 12-3.

$$d\varepsilon_x = \frac{1}{E_x}\left[\left(\frac{n}{m} + m\,v_{xx}\right)\left(m\,d\sigma_x\right) - m\,v_{xx}\,dI_1\right] \tag{12-1}$$

$$d\varepsilon_y = \frac{1}{E_x}\left[d\sigma_y - (m+1)\,v_{xx}\,d\sigma_x\right] \tag{12-2}$$

$$d\varepsilon_{xy} = \frac{\mu\left[1 + v_{xx}\right]}{E_x}\left(d\sigma_{xy}\right) \tag{12-3}$$

where $d\varepsilon_x$, $d\varepsilon_y$, and $d\varepsilon_{xy}$ are infinitesimal strain increments in horizontal direction, vertical direction, and shear strain increment in xy plane, respectively. Definition f parameters *n*, *m*, and μ were previously defined in equations 9-11 in Chapter VII. As evidenced in these equations, the responses of aggregate systems are functions of these parameters.

DESIGN OF NETWORK ARCHITECTURE

In order to study the impact of network topology and network architecture on the estimation of anisotropic material properties, two network topologies namely feed forward multi layer Perceptron with static back propagation and the generalized feed forward network both with several hidden layers were considered. The details of the network systems are presented in Table 12-1.

The aggregate database was partitioned into three sets of training, cross-validation, and testing data. Sixty percent of the samples were labeled as the training set and used to train the network. Fifteen percent was used as cross-validation, and the remaining twenty five percent were used for testing. The cross-validation data was used to evaluate the generalization capability of the trained network while the testing data was used to assess the performance of the trained neural network on the unseen set of data.

Table 12-1 Mean Square Errors and Standard Deviations for the Trained ANN Models

	Training	
ANN Architecture	***Average RMSE***	***Average STDV***
MLP 18-1-3	0.02641	0.00499
MLP 18-2-3	0.00921	0.00099
MLP 18-3-3	0.00913	0.00305
MLP 18-4-3	0.00692	0.00085
GFF 18-1-3	0.00585	0.00073
GFF 18-2-3	0.00578	0.00091
GFF 18-3-3	0.00573	0.00045
GFF 18-4-3	0.00548	0.00099

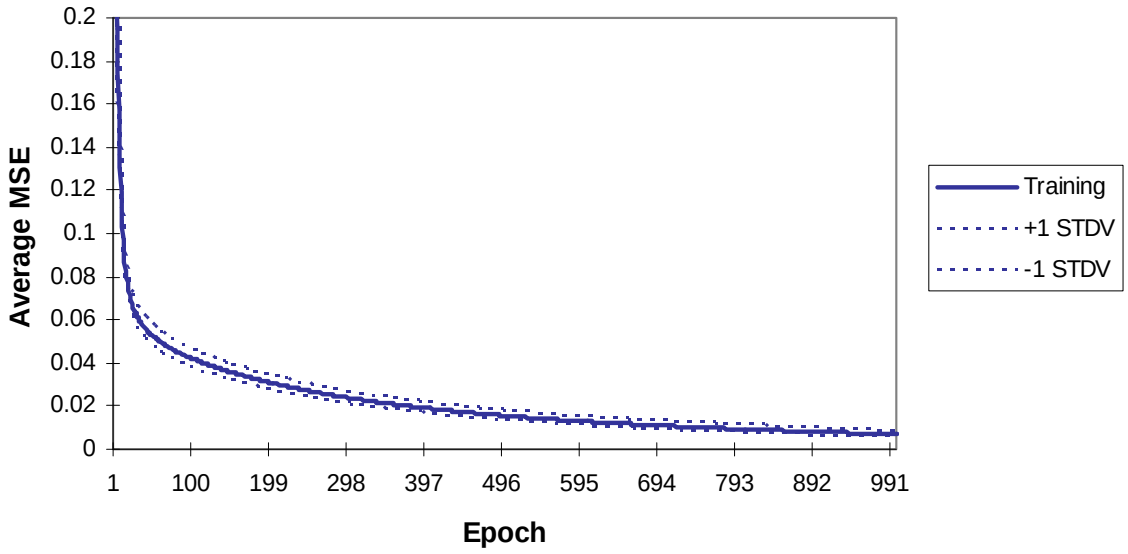

Figure 12-2 Decent of average mean square error with the increase in the number of iterations

Several neural networks were trained using the back-propagation learning algorithm. As illustrated in Figure 12-2, the average root mean square errors (RMSEs) for the training dataset decreased with an increase in the number of iterations. The training was stopped at a point when the least squared error difference between successive 100 epochs was less than a predefined threshold. This was done to avoid overtraining of the network. Training

of several network topologies was performed while increasing the number of hidden layers from one to four. The learning rate was assumed to be 0.001 in this study. The average RMSEs and standard deviations after 1000 iterations for different network architectures are presented in Table 12-1.

PERFORMANCE OF THE NEURAL NETWORK BASED MODELS

The performance of the models in terms of RMSEs on the testing dataset was determined to evaluate the accuracy of the trained neural network in predicting the level of anisotropy in aggregate systems. Table 12-2 presents the RMSEs for each output of the system (E_x/E_y), (G_{xx}/G_{xy}) and (ν_{xy}/ν_{xx}). The RMSEs results for the output of the system with different network architecture suggests that using more than two hidden layers results in slight improvement in the calculated error between the predicted and actual output values. In general, it was observed that the generalized feed forward (GFF) topology performed better in terms of lower RMSEs. This is due to the fact that in GFF networks, connections can jump between the layers and converge in a more efficient way as described earlier in Chapter VI. Therefore, generalized feed forward topology with one hidden layer (GFF 18-1-3) was selected for further analysis of the neural network model.

Table 12-2 Mean Square Error for Testing Dataset

ANN Architecture	Testing RMSE		
	E_x/E_y	G_{xx}/G_{xy}	ν_{xy}/ν_{xx}
MLP 18-1-3	0.00540	0.00466	0.00894
MLP 18-2-3	0.00339	0.00182	0.00302
MLP 18-3-3	0.00297	0.00170	0.00151
MLP 18-4-3	0.00236	0.00142	0.00163
GFF 18-1-3	0.00177	0.00117	0.00260
GFF 18-2-3	0.00146	0.00082	0.00190
GFF 18-3-3	0.00158	0.00115	0.00192
GFF 18-4-3	0.00138	0.00102	0.00156

Plots of predicted versus target values are presented in figures 12-3 to 12-5. Nonlinear mapping of the artificial neural networks was able to provide excellent agreement between the output of the model and actual values from the training database. The plots presented in figures 12-3 to 12-5 are provided for the generalized feed forward topology with one hidden layer (GFF 18-1-3). The comparison was performed on the entire database. Figure 12-3 and figure 12-4 represent good agreement between the predicted and target values for modular ratios E_x/E_y and G_{xx}/G_{xy}.

The significance of the modular ratios E_x/E_y and G_{xx}/G_{xy} is that they are necessary to characterize the anisotropy level in unbound aggregate systems. Smaller modular ratios correspond to more anisotropic systems and higher modular ratios correspond to more isotropic systems. The results presented in Chapter XI revealed the impact of anisotropy level on the orthogonal load distribution capability and performance of unbound and stabilized granular systems. In the sensitivity analysis section of this paper the authors investigated the impact of aggregate features on the anisotropy characterizes E_x/E_y and G_{xx}/G_{xy}.

Strong correlation of coefficient of 0.95 was calculated between the actual and ANN prediction for both modular ratios E_x/E_y and G_{xx}/G_{xy} as shown in figures 12-4 and 12-4. Figure 12-5 illustrates the plot of calculated versus actual values of the ratio of Poisson ratios (ν_{xy}/ν_{xx}). This plot demonstrates good agreement between the neural network model output and target (ν_{xy}/ν_{xx}) values. The correlation of coefficient was calculated as 0.94 as demonstrated in figure 12-5.

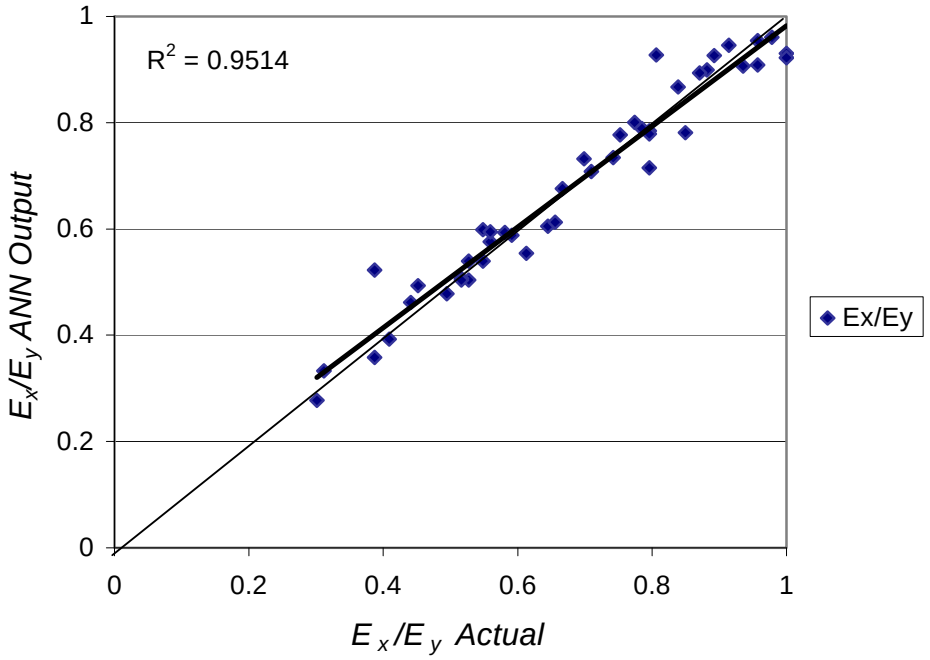

Figure 12-3 Correlation between output of the ANN model and actual values of E_x/E_y

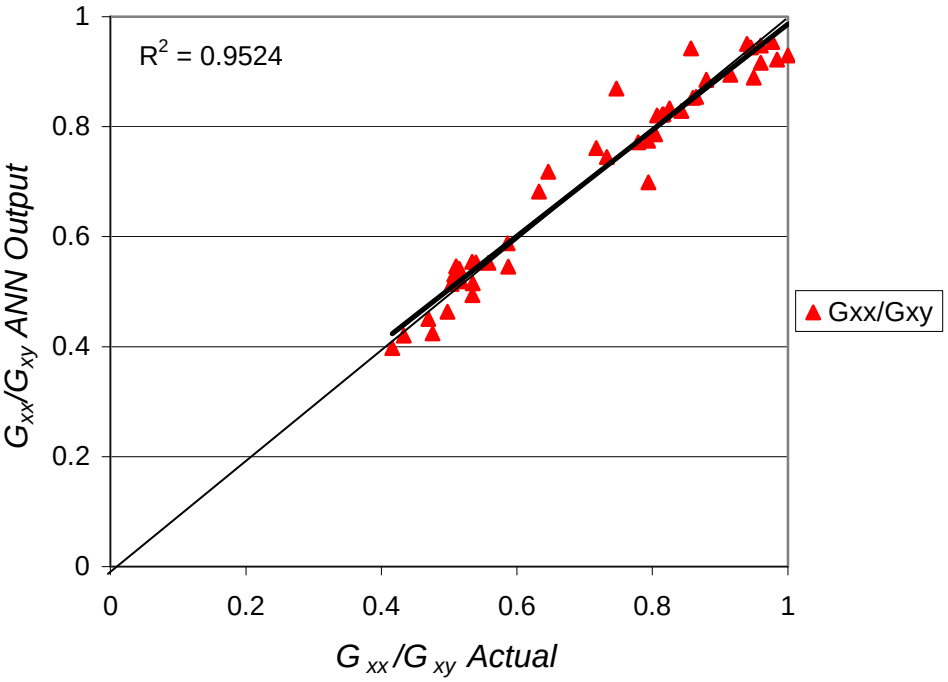

Figure 12-4 Correlation between output of the ANN model and actual values of G_{xx}/G_{xy}

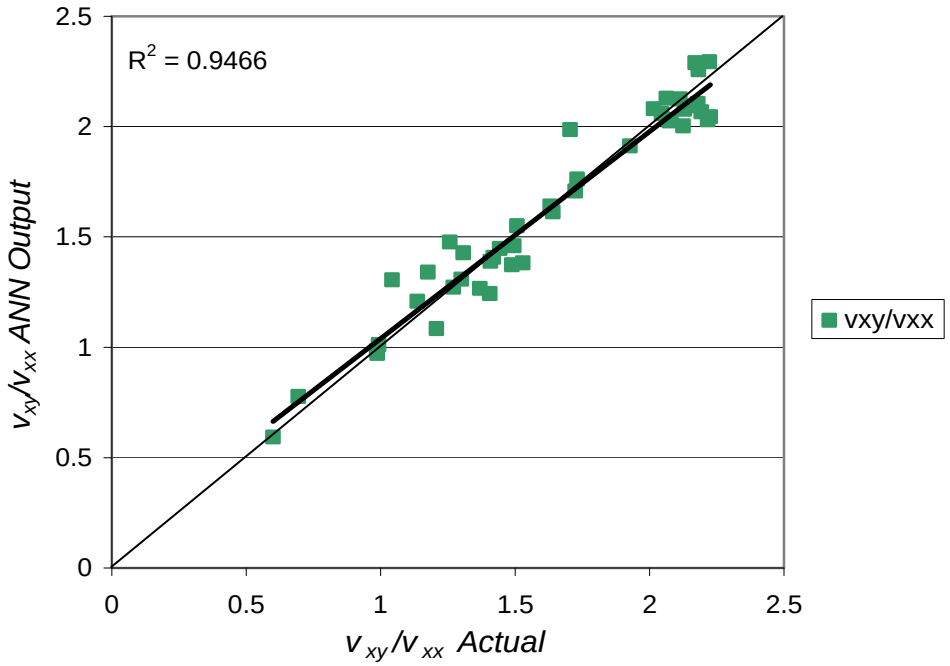

Figure 12-5 Correlation between output of the ANN model and actual values of ν_{xy}/ν_{xx}

SENSITIVITY ANALYSIS OF THE ANN MODEL

Sensitivity analysis provides insight regarding the level of contribution of the aggregate features to the anisotropic output parameters of the neural network model. The sensitivity function presented in Chapter VI indicates the relative degree of the influence of aggregate features on the output of the model over the predefined range of the independent variables. The sensitivity of the model was assessed within two standard deviations of the mean for each aggregate feature. Smaller values of the sensitivity function presented in equation 6 correspond to situations where the output is relatively insensitive to the parameter varied. A higher value of the sensitivity function denotes a greater impact of aggregate feature on the output of the model. It is worth mentioning here that for nonlinear models such as neural networks, the sensitivity may change in a nonlinear fashion over the range of input parameters.

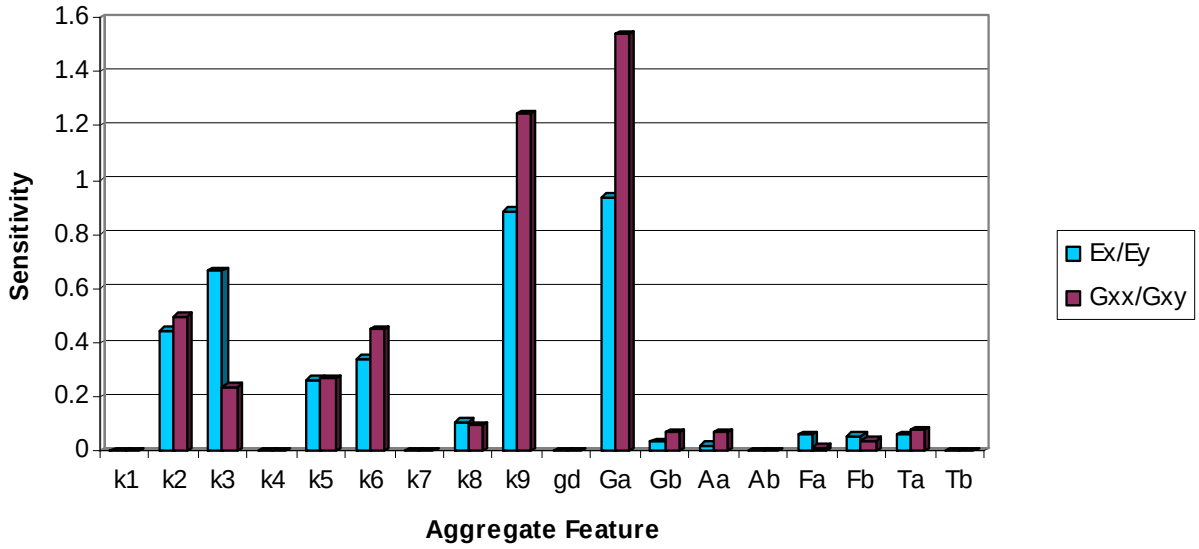

Figure 12-6 Sensitivity of the aggregate features on the output of the model

Figure 12-6 presents the impact of aggregate features on the output of the neural network model. As previously mentioned in this chapter, the significance of the modular ratios E_x/E_y and G_{xx}/G_{xy} is the fact that they have been used to characterize the anisotropy level of aggregate systems. Figure 12-6 demonstrates the impact of hardening and softening parameters of the constitutive equations presented in equations 10-) through -(12 on the modular ratios E_x/E_y and G_{xx}/G_{xy}. Among the parameters in the constitutive equations (k-values), the softening exponent of the shear modulus (k_9) was found to have the highest influence on the level of anisotropy of the system followed by (k_3) and (k_2) softening parameter and hardening parameters of vertical modulus (E_y), respectively. The sensitivity results in figure 12-6 emphasize the importance of particle size distribution on the level of the anisotropy of the system. The scale parameter of the cumulative Weibull distribution (G_α) characterizes the uniformity of the gradations (distribution of particles over the range of sieve sizes) and maximum aggregate size in the mix.

Figure 12-7 through 12-10 present the sensitivity of the output of the model (E_x/E_y) and (G_{xx}/G_{xy}) upon variation of the input features of the model. Figure 12-7 illustrates the impact of the varied scale parameter of the particle size distribution (G_α) on the modular ratios. This plot shows that the model predicts that uniform gradations

(gradations with even distributions of particles over the range of sieve sizes) have higher modular ratios (E_x/E_y) and (G_{xx}/G_{xy}), which are synonymous with less anisotropic systems. This is intuitively true because in uniform distributions the space trapped among larger particles can be filled with smaller particles resulting in more contact points, stronger force chains, and consequently better orthogonal load distribution capability of the system.

Figure 12-8 demonstrates the impact of particle angularity on the output of the model. This plot indicates that aggregate systems consisting of more angular particles show less anisotropic behavior. Considering the fact that the load is distributed and dissipated through the aggregate layers through particle interlock, aggregate systems with more angular particles provide higher friction forces among aggregate particles, which contribute to a stiffer aggregate matrix with less directional dependency of the material properties.

Figure 12-9 shows the impact of particle form parameter (F_α) on the output of the neural network model. A higher form parameter (F_α) corresponds to more flat and elongated aggregates while lower (F_α) values correspond to more cubical particles. This plot shows the capability of the model to predict the increase in the anisotropy of the system when more flat and elongated particles are present in the mix. This can be explained with the fact that the flat and elongated particles tend to reorient themselves with the horizontal plane upon compaction. This difference results in significant directional dependency of the material properties in particulate systems.

Figure 12-10 illustrates the impact of varying particle texture parameter (T_α) on the modular ratios (E_x/E_y) and (G_{xx}/G_{xy}). Higher (T_α) values correspond to particles with rough asperities at the surface while smaller (T_α) values correspond to smooth and polished aggregates. This plot shows that the neural network model predicts less anisotropic systems when more roughly textured particles are present in the mix. This has physical sense because aggregate systems consisting of roughly textured particles improve particle interlock and result in higher friction forces among the particles and consequently reduce the anisotropy of the system.

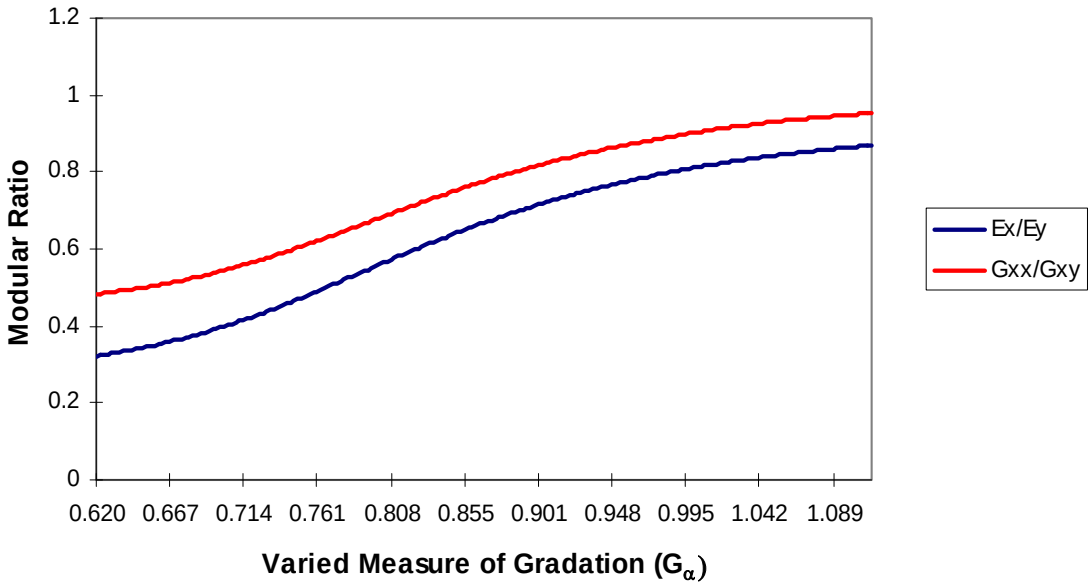

Figure 12-7 Sensitivity of the modular ratios to varied measure of gradation parameter (G_α)

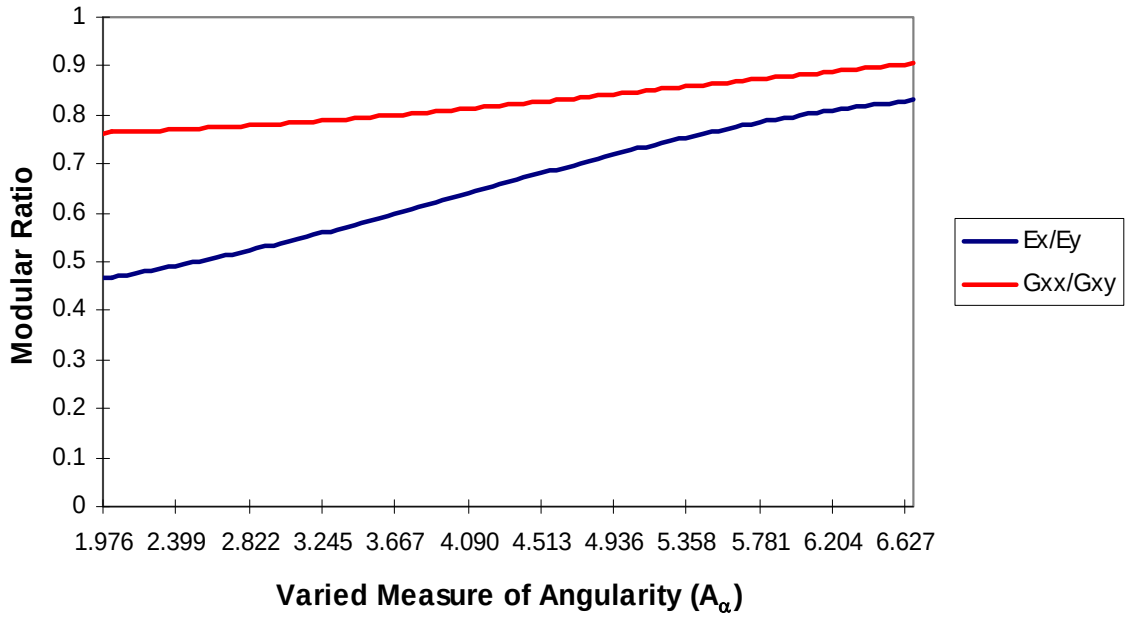

Figure 12-8 Sensitivity of the modular ratios to varied measure of angularity parameter (A_α)

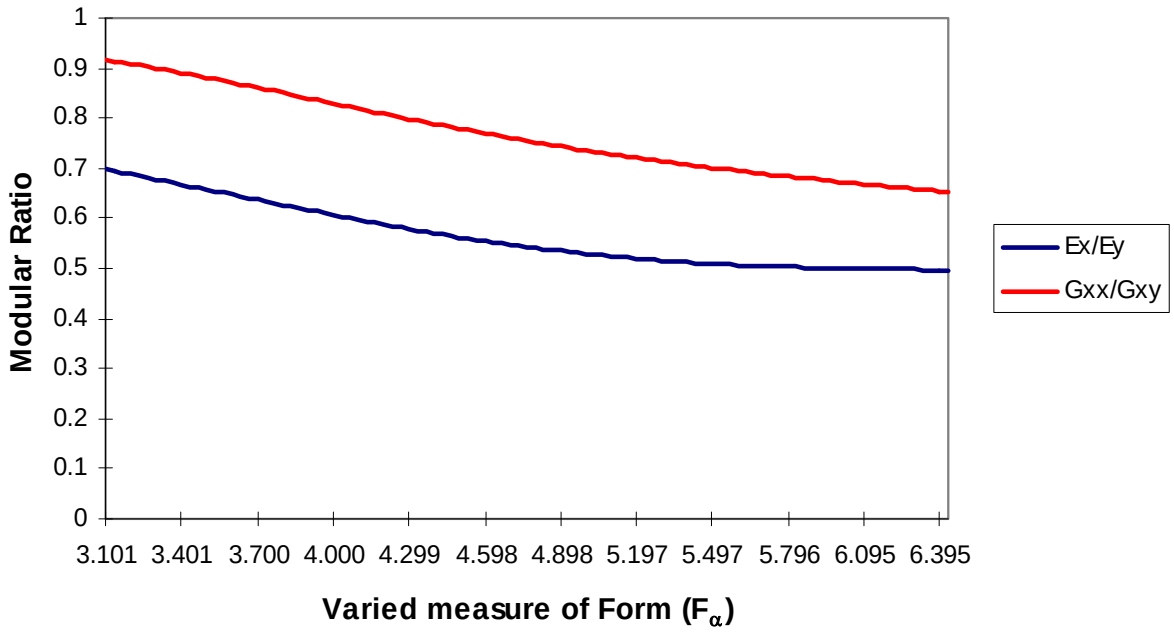

Figure 12-9 Sensitivity of the modular ratios to varied measure of form parameter (F_α)

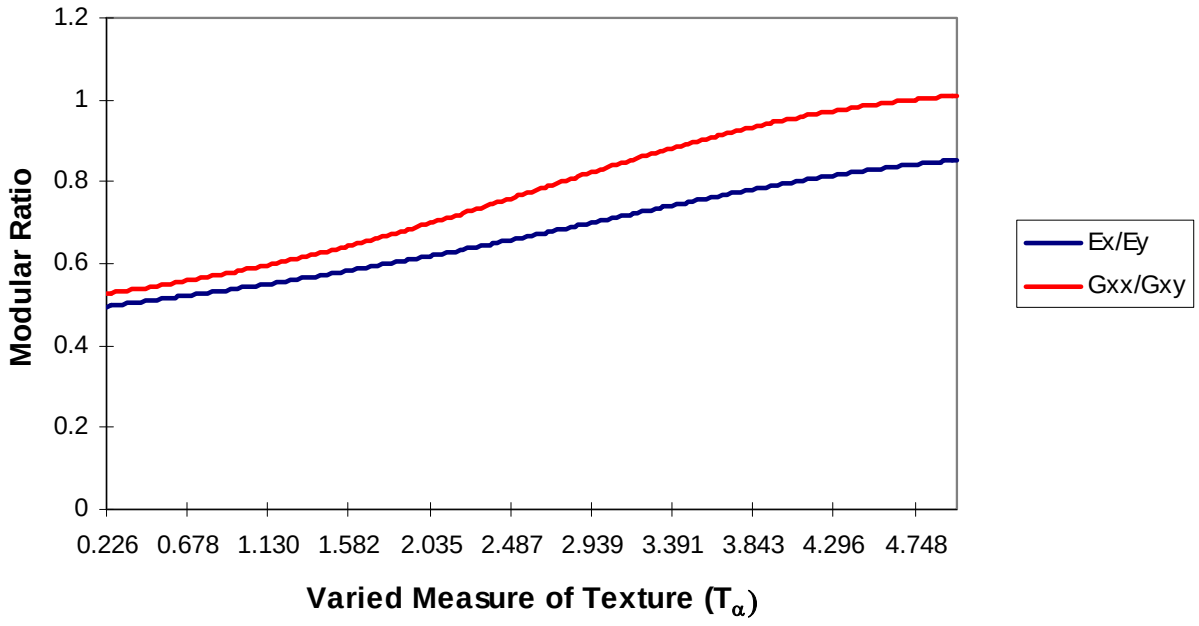

Figure 12-10 Sensitivity of the modular ratios to varied measure of texture parameter (T_α)

The results presented in this section suggest that the sensitivity analysis performed on the ANN model can provide valuable insight regarding the impact of aggregate features on the level of anisotropy of unbound aggregate systems. The level of anisotropy characterized by modular ratios proved to be sensitive to particle size distribution, hardening, and softening exponents of the constitutive equation and the geometry of the aggregate particles.

PATTERN CLASSIFICATION RESULTS

In this part of the study, two methods were employed to extract physically meaningful class discriminatory information using the aggregate database. Investigation of the discriminatory information among the features of the aggregate database was achieved through employing two approaches. In the first approach, the classification was determined through a measure of distance between the distributions of the features of aggregate database. Several measures of distance such as Euclidean distance between the means and Mahalanobis distance between distributions were used to quantify the special distance between the sets of the data.

Hierarchical clustering analysis based on different measures of distance was used to investigate the similarities between the distributions. The significance of this part of the study is that this technique identifies aggregate features with similar patterns. Therefore it provides insight as to unravel the underlying relations and the interaction between the features of the aggregate system. For instance this study revealed that angularity parameter and directional stiffness follow the same pattern.

In the second approach however, Fisher's linear discriminant analysis was performed to classify the data. KNN algorithm was in turn employed to determine the performance of the classifier based on pre-defined class labels.

Aggregate samples were labeled according to lithology, gradation, and moisture state as presented in table 12-3. Lithology provides information on the mineralogy and the origin of the aggregates tested in this study. Three classes of data were assumed as limestone, granite, and gravel according to lithology. Based on particle size distributions, aggregate samples were labeled as coarse, well, and fine-graded aggregates. Finally, moisture state (dry, optimum, or wet) was used as the third criteria for class labels.

Table 12-3 Classification Criteria and Class Labels of the Aggregate Database.

Classification Criteria	**Class Labels**		
Lithology	Limestone (L)	Granite (N)	Gravel (G)
Gradation	Coarse (1)	Well (2)	Fine (3)
Moisture State	Dry (D)	Optimum (O)	Wet (W)

Supervised Clustering Analysis

Supervised clustering analysis was performed on the aggregate samples according to the class labels presented in 12-3. Three classification criteria, namely lithology, gradation, and moisture state were used in this study. Classification based on the lithology of aggregates resulted in a 73% classification rate. Sequential Forward Selection (SFS) algorithm was employed to select the features that minimize the mean square error objective function. Angularity parameter, dry density, and k_6 parameter (exponent of the hardening term for horizontal modulus model) were selected as significant features.

Classification based on gradation resulted in a 62% classification rate. SFS algorithm selected angularity parameter, k_3 and k_9 (exponents of softening terms for vertical and shear modulus, respectively) as most influential features that explain the dynamic of the system.

Classification based on the moisture state resulted in a 52% classification rate, which has the lowest rate compared to other classification criteria. The features selected in this run were k_3 (softening exponent of vertical modulus) and k_7 (multiplier in the shear modulus model).

The best classification rate (73%) was achieved when lithology was considered as the classification criteria. The unsupervised clustering analysis confirmed the fact that angularity plays an important role in the anisotropic behavior of aggregate systems. This

finding is in conformity with the results presented in sensitivity analysis of the anisotropy model in Chapter XI.

Considering the fact that load transfer in particulate media is carried out through particle interactions and aggregate interlock, aggregate systems with more angular particles are less prone to develop plastic deformations when subjected to traffic load.

To check the impact of angularity of aggregates, the angularity parameters were removed from the database, and the algorithm was executed without this parameter. The classification rate was dramatically dropped from 73% to 46%, which demonstrates the significance of this feature of aggregates.

Classifications based on the particle size and moisture state were shown to have a low classification rate.

Hierarchical Clustering Analysis

Hierarchical unsupervised clustering techniques were performed on features of the aggregate database. Two different proximity measures namely Mahalanobis distance and average distance were used to define cluster hierarchy in unsupervised clustering analysis of this study. These similarity measures were employed to find a physically meaningful pattern among the features of the aggregate database.

Equation 4 was used to calculate the Euclidian distance between all pairs of objects in cluster *r* and cluster *s*. n_r and n_s in equation 12-4 are the number of samples in cluster *r* and cluster *s*, respectively.

$$d(r,s) = \frac{1}{n_r . n_s} \sum_{i=1}^{n_r} \sum_{j=1}^{n_s} dist(x_{ri}, x_{sj}) \qquad (12\text{-}4)$$

Equation 12-5 was used to calculate the Mahalanobis distance. Mahalanobis distance is widely used as a measure of proximity of distributions in the clustering analysis.

$$dist(x_{ri}, x_{sj}) = (x_{ri} - x_{sj})D^{-1}(x_{ri} - x_{sj})^T \quad (12\text{-}5)$$

As evidenced in this equation, the distance between the pairs of data points is normalized by covariance matrix D. Therefore this measure is less sensitive to outliers of the system and typically results in better classification rates.

After choosing the proximity measure in each method, K-means algorithm was used to find the matching samples in each cluster. K-means algorithm is used when the number of clusters is previously determined. In other words K-means algorithm will produce exactly K different groups of data with greatest possible distinction.

K-means algorithm arbitrarily assigns one sample as the cluster center and calculates the sample mean of each cluster. Then iteratively reassigns samples with nearest means to the cluster centroids. This algorithm continues until the classification of the samples stays the same compared to previous iteration.

Figure 12-11 shows the hierarchical clustering of the features using average distance as proximity measure. Figure 12-12 presents clustering of the features according to Mahalanobis distance of the features.

Results from figure 12-11 and 12-12 were found to be very close to each other. The dendograms illustrated in figure 12-11 indicates that k_4 and k_1 have closest patterns in the dataset, which is in conformity with the prior knowledge of the behavior of aggregate systems. k_1 and k_4 are the multipliers (intercepts) of the elastic modulus in vertical and horizontal directions, respectively.

Figures 12-11 and 12-12 show the similarity of patterns between softening parameters (k_3 and k_9) and water content (w). It is well established in unbound literature that ingress of moisture in unbound aggregate systems results in loss of stiffness in orthogonal directions causes accelerated rutting. The reduction of stiffness properties in

unbound systems are reflected by an increase in softening parameter in the model. Therefore the patterns of softening parameter and water content were expected to be closely related as confirmed in this study.

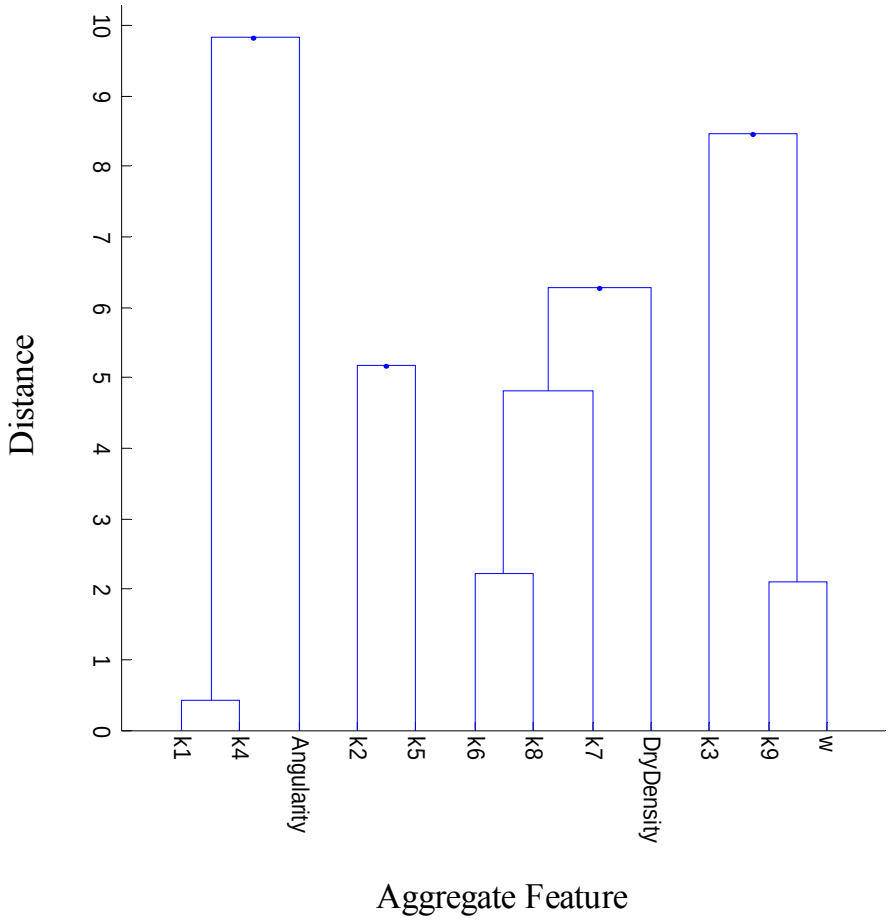

Figure 12-11 Hierarchical clustering of the features using Euclidean distance as the measure of proximity

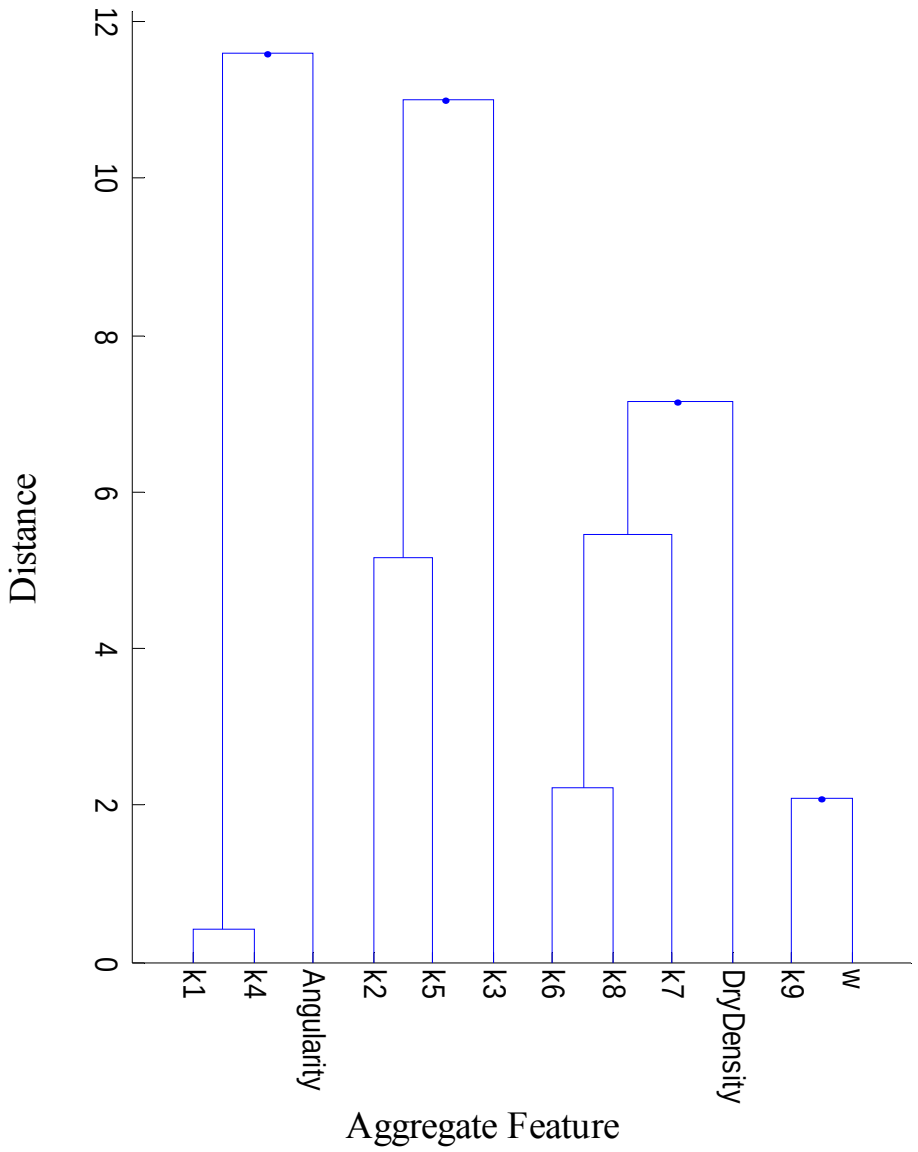

Figure 12-12 Hierarchical clustering of the features using Mahalanobis distance as proximity measure

Discriminant Analysis of the Aggregate Database

In another effort, Fisher's linear discriminant criterion was used as a means to provide class separability information among the features of the aggregate database. Initially the eigenvalues and eigenvectors of Fisher's criterion (S_W^{-1} S_B) were determined, and the

data were projected onto the two principal components with highest eigenvalues. Figure 12-13 presents the plot of eigenvalues for Fisher's criterion. The knee in the plot suggests that the first two principal components of Fisher's criterion (S_W^{-1} S_B) can reasonably explain the variation of the data and the dynamic of the system.

KNN classifier with different values of K (number of neighbors) was executed on the projected data to determine the performance of the classifier. More detail on the KNN algorithm has been provided in Chapter VII.

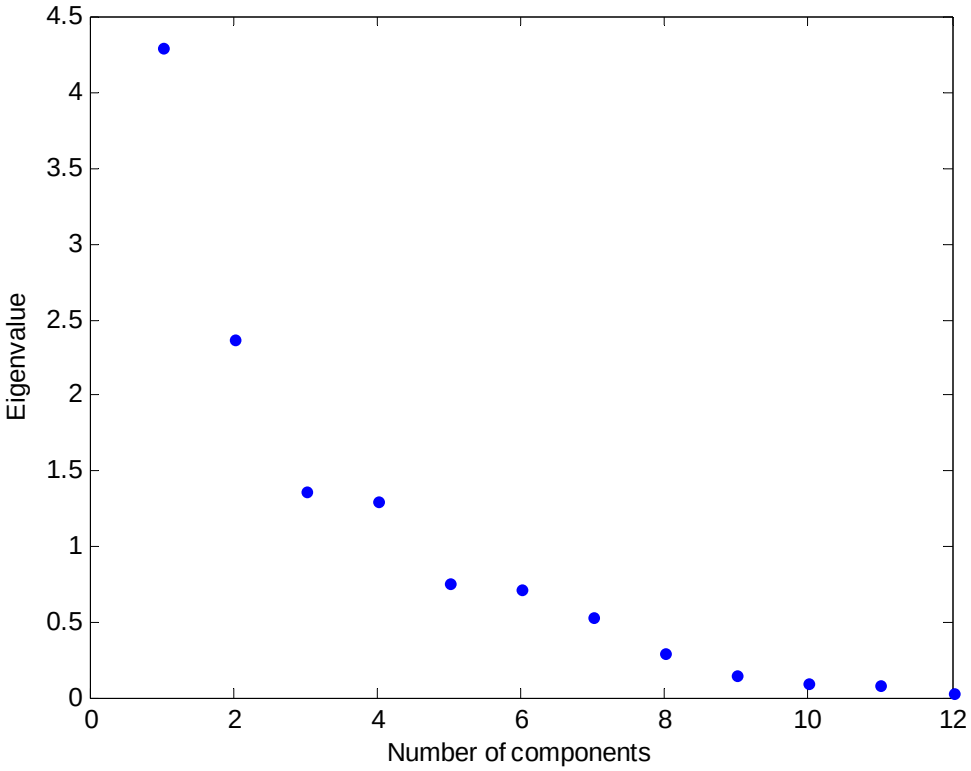

Figure 12-13 Plot of eigenvalues of Fishers' criterion (S_W^{-1} S_B)

Figure 12-14 presents the classification rates for both raw data and the projected data after applying KNN classifier on projected data. The bandwidth or K-value was assumed to be 5.

The classification performance results clearly demonstrate the capability of Fisher's discriminant criterion to provide class discriminatory information when the true class labels were considered to be according to lithology.

Figure 12-14 shows that best classification (93%) was achieved through applying KNN algorithm to projected data. This figure also suggests that this technique was not able to provide class discriminatory information when particle size distributions and moisture state were considered as true class labels.

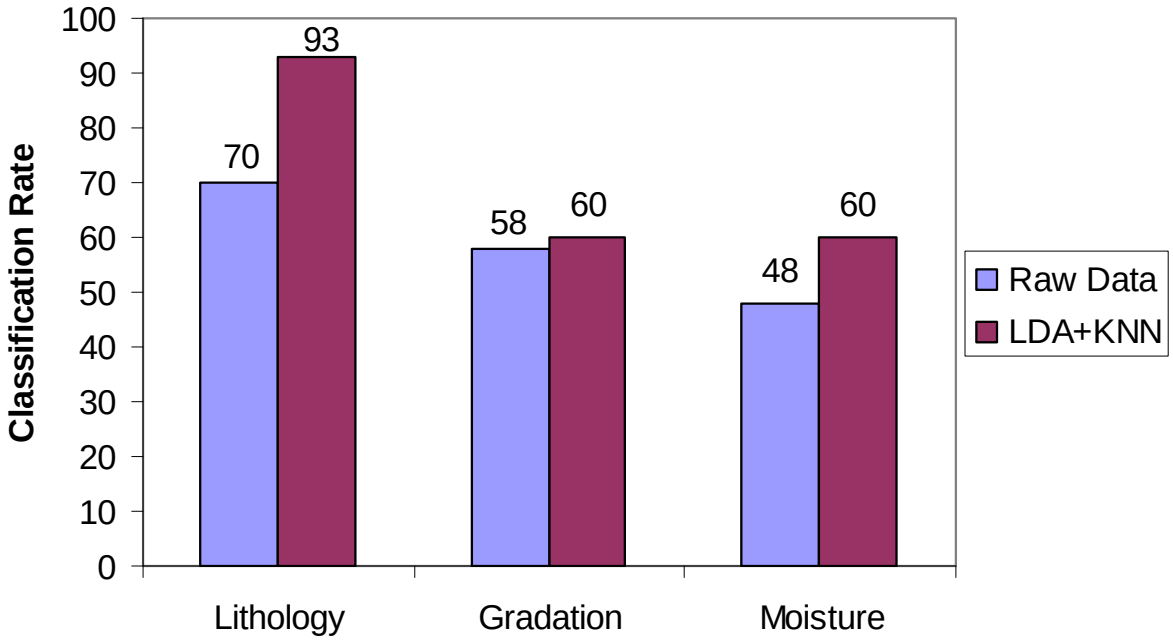

Figure 12-14 Performance of the classifier with respect to predefined class labels

Figure 12-15 shows that LDA when accompanied by KNN classifier was able provide good classification between aggregate samples. This figure shows that gravel aggregates were fully separated using LDA+KNN classifier while some misclassifications exists in limestone and granite materials. This plot also shows limestone and gravel materials have more condensed projections compared to granite materials. This could be due to the

method of identifying aggregate types for construction purposes where limestone and gravel have more distinct definitions compared to granite materials.

Figure 12-16 illustrates the distribution of the observations before application of LDA projection and KNN. This plot is presented to emphasize the significance of LDA+KNN method as a means to provide suitable class discriminatory information between aggregate samples. Figures 12-17 through 12-20 present distributions of the classes of the data with regard to different class labels.

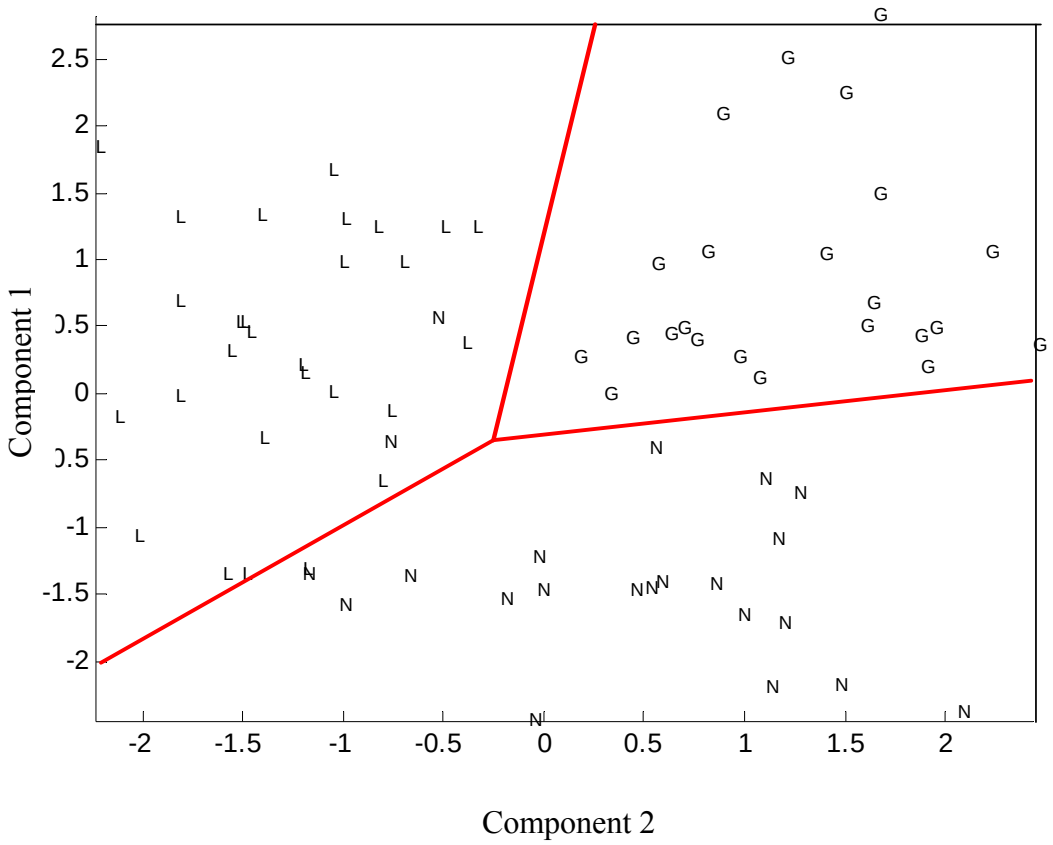

Figure 12-15 Classification using LDA+KNN projection based on lithology
(L: Limestone, N: Granite, and G: Gravel)

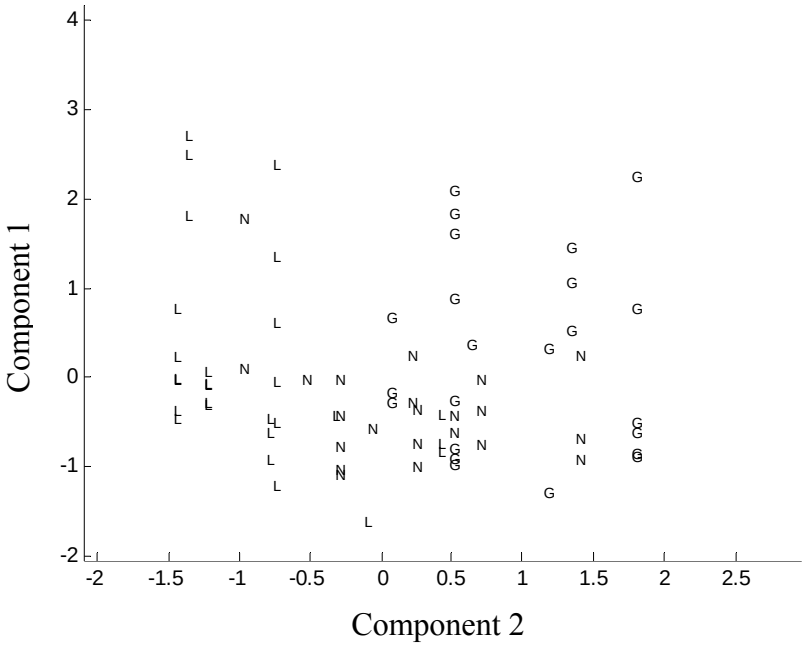

Figure 12-16 Classification using LDA projection based on lithology
(L: Limestone, N: Granite, and G: Gravel)

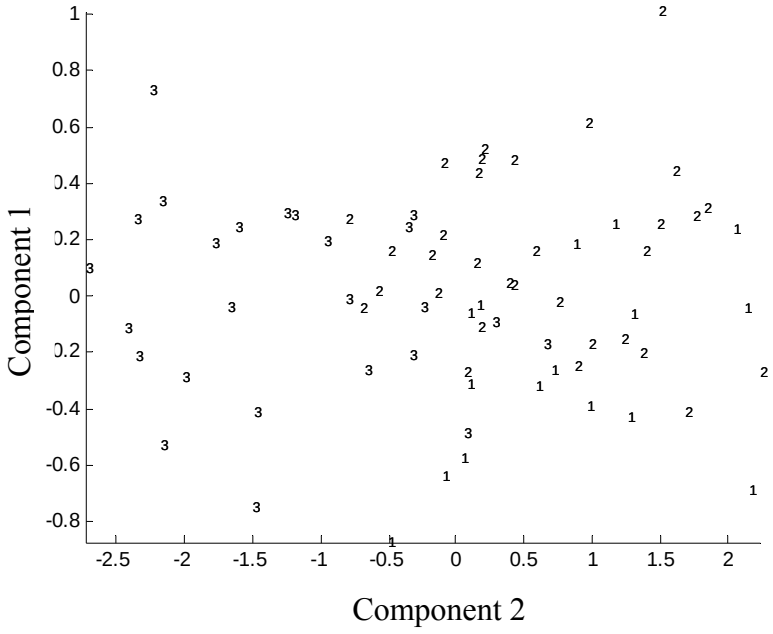

Figure 12-17 Classification using LDA+KNN projection based on gradation
(1: Coarse, 2: Well, and 3: Fine)

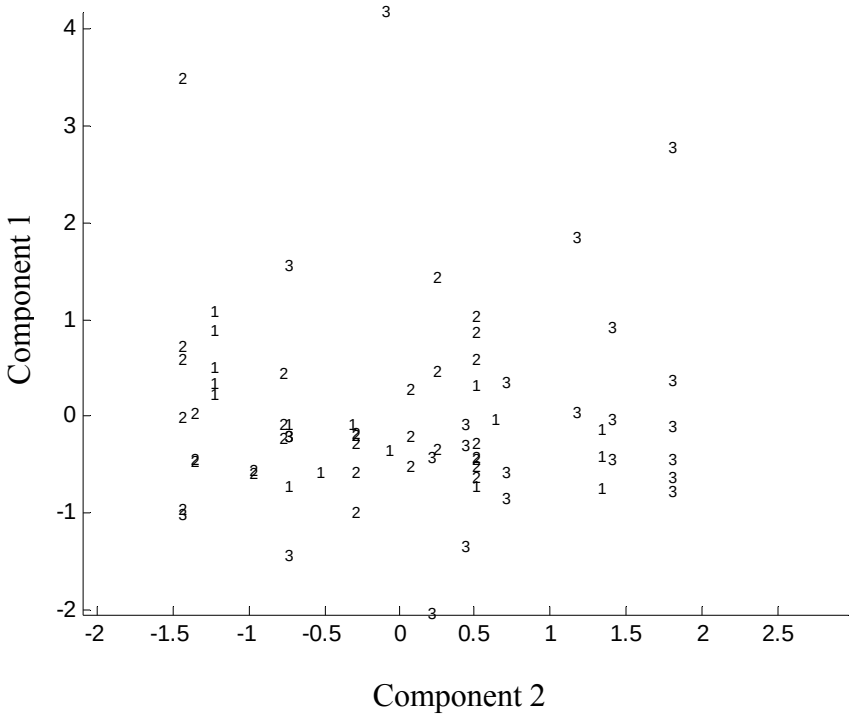

Figure 12-18 Classification using LDA projection based on gradation
(1: Coarse, 2: Well, and 3: Fine)

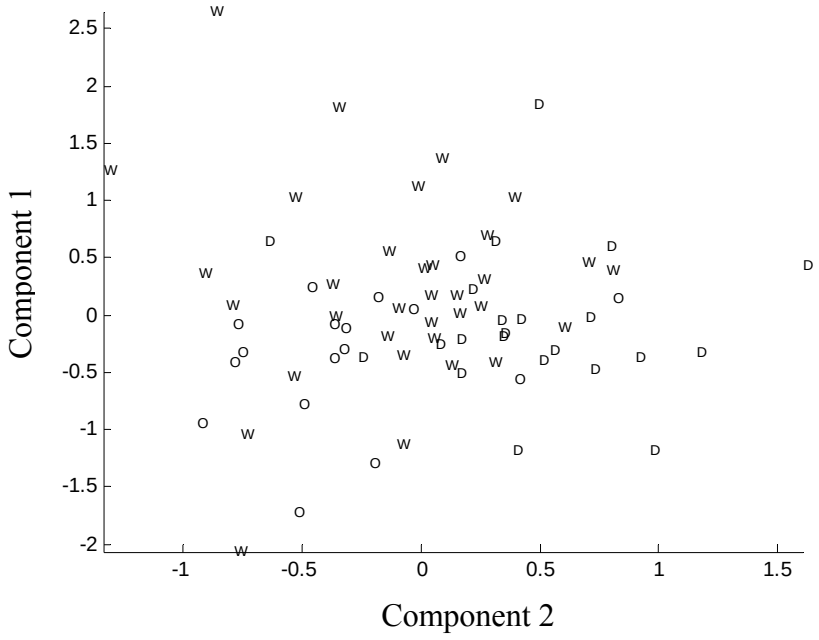

Figure 12-19 Classification using LDA+KNN projection based on moisture state
(D: Dry, O: Optimum, and W: Wet)

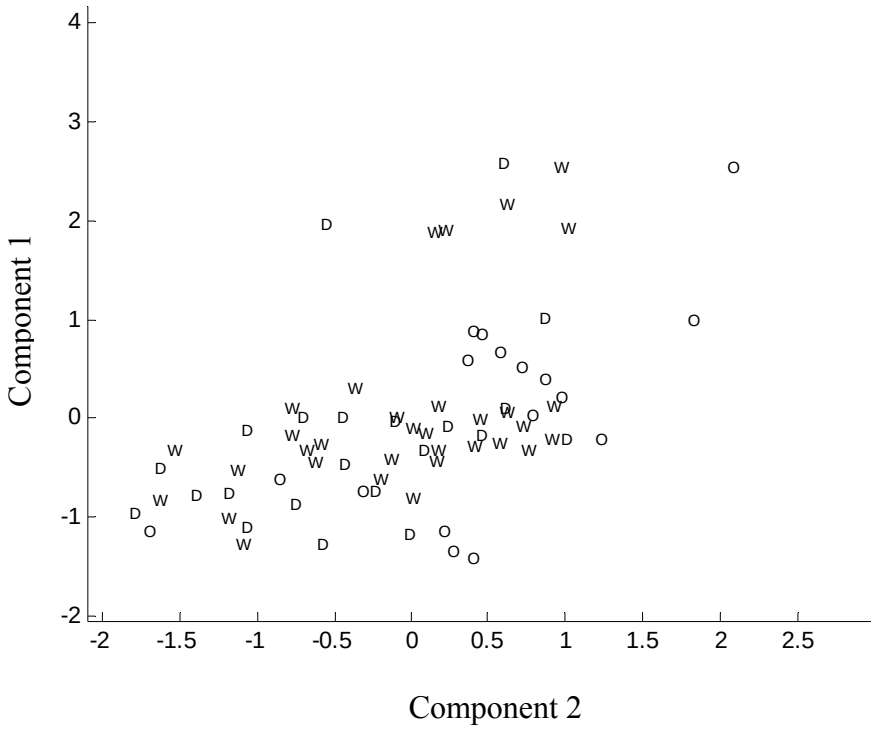

Figure 12-20 Classification using LDA projection based on moisture state (D: Dry, O: Optimum, and W: Wet)

CHAPTER XIII

CONCLUSIONS AND RECOMMENDATIONS

CONCLUSIONS AND SUMMARY OF FINDINGS

The goal of this dissertation was to investigate the significance of anisotropic modeling of aggregate layers for the design and performance prediction of pavement foundations. As a complimentary objective, statistical pattern recognition techniques were employed to identify aggregate features that contribute to anisotropic behavior of unbound particulate systems. This was achieved through broad laboratory testing of various aggregate systems as well as finite element modeling and analysis of pavement sections.

A comprehensive aggregate database was created to evaluate the impact of aggregate features that influence anisotropic behavior of aggregate systems at different conditions. Aggregates with different lithology were selected to investigate the impact of mineralogy and the geographical location of the quarry on the mechanical behavior of aggregate systems. Several gradations with varying fine contents were designed over the course of this study. Aggregate samples were molded at optimum moisture content, dry of optimum moisture content, and wet of optimum moisture content to evaluate moisture susceptibility of the aggregate systems. The impact of stabilizer content was also investigated in this dissertation. Low levels of type I cement were incrementally added to the systems to study the impact of chemical bonding agents on performance of aggregate systems.

Anisotropic solutions were employed in this study to calculate critical responses of aggregate systems under simulated wheel load. Aggregate layers were considered as stress sensitive and cross-anisotropic materials. This dissertation also opens the door to application of the unified strength theory for the performance prediction of aggregate layers. Previous work on the application of plasticity theory and failure functions was quite limited due to unrealistic nature of isotropic characterization of aggregate bases. Isotropic modeling of pavement layers typically results in high tensile stresses at the

bottom of unbound layers. Using these unrealistic stresses in the failure functions induces significant systematic error on the assessment of the stability of pavements. On the other hand, employing anisotropic solutions result in significant reduction or elimination of tensile stresses in the unbound layers. Previous studies showed that nonlinear and anisotropic solutions had a closer match to field measurements as opposed to linear isotropic solutions. Therefore prediction of the stability of pavement foundations using plasticity theory is more reliable when the responses in the model were calculated using anisotropic solutions. Based on strength theory, a criterion was developed to ensure the stability of aggregate layers subjected to heavy wheel loads. This criterion employs Drucker-Prager's failure postulate constrained by Mohr-Coulomb failure criterion to define an upper bound limit. The stress combinations that fall within the threshold represent stable conditions while stress states that surpass the upper bound limit represent conditions at which the aggregate layer is prone to develop accelerated plastic deformations. This protocol provides a mechanistic approach to ascertain the reliability of the design in flexible pavements.

The following sections provide important observations and summary of the findings pertaining to laboratory characterization and analysis of unbound as well as stabilized aggregate systems. The categorized conclusions will be accompanied by suggestions for feature work and research potential in the area of analysis and design of pavement foundations.

Conclusions Related to Stabilization Study

Specimens of aggregate systems with various densities, moisture contents, stabilizer contents, and fines contents were tested to evaluate the synergistic impact of these features on the material properties and responses of unbound aggregate systems. The emphasis was on exploring the potential of using quarry fines in aggregate layers as a sustainable approach for the design of green highways. The intent was to maintain the flexibility of the aggregate systems by adding a small amount of stabilizer and yet to

provide acceptable properties of the high-fines bases, especially under wet or near saturation conditions. In maintaining flexibility, the intent was also to eliminate or at least reduce the potential of initiation and propagation of cracks in the stabilized system due to rigidity of fine aggregate matrix. The laboratory performance of the aggregate systems was assessed through measuring the anisotropic nonlinear stiffness properties, permanent deformation under repeated loading and unconfined compressive strength. In addition, the resilient properties were used in a finite element program to model the responses of aggregate systems subjected to simulated wheel load. Shear strength ratio was in turn used as the measure of field performance of aggregate layers.

The laboratory test results confirmed findings from previous studies and field experience that the increase in fines content in unbound systems has a detrimental effect on the resilient properties and deformation potential of unbound systems. Laboratory performance results revealed that an increase in the fines content in unbound systems at high saturation levels dramatically diminished the quality of performance. However, aggregate systems with higher fines benefited considerably from low percentages of cement stabilizer.

The study of stabilized systems revealed that the moduli ratio was increased as more bonding agents were introduced to the systems. In other words incremental addition of chemical stabilizers to high fines content systems potentially reduced the directional dependency of material properties and therefore which is synonymous with superior performance in terms of better orthogonal load distribution capacity when under traffic load.

The permanent deformation and unconfined compressive strength test results confirmed the findings from the finite element analysis of the pavement structure, which demonstrated the potential of achieving superior performance in lightly stabilized high fine content aggregate systems.

It was found that with the proper design of fines content, stabilizer content, and control of moisture, the performance of the stabilized systems with high fines contents

can perform equivalent or even better than the systems with standard fines content. This was clearly evidenced by enhancing the resilient properties (increase in directional stiffness and decrease in anisotropy), decreasing the rate and magnitude of permanent deformation, and increasing compressive strength of high fines content stabilized systems.

Conclusions Related to Investigation of Aggregate Features That Influence the Anisotropic Behavior of Aggregate Layers

The objective of this study was to establish a procedure to determine the level of anisotropy of aggregate systems based on the features of the aggregate database. Stress-induced directional dependency of material properties was evaluated based on multiple variable dynamic confining pressure stress path tests for 10 aggregate sources. This stress path protocol was able to simulate the rotation of principal stresses under the wheel load. The cross-anisotropic modular ratios were used as indicators of the level of anisotropy in this effort. Various gradations and saturation levels were considered for each aggregate source. Particles geometry was characterized using the Aggregate Imaging System (AIMS). The cumulative Weibull distribution function was used to describe aggregate size and aggregate geometrical characteristics. The fine portion of the gradation was characterized by the Rigden voids test and the methylene blue test to account for fine particle shape properties and deleterious effect of plastic fines on volumetric stability of aggregate layers. A model that relates modular ratios (measure of anisotropy) to aggregate properties was developed. This model provides a simple and cost-effective means to determine the anisotropy level of aggregate samples with a few simple and routine tests.

The sensitivity analysis of the anisotropy model revealed that modular ratios (G_{xx}/G_{xy}) and (E_x/E_y) are highly sensitive to particle geometry. Analysis of the aggregate database suggests that aggregate systems consisting of more angular and less polished particles were less anisotropic. The interactions of aggregate particles can be explained

through contact surfaces and friction forces between particles. The hypothesis is that an increase in angularity and texture increases aggregate friction and interlock in all directions leading to a reduction in the anisotropy of the system. On the other hand, more elongated particles tend to re-orient themselves under loading to the horizontal plane leading to more anisotropic systems.

Finite element analysis was used to calculate pavement responses under simulated traffic load. The base layer was modeled as a nonlinear, stress sensitive and cross-anisotropic material. The performance of the aggregate system was determined using the shear strength ratio, which is defined as the ratio of octahedral shear stress to shear strength. For a given vertical modulus, the results show that better performance (lower SSR) is related to less anisotropic aggregate systems.

The anisotropy model developed in this study offers the opportunity to investigate the impact of aggregate features on the performance of unbound aggregate systems. This approach can be used as a quality control tool for aggregate producers and pavement design engineers.

Conclusions Related to Application of Non-traditional Mathematical Techniques

The objective of this task was to investigate the capability of pattern recognition techniques to reveal the underlying relations between the features of the aggregate database. In another effort Neural Network techniques were employed to accurately predict the level of anisotropy of the systems based on measured/calculated aggregate features in the database. Several neural network models with different topologies were developed, and the performances of the models were assessed based on an unseen set of data.

A parametric analysis was performed to study the interactions of the input and output of the model. The sensitivity analysis performed on the ANN model provides valuable insight regarding the impact of aggregate features on the level of anisotropy of

unbound aggregate systems. The level of anisotropy proved to be most sensitive to particle size distribution, hardening, and softening parameters and the geometry of the aggregate particles.

RECOMMENDATIONS FOR FUTURE WORK

It is crucial to study the influence of environmental cycles on the mechanical response and performance of aggregate systems. In this study none of the stress path tests of aggregate systems were performed under freeze-thaw conditions. Therefore caution should be exercised before generalizing the results and findings of this dissertation to cold regions. This is more significant where stabilized high fines content layers are of interest as an alternative design. Therefore, the results presented in this study are limited to environments where freeze-thaw damage is not a major concern. As a continuation to this study, future research potential can include evaluation of the influence of freezing and thawing on the performance of the unbound and stabilized aggregate systems.

Application of variable dynamic confining pressure stress path tests for characterization of permanent deformation properties of unbound aggregate systems needs to be investigated. Current repeated load permanent deformation loading protocols are based on constant confining pressure stress path tests, which do not resemble field conditions and extensively discussed and refuted in this dissertation. It is well established in the geotechnical literature that permanent deformation of geomaterials is highly impacted by the stress history and the stress regimen. The rotation of principal stresses by approaching and departing wheel load results in oscillation between extension and compression stress regimens. This behavior cannot be captured by constant confining pressure stress path protocols, and therefore the plastic deformation measured by this test does not represent field rutting. Future research on developing permanent deformation models based on VDCP tress paths deems necessary to mechanistically characterize the rutting potential in flexible pavements.

Another future research potential is the calibration of the pavement performance prediction functions based on anisotropic solutions. The current pavement life functions, widely referred to as transfer functions by pavement industry, were based on isotropic characterization of pavement materials. Pavement life is quantified by the number of passages of standard axle to reach failure as a function of material properties and responses calculated using isotropic solutions. We established in this dissertation that anisotropy is an inherent characteristic of unbound layers and significantly impact the distribution of stresses imparted by traffic loads. Therefore it is critical to calibrate the existing transfer functions to accommodate directional dependency of material properties in pavement layers.

Another area of research pertaining to unbound systems is the utilization of imaging techniques such as X-Ray computed tomography in conjunction with distinct element methods to characterize distributions of particle contacts in aggregate systems. The distributions of particle orientations can be used to construct the micro-structure tensor, which is used in the constitutive equations. Constitutive equations consisting of both micro-structure tensor and stress tensor are ideal forms for characterization of geomaterials. Characterization of change in micro-structure tensor due to re-orientation of particles subjected to stress path tests provides valuable insight regarding the mechanisms of shear banding and failure in geomaterials.

REFERENCES

Abelev, A., and Lade, P. (2003). "Effects of Cross Anisotropy on Three-Dimensional Behavior of Sand. I: Stress-Strain Behavior and Shear Banding." *Journal of Engineering Mechanics*, 129(2), 160-166.

Adu-Osei, A., Little, D., and Lytton, R. (2001). "Cross-anisotropic Characterization of Unbound Granular Materials." *Transportation Research Record: Journal of the Transportation Research Board*, 1757(-1), 82-91.

Ahn, N., and Fowler, D. W. (1999) "Past and Current Fines Research." *ICAR (International Center for Aggregate Research) 7th annual Symposium*, University of Texas at Austin.

Andrei, D., Witczak, M., Schwartz, C., and Uzan, J. (2004). "Harmonized Resilient Modulus Test Method for Unbound Pavement Materials." *Transportation Research Record: Journal of the Transportation Research Board*, 1874(-1), 29-37.

Atkinson, J. (2000). "Nonlinear Soil Stiffness in Routine Design." *Geotechnique*, 50(5), 487-588.

Ayres, M., and Witczak, M. (1998). "AYMA: Mechanistic Probabilistic System To Evaluate Flexible Pavement Performance." *Transportation Research Record: Journal of the Transportation Research Board*, 1629(-1), 137-148.

Barenberg, E., and Thompson, M. (1992). "Calibrated Mechanistic Design Procedure for Pavements, Phase 2 NCHRP 1-26." National Cooperative Highway Research Program/Transportation Research Board, National Research Council, Washington, DC.

Barker, W., and Brabston, W. (1975). "Development of a Structural Design Procedure for Flexible Pavements." Technical Report S-75-17, Department of the Army, WES.

Bateman, A. (2003). "Dufferin implements cost effective improvements, breaks with tradition." *Aggregates & Road building Magazine*, May/ June 2003,16-24.

Bathurst, R., and Rothenburg, L. (1990). "Observations on Stress-Force-Fabric Relationships in Idealized Granular Materials." *Mech. Mater*, 9, 65-80.

Bayrak, M., and Ceylan, H. (2008). "Neural Network-Based Approach for Analysis of Rigid Pavement Systems Using Deflection Data." *Transportation Research Record: Journal of the Transportation Research Board*, 2068(-1), 61-70.

Bishop, C. (1995). *Neural Networks for Pattern Recognition*, Oxford University Press, USA.

Bolen, W. P., Kalyoncu, R. S., Tepordei, V. V., and van Oss, H. G. (1996). *"U.S. Geological Survey Minerals Yearbook."* 940 p.

Brown, D. (1996) "Use of Waste Fines as Backfill Material." *ICAR (International Center for Aggregate Research) 4th Annual Symposium.* University of Texas at Austin.

Brown, D., and Pappin, J. (1985). "Modeling of granular materials in pavements."

Brown, S. (1974). "Repeated Load Testing of a Granular Material." *Journal of the Geotechnical Engineering Division*, 100(7), 825-841.

Ceylan, H., Guclu, A., Tutumluer, E., and Thompson, M. (2005). "Backcalculation of Full-Depth Asphalt Pavement Layer Moduli Considering Nonlinear Stress-Dependent Subgrade Behavior." *International Journal of Pavement Engineering*, 6(3), 171-182.

Cokca, E., and Birand, A. (1993). "Determination of Cation Exchange Capacity of Clayey Soils by the Methylene Blue Test." *ASTM geotechnical testing journal*, 16(4), 518-524.

De Rezende, L. R., and De Carvalho, J. C. (2003). "The use of Quarry Waste in Pavement Construction." *Resources, Conservation and Recycling*, 39(1), 91-105.

Desai, C., Krempl, E., Kiousis, P., and Kundu, T. (1987). "Constitutive Laws for Engineering Materials: Theory and Applications. Vol. I." *Tucson*, 1987.

Djamarani, K., and Clark, I. (1997). "Characterization of Particle Size Based on Fine and Coarse Fractions." *Powder Technology*, 93(2), 101-108.

Duda, R., and Hart, P. (1973). *Pattern Classification and Scene Analysis*, John Wiley and Sons, New York.

Duda, R., Hart, P., and Stork, D. (2001). *Pattern Classification*, Wiley New York.

El-Sohby, M. (1969). "Deformation of Sands under Constant Stress Ratios." Proceedings of 7th International Soil Mechanics and Foundation Engineering, Mexico,1,111-119.

Fernando, E. (1997). "Applicability of New Flexible Pavement Smoothness Specification for Asphalt Overlays." *Transportation Research Record: Journal of the Transportation Research Board*, 1575(-1), 18-24.

Fioravante, V., and Capoferri, R. (2000). "On the use of Multi-Directional Piezoelectric Transducers in Triaxial Testing." *Mh*, 100(13), 13.

Fityus, S., Smith, D., and Jennar, A. (2000). "Surface Area Using Methylene Blue Adsorption as a Measure of Soil Expansion." Proceedings of International Conference on Geotechnical and Geological Engineering Geoeng-2000, Melbourne, 19-24

Gray, J. E. (1962). "Characteristics of Graded Coarse Aggregates Determined by Triaxial Tests." *Engineering Research Bulletin*, Alexandria, VA.

Hardin, B. "The Nature of Stress-Strain Behavior of Soils." 3-90.

Hicks, R., Monismith, C. (1971) "Factors Influencing the Resilient Response of Granular Materials." In *Highway Research Record 345*, TRB, National Research Council, Washington, D.C., 15-31.

Hoek, E., and Brown, E. (1997). "Practical Estimates of Rock Mass Strength." *International Journal of Rock Mechanics and Mining Sciences*, 34(8), 1165-1186.

Hornych, P., Kazai, A., and Quibel, A. "Modeling a Full-Scale Experiment of Two Flexible Pavement Structures with Unbound Granular Bases." Proceeding of 5th Unbound Aggregates in Roads (UNBAR5) Symposium, University of Nottingham, UK, 359-367.

Hudson, W. R., Little, D. N., Razmi, A. M., Anderson, V., and Weissmann, A. (1997). "An Investigation of the Status of By-Product Fines in the USA. Research Report for Project "Uses of By-Product Fines." The University of Texas-Austin.

Ishai, O. (1994). *Engineering Mechanics of Composite Materials*, Oxford University Press New York.

Jiang, G., Tatsuoka, F., Flora, A., and Koseki, J. (1997). "Inherent and Stress-State-Induced Anisotropy in Very Small Strain Stiffness of a Sandy Gravel." *Geotechnique*, 47(3), 509-521.

Johnson, W., and Wallis, R. (1982) "Fatigue Behavior of Continuous Fiber Silicon Carbide/Aluminum Composites." Damage in Composite Materials, ASTM STP 775, American Society of testing and Materials, Philadelphia, 83-102.

Kanatani, K. (1984). "Stereological Determination of Structural Anisotropy." *International Journal of Engineering Science*, 22(5), 531-546.

Khazanovich, L., and Roesler, J. (1997). "DIPLOBACK: Neural-Network-Based Backcalculation Program for Composite Pavements." *Transportation Research Record: Journal of the Transportation Research Board*, 1570(-1), 143-150.

Kheder, S. (1985). "Deformation Characteristics of Granular Base Course in Flexible Pavements." *Transp. Res. Board*, 1043, 131-138.

Kim, S., Little, D., and Masad, E. (2005). "Simple Methods to Estimate Inherent and Stress-Induced Anisotropy of Aggregate Base." *Transportation Research Record: Journal of the Transportation Research Board*, 1913(-1), 24-31.

Lade, P. (2008). "Failure Criterion for Cross-Anisotropic Soils." *Journal of Geotechnical and Geoenvironmental Engineering*, 134, 117.

Lade, P., and Musante, H. "Failure Conditions in Sand and Remolded Clay." *Proc., 9th Int. Conf. on Soil Mechanics and Foundation Engineering*, Vol. 1, Tokyo, Japan, 181–186.

Lade, P., and Nelson, R. (1987). "Modelling the elastic behaviour of granular materials." *International Journal for Numerical and Analytical Methods in Geomechanics*, 11(5).

Lade, P., and Wasif, U. (1988). "Effects of Height-to-Diameter Ratio in Triaxial Specimens on the Behaviour of Cross-Anisotropic Sand." *Advanced triaxial testing of soil and rock*, 706-714.

Lekhnitskii, S. (1963). *Theory of Elasticity of an Anisotropic ElasticBody*, Holden-Day San Francisco.

Lings, M., Pennington, D., and Nash, D. (2000). "Anisotropic stiffness parameters and their Measurement in a Stiff Natural Clay." *Geotechnique*, 50(2), 109-125.

Ljung, L. (1999). *"System Identification: Theory for the User. 1999."* Prentice-Hall, Upper Saddle River, NJ.

Lo, S., and Lee, I. (1990). "Response of Granular Soil along Constant Stress Increment Ratio Path." *Journal of Geotechnical Engineering*, 116(3), 355-376.

Love, A. (1944). *A Treatise on the Mathematical Theory of Elasticity*, Courier Dover Publications. US.

Lytton, R. "Foundations and pavement on unsaturated soils." 1st International Conference on Unsaturated Soils, Paris, 1201-1220.

Machemehl, C. (1996). "The Future of the Aggregate Industry." *4th Annual Aggregates Symposium, International Center for Aggregate Research,* Atlanta, GA.

Manning, D., and Vetterlein, J. (2004). "Exploitation and Use of Quarry Fines." *087/MIST2/DACM/01*, MIRO Mineral Solutions, Manchester, UK.

Maree, J. (1978). "Design Parameters for Crushed Stone in Pavements." M Eng. Thesis (in Afrikaans). Pretoria: University of Pretoria, Department of Civil Engineering, Faculty of Engineering, University of Pretoria, South Africa.

Masad, E., Tashman, L., Little, D., and Zbib, H. (2005). "Viscoplastic modeling of Asphalt Mixes with the Effects of Anisotropy, Damage and Aggregate Characteristics." *Mechanics of Materials*, 37(12), 1242-1256.

Mehrabadi, M., Nemat-Nasser, S., and Oda, M. (1982). "On Statistical Description of Stress and Fabric in Granular Materials." *International Journal for Numerical and Analytical Methods in Geomechanics*, 6(1), 95-108.

Meier, R., Alexander, D., and Freeman, R. (1997). "Using Artificial Neural Networks as a Forward Approach to Backcalculation." Transportation Research Record: Journal of the Transportation Research Board, 1570(-1), 126-133.

Miller, J., and Bellinger, W. (2003). "Distress Identification Manual for the Long-Term Pavement Performance Program." Rep. FHWA-RD-03-031 (Federal Highway Administration, 2003), http://www.tfhrc. gov/pavement/ltpp/reports/03031/03031. pdf (access: March 2004).

Moossazadeh, J., and Witczak, M. (1981). "Prediction of Subgrade Moduli for Soil that Exhibits Nonlinear Behavior." Transportation Research Record 810, TRB, National Research Council, Washington, D.C., 9-17.

Nevins, M., and Weintritt, D. (1967). "Determination of Cation Exchange Capacity by Methylene Blue Adsorption." *Ceramic Bulletin*, 46(6), 587-592.

Ng, A. (2001). "Random Scattering and Anisotropic Turbulence of Shear Alfven Wave Packets." *The Astrophysical Journal*, 548(1), 318-322.

Ni, S. (1987). *Dynamic Properties of Sand Under True Triaxial Stress States from Resonant/column Torsional Shear Tests*, University of Texas at Austin. PhD. Dissertation.

Oda, M. (1972). "Deformation Mechanism of Sand in Triaxial Compression Tests." *Soils and Foundations*, 12(4), 45-63.

Oda, M., Nemat-Nasser, S., and Mehrabadi, M. (1982). "A Statistical Study of Fabric in a Random Assembly of Spherical Granules." *International Journal for Numerical and Analytical Methods in Geomechanics*, 6(1), 95-108.

Owusu-Ababio, S. (1998). "Effect of Neural Network Topology on Flexible Pavement Cracking Prediction." *Computer-Aided Civil and Infrastructure Engineering*, 13(5), 349-355.

Parker, F. "Crushed Stone Fines for Mechanically Stabilized Earth Walls." *4th Annual Symposium, International Center for Aggregate Research*, University of Texas at Austin.

Parkin, A., Gerrard, C., and Willoughby, D. (1968). "Discussion: Deformation of Sand in Shear." *Journal of the Soil Mechanics and Foundations Division*, 94(SM 1), 336-340.

Pickering, D. (1970). "Anisotropic Elastic Parameters for Soil." *Geotechnique*, 20(3), 271–276.

Pietruszczak, S., and Mroz, Z. (2001). "On Failure Criteria for Anisotropic Cohesive-Frictional Materials." *International Journal for Numerical and Analytical Methods in Geomechanics*, 25(5).

Rauhut, J., Lytton, R., and Darter, M. (1984). "Pavement Damage Functions for Cost Allocation Volume 1, Damage Functions and Load Equivalence Factors." Report No. FHWA/RD-84/018, Federal Highway Administration.

Raymond, G. (1970). "Discussion: Stresses and Displacements in a Cross-Anisotropic Soil." *Geotechnique*, 20, 456-458.

Rockliff, D. (1996). "Low-Grade Quarry Products, Reclaimed Aggregates and Inert Wastes their use in Unbound Mixtures for Road Pavements." *Waste Management*, 16(1-3) pp 83-85.

Seberras, D. (2000). "Little John" Improves Productivity, Reduces Fines." Aggregates & Roadbuilding Magazine, 57, 24-31.

Seed, H., Mitry, F., Monismith, C., and Chan, C. (1967) "Factors Influencing the Resilient Deformations of Untreated Aggregate Base in Two-Layer Pavements Subjected to Repeated Loading." Highway Research Record 190, HRR, National Research Council, Washington D.C., 19-57.

Shaw, P. (1980). *Stress-strain Relationships for Granular Materials under Repeated Loading*, PhD Dissertation, School of Civil Engineering, University of Nottingham, UK.

Simonsen, E., Janoo, V. C., and Isacsson, U. (2002). "Resilient Properties of Unbound Road Materials during Seasonal Frost Conditions." *Journal of Cold Regions Engineering*, 16(1), 28-50.

Team, W. (2000). "WesTrack Final Report Part III—Project Overview." *Draft Report submitted to FHWA*.

Thadkamalla, B. G., and George., K. P. (1995). "Characterization of Subgrade Soils at Simulated Field Moisture." Transportation Research Record 1481, Journal of Transportation Research Board, National Research Council, Washington, D.C., 21-28.

Theyse, H., De Beer, M., and Rust, F. (1996). "Overview of South African mechanistic pavement design method." *Transportation Research Record: Journal of the Transportation Research Board*, 1539(1), 6-17.

Theyse, H., Maina, J., and Kannemeyer, L. (2007) "Revision of the South African Flexible Pavement Design Method; Mechanistic-Empirical Components." Proceedings of the 9th Conference on Asphalt Pavements for Southern Africa (CAPSA), , Gaborone, Botswana, 256-292.

Theyse, H., and Transportek, C. (2002). "Stiffness, Strength, and Performance of Unbound Aggregate Material: Application of South African HVS and Laboratory results to California Flexible Pavements." Report produced under the auspices of the California Partnered Pavement Research Program for the California Department of Transportation. University of California Berkeley,76.

Thompson, M. (1990a). "NCHRP 1-26: Calibrated Mechanistic Structural Analysis Procedures for Pavements, Volume II-Appendices, Prepared for the National Cooperative Highway Research Program, Transporation Research Program." Transportation Research Board, National Research Council, Washington, D.C.

Thompson, M. (1999). "Hot-mix Asphalt Overlay Design Concepts for Rubblized Portland Cement Concrete Pavements." Transportation Research Record: Journal of the Transportation Research Board, 1684(-1), 147-155.

Thompson, M. R. (1990b). "NCHRP 1-26: Calibrated Mechanistic Structural Analysis Procedures for Pavements, Volume II - Appendices, Prepared for the National Cooperative Highway Research Program, Transporation Research Program." *Transportation Research Board, National Research Council,Washington, D.C.*

Thompson, M. R. (1992). "*NCHRP 1-26:* Calibrated Mechanistic Structural Analysis Procedures for Pavements Phase 2, Volume II - Appendices, Prepared for the National Cooperative Highway Research Program, Transporation Research Program," *Transportation Research Board, National Research Council, Washington, D.C.* .

Touahamia, M., Sivakumar, V., and McKelvey, D. (2002). "Shear Strength of Reinforced-Recycled Material." *Construction and Building Materials*, 16(6), 331-339.

Tutumluer, E., and Kim, I. (2003). "Permanent Deformation Behavior of Airport Pavement Granular Layers." Transportation Research Board: Journal of the

Transportation Research Board, No. 1913, Transportation Research Board of the National Academies, Washington, D.C., 41-49.

Tutumluer, E., Little, D., and Kim, S. (2003). "Validated Model for Predicting Field Performance of Aggregate Base Courses." *Transportation Research Record: Journal of the Transportation Research Board*, 1837(-1), 41-49.

Tutumluer, E., and Seyhan, U. (1999). "Laboratory Determination of Anisotropic Aggregate Resilient Moduli Using an Innovative Test Device." *Transportation Research Record: Journal of the Transportation Research Board*, 1687(-1), 13-21.

Uzan, J. (1985). "Characterization of granular material." Transportation Research Record 1022, TRB, National Research Council, Washington, D.C., 52-59

Uzan, J. (1999). "Granular Material Characterization for Mechanistic Pavement Design." *Journal of Transportation Engineering*, 125, 108.

Uzan, J. (2004). "Permanent Deformation in Flexible Pavements." *Journal of Transportation Engineering*, 130, 6.

Vesic, A. S. (1970). "Expansion of Cavities in Infinite Soil Mass." *Journal of Geotechnical Engineering, ASCE*, 98(SM3), 265-290.

Witczak, M., and Uzan, J. (1988). "The Universal Airport Pavement Design System, *Report I of IV: Granular Material Characterization.*" University of Maryland, Dept. of CE. College Park.

Wood, S. A. (1995) "Pond fines: Waste not. Want Not-Industry Commitment to By-Product Fines." *3rd Annual Aggregate Symposium*, University of Texas at Austin, 1-7.

Yu, S. (1993). "General Stress-Dependent Elastic Moduli for Cross-Anisotropic Soils." *Journal of Geotechnical Engineering*, 119, 1568.

APPENDIX A

TABLE OF MATERIAL PROPERTIES

Table A-1 Anisotropic Material Properties for Gradation V1 at Optimum Moisture Content and with 0 Percent Stabilizer

σ_1 (kPa)	σ_3 (kPa)	I (kPa)	τ_{oct} (kPa)	E_x (kPa)	E_y (kPa)	G_{xy} (kPa)	G_{xx} (kPa)	ν_{xy}	ν_{xx}
50	25	100	11.79	407999	890773	275735	159715	0.06	0.28
70	40	150	14.14	604957	1006382	358166	284996	0.07	0.06
130	60	250	33.00	586732	1260794	382653	257851	0.08	0.14
150	70	290	37.71	655110	1534296	501672	253912	0.10	0.29
220	120	460	47.14	874550	1585566	554187	395713	0.07	0.11
250	140	530	51.85	926828	1777538	621547	429220	0.09	0.08
250	120	490	61.28	782687	2403273	635593	253537	0.26	0.54
250	105	460	68.35	799426	2170726	609756	287506	0.18	0.39

Table A-2 Anisotropic Material Properties for Gradation V2 at Optimum Moisture Content and with 0 Percent Stabilizer

σ_1 (kPa)	σ_3 (kPa)	I (kPa)	τ_{oct} (kPa)	E_x (kPa)	E_y (kPa)	G_{xy} (kPa)	G_{xx} (kPa)	ν_{xy}	ν_{xx}
40	25	90	7.07	54772	254237	37552	22071	0.09	0.24
50	25	100	11.79	54800	327355	37074	22548	0.08	0.22
70	40	150	14.14	136783	430444	103591	58355	0.12	0.17
130	60	250	33.00	212539	632105	145773	94609	0.08	0.12
150	70	290	37.71	273992	934316	235849	100946	0.14	0.36
170	100	370	33.00	262203	995824	259516	94036	0.17	0.39
220	120	460	47.14	345603	1062527	279503	140149	0.14	0.23
250	140	530	51.85	378461	1310265	313370	140675	0.18	0.35
250	120	490	61.28	376636	1460939	361156	129749	0.17	0.45
250	105	460	68.35	392732	1587452	319602	143293	0.20	0.37

Table A-3 Anisotropic Material Properties for Gradation V3 at Optimum Moisture Content and with 0 Percent Stabilizer

σ_1 (kPa)	σ_3 (kPa)	I (kPa)	τ_{oct} (kPa)	E_x (kPa)	E_y (kPa)	G_{xy} (kPa)	G_{xx} (kPa)	ν_{xy}	ν_{xx}
50	25	100	11.79	282735	999478	235110	108391	0.03	0.30
130	60	250	33.00	658052	1209481	390625	319481	0.06	0.03
150	70	290	37.71	757207	1451523	513699	298408	0.11	0.27
250	140	530	51.85	897040	1615723	554187	404778	0.12	0.11
250	120	490	61.28	1140855	2014781	568182	490644	0.15	0.16
250	105	460	68.35	877957	1867575	558313	361331	0.15	0.21

Table A-4 Anisotropic Material Properties for Gradation V4 at Optimum Moisture Content and with 0 Percent Stabilizer

σ_1 (kPa)	σ_3 (kPa)	I (kPa)	τ_{oct} (kPa)	E_x (kPa)	E_y (kPa)	G_{xy} (kPa)	G_{xx} (kPa)	ν_{xy}	ν_{xx}
40	25	90	7.07	506078	975507	342466	188231	0.04	0.34
50	25	100	11.79	680883	1151239	423968	274879	0.13	0.24
70	40	150	14.14	793574	1209709	465839	341594	0.09	0.16
130	60	250	33.00	856913	1448135	553506	328353	0.13	0.30
170	100	370	33.00	962594	1707956	614754	392228	0.14	0.23
220	120	460	47.14	830130	2037554	655977	290660	0.19	0.43
250	140	530	51.85	1275576	2979479	698758	574886	0.25	0.11
250	120	490	61.28	800970	2476130	673653	244088	0.31	0.64

Table A-5 Anisotropic Material Properties for Gradation V1 at Wet of Optimum Moisture State and with 0 Percent Stabilizer

σ_1 (kPa)	σ_3 (kPa)	I (kPa)	τ_{oct} (kPa)	E_x (kPa)	E_y (kPa)	G_{xy} (kPa)	G_{xx} (kPa)	ν_{xy}	ν_{xx}
40	25	90	7.07	72962	467291	52588	30067	0.15	0.21
50	25	100	11.79	66942	387321	61779	26685	0.07	0.25
70	40	150	14.14	158958	406815	125839	83535	0.11	-0.05
130	60	250	33.00	183730	651261	141777	70366	0.13	0.31
150	70	290	37.71	288403	792113	227964	106333	0.14	0.36
170	100	370	33.00	334617	713910	234742	141449	0.14	0.18
220	120	460	47.14	409054	745146	257437	191455	0.08	0.07
250	140	530	51.85	490193	886248	303235	224969	0.10	0.09
250	120	490	61.28	435410	1392751	296834	167094	0.21	0.30
250	105	460	68.35	418325	1012693	284810	182941	0.10	0.14

Table A-6 Anisotropic Material Properties for Gradation V2 at Wet of Optimum Moisture State and with 0 Percent Stabilizer

σ_1 (kPa)	σ_3 (kPa)	I (kPa)	τ_{oct} (kPa)	E_x (kPa)	E_y (kPa)	G_{xy} (kPa)	G_{xx} (kPa)	ν_{xy}	ν_{xx}
40	25	90	7.07	200143	416710	98307	97072	0.05	0.03
50	25	100	11.79	130036	470040	96154	49476	0.08	0.31
70	40	150	14.14	269782	474421	153689	143201	0.07	-0.06
130	60	250	33.00	227430	637046	146628	92389	0.11	0.23
150	70	290	37.71	301509	881960	226244	109708	0.13	0.37
170	100	370	33.00	375139	779960	261780	162614	0.10	0.15
220	120	460	47.14	425723	876274	268176	188988	0.09	0.13
250	140	530	51.85	486107	1025855	326560	218042	0.09	0.11
250	120	490	61.28	351126	1461822	300000	115565	0.24	0.52
250	105	460	68.35	368657	1072980	258621	159897	0.09	0.15

Table A-7 Anisotropic Material Properties for Gradation V3 at Wet of Optimum Moisture State and with 0 Percent Stabilizer

σ_1 (kPa)	σ_3 (kPa)	I (kPa)	τ_{oct} (kPa)	E_x (kPa)	E_y (kPa)	G_{xy} (kPa)	G_{xx} (kPa)	ν_{xy}	ν_{xx}
50	25	100	11.79	55278	328066	48860	21188	0.07	0.30
70	40	150	14.14	108024	287415	77399	57678	0.07	-0.06
130	60	250	33.00	96401	456156	73638	37888	0.11	0.27
150	70	290	37.71	136949	632217	117925	51762	0.10	0.32
170	100	370	33.00	181633	508474	143678	87660	0.10	0.04
220	120	460	47.14	202045	582179	141598	101413	0.08	0.00
250	140	530	51.85	258238	695468	181598	131577	0.09	-0.02
250	120	490	61.28	157029	1173503	156467	54509	0.20	0.44
250	105	460	68.35	136347	1158008	139147	46841	0.17	0.46

Table A-8 Anisotropic Material Properties for Gradation V1 at Optimum Moisture Content and with 1 Percent Stabilizer

σ_1 (kPa)	σ_3 (kPa)	I (kPa)	τ_{oct} (kPa)	E_x (kPa)	E_y (kPa)	G_{xy} (kPa)	G_{xx} (kPa)	ν_{xy}	ν_{xx}
40	25	90	7.07	304847	681939	154776	130901	0.11	0.16
50	25	100	11.79	342322	820023	187032	56475	0.11	2.03
70	40	150	14.14	458693	777046	274725	208341	0.09	0.10
130	60	250	33.00	544205	968725	321888	258786	0.06	0.05
150	70	290	37.71	643812	1295099	431034	254109	0.12	0.27
170	100	370	33.00	714515	1313584	464396	302214	0.12	0.18
220	120	460	47.14	843767	1296535	479744	418307	0.06	0.01
250	140	530	51.85	922733	1526293	548780	457096	0.08	0.01
250	120	490	61.28	799461	2122272	548780	276792	0.23	0.44
250	105	460	68.35	785377	1855399	533175	312232	0.14	0.26

Table A-9 Anisotropic Material Properties for Gradation V2 at Optimum Moisture Content and with 1 Percent Stabilizer

σ_1 (kPa)	σ_3 (kPa)	I (kPa)	τ_{oct} (kPa)	E_x (kPa)	E_y (kPa)	G_{xy} (kPa)	G_{xx} (kPa)	ν_{xy}	ν_{xx}
50	25	100	11.79	619215	666686	292740	297654	0.05	0.04
70	40	150	14.14	1015995	768792	389004	435227	0.14	0.17
130	60	250	33.00	962041	1077504	423729	344950	0.25	0.39
150	70	290	37.71	1251790	1020801	510031	551415	0.08	0.14
170	100	370	33.00	1348871	1056840	528914	617447	0.09	0.09
220	120	460	47.14	1343106	1174157	556931	649303	0.09	0.03
250	140	530	51.85	1295081	1273401	608108	626437	0.07	0.03
250	120	490	61.28	1057167	1723858	609756	327120	0.33	0.62
250	105	460	68.35	1148131	1623244	614754	390644	0.24	0.47

Table A-10 Anisotropic Material Properties for Gradation V3 at Optimum Moisture Content and with 1 Percent Stabilizer

σ_1 (kPa)	σ_3 (kPa)	I (kPa)	τ_{oct} (kPa)	E_x (kPa)	E_y (kPa)	G_{xy} (kPa)	G_{xx} (kPa)	ν_{xy}	ν_{xx}
40	25	90	7.07	528203	879104	295119	214035	0.10	0.23
50	25	100	11.79	316946	1023836	258621	117660	0.03	0.35
70	40	150	14.14	632468	1305290	431530	252224	0.12	0.25
130	60	250	33.00	778930	1510339	530035	340161	0.07	0.14
150	70	290	37.71	997202	1725886	627615	441029	0.07	0.13
170	100	370	33.00	1012444	1790483	665779	438313	0.07	0.15
220	120	460	47.14	1074580	2001887	732899	458164	0.08	0.17
250	140	530	51.85	1025617	2428077	800712	396509	0.13	0.29
250	120	490	61.28	875993	2784545	815217	262394	0.26	0.67
250	105	460	68.35	1134939	2597932	812274	406530	0.17	0.40

Table A-11 Anisotropic Material Properties for Gradation V4 at Optimum Moisture Content and with 1 Percent Stabilizer

σ_1 (kPa)	σ_3 (kPa)	I (kPa)	τ_{oct} (kPa)	E_x (kPa)	E_y (kPa)	G_{xy} (kPa)	G_{xx} (kPa)	ν_{xy}	ν_{xx}
50	25	100	11.79	209922	1069731	417362	57089	0.02	0.84
70	40	150	14.14	1130948	1129021	513347	534791	0.07	0.06
130	60	250	33.00	1297191	1524061	632378	489100	0.14	0.33
150	70	290	37.71	1418332	1663261	810373	539831	0.11	0.31
170	100	370	33.00	1178796	1826704	768443	441036	0.11	0.34
220	120	460	47.14	1276425	1878665	803571	577303	0.06	0.11
250	140	530	51.85	1211750	1948413	786713	576703	0.04	0.05
250	120	490	61.28	1743137	1932056	842697	937933	0.03	0.07
250	105	460	68.35	2169333	2018993	916497	1068483	0.06	0.02

Table A-12 Anisotropic Material Properties for Gradation V1 at Wet of Optimum Moisture State and with 1 Percent Stabilizer

σ_1 (kPa)	σ_3 (kPa)	I (kPa)	τ_{oct} (kPa)	E_x (kPa)	E_y (kPa)	G_{xy} (kPa)	G_{xx} (kPa)	ν_{xy}	ν_{xx}
40	25	90	7.07	82239	274590	68683	36221	0.14	0.14
50	25	100	11.79	104268	381624	88235	44905	0.13	0.16
70	40	150	14.14	150097	516374	124792	54228	0.18	0.38
130	60	250	33.00	255484	758751	178147	91377	0.15	0.40
150	70	290	37.71	372933	914505	269300	138598	0.15	0.35
170	100	370	33.00	365429	821428	269300	146501	0.16	0.25
220	120	460	47.14	467796	976808	304465	203513	0.11	0.15
250	140	530	51.85	572000	1169904	372517	252614	0.13	0.13
250	120	490	61.28	539828	1216003	362319	212786	0.13	0.27
250	105	460	68.35	516822	1297108	362903	199890	0.14	0.29

Table A-13 Anisotropic Material Properties for Gradation V2 at Wet of Optimum Moisture State and with 1 Percent Stabilizer

σ_1 (kPa)	σ_3 (kPa)	I (kPa)	τ_{oct} (kPa)	E_x (kPa)	E_y (kPa)	G_{xy} (kPa)	G_{xx} (kPa)	ν_{xy}	ν_{xx}
70	40	150	14.14	196789	623668	156250	65420	0.19	0.50
130	60	250	33.00	244571	809577	181818	90465	0.13	0.35
150	70	290	37.71	348563	954529	278293	130582	0.14	0.33
170	100	370	33.00	356315	888702	279851	150976	0.15	0.18
220	120	460	47.14	432137	1040738	304878	194791	0.10	0.11
250	140	530	51.85	479221	1183800	358852	215356	0.08	0.11
250	120	490	61.28	473564	1319736	363489	196021	0.11	0.21
250	105	460	68.35	486772	1347931	367647	201206	0.11	0.21

Table A-14 Anisotropic Material Properties for Gradation V3 at Wet of Optimum Moisture State and with 1 Percent Stabilizer

σ_1 (kPa)	σ_3 (kPa)	I (kPa)	τ_{oct} (kPa)	E_x (kPa)	E_y (kPa)	G_{xy} (kPa)	G_{xx} (kPa)	ν_{xy}	ν_{xx}
40	25	90	7.07	226158	437020	110698	107786	0.08	0.05
70	40	150	14.14	382245	642307	234375	153818	0.15	0.24
130	60	250	33.00	404385	790550	246305	153448	0.14	0.32
150	70	290	37.71	601111	1016625	366748	227937	0.13	0.32
170	100	370	33.00	684292	933550	373134	293750	0.13	0.16
220	120	460	47.14	715003	1000918	384615	328208	0.09	0.09
250	140	530	51.85	767216	1116992	417440	353979	0.10	0.08
250	120	490	61.28	764414	1180050	425331	324840	0.12	0.18
250	105	460	68.35	718482	1162057	405405	302426	0.11	0.19

Table A-15 Anisotropic Material Properties for Gradation V4 at Wet of Optimum Moisture State and with 1 Percent Stabilizer

σ_1 (kPa)	σ_3 (kPa)	I (kPa)	τ_{oct} (kPa)	E_x (kPa)	E_y (kPa)	G_{xy} (kPa)	G_{xx} (kPa)	ν_{xy}	ν_{xx}
50	25	100	11.79	187211	956502	328947	52492	0.02	0.78
70	40	150	14.14	1604654	1086057	543085	760530	0.20	0.05
130	60	250	33.00	1172671	1295674	563698	523836	0.08	0.12
150	70	290	37.71	1908010	1422082	742942	1097072	0.02	-0.13
170	100	370	33.00	1200422	1642764	711913	473949	0.09	0.27
220	120	460	47.14	1683841	1660659	755034	1024119	0.03	-0.18
250	140	530	51.85	1135025	1992203	778547	458207	0.10	0.24
250	120	490	61.28	1434526	1890862	815217	666907	0.05	0.08
250	105	460	68.35	1654365	1947381	835499	782112	0.07	0.06

Table A-16 Anisotropic Material Properties for Gradation V1 at Optimum Moisture Content and with 2 Percent Stabilizer

σ_1 (kPa)	σ_3 (kPa)	I (kPa)	τ_{oct} (kPa)	E_x (kPa)	E_y (kPa)	G_{xy} (kPa)	G_{xx} (kPa)	ν_{xy}	ν_{xx}
40	25	90	7.07	492561	767923	253300	198970	0.15	0.24
50	25	100	11.79	223342	855143	225904	77842	0.03	0.43
70	40	150	14.14	597390	859463	327941	313661	0.06	-0.05
130	60	250	33.00	663564	1120585	391645	319188	0.06	0.04
150	70	290	37.71	828225	1342073	515464	367732	0.07	0.13
220	120	460	47.14	1022087	1420501	559701	536876	0.05	-0.05
250	140	530	51.85	1098606	1568120	625000	564847	0.05	-0.03
250	120	490	61.28	860615	2193155	613079	290246	0.24	0.48
250	105	460	68.35	953928	1727227	601604	407754	0.10	0.17

Table A-17 Anisotropic Material Properties for Gradation V2 at Optimum Moisture Content and with 2 Percent Stabilizer

σ_1 (kPa)	σ_3 (kPa)	I (kPa)	τ_{oct} (kPa)	E_x (kPa)	E_y (kPa)	G_{xy} (kPa)	G_{xx} (kPa)	ν_{xy}	ν_{xx}
40	25	90	7.07	50300	141000	37800	23955	0.02	0.05
50	25	100	11.79	34700	174000	40300	12919	0.02	0.34
70	40	150	14.14	79100	219000	66100	30778	0.06	0.29
130	60	250	33.00	103000	318000	97900	35690	0.09	0.44
150	70	290	37.71	79000	388000	110000	24428	0.07	0.62
170	100	370	33.00	170000	403000	134000	65334	0.10	0.30
220	120	460	47.14	206000	476000	150000	81423	0.11	0.27
250	140	530	51.85	166000	490000	164000	56617	0.09	0.47
250	120	490	61.28	180000	485000	156000	66176	0.09	0.36
250	105	460	68.35	155000	518000	151000	56323	0.08	0.38

Table A-18 Anisotropic Material Properties for Gradation V3 at Optimum Moisture Content and with 2 Percent Stabilizer

σ_1 (kPa)	σ_3 (kPa)	I (kPa)	τ_{oct} (kPa)	E_x (kPa)	E_y (kPa)	G_{xy} (kPa)	G_{xx} (kPa)	ν_{xy}	ν_{xx}
40	25	90	7.07	733489	1374930	422259	240011	0.24	0.53
50	25	100	11.79	592193	1222316	468750	197372	0.05	0.50
70	40	150	14.14	952945	1521807	599042	361921	0.16	0.32
130	60	250	33.00	978342	1828911	648508	372954	0.13	0.31
150	70	290	37.71	908589	1937410	748503	317822	0.08	0.43
170	100	370	33.00	1161810	2021459	790306	463954	0.10	0.25

Table A-19 Anisotropic Material Properties for Gradation V4 at Optimum Moisture Content and with 2 Percent Stabilizer

σ_1 (kPa)	σ_3 (kPa)	I (kPa)	τ_{oct} (kPa)	E_x (kPa)	E_y (kPa)	G_{xy} (kPa)	G_{xx} (kPa)	ν_{xy}	ν_{xx}
130	60	250	33.00	832274	2277659	709891	288589	0.16	0.44
170	100	370	33.00	1127521	2630655	899820	427490	0.09	0.32
220	120	460	47.14	1222085	2422041	933610	508908	0.06	0.20
250	140	530	51.85	1351765	2625103	953390	558421	0.10	0.21

Table A-20 Anisotropic Material Properties for Gradation V1 at Wet of Optimum Moisture State and with 2 Percent Stabilizer

σ_1 (kPa)	σ_3 (kPa)	I (kPa)	τ_{oct} (kPa)	E_x (kPa)	E_y (kPa)	G_{xy} (kPa)	G_{xx} (kPa)	ν_{xy}	ν_{xx}
50	25	100	11.79	134192	374232	107759	53336	0.18	0.26
70	40	150	14.14	201945	372949	138122	103562	0.09	-0.03
130	60	250	33.00	260296	722902	183824	99854	0.15	0.30
150	70	290	37.71	334493	935565	266430	127229	0.14	0.31
170	100	370	33.00	363407	835339	281955	170735	0.12	0.06
220	120	460	47.14	506031	883396	319149	303969	0.04	-0.17
250	120	490	61.28	640464	1045789	362903	207432	0.09	0.54
250	105	460	68.35	552658	1132342	371287	320014	0.05	-0.14

Table A-21 Anisotropic Material Properties for Gradation V2 at Wet of Optimum Moisture State and with 2 Percent Stabilizer

σ_1 (kPa)	σ_3 (kPa)	I (kPa)	τ_{oct} (kPa)	E_x (kPa)	E_y (kPa)	G_{xy} (kPa)	G_{xx} (kPa)	ν_{xy}	ν_{xx}
50	25	100	11.79	110631	392056	89928	46511	0.13	0.19
70	40	150	14.14	154289	465560	140449	66743	0.18	0.16
130	60	250	33.00	283071	771990	202156	111018	0.13	0.27
150	70	290	37.71	402806	1003147	292398	149358	0.15	0.35
170	100	370	33.00	395383	892633	292398	158263	0.15	0.25
220	120	460	47.14	505901	1022787	328947	224207	0.10	0.13
250	140	530	51.85	559811	1176741	378788	239322	0.12	0.17
250	120	490	61.28	537579	1262602	374376	214663	0.13	0.25
250	105	460	68.35	571001	1280959	376884	238019	0.12	0.20

Table A-22 Anisotropic Material Properties for Gradation V3 at Wet of Optimum Moisture State and with 2 Percent Stabilizer

σ_1 (kPa)	σ_3 (kPa)	I (kPa)	τ_{oct} (kPa)	E_x (kPa)	E_y (kPa)	G_{xy} (kPa)	G_{xx} (kPa)	ν_{xy}	ν_{xx}
50	25	100	11.79	128190	340346	90253	57084	0.10	0.12
70	40	150	14.14	200182	441928	145914	86908	0.14	0.15
130	60	250	33.00	271537	616304	169300	115807	0.09	0.17
150	70	290	37.71	366454	799784	258176	140675	0.12	0.30
220	120	460	47.14	528035	941264	322812	235445	0.10	0.12
250	140	530	51.85	557005	1074495	357143	251539	0.09	0.11
250	120	490	61.28	578756	1125806	376884	248576	0.10	0.16
250	105	460	68.35	582115	1153167	365854	240849	0.11	0.21

Table A-23 Anisotropic Material Properties for Gradation V4 at Wet of Optimum Moisture State and with 2 Percent Stabilizer

σ_1 (kPa)	σ_3 (kPa)	I (kPa)	τ_{oct} (kPa)	E_x (kPa)	E_y (kPa)	G_{xy} (kPa)	G_{xx} (kPa)	ν_{xy}	ν_{xx}
50	25	100	11.79	172481	420253	117925	73349	0.10	0.18
70	40	150	14.14	262003	549253	178571	107589	0.15	0.22
130	60	250	33.00	359129	746230	212766	140382	0.11	0.28
150	70	290	37.71	476990	939285	302419	178353	0.14	0.34
220	120	460	47.14	609995	946891	343511	269901	0.11	0.13
250	140	530	51.85	718569	1003387	383959	372743	0.07	-0.04
250	120	490	61.28	741061	1120595	403226	335002	0.11	0.11
250	105	460	68.35	662417	1144670	383305	271932	0.12	0.22

APPENDIX B

TABLES OF MODULAR RATIOS

Table B-1 Modular Ratios for Gradation V1 at Optimum Moisture Content and with 0 Percent Stabilizer

σ_1 (kPa)	σ_3 (kPa)	I (kPa)	τ_{oct} (kPa)	E_x/E_y	G_{xy}/E_y	G_{xx}/G_{xy}
50	25	100	11.79	0.46	0.31	0.58
70	40	150	14.14	0.60	0.36	0.80
130	60	250	33.00	0.47	0.30	0.67
150	70	290	37.71	0.43	0.33	0.51
220	120	460	47.14	0.55	0.35	0.71
250	140	530	51.85	0.52	0.35	0.69
250	120	490	61.28	0.33	0.26	0.40
250	105	460	68.35	0.37	0.28	0.47

Table B-2 Modular Ratios for Gradation V2 at Optimum Moisture Content and with 0 Percent Stabilizer

σ_1 (kPa)	σ_3 (kPa)	I (kPa)	τ_{oct} (kPa)	E_x/E_y	G_{xy}/E_y	G_{xx}/G_{xy}
40	25	90	7.07	0.22	0.15	0.59
50	25	100	11.79	0.17	0.11	0.61
70	40	150	14.14	0.32	0.24	0.56
130	60	250	33.00	0.34	0.23	0.65
150	70	290	37.71	0.29	0.25	0.43
170	100	370	33.00	0.26	0.26	0.36
220	120	460	47.14	0.33	0.26	0.50
250	140	530	51.85	0.29	0.24	0.45
250	120	490	61.28	0.26	0.25	0.36
250	105	460	68.35	0.25	0.20	0.45

Table B-3 Modular Ratios for Gradation V3 at Optimum Moisture Content and with 0 Percent Stabilizer

σ_1 (kPa)	σ_3 (kPa)	I (kPa)	τ_{oct} (kPa)	E_x/E_y	G_{xy}/E_y	G_{xx}/G_{xy}
50	25	100	11.79	0.28	0.24	0.46
130	60	250	33.00	0.54	0.32	0.82
150	70	290	37.71	0.52	0.35	0.58
250	140	530	51.85	0.56	0.34	0.73
250	120	490	61.28	0.57	0.28	0.86
250	105	460	68.35	0.47	0.30	0.65

Table B-4 Modular Ratios for Gradation V4 at Optimum Moisture Content and with 0 Percent Stabilizer

σ_1 (kPa)	σ_3 (kPa)	I (kPa)	τ_{oct} (kPa)	E_x/E_y	G_{xy}/E_y	G_{xx}/G_{xy}
40	25	90	7.07	0.52	0.35	0.55
50	25	100	11.79	0.59	0.37	0.65
70	40	150	14.14	0.66	0.39	0.73
130	60	250	33.00	0.59	0.38	0.59
170	100	370	33.00	0.56	0.36	0.64
220	120	460	47.14	0.41	0.32	0.44
250	140	530	51.85	0.43	0.23	0.82
250	120	490	61.28	0.32	0.27	0.36

Table B-5 Modular Ratios for Gradation V1 at Wet of Optimum Moisture State and with 0 Percent Stabilizer

σ_1 (kPa)	σ_3 (kPa)	I (kPa)	τ_{oct} (kPa)	E_x/E_y	G_{xy}/E_y	G_{xx}/G_{xy}
40	25	90	7.07	0.16	0.11	0.57
50	25	100	11.79	0.17	0.16	0.43
70	40	150	14.14	0.39	0.31	0.66
130	60	250	33.00	0.28	0.22	0.50
150	70	290	37.71	0.36	0.29	0.47
170	100	370	33.00	0.47	0.33	0.60
220	120	460	47.14	0.55	0.35	0.74
250	140	530	51.85	0.55	0.34	0.74
250	120	490	61.28	0.31	0.21	0.56
250	105	460	68.35	0.41	0.28	0.64

Table B-6 Modular Ratios for Gradation V2 at Wet of Optimum Moisture State and with 0 Percent Stabilizer

σ_1 (kPa)	σ_3 (kPa)	I (kPa)	τ_{oct} (kPa)	E_x/E_y	G_{xy}/E_y	G_{xx}/G_{xy}
40	25	90	7.07	0.48	0.24	0.99
50	25	100	11.79	0.28	0.20	0.51
70	40	150	14.14	0.57	0.32	0.93
130	60	250	33.00	0.36	0.23	0.63
150	70	290	37.71	0.34	0.26	0.48
170	100	370	33.00	0.48	0.34	0.62
220	120	460	47.14	0.49	0.31	0.70
250	140	530	51.85	0.47	0.32	0.67
250	120	490	61.28	0.24	0.21	0.39
250	105	460	68.35	0.34	0.24	0.62

Table B-7 Modular Ratios for Gradation V3 at Wet of Optimum Moisture State and with 0 Percent Stabilizer

σ_1 (kPa)	σ_3 (kPa)	I (kPa)	τ_{oct} (kPa)	E_x/E_y	G_{xy}/E_y	G_{xx}/G_{xy}
50	25	100	11.79	0.17	0.15	0.43
70	40	150	14.14	0.38	0.27	0.75
130	60	250	33.00	0.21	0.16	0.51
150	70	290	37.71	0.22	0.19	0.44
170	100	370	33.00	0.36	0.28	0.61
220	120	460	47.14	0.35	0.24	0.72
250	140	530	51.85	0.37	0.26	0.72
250	120	490	61.28	0.13	0.13	0.35
250	105	460	68.35	0.12	0.12	0.34

Table B-8 Modular Ratios for Gradation V1 at Optimum Moisture Content and with 1 Percent Stabilizer

σ_1 (kPa)	σ_3 (kPa)	I (kPa)	τ_{oct} (kPa)	E_x/E_y	G_{xy}/E_y	G_{xx}/G_{xy}
40	25	90	7.07	0.45	0.23	0.85
50	25	100	11.79	0.42	0.23	0.30
70	40	150	14.14	0.59	0.35	0.76
130	60	250	33.00	0.56	0.33	0.80
150	70	290	37.71	0.50	0.33	0.59
170	100	370	33.00	0.54	0.35	0.65
220	120	460	47.14	0.65	0.37	0.87
250	140	530	51.85	0.60	0.36	0.83
250	120	490	61.28	0.38	0.26	0.50
250	105	460	68.35	0.42	0.29	0.59

Table B-9 Modular Ratios for Gradation V2 at Optimum Moisture Content and with 1 Percent Stabilizer

σ_1 (kPa)	σ_3 (kPa)	I (kPa)	τ_{oct} (kPa)	E_x/E_y	G_{xy}/E_y	G_{xx}/G_{xy}
50	25	100	11.79	0.93	0.44	1.02
70	40	150	14.14	1.32	0.51	1.12
130	60	250	33.00	0.89	0.39	0.81
150	70	290	37.71	1.23	0.50	1.08
170	100	370	33.00	1.28	0.50	1.17
220	120	460	47.14	1.14	0.47	1.17
250	140	530	51.85	1.02	0.48	1.03
250	120	490	61.28	0.61	0.35	0.54
250	105	460	68.35	0.71	0.38	0.64

Table B-10 Modular Ratios for Gradation V3 at Optimum Moisture Content and with 1 Percent Stabilizer

σ_1 (kPa)	σ_3 (kPa)	I (kPa)	τ_{oct} (kPa)	E_x/E_y	G_{xy}/E_y	G_{xx}/G_{xy}
40	25	90	7.07	0.60	0.34	0.73
50	25	100	11.79	0.31	0.25	0.45
70	40	150	14.14	0.48	0.33	0.58
130	60	250	33.00	0.52	0.35	0.64
150	70	290	37.71	0.58	0.36	0.70
170	100	370	33.00	0.57	0.37	0.66
220	120	460	47.14	0.54	0.37	0.63
250	140	530	51.85	0.42	0.33	0.50
250	120	490	61.28	0.31	0.29	0.32
250	105	460	68.35	0.44	0.31	0.50

Table B-11 Modular Ratios for Gradation V4 at Optimum Moisture Content and with 1 Percent Stabilizer

σ_1 (kPa)	σ_3 (kPa)	I (kPa)	τ_{oct} (kPa)	E_x/E_y	G_{xy}/E_y	G_{xx}/G_{xy}
50	25	100	11.79	0.20	0.39	0.14
70	40	150	14.14	1.00	0.45	1.04
130	60	250	33.00	0.85	0.41	0.77
150	70	290	37.71	0.85	0.49	0.67
170	100	370	33.00	0.65	0.42	0.57
220	120	460	47.14	0.68	0.43	0.72
250	140	530	51.85	0.62	0.40	0.73
250	120	490	61.28	0.90	0.44	1.11
250	105	460	68.35	1.07	0.45	1.17

Table B-12 Modular Ratios for Gradation V1 at Wet of Optimum Moisture State and with 1 Percent Stabilizer

σ_1 (kPa)	σ_3 (kPa)	I (kPa)	τ_{oct} (kPa)	E_x/E_y	G_{xy}/E_y	G_{xx}/G_{xy}
40	25	90	7.07	0.30	0.25	0.53
50	25	100	11.79	0.27	0.23	0.51
70	40	150	14.14	0.29	0.24	0.43
130	60	250	33.00	0.34	0.23	0.51
150	70	290	37.71	0.41	0.29	0.51
170	100	370	33.00	0.44	0.33	0.54
220	120	460	47.14	0.48	0.31	0.67
250	140	530	51.85	0.49	0.32	0.68
250	120	490	61.28	0.44	0.30	0.59
250	105	460	68.35	0.40	0.28	0.55

Table B-13 Modular Ratios for Gradation V2 at Wet of Optimum Moisture State and with 1 Percent Stabilizer

σ_1 (kPa)	σ_3 (kPa)	I (kPa)	τ_{oct} (kPa)	E_x/E_y	G_{xy}/E_y	G_{xx}/G_{xy}
70	40	150	14.14	0.32	0.25	0.42
130	60	250	33.00	0.30	0.22	0.50
150	70	290	37.71	0.37	0.29	0.47
170	100	370	33.00	0.40	0.31	0.54
220	120	460	47.14	0.42	0.29	0.64
250	140	530	51.85	0.40	0.30	0.60
250	120	490	61.28	0.36	0.28	0.54
250	105	460	68.35	0.36	0.27	0.55

Table B-14 Modular Ratios for Gradation V3 at Wet of Optimum Moisture State and with 1 Percent Stabilizer

σ_1 (kPa)	σ_3 (kPa)	I (kPa)	τ_{oct} (kPa)	E_x/E_y	G_{xy}/E_y	G_{xx}/G_{xy}
40	25	90	7.07	0.52	0.25	0.97
70	40	150	14.14	0.60	0.36	0.66
130	60	250	33.00	0.51	0.31	0.62
150	70	290	37.71	0.59	0.36	0.62
170	100	370	33.00	0.73	0.40	0.79
220	120	460	47.14	0.71	0.38	0.85
250	140	530	51.85	0.69	0.37	0.85
250	120	490	61.28	0.65	0.36	0.76
250	105	460	68.35	0.62	0.35	0.75

Table B-15 Modular Ratios for Gradation V4 at Wet of Optimum Moisture State and with 1 Percent Stabilizer

σ_1 (kPa)	σ_3 (kPa)	I (kPa)	τ_{oct} (kPa)	E_x/E_y	G_{xy}/E_y	G_{xx}/G_{xy}
50	25	100	11.79	0.20	0.34	0.16
70	40	150	14.14	1.48	0.50	1.40
130	60	250	33.00	0.91	0.44	0.93
150	70	290	37.71	1.34	0.52	1.48
170	100	370	33.00	0.73	0.43	0.67
220	120	460	47.14	1.01	0.45	1.36
250	140	530	51.85	0.57	0.39	0.59
250	120	490	61.28	0.76	0.43	0.82
250	105	460	68.35	0.85	0.43	0.94

Table B-16 Modular Ratios for Gradation V1 at Optimum Moisture Content and with 2 Percent Stabilizer

σ_1 (kPa)	σ_3 (kPa)	I (kPa)	τ_{oct} (kPa)	E_x/E_y	G_{xy}/E_y	G_{xx}/G_{xy}
40	25	90	7.07	0.64	0.33	0.79
50	25	100	11.79	0.26	0.26	0.34
70	40	150	14.14	0.70	0.38	0.96
130	60	250	33.00	0.59	0.35	0.81
150	70	290	37.71	0.62	0.38	0.71
220	120	460	47.14	0.72	0.39	0.96
250	140	530	51.85	0.70	0.40	0.90
250	120	490	61.28	0.39	0.28	0.47
250	105	460	68.35	0.55	0.35	0.68

Table B-17 Modular Ratios for Gradation V2 at Optimum Moisture Content and with 2 Percent Stabilizer

σ_1 (kPa)	σ_3 (kPa)	I (kPa)	τ_{oct} (kPa)	E_x/E_y	G_{xy}/E_y	G_{xx}/G_{xy}
40	25	90	7.07	0.36	0.27	0.63
50	25	100	11.79	0.20	0.23	0.32
70	40	150	14.14	0.36	0.30	0.47
130	60	250	33.00	0.32	0.31	0.36
150	70	290	37.71	0.20	0.28	0.22
170	100	370	33.00	0.42	0.33	0.49
220	120	460	47.14	0.43	0.32	0.54
250	140	530	51.85	0.34	0.33	0.35
250	120	490	61.28	0.37	0.32	0.42
250	105	460	68.35	0.30	0.29	0.37

Table B-18 Modular Ratios for Gradation V3 at Optimum Moisture Content and with 2 Percent Stabilizer

σ_1 (kPa)	σ_3 (kPa)	I (kPa)	τ_{oct} (kPa)	E_x/E_y	G_{xy}/E_y	G_{xx}/G_{xy}
40	25	90	7.07	0.53	0.31	0.57
50	25	100	11.79	0.48	0.38	0.42
70	40	150	14.14	0.63	0.39	0.60
130	60	250	33.00	0.53	0.35	0.58
150	70	290	37.71	0.47	0.39	0.42
170	100	370	33.00	0.57	0.39	0.59

Table B-19 Modular Ratios for Gradation V4 at Optimum Moisture Content and with 2 Percent Stabilizer

σ_1 (kPa)	σ_3 (kPa)	I (kPa)	τ_{oct} (kPa)	E_x/E_y	G_{xy}/E_y	G_{xx}/G_{xy}
130	60	250	33.00	0.37	0.31	0.41
170	100	370	33.00	0.43	0.34	0.48
220	120	460	47.14	0.50	0.39	0.55
250	140	530	51.85	0.51	0.36	0.59

Table B-20 Modular Ratios for Gradation V1 at Wet of Optimum Moisture State and with 2 Percent Stabilizer

σ_1 (kPa)	σ_3 (kPa)	I (kPa)	τ_{oct} (kPa)	E_x/E_y	G_{xy}/E_y	G_{xx}/G_{xy}
50	25	100	11.79	0.36	0.29	0.49
70	40	150	14.14	0.54	0.37	0.75
130	60	250	33.00	0.36	0.25	0.54
150	70	290	37.71	0.36	0.28	0.48
170	100	370	33.00	0.44	0.34	0.61
220	120	460	47.14	0.57	0.36	0.95
250	120	490	61.28	0.61	0.35	0.57
250	105	460	68.35	0.49	0.33	0.86

Table B-21 Modular Ratios for Gradation V2 at Wet of Optimum Moisture State and with 2 Percent Stabilizer

σ_1 (kPa)	σ_3 (kPa)	I (kPa)	τ_{oct} (kPa)	E_x/E_y	G_{xy}/E_y	G_{xx}/G_{xy}
50	25	100	11.79	0.28	0.23	0.52
70	40	150	14.14	0.33	0.30	0.48
130	60	250	33.00	0.37	0.26	0.55
150	70	290	37.71	0.40	0.29	0.51
170	100	370	33.00	0.44	0.33	0.54
220	120	460	47.14	0.49	0.32	0.68
250	140	530	51.85	0.48	0.32	0.63
250	120	490	61.28	0.43	0.30	0.57
250	105	460	68.35	0.45	0.29	0.63

Table B-22 Modular Ratios for Gradation V3 at Wet of Optimum Moisture State and with 2 Percent Stabilizer

σ_1 (kPa)	σ_3 (kPa)	I (kPa)	τ_{oct} (kPa)	E_x/E_y	G_{xy}/E_y	G_{xx}/G_{xy}
50	25	100	11.79	0.38	0.27	0.63
70	40	150	14.14	0.45	0.33	0.60
130	60	250	33.00	0.44	0.27	0.68
150	70	290	37.71	0.46	0.32	0.54
220	120	460	47.14	0.56	0.34	0.73
250	140	530	51.85	0.52	0.33	0.70
250	120	490	61.28	0.51	0.33	0.66
250	105	460	68.35	0.50	0.32	0.66

Table B-23 Modular Ratios for Gradation V4 at Wet of Optimum Moisture State and with 2 Percent Stabilizer

σ_1 (kPa)	σ_3 (kPa)	I (kPa)	τ_{oct} (kPa)	E_x/E_y	G_{xy}/E_y	G_{xx}/G_{xy}
50	25	100	11.79	0.41	0.28	0.62
70	40	150	14.14	0.48	0.33	0.60
130	60	250	33.00	0.48	0.29	0.66
150	70	290	37.71	0.51	0.32	0.59
220	120	460	47.14	0.64	0.36	0.79
250	140	530	51.85	0.72	0.38	0.97
250	120	490	61.28	0.66	0.36	0.83
250	105	460	68.35	0.58	0.33	0.71

APPENDIX C

FINES UNDER LIGHT MICROSCOPE

Figure C-1 Light Microscope Image of Granite Materials (A8) Smaller than 0.15 mm (Passing Sieve #100)

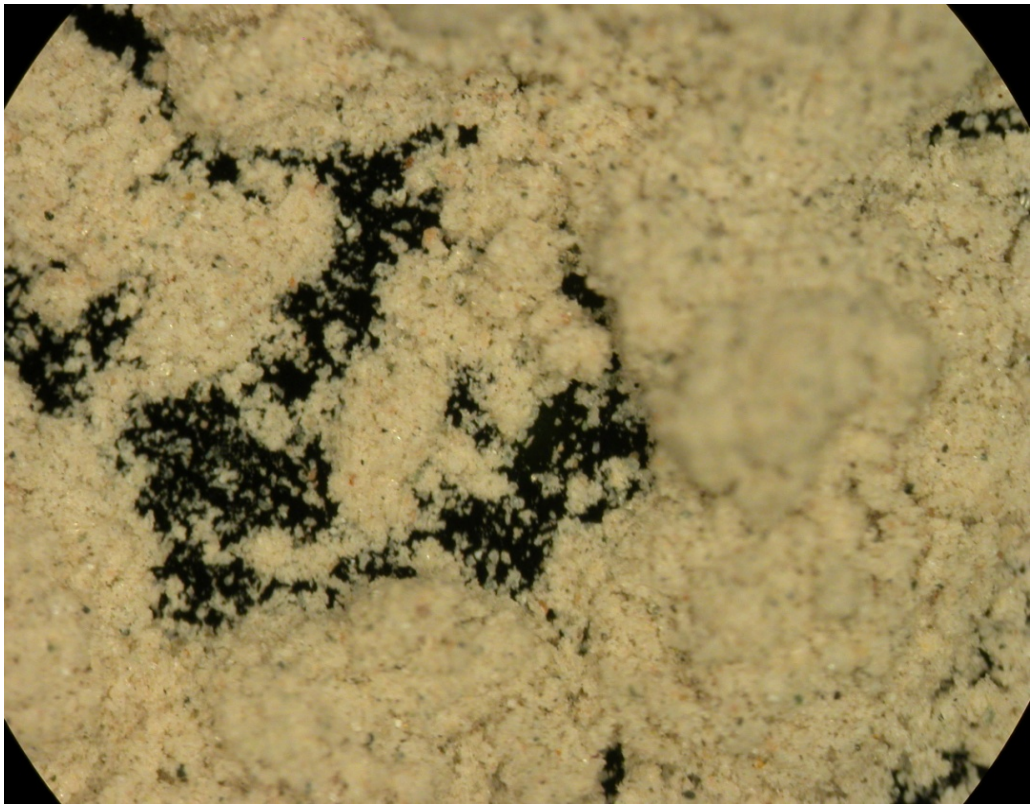

Figure C-2 Light Microscope Image of Granite Materials (A8) Smaller than 0.075 mm (Passing Sieve #200)

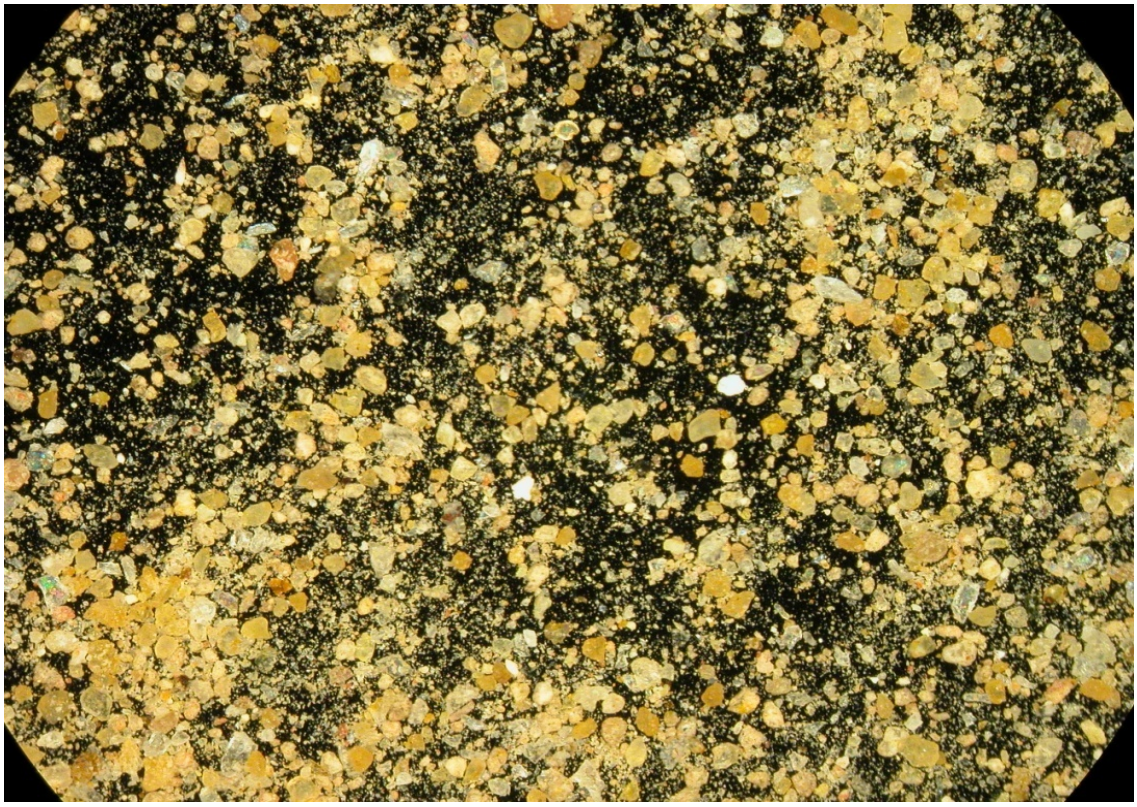

Figure C-3 Light Microscope Image of Siliceous Gravel (A5) Smaller than 0.15 mm (Passing Sieve #100)

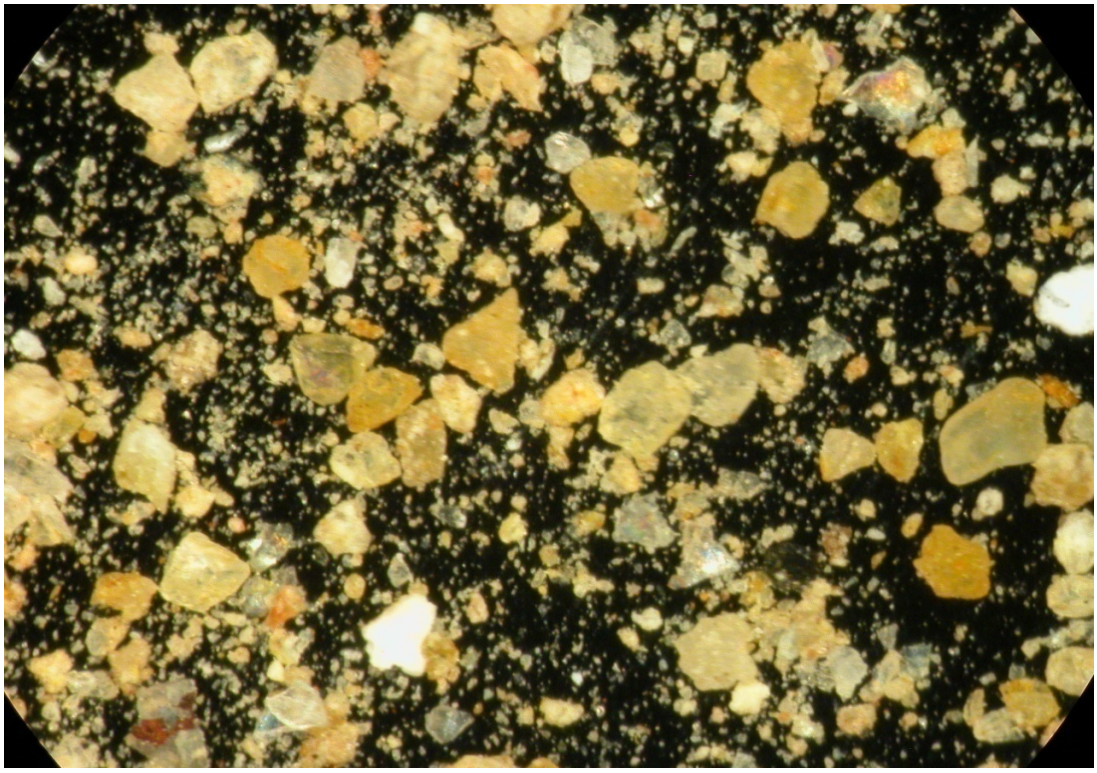

Figure C-4 Light Microscope Image of Siliceous Gravel (A5) Smaller than 0.075 mm (Passing Sieve #200)

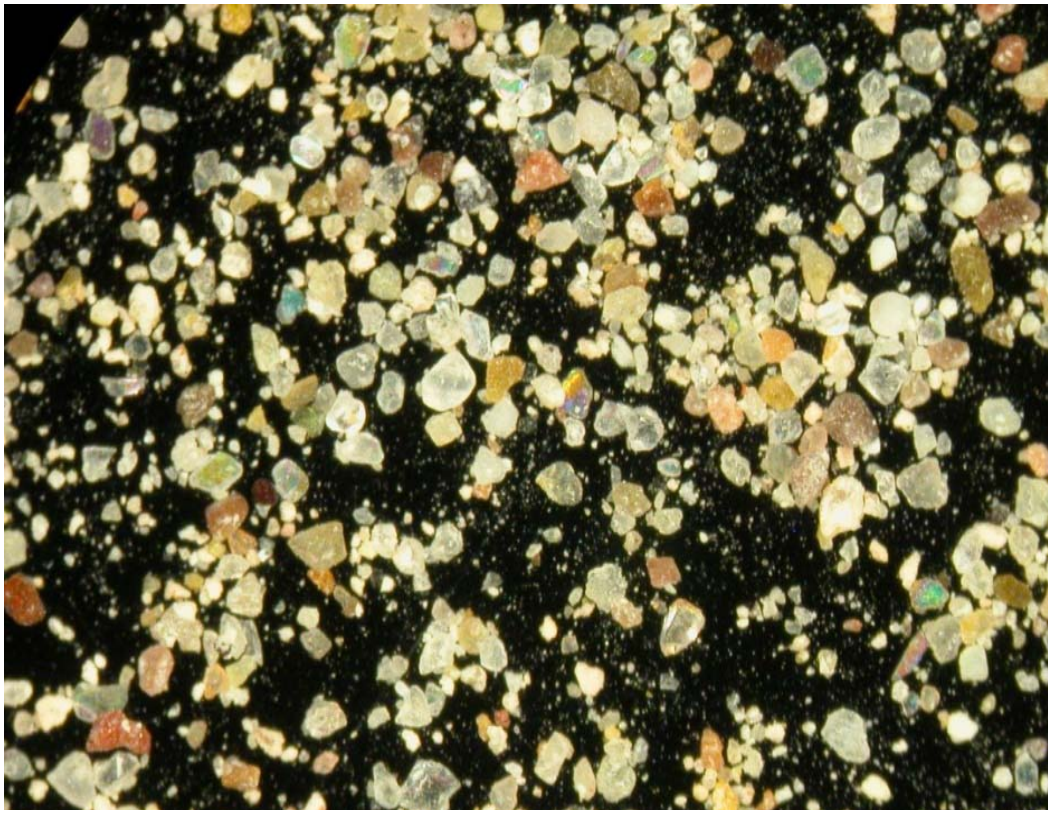

Figure C-5 Light Microscope Image of Siliceous Gravel (A6) Smaller than 0.15 mm (Passing Sieve #100)

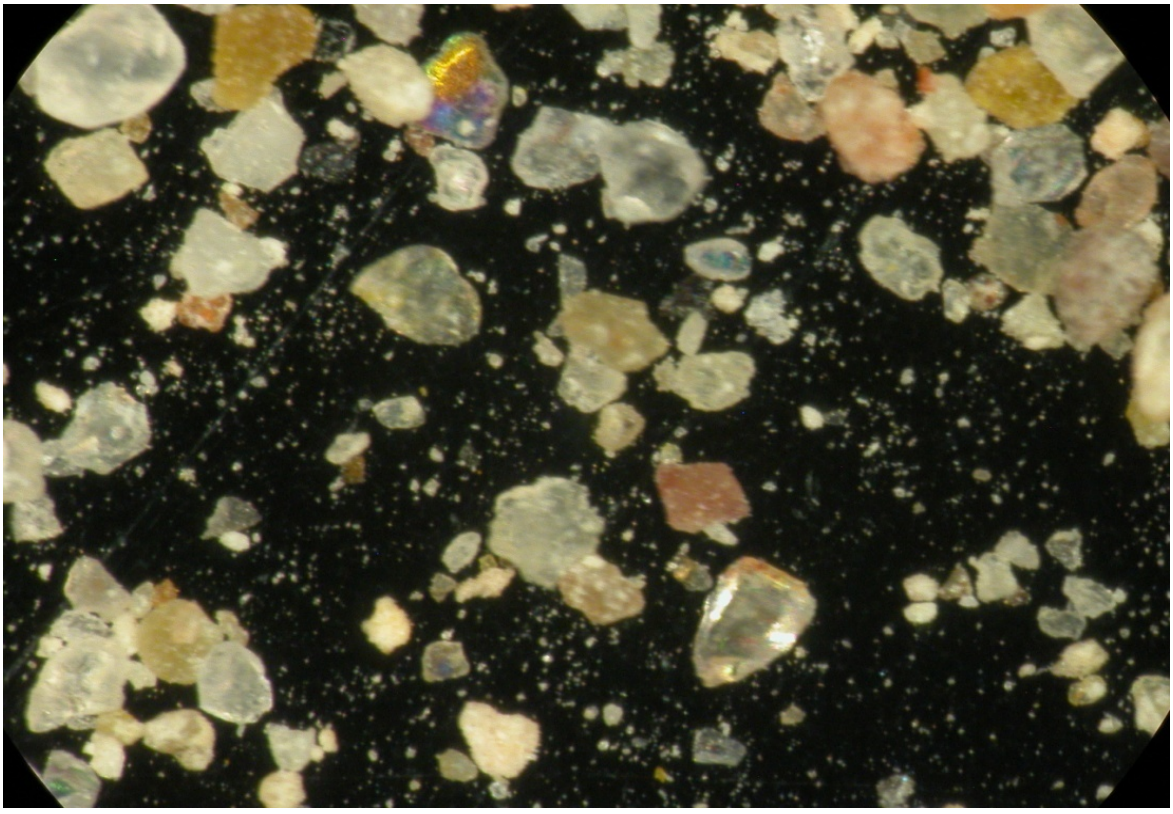

Figure C-6 Light Microscope Image of Siliceous Gravel (A6) Smaller than 0.075 mm (Passing Sieve #200)

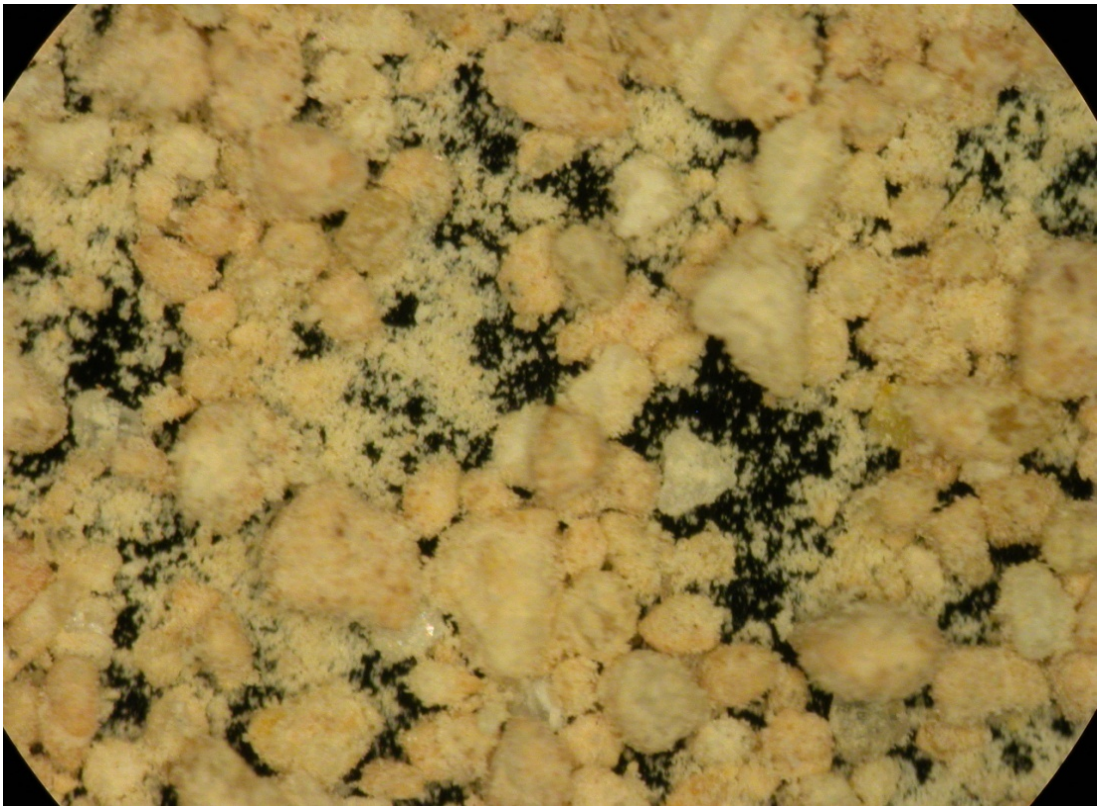

Figure C-7 Light Microscope Image of Limestone (A7) Smaller than 0.15 mm (Passing Sieve #100)

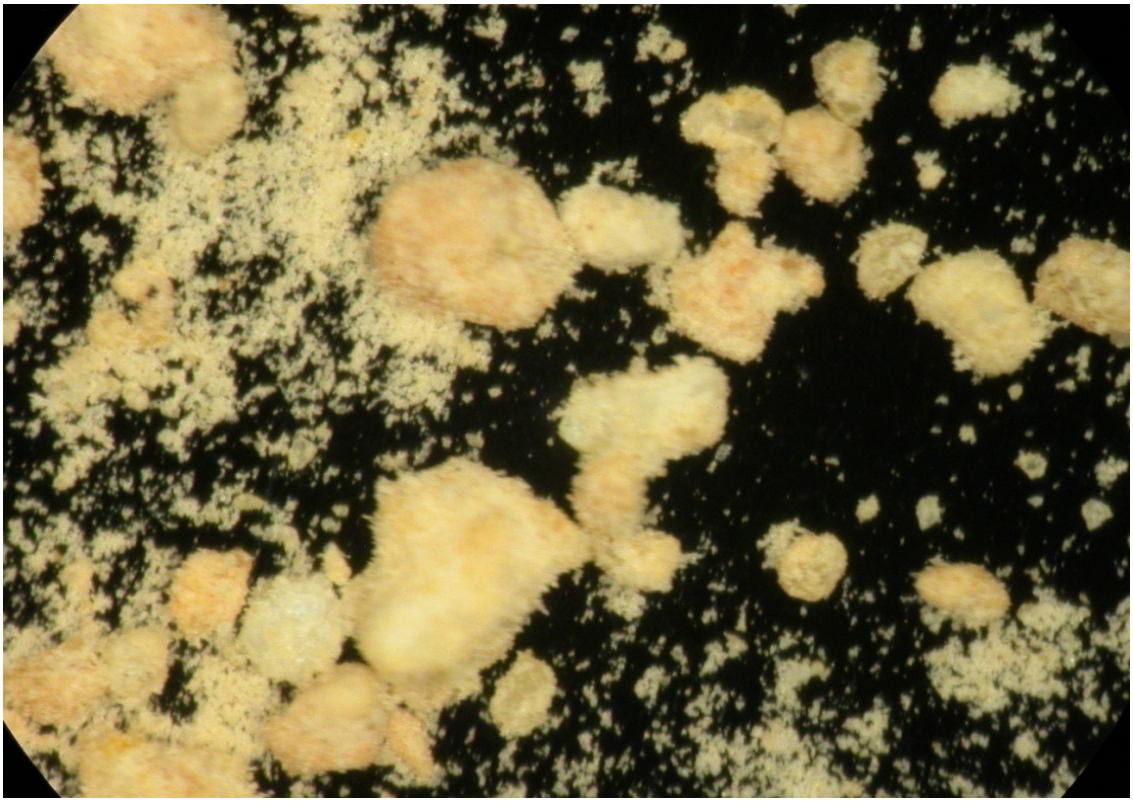

Figure C-8 Light Microscope Image of Limestone (A7) Smaller than 0.075 mm (Passing Sieve #200)

Figure C-9 Light Microscope Image of Limestone (A2) Smaller than 0.15 mm (Passing Sieve #100)

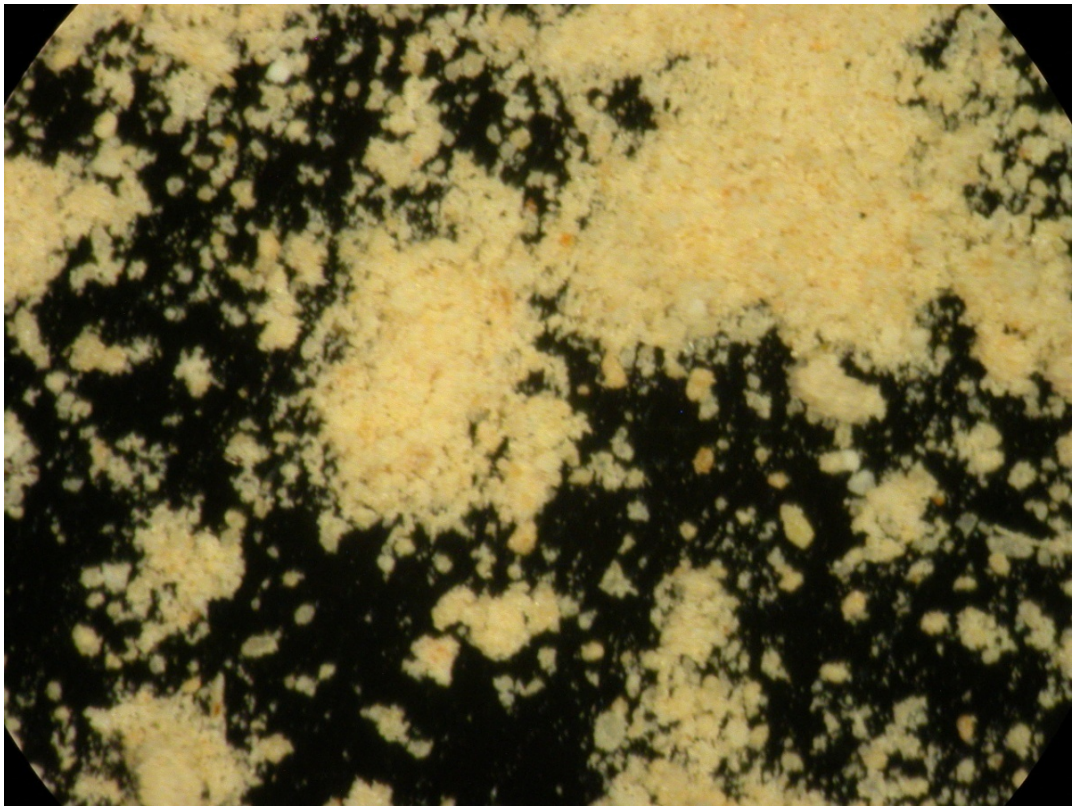

Figure C-10 Light Microscope Image of Limestone (A2) Smaller than 0.075 mm (Passing Sieve #200)

VITA

Name:	Reza Salehi Ashtiani
Address:	Zachry Department of Civil Engineering CE/TTI Tower Texas A&M University, MS 3135 College Station, TX 77843-3135
Email Address:	reza@tamu.edu
Education:	B.S., Civil Engineering Azad University of Tehran, Tehran, Iran, 1996 M.S., Transportation Engineering Tarbiat Modarres University, Tehran, Iran, 2000 Ph.D. Pavements and Materials Engineering Texas A&M University, USA, 2009
Research Interests:	Unsaturated Soil Mechanics Chemical Stabilization of Geomaterials Numerical Analysis of Geomaterials Pavement Analysis and Design Pattern Recognition Operation Research

Reza Salehi received his Bachelor of Science degree in Civil Engineering from The Azad University of Tehran, Iran, in 1996. He entered the Transportation Engineering program at Tarbiat Modarres University in Tehran, Iran, in 1998 and received his Master of Science degree in September 2000. In 2004 Reza continued at his education in the Ph.D. program at Texas A&M University with the emphasis on civil engineering materials. Reza was involved in several consulting and government funded research projects during his course of graduate work at Texas A&M University. His research interests include but not limited to unsaturated soil mechanics, analysis and design of civil engineering infrastructure, pavement analysis and design, numerical analysis of geomaterials, traffic assignment problems, and operational research.